ANL-05/21

Diagnostic Examination of Generation 2 Lithium-Ion Cells and Assessment of Performance Degradation Mechanisms

prepared by
Chemical Engineering Division
Argonne National Laboratory

**Argonne National Laboratory is managed by
The University of Chicago for the U. S. Department of Energy**

**Research funded by U.S. DOE's FreedomCAR and
Vehicle Technologies Program**

About Argonne National Laboratory
Argonne is managed by The University of Chicago for the U.S. Department of Energy under contract W-31-109-Eng-38. The Laboratory's main facility is outside Chicago, at 9700 South Cass Avenue, Argonne, Illinois 60439. For information about Argonne and its pioneering science and technology programs, see www.anl.gov.

Availability of This Report
This report is available, at no cost, at http://www.osti.gov/bridge. It is also available on paper to U.S. Department of Energy and its contractors, for a processing fee, from:

U.S. Department of Energy
Office of Scientific and Technical Information
P.O. Box 62
Oak Ridge, TN 37831-0062
phone (865) 576-8401
fax (865) 576-5728
reports@adonis.osti.gov

Advanced Technology Development Program
for Lithium-Ion Batteries

ANL-05/21

Diagnostic Examination of Generation 2 Lithium-Ion Cells and Assessment of Performance Degradation Mechanisms

Edited by

Daniel P. Abraham

Contributors from

Argonne National Laboratory
Brookhaven National Laboratory
Lawrence Berkeley National Laboratory
University of Illinois at Urbana-Champaign

July 2005

CONTENTS

FIGURES

TABLES

CONTRIBUTORS

Argonne National Laboratory
Daniel P Abraham
Dennis W. Dees
Gary L. Henriksen
Jamie Knuth
Evangeline Reynolds
Rex Gerald
Andrew Jansen
Yoo-Eup Hyung
Ilias Belharouak
Michael Stoll

Lawrence Berkeley National Laboratory
Vincent Battaglia
Elton Cairns
John Kerr
Marie Kerlau
Robert Kostecki
Jinglei Lei
Kathryn McCarthy
Frank McLarnon
Laura Norin
Jeffrey Reimer
Thomas Richardson
Philip Ross
Steven Sloop
Xiangyun Song
Vera Zhuang

University of Illinois at Urbana-Champaign
Ernest Sammann
Scott MacLaren
Richard Haasch
Ray Twesten
Mauro Sardela

Brookhaven National Laboratory
Mahalingam Balasubramanian
James McBreen
Kyung–Yoon Chung
Xiao Qing Yang
Won–Sub Yoon

ACKNOWLEDGEMENTS

This report was supported by the Assistant Secretary of Energy Efficiency and Renewable Energy, Office of FreedomCar & Vehicle Technologies, of the U.S. Department of Energy under Contract Nos. W-31-109-ENG-38 (ANL), DE-AC02-98CH10886 (BNL), and DE-AC03-76SF00098 (LBNL). The contributors to this report acknowledge the financial support of the DOE Office of FreedomCAR & Vehicle Technologies and are especially grateful to Tien Duong, Dave Howell, and Jack Deppe. We also gratefully acknowledge the contributions and cooperation of all ATD program participants and reviewers. We are especially grateful to Ira Bloom at ANL and Jon Christopherson at INL for the 18650 cell data. We acknowledge the contributions of Ivan Petrov and Judy Bauer from the Center for Microanalysis of Materials (CMM) at the University of Illinois at Urbana-Champaign (UIUC); this facility is partially supported by the U.S. Department of Energy under grant DEFG02-91ER45439.

GLOSSARY OF TERMS

AC	alternating current
AFM	atomic force microscopy
ANL	Argonne National Laboratory
ASI	area-specific impedance (ohm-cm^2)
ATD	Advanced Technology Development
ATR	attenuated total reflection
BNL	Brookhaven National Laboratory
BSF	battery scaling factor
CSAFM	current-sensing atomic force microscopy
CE	capillary electrophoresis
CF	capacity fade
DEC	diethyl carbonate
DEDOHC	diethyl-2,5-dioxahexane carboxylate
DMC	dimethyl carbonate
DMDOHC	dimethyl-2,5-dioxahexane carboxylate
DME	dimethoxy ethane
DMF	dimethyl formamide
DOE	U.S. Department of Energy
EC	ethylene carbonate
EDX	energy dispersive X-ray analysis
EELS	electron energy loss spectroscopy
EMC	ethyl methyl carbonate
EMDOHC	ethyl methyl-2,5-dioxahexane carboxylate
EOC	end of charge
EOL	end of life
EXAFS	extended X-ray absorption fine structure
EY	electron yield
FFT	fast Fourier transform
FID	flame ionization detector
FTIR	Fourier transform infrared
FY	fluorescence yield
GC	gas chromatography
GC-MS	gas chromatography mass spectrometry
GPC	gel permeation chromatography
Gen 1 (+)	$LiNi_{0.8}Co_{0.2}O_2$ cathode
Gen 1 (–)	MCMB:SFG-6 (82:18)
Gen 1 electrolyte	1.2 M $LiPF_6$ EC:DEC (1:1 by wt)
Gen 2 cells	ATD Generation 2 baseline cells
Gen 2 (+)	$LiNi_{0.8}Co_{0.15}Al_{0.05}O_2$ cathode
Gen 2 (–)	MAG-10 synthetic graphite anode
Gen 2 electrolyte	1.2 M $LiPF_6$ EC:EMC (3:7 by wt)
HEV	hybrid electric vehicle
HF	hydrogen fluoride (hydrofluoric acid)

HPLC	high-performance liquid chromatography
HPPC test	hybrid pulse power characterization test
HREM	high-resolution electron microscopy
HRTEM	high-resolution transmission electron microscopy
ICP-MS	inductively coupled plasma mass spectrometry
INL	Idaho National Laboratory
IR	infrared
LBNL	Lawrence Berkeley National Laboratory
LiBOB	lithium bis (oxalato) borate
MCMB	mesocarbon microbeads
MS	mass spectroscopy (or mass spectrometer)
mol wt	molecular weight
NMR	nuclear magnetic resonance
NSLS	National Synchrotron Light Source
PC	propylene carbonate
PE	polyethylene
PEO	poly(ethylene) oxide
PF	power fade
PNGV	Partnership for a New Generation of Vehicles
PP	polypropylene
ppm	part(s) per million (by weight)
PVA	polyvinyl alcohol
PVDF	polyvinylidene fluoride
PSD	position sensitive detector
RE cell	reference electrode cell
RPT	reference performance testing
RT	room temperature
SAED	selected-area electron diffraction
SEI	solid electrolyte interface
SEM	scanning electron microscopy
SIMS	secondary ion mass spectroscopy
SOC	state of charge
SPM	scanning probe microscopy
STM	scanning tunneling microscopy
TCD	thermal conductivity detector
TEM	transmission electron microscopy
THF	tetrahydrofuran
UHV	ultrahigh vacuum
Var C cells	Generation 2 Variant C cells
XANES	X-ray absorption near edge spectra
XAS	X-ray absorption spectroscopy
XPS	X-ray photoelectron spectroscopy
XRD	X-ray diffraction

DIAGNOSTIC EXAMINATION OF GENERATION 2 LITHIUM-ION CELLS AND ASSESSMENT OF PERFORMANCE DEGRADATION MECHANISMS

Edited by

Daniel P. Abraham

ABSTRACT

The Advanced Technology Development (ATD) Program is a multi-laboratory effort to assist industrial developers of high-power lithium-ion batteries overcome the barriers of cost, calendar life, abuse tolerance, and low-temperature performance so that this technology may be rendered practical for use in hybrid electric vehicles (HEVs). Included in the ATD Program is a comprehensive diagnostics effort conducted by researchers at Argonne National Laboratory (ANL), Brookhaven National Laboratory (BNL), and Lawrence Berkeley National Laboratory (LBNL). The goals of this effort are to identify and characterize processes that limit lithium-ion battery performance and calendar life, and ultimately to describe the specific mechanisms that cause performance degradation.

This report is a compilation of the diagnostics effort conducted since spring 2001 to characterize Generation 2 ATD cells and cell components. The report is divided into a main body and appendices. Information on the diagnostic approach, details from individual diagnostic techniques, and details on the phenomenological model used to link the diagnostic data to the loss of 18650-cell electrochemical performance are included in the appendices. The main body of the report includes an overview of the 18650-cell test data, summarizes diagnostic data and modeling information contained in the appendices, and provides an assessment of the various mechanisms that have been postulated to explain performance degradation of the 18650 cells during accelerated aging.

This report is intended to serve as a ready reference on ATD Generation 2 18650-cell performance and provide information on the tools for diagnostic examination and relevance of the acquired data. A comprehensive account of our experimental procedures and resulting data may be obtained by consulting the various references listed in the text. We hope that this report will serve as a roadmap for the diagnostic analyses of other lithium-ion technologies being evaluated for HEV applications. It is our hope that the information contained in this report will lead to the development of new lithium-ion cell chemistries and designs that will meet the 15-year cell calendar-life goal established by DOE's FreedomCar and Fuel Partnership.

1 INTRODUCTION

Lithium-ion batteries currently power millions of portable electronic devices all over the world. These cells have high energy densities, excellent cycle life, wide operating temperature ranges and long shelf lives. Because of their relatively high power densities, lithium-ion cells are also attractive as energy storage devices for hybrid electric vehicles (HEVs) [1]. These devices are required to deliver and accept high-power pulses during vehicle acceleration (rapid discharge capability) and braking (rapid charging capability). Because cell discharging and charging involve lithium-ion diffusion within the electrolyte, through the electrolyte-electrode interface, and through the electrode, any resistance to charge movement contributes to the internal impedance of the cell. An increase in impedance consequently degrades the power performance of the cells.

The performance of 18650-type (18 mm diameter, 65 mm length) lithium-ion cells specifically designed for high-power applications is being evaluated as part of the U.S. Department of Energy's (DOE's) Advanced Technology Development (ATD) Program [2–4]. These cells are tested under various accelerated aging conditions to determine calendar-life and cycle-life performance. Changes during cell testing are determined by C/1 and C/25 capacity measurements, and by hybrid pulse-power characterization (HPPC) and electrochemical impedance spectroscopy (EIS) measurements. The resulting data indicate that capacity fade and impedance rise are determined by several factors that include aging temperature, cell voltage (i.e., state of charge), cycling parameters, and electrode material composition. All groups of cells studied to date reach end of life because of increasing impedance and corresponding power loss. Deriving performance degradation mechanisms from the 18650 cell test results is difficult, however, because the measured data are a superposition of several processes occurring in the cell.

In an effort to identify the sources of capacity fade and impedance rise, various diagnostic tools were used to examine the nature and extent of physical, chemical, and structural changes in the cell and cell components that resulted from the accelerated aging [5–24]. Capacity and impedance data were obtained on electrodes harvested from the 18650 cells to identify the positive and negative electrode contributions to cell impedance rise. Electrode and separator materials were characterized by various microscopy, spectroscopy, and diffraction techniques to determine the extent of aging-induced material degradation. Changes in the cell electrolyte and gases generated during cell aging were monitored to identify possible electrode-electrolyte reactions. A phenomenological cell model was developed and used to study and identify possible phenomena that could cause the observed impedance rise [25]. Understanding performance degradation mechanisms is critical to the development of new lithium-ion cell chemistries that can meet the 15-year cell calendar life goal established by DOE's FreedomCar and Fuel Partnership. This understanding is also required to establish a physical basis for the application of algorithms that predict long-term cell lifetimes based on short-term cell test data, as illustrated by the Technology Life Verification Test (TLVT) Manual [26].

This report presents data from the diagnostic examination of ATD Generation 2 lithium-ion cells and outlines our current understanding of the cell degradation processes. It is divided into a main body and appendices. The main body of the report (1) includes an overview of the 18650 cell test data, (2) summarizes diagnostic data that were used to identify cell components and physicochemical processes that give rise to impedance rise and capacity fade, (3) presents the analysis of a phenomenological model that links the diagnostic findings to the observed cell aging characteristics, and (4) assesses the strengths and weaknesses of various mechanisms postulated to explain the degradation in cell performance. The appendices contain information on the diagnostic approach, details from individual diagnostic techniques, and details of the phenomenological model. The overall process for the diagnostic evaluation of a generic lithium ion battery technology is described in Appendix A. Detailed information from the various diagnostic tests is contained in Appendices B through G. Information on the phenomenological model is presented in Appendix H.

2 GEN 2 CELL DESCRIPTION

The cells were of the standard 18650 size; however, they were custom-designed for better high-power performance and better hermeticity. The cells employed 10 tabs along the length of both the positive and negative electrodes to reduce the resistance associated with the current collection system during high-current charge and discharge pulses. Also, the cells employed an aluminum case, which was connected to the positive electrode, and the cells were sealed by a laser weld. All cells were leak-checked, to ensure a high degree of hermeticity, prior to being shipped.

Table 1 lists details of electrode construction and cell chemistry employed in the Generation 2 (Gen 2) baseline cells, which had a starting C/1 capacity of ~1 Ah. The electrode materials were selected on the basis of material screening tests of advanced low-cost materials available from international suppliers in 2000. The electrolyte formulation was developed jointly by Argonne National Laboratory (ANL) and the U.S. Army Research Laboratory (ARL) and made for the ATD program by Quallion, LLC, the same company that designed and built the Gen 2 high-power 18650 cells to ANL specifications.

Table 1. Gen 2 Cell Chemistry (average electrode active area = 846.3 cm^2)

Positive Electrode	**Negative Electrode**
84 wt% $LiNi_{0.8}Co_{0.15}Al_{0.05}O_2$ (Fuji CA1505)	92 wt% MAG-10 graphite (Hitachi)
8 wt% PVdF binder (Kureha KF-1100)	8 wt% PVdF binder (Kureha #C)
4 wt% SFG-6 graphite (Timical)	
4 wt% carbon black (Chevron)	
8 mg/cm^2 loading density	4.9 mg/cm^2 loading density
35-µm-thick coating/side	35-µm-thick coating/side
30-µm-thick Al current collector	18-µm-thick Cu current collector
Electrolyte	**Separator**
1.2 M $LiPF_6$ in EC:EMC (3:7)	25 µm thick (Celgard 2300)

A second group of cells, termed the Variant C (Var C) cells, was built using a cell chemistry that was very similar to that shown in Table 1, except that the level of aluminum dopant in the positive electrode active material was increased from 5% to 10%. This $LiNi_{0.8}Co_{0.1}Al_{0.1}O_2$ material was produced by Fuji Chemical, using the same spray drying process that was used for making the $LiNi_{0.8}Co_{0.15}Al_{0.05}O_2$ used in the Gen 2 cells, and both materials were subjected to the same calcination process. The Var C cells had a starting C/1 capacity of ~0.8 Ah.

3 ACCELERATED AGING TESTS ON 18650 CELLS

3.1 CELL TESTING PROTOCOL AND OTHER DETAILS

After formation cycling by the manufacturer (Quallion, LLC), the cells were shipped to ANL or Idaho National Laboratory (INL) for accelerated aging. The test regime and the laboratory responsible for the testing are given in Table 2. The calendar-life cells were subjected to a daily 3C current pulse at temperature for 28 consecutive days to monitor cell impedance changes, as defined in the test manual [27]. The cycle-life cells were aged using the BSF-scaled, 25-Wh profile of Reference 26. End of life for all cells was arbitrarily defined as 30% power fade (PF); some cells, however, were cycled to ~50% PF to determine their long-term aging characteristics. Throughout the testing, selected cells were removed at predetermined intervals and forwarded to the diagnostic team for disassembly and evaluation.

Table 2. Gen 2 Cell Test Conditions

	Gen 2		Var C	
Testing Laboratory	Calendar[a]	Cycle[a]	Calendar[a]	Cycle[a]
ANL	14 cells, 55°C 2 cells, 45°C		10 cells, 45°C	
INL		14 cells, 25°C 14 cells, 45°C		14 cells, 45°C

[a] Calendar- and cycle-life testing were performed at 60% SOC, which, based on the initial $C_1/25$ tests, corresponded to 3.723 and 3.741 V for the Gen 2 and Var C cells, respectively.

Reference Performance Tests (RPTs) at 25°C were conducted on all cells at 4-week intervals to determine changes in capacity, impedance, and power. The RPT sequence for the cells tested at ANL and INL are given in Table 3. The cells were discharged from 4.1 to 3 V, to determine the C/1 and C/25 discharge capacities. The low-current hybrid pulse power characterization (L-HPPC) tests were used to determine cell impedance and dynamic power capability; a description of the L-HPPC test is provided in Reference 26. Electrochemical impedance spectroscopy (EIS) was used to determine cell impedance over a range of applied frequencies with a 5-mV sinusoidal perturbation about the 60% state of charge (SOC) open circuit voltage. An extensive analysis of the 18650 cell capacity and impedance data is available in Reference 4. Only representative data are discussed in this report.

Table 3. Reference Performance Test Sequence

Temperature, ^{o}C	ANL (Calendar Life)	INL (Cycle Life)
25	C_1/1 discharge	C_1/1 discharge
25	C_1/25 discharge	L-HPPC
25	C_1/25 charge	C_1/25 discharge
25	EIS at 60% SOC	C_1/25 charge
25	L-HPPC	EIS at 60% SOC

3.2 18650 CELL CAPACITY DATA

Capacity decreased as the cells aged. The capacity decrease has a strong temperature dependence, as shown in Figure 1. For example, the C/25 capacity decrease at 45°C is greater than that at 25°C, especially during the early weeks of aging. The capacity loss also shows a marked dependence on the cycling rate. In the early weeks of aging, the decrease in C/25 capacity is greater than that of the C/1 capacity. During the later stages of aging, the decrease in C/1 capacity is more rapid. The onset of the rapid C/1 capacity decline is accelerated by higher aging temperatures. For instance, in Figure 1, the 45°C and 25°C cells show this behavior after ~28 weeks and ~52 weeks of aging, respectively.

The observed capacity loss is also affected by cell aging protocols. Figure 2 compares the C/1 and C/25 capacity fades of calendar-life and cycle-life aged cells at 45°C. The C/25 data for the calendar-life and cycle-life aged cells are very similar, whereas the C/1 capacity loss is greater for the cycle-life cells. The onset of the rapid C/1 capacity decline appears to be earlier for the cycle-life cells. For instance, the data in Figure 2 show that the rapid C/1 capacity decline occurs after ~28 weeks and ~36 weeks of aging for the cycle-life and calendar-life cells, respectively.

The composition of the oxide in the positive electrode also affects the capacity data. Figure 3 compares the C/1 and C/25 capacity fades of Gen 2 and Var C cells that were cycle-life aged cells at 45°C. The capacity losses of the Gen 2 cells are greater than those of the Var C cells, especially during the early weeks of aging. The Var C cells also show the rapid C/1 decline, albeit at a lower rate than the Gen 2 cells and at a later period. Figure 3, for example, shows that the rapid C/1 capacity decline occurs after ~28 weeks and ~68 weeks of aging for the Gen 2 and Var C cells, respectively. Because the only known difference between the Gen 2 and Var C cells is the oxide composition, the data suggest that the additional Al in the Var C oxide delays the rapid C/1 decline during cell aging.

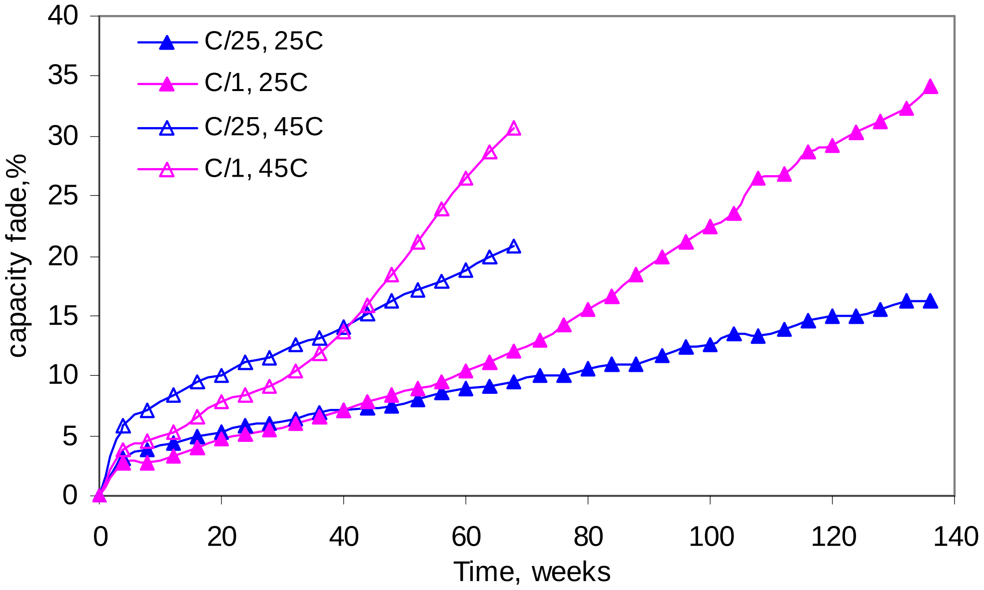

Fig. 1. Comparison of C/1 and C/25 Discharge Capacity Fade Data Measured at 25°C from 18650 Cells Cycle-Life Aged at 25°C and 45°C.

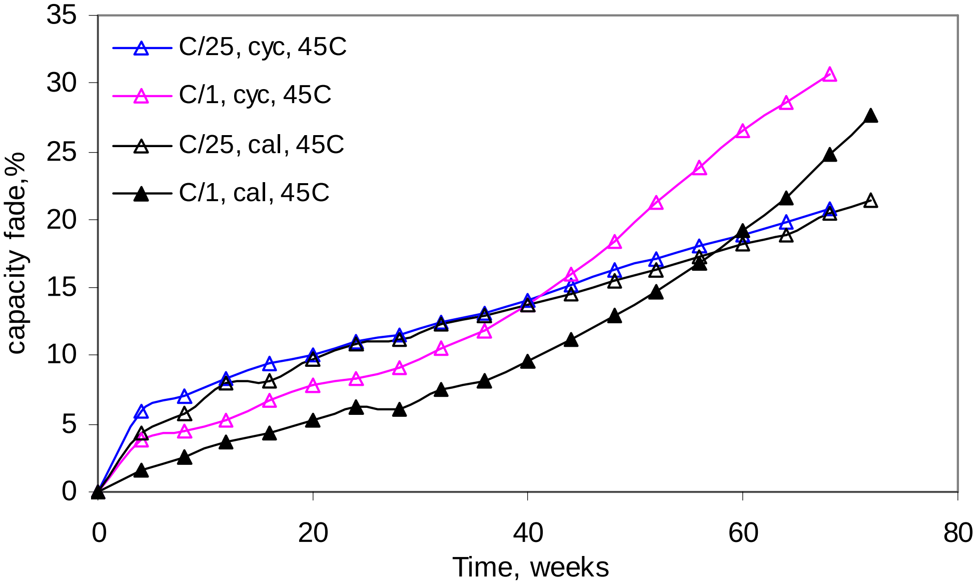

Fig. 2. Comparison of C/1 and C/25 Discharge Capacity Fade Data Measured at 25°C from 18650 Cells Calendar-Life and Cycle-Life Aged at 45°C.

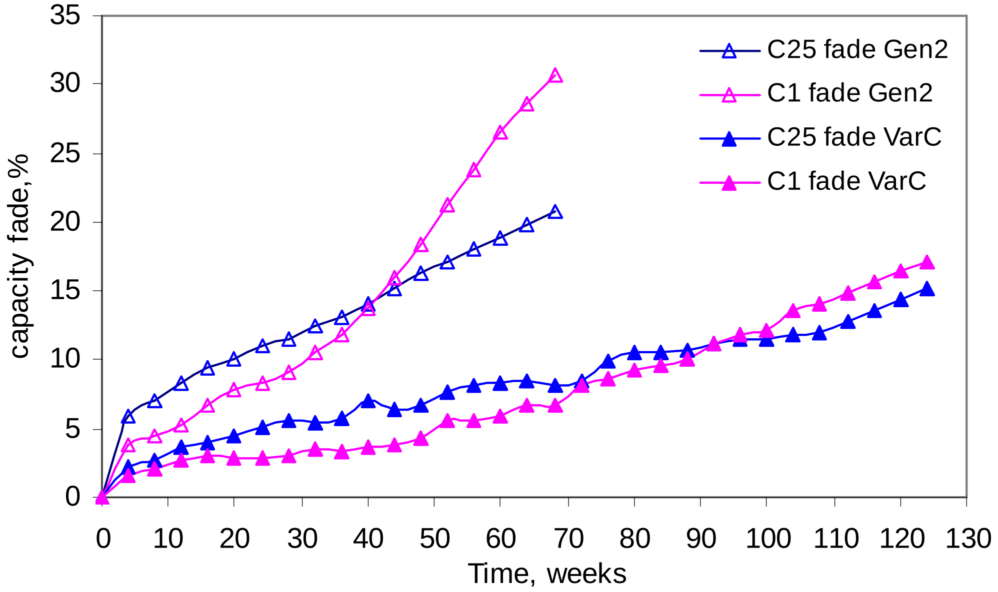

Fig. 3. Comparison of C/1 and C/25 Discharge Capacity Fade Data Measured at 25°C from Gen 2 and Var C 18650 cells Cycle-Life Aged at 45°C.

3.3 18650 CELL IMPEDANCE DATA

As the cells age, the area-specific impedance (ASI) increases. Like the capacity data, the ASI increase also depends upon aging temperature, aging protocol, and the oxide composition. Figure 4 shows the 18-s discharge ASI increase, calculated at 60% SOC, as a function of time for representative Gen 2 and Var C cells. It is evident that the rate of impedance rise is relatively rapid in the first 4 to 8 weeks of aging (Region 1), slower during an intermediate aging period (Region 2), and relatively rapid again at longer aging periods (Region 3).

For the Gen 2 cells, it is apparent that the ASI increase at 45°C is greater than the ASI increase at 25°C. In addition, the ASI increase for the 45°C cycle-life cells is greater than that of the 45°C calendar-life cells; this aging protocol difference becomes apparent only after about 28 weeks of aging. The Var C cells show a faster impedance rise than the Gen 2 cells during the first 4 weeks of aging; after this period, the rate of impedance rise of the Var C cells slows down. Furthermore, the impedance rise for the Var C cycle-life cells is greater than that for the corresponding calendar-life cells.

The Gen 2 cells show a relatively rapid impedance rise during the later periods of aging; this behavior is also present, though not as marked, for the Var C cells. The onset of this rapid impedance rise corresponds roughly to the onset of the rapid C/1 capacity decline observed in the capacity data. As was observed for the capacity data, this onset shows a dependence on aging temperature, aging protocol, and oxide composition. For example, the cycle-life Gen 2 cells aged at 45°C and 25°C show the rapid impedance rise after ~32 weeks and ~48 weeks of aging, respectively; the calendar-life Gen 2 cells aged at 45°C show this onset after ~36 weeks. The onset is significantly delayed and very subtle for the Var C cells; the rate of impedance rise in

Region 3 is also much lower than that for the Gen 2 cells. For example, the Var C cycle-life and calendar-life cells reach the onset of Region 3 only after ~72 and ~92 weeks at 45°C, respectively. The data suggest that the additional Al in the Var C oxide retards the onset of Region 3.

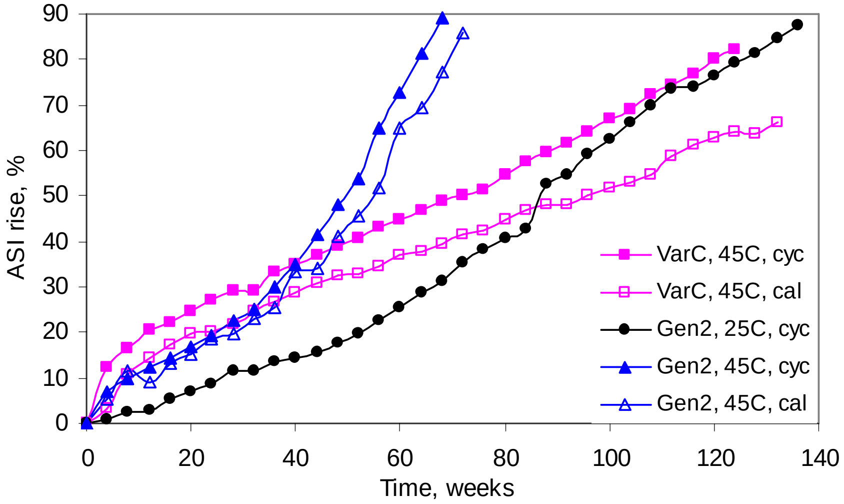

Fig. 4. Representative ASI (18-s Discharge, 60% SOC) vs. Time Data Measured at 25°C for Gen 2 and Var C 18650 Cells.

Additional impedance information was obtained from EIS measurements on the 18650 cells. Representative data over the 10 kHz to 0.01 Hz frequency range obtained at a cell voltage of 3.72 V are shown in Figure 5. Each curve shows impedance data measured at room temperature after the Gen 2 cell was aged at 45°C and 60% SOC for the indicated period. At each measurement, the data show a high-frequency tail (>1 kHz), a depressed semicircular arc at mid-frequencies (to ~1 Hz), and a low-frequency (<1 Hz) Warburg tail. These features are readily apparent in the inset figure that shows only the 0-week data. The high-frequency tail is probably an artifact arising from the interaction of the impedance analyzer with the low-impedance cell. The mid-frequency arc is typically associated with interfacial impedance resulting from charge-transfer reactions proceeding simultaneously on both electrodes, while the low-frequency tail is typically associated with diffusional impedance.

On aging, the high-frequency reactance minimum does not change appreciably, but the low-frequency reactance minimum does. The frequencies at the low-frequency reactance minimum decrease from 2.5 Hz for the 0-week aged cell to 0.4 Hz for the 88-week aged cell, which suggests that cell processes slow down on aging. In addition, the mid-frequency arc width (R_w) that is the portion along the real axis between the high-frequency and low-frequency reactance minima increases on aging, which signifies an increase in the interfacial impedance of the cell.

Very low-frequency (to 0.0001 Hz) alternating current (AC) impedance data obtained on 18650 cells also provided useful information, especially for cells that were aged for longer periods. Figure 6 compares data from two Gen 2 cells that showed 0% and 60% ASI increases. The Warburg tail of the higher impedance cell displays a significantly higher resistance at the very low frequencies, which indicates that diffusion phenomena play an important role in the impedance increases observed after long-term cell aging, such as in Region 3.

Although the HPPC and EIS data from the 18650 cells are valuable, the information cannot identify the electrodes or mechanisms that produce the changes in impedance on aging. That information can only be obtained by examining electrodes harvested from the aged cells.

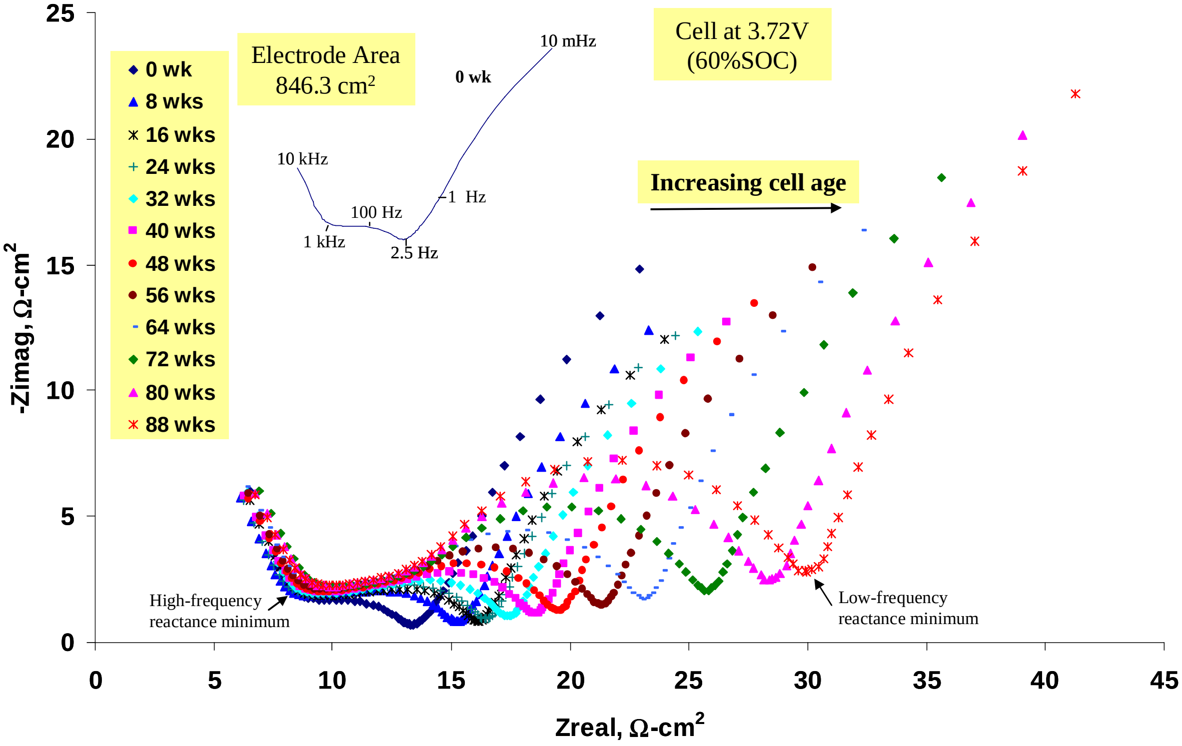

Fig. 5. Representative EIS Data (25°C, 10 kHz–0.01 Hz) from a Gen 2 18650 Cell Aged at 45°C. The inset figure shows frequency locations for the 0-week data.

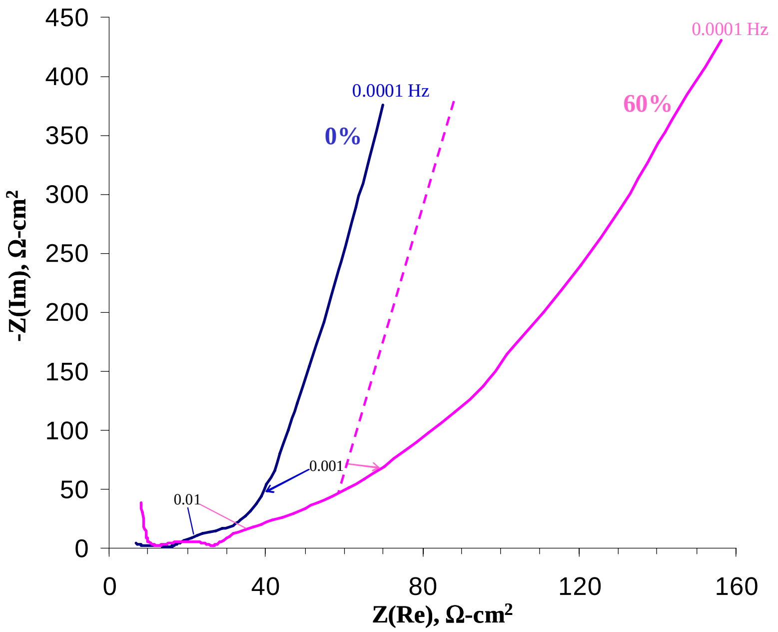

Fig. 6. EIS Data (25°C, 10 kHz–0.01 Hz, 3.72 V) from Gen 2 Cells Showing 0% and 60% ASI Rises. The dashed line represents expected behavior of the aged cell in the absence of significant Warburg impedance.

4 CELL DISASSEMBLY, GAS ANALYSIS, AND ELECTROLYTE STUDY

4.1 CELL DISASSEMBLY

The 18650 cells were typically discharged to 3.1 V (0% SOC) before disassembly. A cell puncture/gas collection fixture was used to collect and determine gas volumes in the cells. Gas composition was determined using a He carrier gas with a Hewlett-Packard (HP) 6890 series gas chromatograph. A thermal conductivity detector was used to study noncombustible gases, and a HP 5973 mass selective detector was used to study hydrocarbon gases. The punctured cells were centrifuged to extract the electrolyte; typically 1 mL electrolyte was collected from each cell. Final disassembly was conducted in an inert-atmosphere glove box, and components were stored in a sealed mason jar for diagnostic examination. The entire process was conducted so that the harvested electrodes, electrolyte, and separator were never exposed to the ambient atmosphere.

4.2 GAS ANALYSIS

The volumes of gases generated in the 18650 cells are shown in Figure 7. Formation cycling produces the largest quantity of gas, ~1.5 to 2 mL, for the various cells. After this, the largest increase in gas volume, ~0.5 to 1 mL, occurs during the first 4 weeks of aging. As aging progresses, the amount of gas generated appears to increase very gradually. Although the data are insufficient to make definitive conclusions, it appears that the rate of gas generation is somewhat greater at 55°C than at 45°C.

Representative gas analysis data from the 18650 cells are shown in Figure 8; more data are presented in Appendix B. The hydrocarbons, methane, ethane, and ethylene appear to be the dominant species after formation cycling, and apparently result from electrolyte reduction reactions that produce the graphite solid electrolyte interface (SEI) layer. The main trend on cell aging is the relative increase in CO content. The hydrocarbon content also appears to increase, though very gradually. The trend in the cell CO_2 content on aging is not very clear; the content appears to increase in the initial weeks of aging, but then shows a decreasing trend.

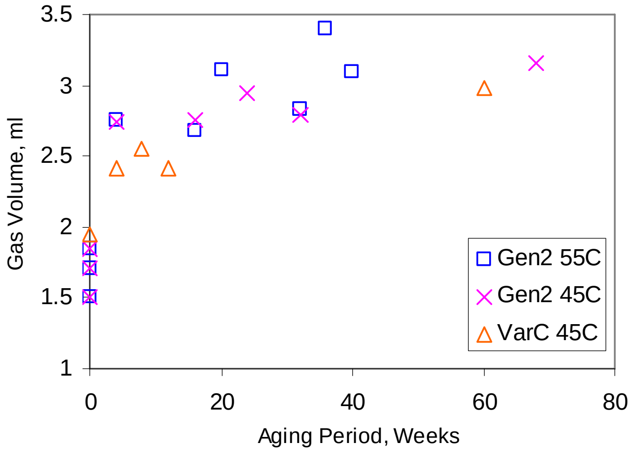

Fig. 7. Volumes of Gases Generated in 18650 Cells during Cell Aging.

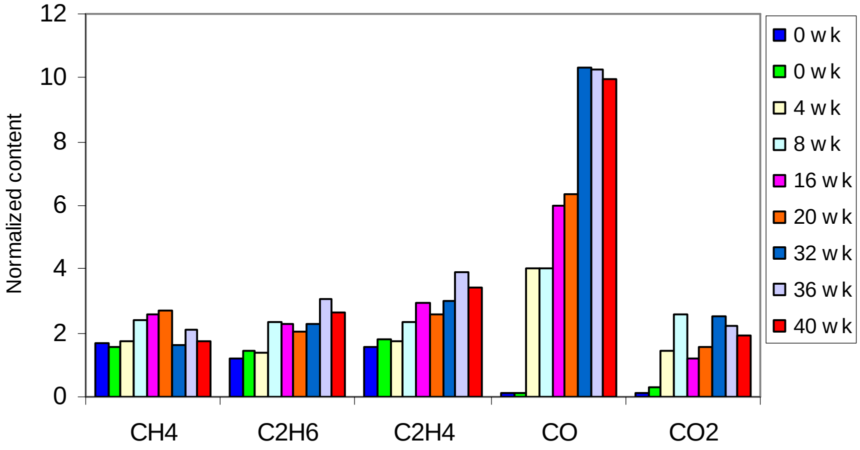

Fig. 8. Gas Analysis Data from Gen 2 Calendar-Life Cells Aged at 55°C up to 40 Weeks. The 0-week cells were formed but not aged.

4.3 ELECTROLYTE STUDY

The cell electrolyte contained 1 M $LiPF_6$ in an EC:EMC solvent. Formation cycling-induced transesterification reactions converted the binary solvent to a multi-component mixture. The cell reactions are as follows:

$$2EMC \leftrightarrow DMC + DEC \quad (1)$$

These linear carbonates react further with EC to form DMDOHC, EMDOHC, and DEDOHC, according to the reactions shown below:

$$CH_2CH_2OCO_2 + CH_3OCO_2CH_3 \leftrightarrow CH_3OCO_2CH_2CH_2O_2COCH_3 \quad (2)$$

$$CH_2CH_2OCO_2 + CH_3CH_2OCO_2CH_3 \leftrightarrow CH_3CH_2OCO_2CH_2CH_2O_2COCH_3 \quad (3)$$

$$CH_2CH_2OCO_2 + CH_3CH_2OCO_2CH_2CH_3 \leftrightarrow CH_3CH_2OCO_2CH_2CH_2O_2COCH_2CH_3 \quad (4)$$

The additional solvent components are not observed when the electrolyte is simply heated to 55°C for 24 h; they are observed only in cycled cells, which suggests that the transesterification reactions may result from an electrochemically induced reaction at this temperature. However, at temperatures of 70°C and higher, the transesterification reactions proceed relatively rapidly.

When initially extracted, the electrolytes were colorless, even from highly aged cells. Analysis of these electrolytes by Fourier transform infrared (FTIR) spectroscopy did not show any organic or polymeric compounds that may have resulted from cell aging. But proton nuclear magnetic resonance (NMR) measurements showed small quantities of oligo-ethylene oxides in electrolyte from a highly aged cell. Gas chromatography (GC) and gel permeation chromatography (GPC) data also showed evidence of oligomers, which implies the presence of a polymerization reaction in the electrolytes. In addition, ^{19}F and ^{31}P NMR spectra obtained on electrolyte from another highly aged cell showed spectra that correspond to mono- ($OPF(OR)_2$) and difluorophospates ($OPF_2(OR)$), thereby indicating the relative instability of $LiPF_6$ in EC:EMC under the cell aging conditions. In the electrolyte, the $LiPF_6$ salt is known to exist in equilibrium with LiF and PF_5 according to the equation:

$$LiPF_{6\,(sol)} \leftrightarrow LiF_{\,(s)} + PF_{5\,(sol)} \quad (5)$$

The forward reaction is favored by higher testing temperatures. If some of the LiF precipitates out of solution, the PF_5 is free to react with species in its proximity. The PF_5 can react with trace impurities of water or alcohol to generate POF_3 that can further react with the carbonate solvents [28] to form the observed organofluorophosphate compounds.

The HF and H_2O contents of the electrolyte as a function of cell age were not determined. But the elemental concentrations of Ni, Co, and Al were determined by inductively coupled plasma mass spectrometry (ICP-MS). Small amounts of Ni (ppm level), Co (sub-ppm level), and Al (ppm level) were detected in electrolyte from a cell that underwent only formation cycling. We do not know whether these elements were released into solution as a consequence of voltage cycling, or whether such release occurs when the positive electrode is simply immersed in the electrolyte. With increasing cell age, the amounts of Ni, Co, and Al in the electrolyte decreased, which suggests that (a) oxide corrosion, if any, is most prevalent during formation cycling, and/or (b) the elements precipitate out of solution onto some solid surface in the cell, which may include the negative electrode surface.

5 ELECTROCHEMISTRY OF HARVESTED ELECTRODES

5.1 ELECTRODE PREPARATION AND EXPERIMENTAL PROCEDURE

Electrochemical tests were conducted on the electrodes harvested from the 18650 cells to determine the effect of aging on electrode performance. The coating on one side of the double-sided electrode laminate was removed before electrochemical measurements were conducted. To obtain reliable and reproducible data, the coating removal was conducted in an Ar (or He) atmosphere glove box.

Electrochemical data were obtained on electrodes harvested from more than 24 cells tested under various conditions, and showed a range of capacity and power loss. Reference electrode cells were prepared to determine the relative contributions of the positive and negative electrodes to impedance rise. The reference electrode cells were assembled with 15.5-cm^2 electrodes, two Celgard 2325 separators enveloping a Li-Sn reference electrode, and fresh electrolyte. Details on the Li-Sn micro-reference electrode, cell assembly, test equipment, and test procedures are discussed elsewhere [19].

Coin cells (2032-type) were assembled with 1.6-cm^2 area samples punched from the harvested electrodes, lithium-metal counter electrode, fresh Celgard 2325 separator, and fresh electrolyte to determine the effect of aging on electrode capacity. The cells containing the positive electrode (cathode) were cycled from 3 to 4.3 V, and the cells containing the negative electrode (anode) were cycled from 0 to 1.5 V. The cycling was conducted at various current densities (~C/5 to C/200) to determine the effect of cycling rate on electrode capacity. For some electrodes, data were obtained at both room temperature and at 55°C. The effect of rinsing on electrode performance was also studied.

Although precautions were taken to minimize testing artifacts during material preparation and cell assembly, it should be noted that all measurements obtained with harvested electrodes have an inherent uncertainty associated with 18650 cell disassembly. In addition, the electrode stack pressure, gas environment, electrolyte composition, and electrode surface films in the harvested electrode cells are probably different from those in the 18650 cells. In spite of these differences, however, distinct trends were observed in the harvested electrode cell data that have been used to draw general conclusions about electrode behavior during aging of the 18650 cells.

5.2 IMPEDANCE DATA

Room-temperature EIS data obtained on the harvested electrode cells at a full cell voltage of 3.72 V are shown in Figure 9. The validity of the electrode impedance data was confirmed by matching the full cell data with the sum of the positive and negative electrode data from the reference electrode cells. In general, the full cell impedance increase trends were consistent with the impedance changes displayed by the corresponding 18650 cells.

It is evident from Figure 9 that for both the Gen 2 and Var C cells, the positive electrode is the main contributor to the full cell impedance. In addition, the main increase of the positive electrode impedance is in the mid-frequency semicircular arc, which suggests that the charge-transfer and mass-transfer characteristics at the positive electrode-electrolyte interface degrade on aging. The negative electrode impedance data were all similar, within a range of experimental uncertainty. The EIS data trends were consistent with the ASI data trends determined by the HPPC test on harvested electrode materials, which are reported in Appendix D.

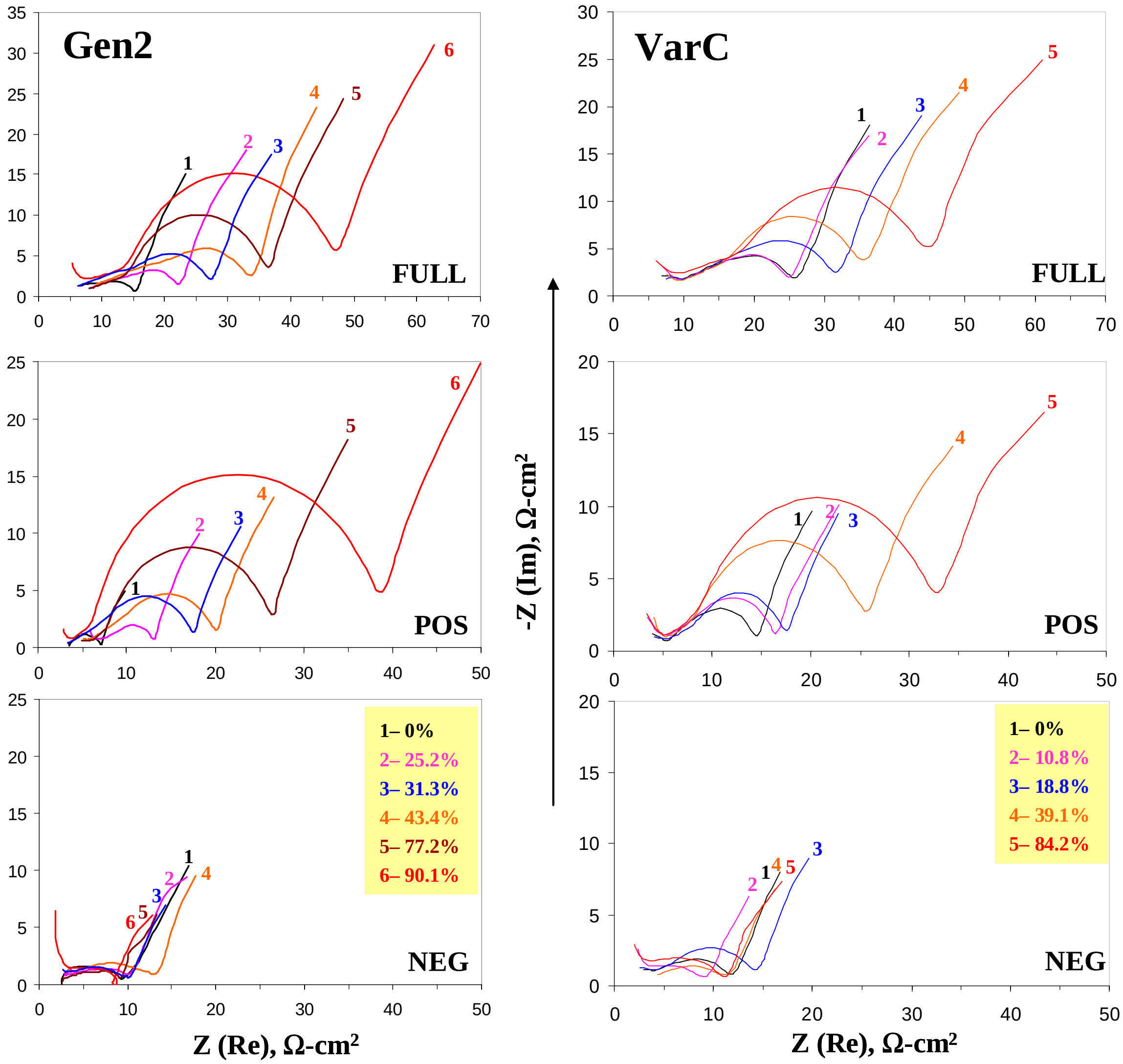

Fig. 9. EIS Data (RT, 25 kHz–0.01 Hz) from RE Cells for the Full Cell and Positive and Negative Electrodes Harvested from Gen 2 and Var C Cells. The ASI rises of the 18650 cells are indicated in the figures.

To shed further light on the impedance increase, we obtained EIS data to low frequencies on the harvested electrodes. For the 0% PF positive electrode (see Figure 10), the impedance curve is almost parallel to the Y axis for frequencies below 1 mHz, which indicates that the electrochemical processes below this frequency are mainly capacitive. Cell aging significantly changes the low-frequency portion of the positive electrode, increasing both the resistive and capacitive components. Because the low-frequency portion appears to be an extension of the Warburg tail that is typical of diffusion-related processes, the impedance increase indicates an increased difficulty of lithium transport into and through the oxide particles, i.e., a “slowing” of the oxide particles with increasing cell age. The differences in the negative electrode responses at low frequencies were insignificant compared with those of the positive electrode. It is clear that the significantly higher resistance displayed by aged cells during EIS testing to low frequencies are associated with diffusion phenomena in the positive electrode.

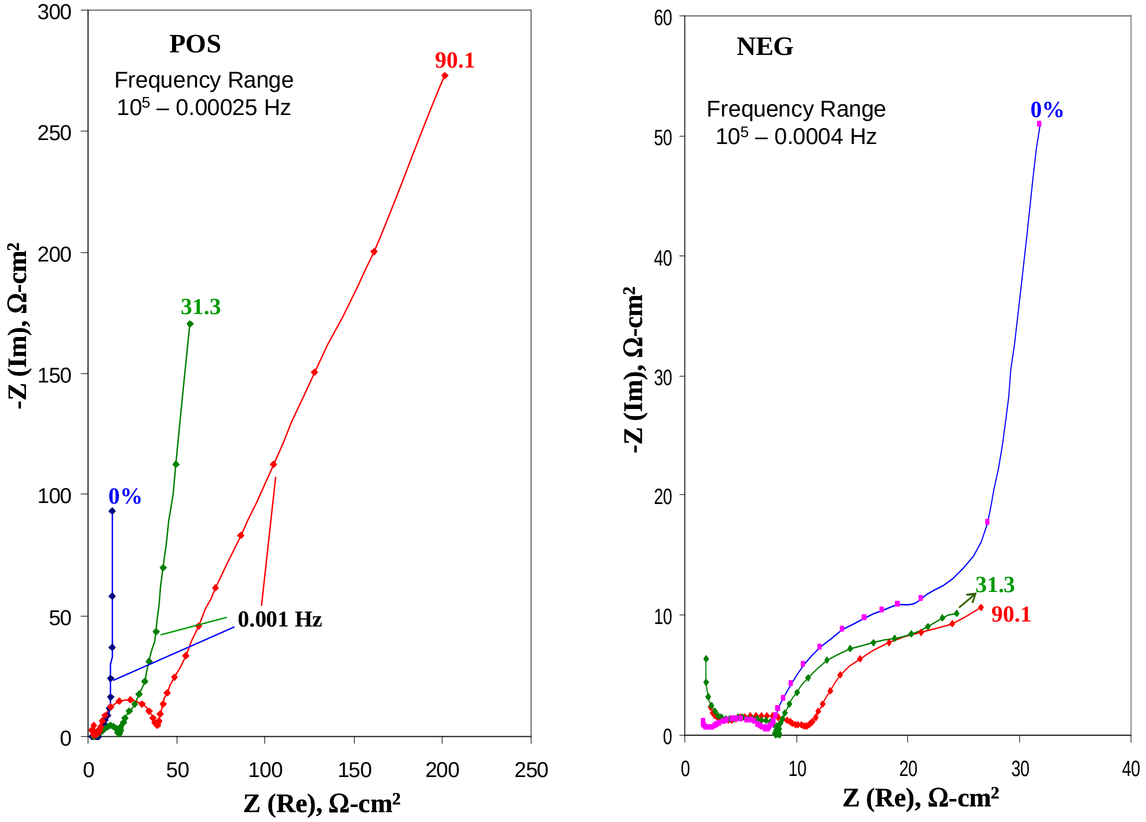

Fig. 10. EIS Data (RT, 3.72 V) from RE Cells Containing Electrodes Harvested from Gen 2 Cells. The ASI rises of the 18650 cells are indicated in the figures.

Testing temperature had a significant effect on the EIS data—details are provided in Appendix D. In general, increasing the test temperature lowered the cell impedance by reducing the impedance at both the positive and negative electrodes. The reduction in the positive electrode mid-frequency arc width (R_w) with test temperature indicates that the electrode-electrolyte interfacial feature(s) responsible for R_w is/are responsive to testing temperature: the higher the test temperature, the less the effect of this interfacial feature. The Warburg impedance tail, on the other hand, is not significantly changed by testing at different temperatures (20 to 55°C).

In an effort to regain “original” performance, the positive electrodes were washed in various solvents. Electrodes that were soaked in dimethyl carbonate (DMC) before EIS measurements surprisingly showed a higher mid-frequency arc width than the as-harvested electrodes, which suggests that the DMC rinse may have increased impedance by altering the structure of surface films on the oxide particles. On the other hand, an aged positive electrode that was ultrasonically washed with DMC and pressed (to reduce electrode thickness by 15%) before assembly in Swagelok cells showed lower impedance than the as-harvested electrode.

5.3 CAPACITY DATA

5.3.1 Positive Electrode Data

Figure 11 shows representative charge-discharge data (vs. Li metal) obtained with a 0.064-mA current for positive electrodes harvested from cells that were subjected to calendar-life and cycle-life aging and displayed varying degrees of capacity and power fade. It is evident that the coin cell capacities are lower for electrodes that were harvested from 18650 cells that showed greater capacity loss. Because the counter electrode is an infinite source of lithium, the coin cell capacity variations indicate significant changes in the positive electrode during accelerated aging of the 18650 cells. It should be noted, however, that a small portion of the capacity loss might be related to the cell disassembly process: oxide particles have been observed on the separator, especially those from highly aged cells.

In addition to capacity loss, cycling hysteresis becomes more prominent with electrode age: electrodes from early-life cells showed little hysteresis, whereas late-life electrodes showed significant hysteresis. Such hysteresis results from the inability of the material to attain thermodynamic equilibrium during the constant current cycling. The presence of cycling hysteresis indicates that the positive electrode “slows down” on aging, i.e., as it ages, the positive electrode is unable to deliver or accept lithium at rates that were previously possible.

Cycling rate had a significant effect on measured capacity data. Electrodes from early- and mid-life cells showed significant capacity gains and improved cycling hysteresis at lower currents, so that their capacities often equaled that of the 0% capacity fade (CF) electrode. Significant capacity gains and cycling hysteresis improvements were also observed at lower currents for electrodes from highly aged cells. For these electrodes, however, the capacity values were significantly lower than for the 0% CF electrode, and cycling hysteresis was evident in the data even at the low currents employed in our measurements.

The effect of testing temperature on positive electrode capacity is detailed in Appendix D. Higher testing temperatures improve kinetics and lower electrode impedance, as described previously. When tested at 55°C, electrodes from early- and mid-life cells showed capacities that approached that of the 0% CF electrode. On the other hand, the capacities of electrodes from highly aged cells were significantly lower than the 0% CF electrode data, even when measured at 55°C. This capacity fade arises from a combination of electrode impedance and inaccessible charge storage resulting from isolated particles of the active material.

In an attempt to regain their "original" capacity, positive electrodes from aged cells were rinsed in various solvents before cell assembly. Instead of improving electrode capacity, however, the rinse solvents were found to be either ineffective (EC:EMC, H_2O) or to degrade electrode capacity (DMC, supercritical CO_2). Because the rinse protocol was far too gentle to produce oxide particle damage, the data suggested that electrode capacity could be altered by causes that are strictly external to the oxide crystals. The influence of rinse solvent polarity on sample capacity indicated that the "structure" of the cathode surface films is apparently more important than its composition. This surface film structure apparently contains charged species that are bound to the oxide particles and interfere with the motion of Li ions, i.e., increasing the impedance at the oxide surface lowers electrode capacity. On the other hand, electrodes that were ultrasonically washed with DMC and pressed (to reduce electrode thickness by 15%) before assembly in Swagelok cells showed capacities that were comparable to those of fresh electrodes. These data highlighted the mechanical and contact issues that could contribute to cell capacity and power fade.

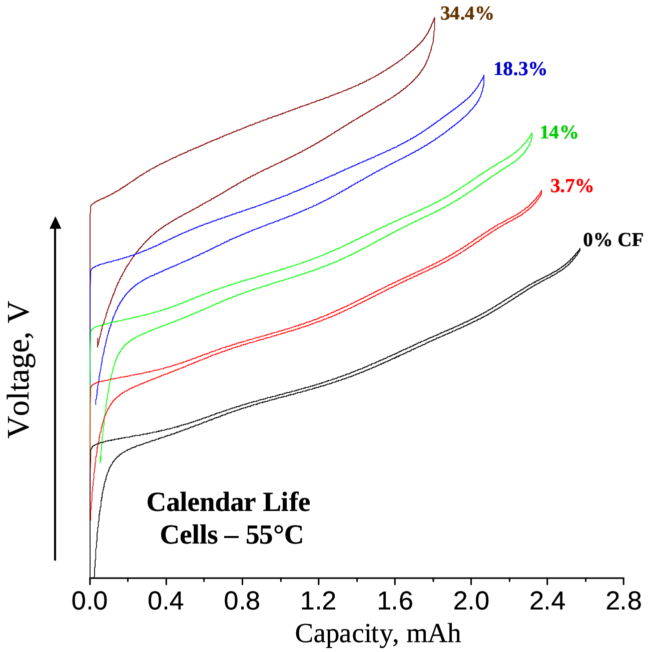

Fig. 11. RT Cycling Data from Harvested Gen 2 Positive Electrodes (vs. Li) Obtained with a 0.064-mA Current in the 3 to 4.3 V Range. Capacity fade of the 18650 cells is indicated in the figures. Curves have been vertically offset for clarity.

5.3.2 Negative Electrode Data

Representative charge-discharge data (vs. Li metal) obtained with a 0.064-mA current for the negative electrodes are shown in Figure 12. All curves displayed the staging effects expected during lithium intercalation-deintercalation into graphite materials [29]. In general, the negative electrode capacities were lower with increasing cell age. In spite of the capacity decrease, however, the graphite electrode had sufficient capacity to accept lithium ions from the positive electrode even for the highly aged cells. That is, even in late-life 18650 cells, metallic lithium was unlikely to plate on the negative electrode during cell charging.

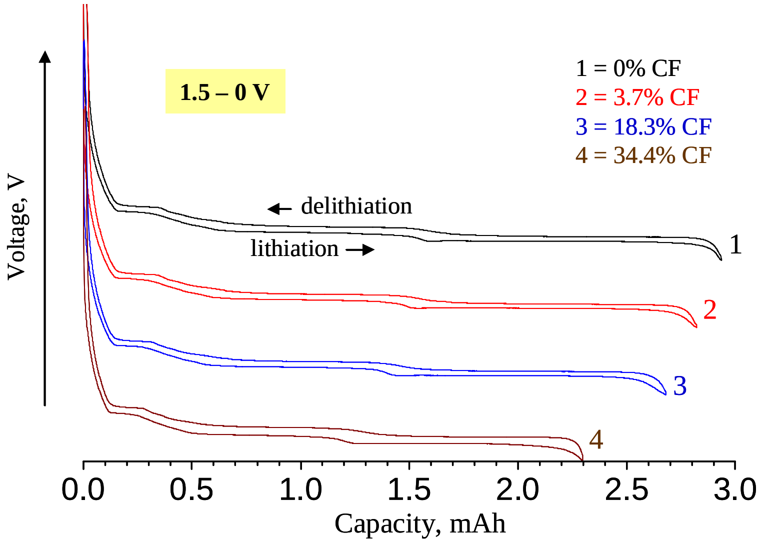

Fig. 12. RT Cycling Data from Harvested Gen 2 Negative Electrodes (vs. Li) Obtained with a 0.064-mA Current in the 1.5 to 0 V Range. Capacity fade of the 18650 cells is indicated in the figures. Curves have been vertically offset for clarity.

For the negative electrodes, cycling hysteresis was observed even for samples that were not aged. Furthermore, except for the highly aged electrodes, the hysteresis behavior of the various samples was quite similar. In addition, the capacity gain from slower rate cycling was very small. These data are all consistent with the observation that the negative electrode impedance change on aging is small.

Capacity measurements were conducted on negative electrode samples that were rinsed in dimethyl carbonate (DMC) solution prior to cycling versus Li metal. Rinsed samples, even from late-life cells, showed capacities that were comparable to those of electrodes that were not aged, indicating that the graphite structure was unchanged. The electrode capacity loss on aging thus apparently results from pore clogging or isolation of graphite particle by electronically insulating surface films that can be washed off in solvents such as DMC.

5.4 SUMMARY OF ELECTROCHEMISTRY DATA

The electrochemistry data from the Gen 2 and Var C cells may be summarized as follows:

- The positive electrode is mainly responsible for cell impedance rise; the negative electrode contribution is small.

- The impedance rise of the positive electrode manifests itself in (a) increasing width of the mid-frequency arc, and (b) increase in the Warburg-tail length. These changes appear to be the result of two distinct, and maybe independent, mechanisms that become prominent in different stages of the cell's life.
- The EIS test temperature affects the physical features that produce the positive electrode mid-frequency arc. The Warburg tail, on the other hand, appears to be independent of temperature in the 20 to 55°C range.
- The C/1 capacity reduction on aging results from factors that include (a) side reactions that consume lithium at the negative electrode and (b) impedance rise that reduces the ability of the positive electrode to deliver and accept lithium.
- The capacity of aged negative electrodes can be restored by DMC rinsing, which indicates that the capacity loss results from pore clogging or isolation of graphite particles by electronically insulating surface films.
- The capacity of aged positive electrodes from Region 2 cells can be regained by increasing cell test temperature, which reduces electrode impedance. Whereas, the capacity of aged electrodes from Region 3 cells cannot be regained by increasing temperature or by gentle rinsing in DMC.

6 PHYSICOCHEMICAL DIAGNOSTICS OF 18650 CELL COMPONENTS

A large variety of physicochemical diagnostic techniques, described in detail elsewhere [30], were employed to study the extent of aging-induced degradation of Gen 2 and Var C cell components. This section presents important results, links together data from various studies, and highlights correlations between observed phenomena and cell performance loss. Detailed information from examination of the various separator, negative electrode, and positive electrode samples are provided in Appendices E, F, and G, respectively.

6.1 SEPARATOR STUDIES

Impedance spectra were obtained on separator samples that were soaked in fresh electrolyte prior to measurement. Each sample was placed between two identical nickel electrodes and held at constant force. Impedance spectra were recorded with a 5-mV perturbation at ~12 different locations on the membrane. The impedance spectra (see Figure 13) displayed features characteristic of a series RC circuit at high frequencies. The high-frequency end of the spectrum, which corresponds to separator ionic resistance, was observed to shift continuously toward higher resistances with increasing cell age. Also, the local membrane resistance became more nonuniform as the cells aged (see Figure 14). It is estimated that separator resistance accounts for ~10–15% of the cell impedance rise on aging.

The fresh and 0% PF separator samples were white in color. The samples showed increasing discoloration with increasing age of the 18650 cells. The separator side adjacent to the positive electrode was observed to have a different coloration from the side adjacent to the negative electrode. Furthermore, the separator appeared to become "stickier" with cell age, i.e., portions of the electrode coatings stuck to the separator during cell disassembly, especially for the mid-life and late-life cells.

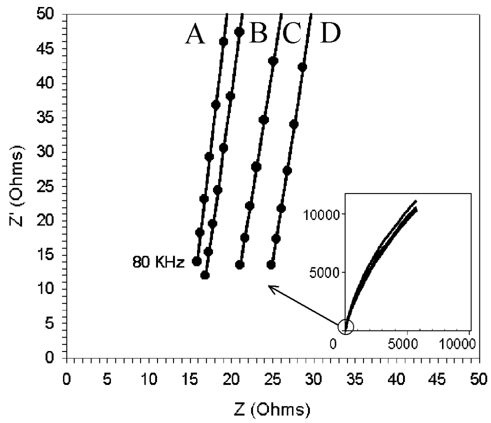

Fig. 13. Impedance Spectra of Separators Removed from (a) Fresh Cell and Cells Stored at 55°C for (b) 8 Weeks, (c) 24 Weeks, and (d) 40 Weeks.

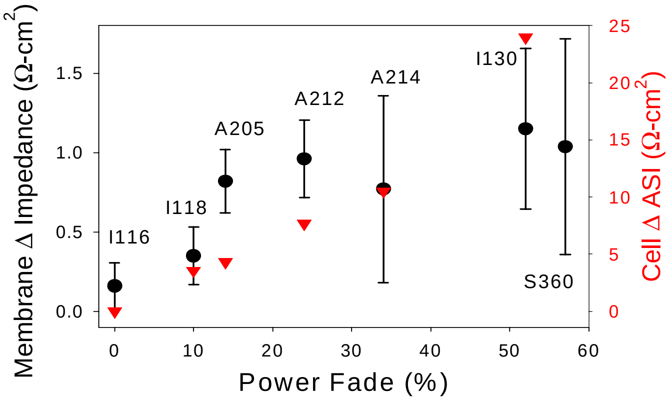

Fig. 14. Change of Celgard 2300 Membrane ASI, Measured at 80 kHz (left ordinate and circles) and Change of Li-Ion Cell ASI, Measured at 3.6 V after Cell Testing (right ordinate and triangles).

Microscopic examination showed the presence of surface deposits on the separator that were especially prominent in highly aged cells. The distribution of these deposits was very nonuniform: portions in contact with the electrode edges showed heavier residue relative to the rest of the separator. Uniform and strong fluorescence was observed from separator portions that extended beyond the edges of the electrodes. In contrast, separator portions in contact with the electrodes displayed a patchy, nonuniform pattern of fluorescent and nonfluorescent spots (Figure 15). The fluorescence is believed to arise from LiPO$_x$:MeF (M=metal) fluorophosphates that are produced from thermal decomposition of the electrolyte during long-term aging. The patchy, nonuniform pattern may arise from the quenching of fluorescence by oxidation and reduction processes at localized areas on the electrode. These electrode-specific redox reactions may also account for the differences (asymmetry) in fluorescence observed between the cathode and anode side of the separators.

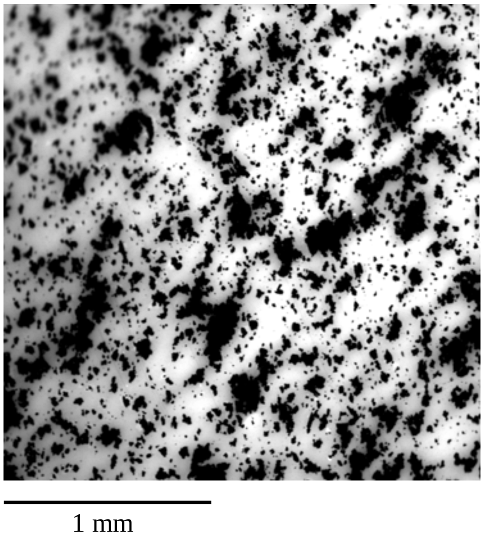

Fig. 15. 2.5 mm × 2.5 mm Fluorescence Image Obtained in the 350- to 580-nm Spectral Range of a Separator Aged in a Cell for 40 Weeks at 55ºC. Bright areas correspond to intense fluorescence emission; dark patches are nonfluorescent.

The surface deposits covering the fibers can reduce both the pore size and homogeneity of the separator, thereby increasing the mean path length of lithium ions. Furthermore, the patchy presence of these deposits can induce a nonuniform current distribution across the cell and accelerate electrode degradation at high-current locations. Membrane swelling can also increase mechanical stress in the cell, which may degrade electrode integrity.

Ultrasonic washing in a DMC-water mixture removed the surface deposits from both sides of the separator. Washed separator samples, even from highly aged cells, showed morphologies that were comparable to those in the 0% PF cells. In addition, electrochemical data obtained from washed fresh and aged separators were found to lie within the bounds of experimental uncertainty. These data indicate that the separator material is not significantly damaged by the cell aging and testing protocols.

6.2 NEGATIVE ELECTRODE STUDIES

A typical image of the fresh electrode showed the characteristic plate-like particles of Mag-10 graphite that are ~5 to 10 μm wide with well-defined active edges; portions of the graphite that flaked off the surface were clearly visible. Micrographs of 0% PF samples showed some rounding of the graphite images, which indicated the presence of a SEI layer. Micrographs of samples from high-power-fade cells showed a distinct rounding of the graphite edges; the surface flakes apparent in the fresh electrode were indistinct in these samples, suggesting the presence of a layer that covered both the graphite surface and edges.

X-ray diffraction data showed the expected diffraction peaks for graphite. Sample data from even highly aged cells were comparable to those from 0% PF cells, which indicated that the cell aging protocol had not significantly altered the graphite structure. However, micro Raman spectroscopic analyses revealed the presence of "severely disordered" carbonaceous materials on the surfaces of aged anodes. A typical Raman spectrum of graphite consists of the E_{2g} active mode or (G) band at ~1,582 cm^{-1} and the A_{1g} mode or (D) band at ~1,360 cm^{-1}, which is associated with the breakage of symmetry occurring at the edges of graphite sheets (see Figure 16). The ratio of D/G integrated peak intensities is inversely proportional to the intra-planar microcrystallite distance L_a and to the size of graphene domains. The D/G ratio was observed to increase noticeably with cell age, which indicated an increase in carbon disorder. Furthermore, with cell age, the D band intensity increased, the G bandwidth broadened significantly, and a new band at ~1,620 cm^{-1}, which is typical of severely disordered carbonaceous materials, appeared in the spectrum. The concentration of the disordered carbon depended strongly on its location in the electrode. Raman mapping showed that the concentration was greater at the electrode/electrolyte interface than at the current collector/electrode interface. The SEI was also more evident on these disordered carbon regions.

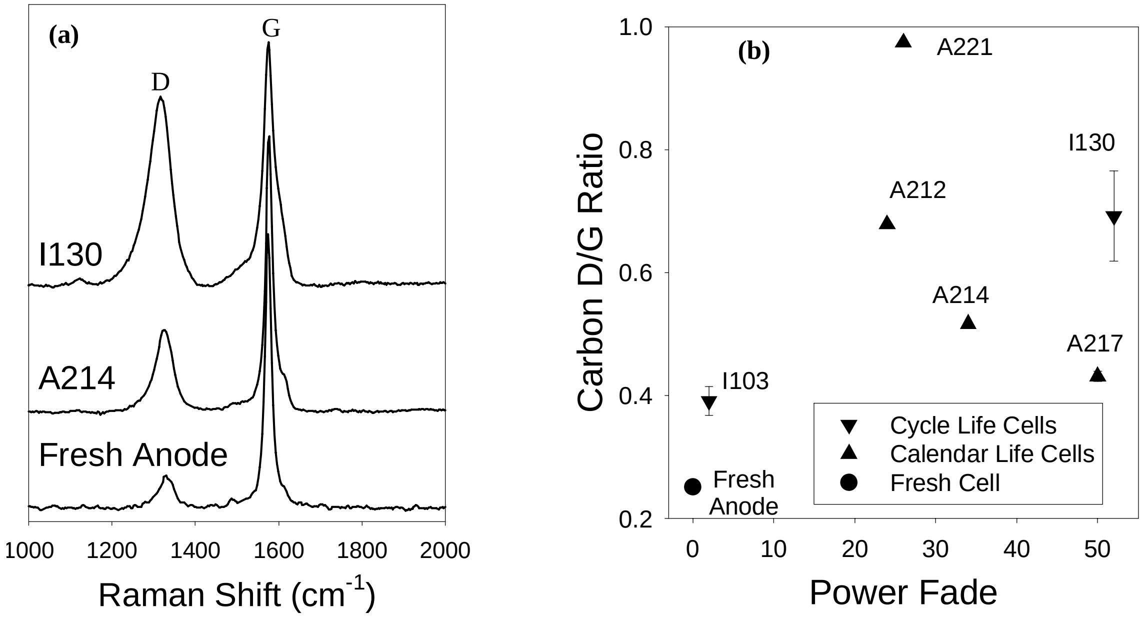

Fig. 16. (a) Average Raman Spectra of Graphite Anodes from Fresh and Aged Gen 2 Cells Showing the D and G Bands and (b) Average Carbon D/G Ratios Calculated from the Raman Microscopy Images of Variously Aged Anodes.

FTIR-attenuated total reflectance (ATR) examination showed the SEI layer on 0% PF anodes was heterogeneous and contained lithium oxalate ($Li_2C_2O_4$), lithium carboxylates (RCOOLi), and lithium methoxide ($LiOCH_3$). Lithium hydroxide (LiOH), methanol (CH_3OH), and, in some cases, lithium hydrogen carbonate ($LiHCO_3$) were also occasionally observed in aged samples. With increasing cell age, the SEI showed (a) a general loss of $-CH_2-$ or $-CH_3$ functionalities, (b) an increase in the proportion of "inorganic" compounds, and (c) some evidence of thermal hydrolysis reactions. However, the FTIR data did not show an obvious increase in SEI layer thickness.

Evidence of increasing SEI layer thickness was observed in X-ray photoelectron spectroscopy (XPS) measurements [20]. XPS spectra were obtained before and periodically after the electrode samples were depth profiled by sputtering with Ar^+ ions. The longer sputtering times required to reveal the graphite active material indicated that the SEI layer on aged electrodes was greater than that on electrodes from 0% PF cells. The XPS data also showed that EC- and EMC-reduction products are dominant in the SEI layer of electrodes from low-power-fade cells, and $LiPF_6$ reaction products are dominant in the SEI layer of electrodes from high-power-fade cells. The data were consistent with the FTIR observations of the absence of lithium alkyl carbonates ($ROCO_2Li$) and Li_2CO_3 and the presence of carboxylate-based compounds in the SEI layer. The alkyl-carboxylate compounds may have formed by EC reduction followed by reaction with CO_2. Reduction of EMC can also result in Li-carboxylates together with Li-alkoxides (ROLi).

Peaks consistent with the presence of carbonates (other than Li_2CO_3), LiF, Li_xPF_y, and $Li_xPF_yO_z$ compounds were observed in the XPS spectra. The presence of trivalent P species (such as PO_3^{3-}) in the SEI layer was seen in the P K-edge X-ray absorption spectroscopy (XAS) data, which indicated the electrochemical reduction of P(V) to P(III) species at anode potentials. The accumulation of inorganic compounds, i.e., $LiPO_x$, Li_2CO_3, LiF, and traces of NiO_x and CoO_x, on the surfaces of aged electrodes was also observed by Raman spectroscopy.

Significant changes in electrode surface topography were revealed by atomic force microscopy (AFM) imaging. Nanocrystalline deposits were observed to accumulate preferentially on graphite flake cross-sections, plane steps, and edges; there was no clear evidence of such deposits on the graphite basal planes. The AFM data were also consistent with an increase in SEI layer thickness with cell age.

Li_2CO_3, which was previously believed to be an important SEI constituent, was not observed in data (FTIR, XPS) from samples that saw no air exposure. One possibility is that Li_2CO_3 never forms in the anode SEI. Alternatively, Li_2CO_3 may form but then reacts immediately with the electrolyte to form other compounds. The carbonate peaks observed in the XPS spectra may be associated with transesterification products in the residual electrolyte components present on the as-harvested electrode surface, which were also observed by gas chromatography mass spectrometry (GC-MS) analysis. The peak may also contain contributions from polyethercarbonates, which may form from base-catalyzed ring opening of EC molecules by alkoxide anions (RO^-) at the negative electrode. The evolution of CO_2 from these ethercarbonates may have produced the poly(ethylene) oxide PEO-like polymers observed in the GPC data of water extracts from the electrode samples. The majority of these polymers had molecular weights (mol wt) in the 500 to 5,000 range, but polymers with ~100,000 mol wt were also observed. Weak peaks, consistent with PEO presence, were also observed in proton NMR spectra of acetonitrile extracts from the electrode samples; however, the PEO quantity did not show the expected increase on aging. More importantly, the FTIR and XPS data indicated that PEO (if present) is not a dominant species in the SEI layer. One possibility is that the PEO-like polymers observed in the GPC and NMR data are generated during extraction by the water or acetonitrile solvents. Another possibility is that the PEO-like polymers react with PF_5 to form organic-fluorinated and organo-phosphorous compounds in the SEI layer.

6.3 POSITIVE ELECTRODE STUDIES

Scanning electron microscopy (SEM) images from the fresh Gen 2 and Var C electrodes showed spherical secondary particles ~5 to 10 µm in diameter that were composed of ~0.2- to 0.5-µm-size primary particles (see Figure 17), ~5- to 10-µm-size plate-like graphite, and irregularly shaped acetylene black agglomerates. The oxide particles were coated with a thin film, which was apparently the polyvinylidene fluoride (PVDF) binder. Micrographs from 0% PF and even highly aged samples were similar to that of the fresh electrode, except for the presence of "surface films" on the oxide particles that included electrolyte residue and the PVDF binder. Oxide particle debris was occasionally observed in highly aged samples.

The microscopy data also indicated that the PVDF binder morphology was relatively unaffected by cell aging. Examination of the current collectors showed that the Al surface was little changed by the aging conditions. These data indicate that the PVDF binder and the Al current collector are unlikely contributors to the positive electrode impedance rise.

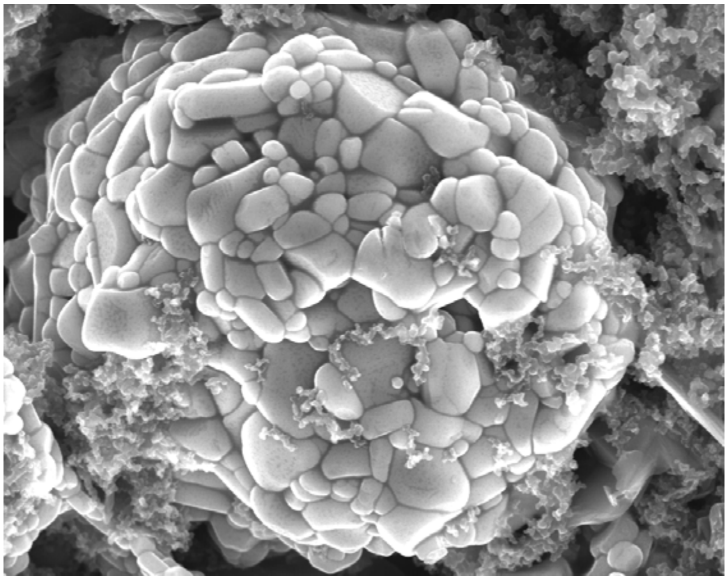

Fig. 17. Micrograph from a Fresh Gen 2 Positive Electrode Showing the $LiNi_{0.8}Co_{0.15}A_{0.05}O_2$ Primary Particles That Make up the Secondary Particle.

Chemical analysis measurement of the overall carbon content of cathode samples from various aged cells indicated that there was no significant loss of the bulk cathode carbons as a result of cell aging. X-ray diffraction data of cathodes from various cells also showed that the shape and position of the carbon peaks were unchanged on aging. However, Raman microscopy images indicated significant changes in the $LiNi_{0.8}Co_{0.15}Al_{0.05}O_2$/elemental-carbon surface concentration ratio at the surface and in the bulk of the composite cathode that accompanied cell storage and cycling at elevated temperatures. The $LiNi_{0.8}Co_{0.15}Al_{0.05}O_2$/elemental-carbon surface concentration ratios (Figure 18) appear to increase monotonically with increasing cell power loss, up to an apparent break point at about 20% cell power loss. Acetylene black was observed to "retreat" at a faster rate than graphite. This carbon retreat occurred faster in cells that were stored at elevated temperatures (45 and 55°C) than in cells stored at 25°C. Also, cycle-life test cells showed faster carbon retreat than did calendar-life test cells. This carbon retreat may be responsible for a loss of electronic conductivity within the composite cathode. The loss of a direct electronic path through the receding carbon matrix could lead to an increased resistance within the cathode composite agglomerate and, eventually, to total isolation of some oxide particles.

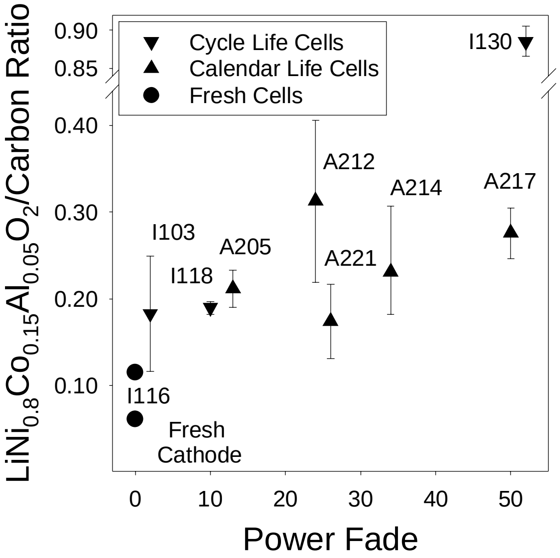

Fig. 18. Average Ratio of Surface Concentration of $LiNi_{0.8}Co_{0.15}A_{0.05}O_2$ Active Material to Carbon Additive Calculated from Raman Microscopy Images of Positive Electrodes Extracted from Gen 2 Cells.

X-ray diffraction measurements on electrodes from cells that were rapidly discharged to 3.1 V showed an increase in the *c* dimension of the $LiNi_{0.8}Co_{0.15}Al_{0.05}O_2$ hexagonal unit cell with cell age, which is consistent with lower lithium contents in oxides of the higher capacity fade electrodes. However, cells that were held at 3.1 V for 24 h showed a much smaller increase in the *c* parameter, which indicated that the apparent lithium loss arises from a rate effect that is mostly a manifestation of electrode impedance.

The rate effect in electrodes from highly aged cells was demonstrated both by ex-situ and in-situ X-ray diffraction (XRD) measurements. High-resolution XRD patterns obtained on electrodes that were rapidly charged to 4.1 V showed the presence of particles at very different states of charge. A significant portion of the material did not participate in charging; the rest was at a nearly uniform SOC (see Figure 19). The data indicated a bimodal distribution of states of charge between well-connected and poorly connected particles in these highly aged electrodes. Some SOC distribution was found even in fresh cathode samples, but in this case, there was fairly rapid relaxation to a uniform SOC. This effect is attributed to redistribution of charge within large, agglomerated secondary particles, perhaps assisted by residual electrolyte within the pores of the agglomerates. Since the SOC of smaller, less agglomerated particles is nearly homogeneous at the end of the test, they do not exhibit this redistribution. The result is a broad XRD peak after relaxation due to the presence of particles with a range of SOC.

The nonuniform behavior of $LiNi_{0.8}Co_{0.15}Al_{0.05}O_2$ secondary particles in a highly aged electrode was also demonstrated by Raman spectroscopy. In-situ spectral monitoring of the SOC of selected oxide particles revealed that the rate at which the oxides deintercalate and intercalate Li ions changes with time and location in the composite electrode. This micro-scale nonuniform charge-discharge performance of the $LiNi_{0.8}Co_{0.15}Al_{0.05}O_2$ particles implies that the local current distribution in the electrodes is also highly nonhomogeneous. Raman spectroscopy data also indicated that electrodes, even from fully discharged cells, contain oxide particles with SOC ranging from (a) fully discharged through (b) partially charged to (c) fully charged. The inability of the oxide particles to achieve a constant SOC may be related to the electrode impedance rise (rate effect) and/or isolation of the active material.

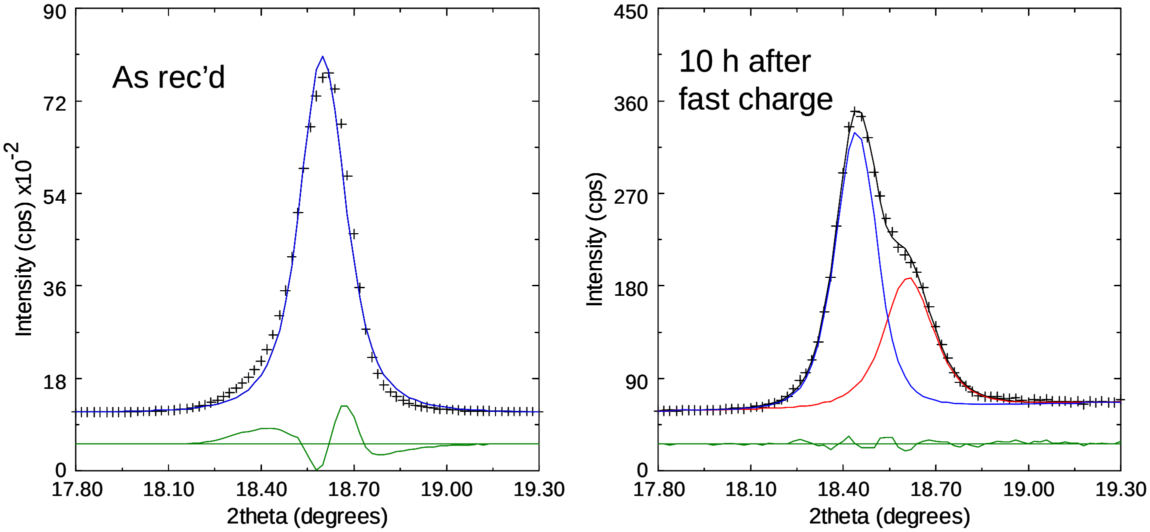

Fig. 19. XRD of Fast-Charged I130 (>50% PF) Gen 2 Positive Electrode Showing Nonuniform Charging of Oxide Particles.

The isolation of active material may result from the $Li_xNi_{1-x}O$ surface layer observed on the $LiNi_{0.8}Co_{0.15}Al_{0.05}O_2$ primary particles, which apparently forms because of oxygen loss from the particle surface (see Figure 20). This $Li_xNi_{1-x}O$ layer may contribute to impedance rise when $x < 0.3$ because the random distribution of Li and Ni ions in the NaCl-type crystal structure lowers the lithium ionic conductivity. Although the $Li_xNi_{1-x}O$ layer thickness did not show a significant change, the relative proportion of oxide particles bearing the layer appeared to increase with cell age. This observation is consistent with transmission electron microscopy-energy dispersive X-ray spectroscopy (TEM-EDX) data that showed a fairly strong correlation of oxygen loss and power fade with significant decreases in total oxygen and O/Ni ratios in electrodes from highly aged cells.

Particle isolation may also be associated with the phosphorus that was detected in measurable amounts on the oxides, but not on the carbon particles. The phosphorus was observed to accumulate at the boundaries between oxide primary particles. The data suggest an electrolyte-induced corrosion process at the interfaces between primary particles that may explain the increased primary particle separation and the fracturing of larger oxide particles into smaller ones occasionally seen in some highly aged electrodes.

Physical damage to the oxide particles was not usually observed during TEM examination. Although point and line defects were occasionally observed in the microstructure, planar defects such as stacking faults and cracks, which could impede the motion of lithium ions, were not common. Some cracking was observed, however, in oxide particles from cells that were aged well beyond their useful life (142% ASI rise). The partial or total separation of oxide particles may lead to impedance rise by (a) reducing the electrochemically active surface area, (b) retarding the direct Li^+ diffusion between primary oxide particles, and/or (c) increasing the Li^+ diffusion path length within the secondary oxide particles by altering the path for particle-to-particle diffusion.

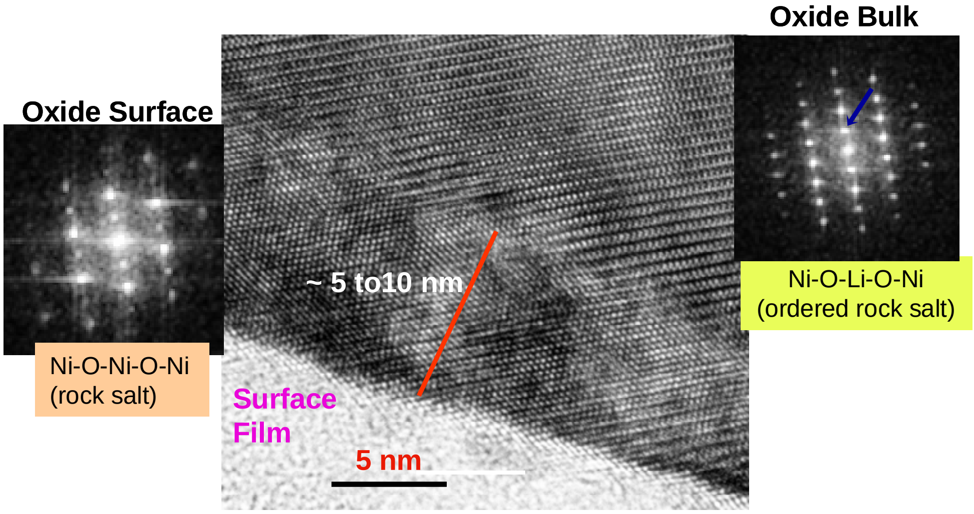

Fig. 20. High-Resolution TEM Image and Fast Fourier Transform Patterns Showing Structural Differences between the Surface and Bulk of $LiNi_{0.8}Co_{0.15}A_{0.05}O_2$ Primary Particles.

Current-sensing AFM (CSAFM) conductance images of fresh individual $LiNi_{0.8}Co_{0.15}Al_{0.05}O_2$ particles embedded in gold substrates revealed that the $LiNi_{0.8}Co_{0.15}Al_{0.05}O_2$ agglomerates were not uniformly conductive, due to poor intergranular electronic contact. Alternatively, the nonuniform conductivity may result from the presence of Li_2CO_3, which is highly insulating, observed on the fresh particle surfaces by FTIR and XPS. CSAFM measurements also showed substantial loss of surface electronic conductance in aged cathodes that increased with cell test temperature and test duration. This observation is consistent with the increasing proportion of apparently insulating compounds formed on the electrode surface with continued cell aging. Such surface films/compounds on or adjacent to the active material could contribute to electrode capacity loss (by isolating particles) and impedance rise (by increasing resistance to lithium-ion transport).

The electrode surface has been studied by several techniques, including FTIR, XPS, Raman spectroscopy, NMR, XAS, and secondary ion mass spectroscopy (SIMS). The preexisting surface layer of Li_2CO_3 on $LiNi_{0.8}Co_{0.15}Al_{0.05}O_2$ particles disappears after electrode immersion in the electrolyte, apparently by the reaction of Li_2CO_3 with acidic species/impurities in the electrolyte. No products of electrolyte reaction with the Gen 2 oxide could be detected by FTIR-ATR, i.e., no organic or polymeric compounds other than electrolyte and PVDF binder were observed in the data (see Figure 21). But the presence of carbon-bearing compounds on the electrode surface, other than PVDF and the electrolyte, was evident in XPS and time of flight (TOF) SIMS data. These data also indicated that polymeric species such as polyethylene oxides, if present, are not a dominant species in the surface films.

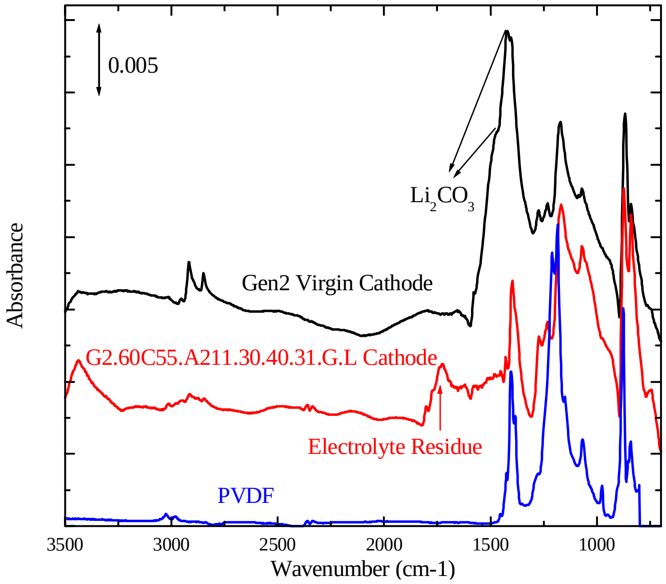

Fig. 21. FTIR-ATR Data from Fresh and Aged Positive Electrode Samples. The spectrum from a PVDF sample is shown for comparison.

The FTIR and XPS data appear to be in contradiction with the results of proton NMR and GPC analysis, which indicated the presence of polyethylene oxides on the electrode surface. The proton NMR data showed strong PEO peaks in water extracts and weak PEO peaks in acetonitrile extracts from electrode samples. The GPC data indicated the formation of higher-molecular-weight polymers during cycling and aging. For the most part, these materials had molecular weights in the range of 300 to 5,000, but polymers with molecular weights in the range of 100,000 also were detected. It should be noted, however, that both the NMR and GPC techniques rely on procedures that extract compounds from the electrode surface. The species thus detected could be an artifact of the extraction process. Also note that the NMR data showed similar PEO contents for the 0% PF and highly aged electrodes, which again suggests that either (a) the PEO detected is an artifact, or (b) the PEO is transformed into other species, such as organophosphate compounds, during cell aging.

The presence on the electrode surface of inorganic constituents, such as LiF, Li_xPOy, and $Li_xPO_yF_z$, which likely result from electrolyte decomposition processes, has been confirmed by various techniques. Raman spectra showed vibration bands that are characteristic of lithium fluorophosphate species. Fluorine and phosphorous K-edge XAS measurements (see Figure 22) indicated LiF, residual PF_6 from the electrolyte salt, and a pentavalent P species (PO_4^{-3}, for example). ^{31}P NMR data showed fluorophosphate compounds on aged harvested electrodes; these species were not observed in spectra of samples ultrasonically washed in DMC. Data from SIMS and XPS measurements are also consistent with the presence of residual PF_6 and phosphate compounds on the electrode surface.

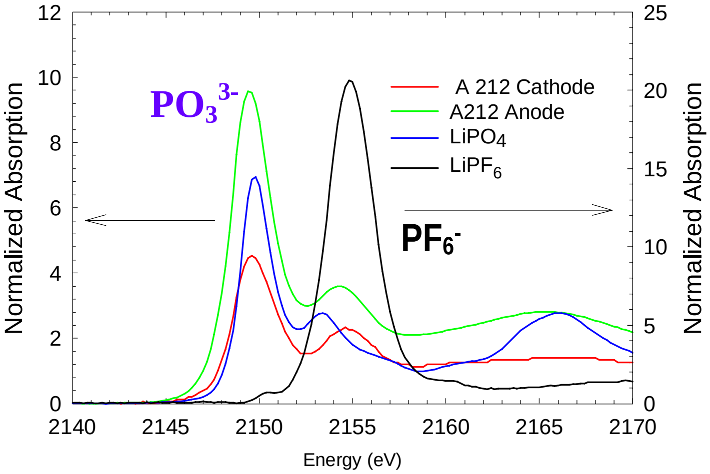

Fig. 22. Typical P K-Edge XAS Data Collected on Samples from a Calendar-Life Cell. Data for Li_3PO_4 and 0.05 M $LiPF_6$ standards are also shown. Note the different scale for the $LiPF_6$ data. Trivalent P compounds are present on the negative electrode; pentavalent P compounds are present on the positive electrode.

The XPS data showed a clear correlation between electrode impedance rise and composition changes in the electrode surface films. The increasing oxygen content of the films with electrode age (Figure 23) suggests that these films are products of electrolyte oxidation, possibly produced by reaction with lattice oxygen. However, the data did not show a direct correlation between the thickness of these surface films and cell age. The observed electrode impedance rise may result from a general degradation of the oxide-electrolyte interface that arises from increased blocking of the edges from which lithium ions enter and leave the oxide particles, combined with increased clogging of the oxide particle pores with cell age.

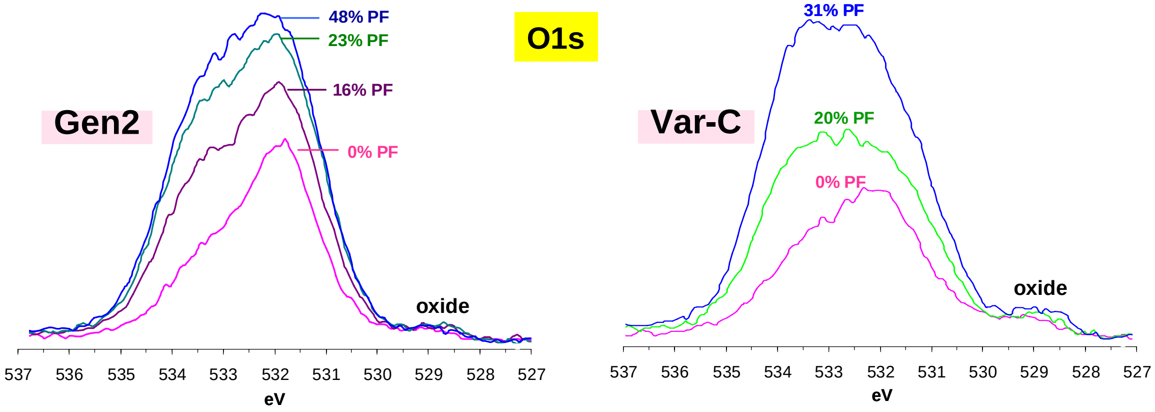

Fig. 23. O1s XPS Spectra from Gen 2 and Var C Positive Electrode Samples Showing Changes with Cell Power Fade. The Y axis (intensity) scales are different for the Gen 2 and Var C samples.

6.4 SUMMARY OF PHYSICOCHEMICAL DIAGNOSTIC DATA

Separator

- The separator is covered by surface deposits that have a fluorescent character. The fluorescence is believed to arise from $LiPO_x$:MeF (M=metal) fluorophosphates that are produced from thermal decomposition of the electrolyte during cell aging.
- Although the separator material does not appear to be damaged by cell aging, clogging of the separator pores by the surface deposits can increase cell impedance.

Negative Electrode

- Cell aging does not damage the graphite in the negative electrode; however, “severely disordered” carbonaceous material was observed on the surfaces of aged anodes. The migration of carbon black from the positive to the negative electrode surface may be an explanation for this observation.
- The negative electrode SEI contains both organic and inorganic constituents, which are electrolyte-solvent and -salt reduction products, respectively. The proportion of the inorganic compounds increases with continued cell aging.
- The SEI layer gets thicker with cell age and produces changes in the negative electrode surface topography.

Positive Electrode

- Aging does not damage the electrode carbons, but the increasing oxide/carbon ratio with cell age indicates an agglomeration of the acetylene black constituent and possibly a migration of carbon away from the electrode.
- The oxide particle bulk does not change significantly with aging; however, in highly aged electrodes, various oxide particles deintercalate and intercalate Li ions at different rates, i.e., the microscale charge-discharge performance of the electrode is very nonhomogeneous, and this behavior appears to worsen with age.
- A $Li_xNi_{1-x}O$ surface layer, which apparently forms because of oxygen loss, is observed on some $LiNi_{0.8}Co_{0.15}Al_{0.05}O_2$ primary particles. The relative proportion of particles bearing this layer appears to increase with cell age.

- P enrichment, observed at the interfaces between primary particles, may suggest an electrolyte-induced corrosion process at these interfaces.
- The electrode surface films contain a mixture of organic and inorganic constituents that include LiF and Li-fluorophosphate compounds. Conflicting data have been obtained on the presence of polymeric species on the electrode surface.
- A correlation was observed between cell impedance rise and composition changes in the electrode surface films. The increasing oxygen content of the films with electrode age suggests that these films are products of electrolyte oxidation, possibly formed by reaction with lattice oxygen.

7 PHENOMENOLOGICAL MODELS

The phenomenological modeling effort is aimed at examining the impedance rise in Gen 2 technology cells. The overall goal of this work is to associate changes that are seen in the post-test diagnostic studies with the loss of electrochemical performance, as measured by the HPPC tests on 18650 cells. The approach taken in this effort is to develop a model based on the analytical diagnostic studies, establish the model parameters, and conduct parametric studies with the model. The parametric studies are conducted to gain confidence with the model, examine degradation mechanisms, and analyze cell limitations. To accomplish these tasks, two versions of the model have been developed. One version simulates the cell response from AC impedance studies, and another model version is utilized for examining HPPC tests. Both of these experimental techniques are used extensively in the program to quantify the cell's electrochemical performance and those of its components. The underlying basis for both models is the same, as are their parameter sets. The modeling effort has concentrated on the positive electrode because of its importance in the cell's overall impedance rise. Additional details on the model are provided in Appendix H.

The general methodology for the phenomenological model follows the work of Professor Newman at LBNL. Concentrated solution theory is used to describe the transport of salt in the electrolyte. Volume-averaged transport equations account for the composite electrode geometry. Electrode kinetics, thermodynamics, and diffusion of lithium in the oxide active particles are also included. The detailed theoretical description of the oxide active material/electrolyte interface, commonly referred to as the solid electrolyte interface, or SEI, is based on post-test analytical diagnostic studies. The SEI region is assumed to be a film on the oxide and an oxide layer at the surface of the oxide. The film on the oxide is taken to be an ill-defined mixture of organic and inorganic material through which lithium ions from the electrolyte must diffuse and/or migrate across to react electrochemically at the surface of the oxide. The lithium is then assumed to diffuse through the oxide surface layer and into the bulk oxide material in the particle. A double-layer capacity is added in parallel with the Butler-Volmer kinetic expression. A localized electronic resistance between the current carrying carbon and the oxide interface can be added, and a secondary film capacitance can also be included.

In the AC impedance version of the model, the pertinent electrochemical reaction, thermodynamic, and transport equations were linearized for a small sinusoidal perturbation. The resulting system of differential equations was solved numerically using a partial differential equation solver over the frequency range of interest. The level of complexity of the model made determining all of its approximately 35 parameters independently a challenge. More than half of the parameters were set by cell construction, obtained from the literature or estimated. Electrode open circuit voltage curves were determined from the slow cycling of half cells. Diffusion, Hittorf, and concentration cell studies were performed on the electrolyte to obtain a set of transport and thermodynamic parameters for the electrolyte. The remaining 10 parameters, most of which were associated with SEI phenomena, were determined from the reference electrode cell measurements. A comparison of the model simulation with the positive electrode experimental AC impedance is given in Figure 24. Even for fresh cells, a bimodal particle size distribution for the positive active material was needed to achieve a reasonable fit to the low-frequency Warburg tail and the best fit was achieved with particles that differ by only a factor of 2.6 in their characteristic diffusion lengths.

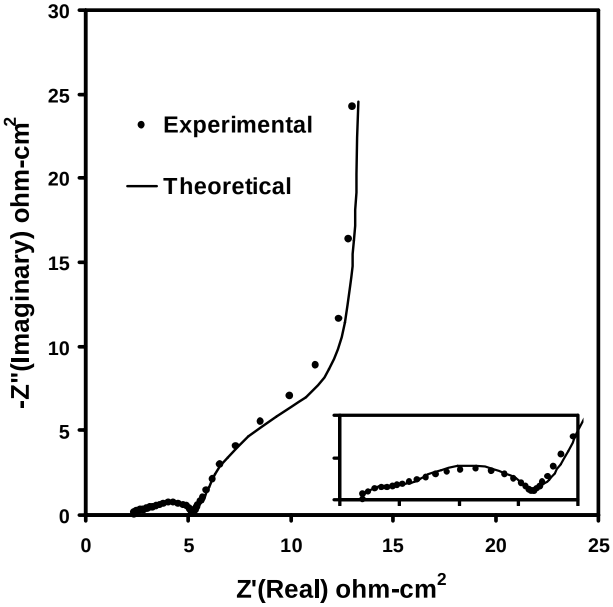

Fig. 24. Comparison of Phenomenological Model with Experiment for the Positive Electrode AC Impedance Data (100 kHz–1 mHz) at 60% State of Charge.

The HPPC version of the model was utilized primarily to gain confidence in the model and for cell optimization studies. The parameter set developed for the positive electrode using the AC impedance version of the model was employed in the HPPC version. HPPC simulations of the positive electrode compared favorably with experimental tests on reference electrode cells. Further, parametric studies with the HPPC version of the model suggest that increasing electrode thickness would improve the initial electrochemical performance, as well as the cell's aging characteristics.

EIS studies on the aging of Gen 2 technology cells, described above, indicate that the interfacial impedance (i.e., the mid-frequency arcs on the Nyquist plot) of the cells grow all through their lives. Furthermore, the low-frequency Warburg diffusional impedance tail also begins to increase late in life. The initiation of the increase in the cell's diffusional impedance roughly corresponds to the change in impedance growth rate (i.e., from square root of time to proportional in time) of the Gen 2 technology cells as measured by the HPPC tests.

The phenomenological AC impedance model was utilized to examine aging effects associated with the positive electrode when only its interfacial impedance increases. Three possible sources for the interfacial impedance increase were identified that are consistent with experimental observations. First, an interfacial impedance increase would result from a degradation of the ionic pathway for lithium ions between the electrolyte in the electrode pores and the bulk oxide active material. This could result from changes in the electrolyte/oxide interfacial structure, composition, and/or properties and would have a direct impact on the positive electrode's interfacial impedance. In addition, the size of the model parameter changes needed to account for the impedance increase suggests that there is a general degradation of the ionic pathway significantly affecting many of the model's interfacial parameters. Second, a loss of positive electrode capacity, particularly isolation of the finer oxide particles, would also cause the interfacial impedance to increase. Simulations based on the measured cell capacity loss suggest that this effect can at best be only a minor contributor to the positive electrode's interfacial impedance increase. Finally, an interfacial impedance increase would result from a degradation of the electronic pathway between the carbon matrix and the oxide active material, provided that the carbon matrix has a sufficiently large double-layer capacitance associated with it. Degradation of the electronic pathway is simulated in the model by a large increase in the electronic resistance between the electronically conducting carbon matrix and oxide active material.

The increase in interfacial impedance of the positive electrode from some combination of the three mechanisms listed above likely continues throughout the life of the cell. While the model is able to estimate an upper bound for the impact of the capacity loss resulting from the isolation of the oxide active material, the model by itself cannot establish the relative importance of the changes in the interfacial ionic pathway vs. changes in the interfacial electronic pathway to the oxide active material. The interfacial ionic pathway tends to be more sensitive to changes in the interface than the electronic pathway for a wide variety of electrochemical systems, including many lithium-ion technologies, which suggests that it is most likely to be the primary source of the impedance increase. Also, it is possible that all three mechanisms are related. As an example, chemical or physical changes in the SEI could cause degradation of the ionic pathway, as well as the electronic pathway, at the oxide interface, which could eventually lead to oxide particle isolation and capacity loss. This type of degradation phenomenon would be consistent with the square root of time impedance growth observed in test cells.

Model simulations indicate that, late in the cell's life, as the diffusional impedance starts to grow, other positive electrode aging phenomena can contribute to the cell's impedance rise. These include a slowing of lithium diffusion within the oxide particles, a loss of electrochemically active area, degradation of electrolyte properties, and a change in electrode microstructure. Degradation of lithium diffusion through the oxide could be caused from changes in the oxide structure (e.g., micro-cracks), but also could result from changes in the intra-granular region between primary particles. A degradation of the intragranular region and the loss of electrochemically active area are both consistent with an extensive general degradation of the oxide primary particles' interfaces. The degradation of electrolyte transport properties and/or a change in electrode microstructure that increases the electrode's tortuosity by approximately a factor of 100 can produce electrode impedances similar to those observed experimentally, but these degradation mechanisms are not commonly supported by the post-test diagnostic results.

8 ASSESSMENT OF VARIOUS PERFORMANCE DEGRADATION MECHANISMS

Various mechanisms have been postulated to explain the performance degradation of the 18650 cells during accelerated aging. These mechanisms, either individually or together, must explain the various dependencies displayed by the cell electrical performance vs. age data, which may be listed as follows:

- Time – cell performance degrades continually with time.
- Temperature – higher testing temperatures accelerate cell performance degradation.
- SOC – performance degradation is greater for cells held at higher states-of-charge.
- Aging protocol – performance degradation is faster for cells that are cycled.
- Oxide composition – although the $LiNi_{0.8}Co_{0.1}Al_{0.1}O_2$ cells (Var C) show greater initial impedance rise, their performance over longer aging periods is better than that of the $LiNi_{0.8}Co_{0.15}Al_{0.05}O_2$ cells (Gen 2) cells.

In addition to these dependencies, the mechanisms must also explain other observations, such as the different "regions" observed in the impedance data and the rapid C/1 decline observed in the capacity data.

The electrochemistry data obtained on the harvested electrodes provide important information on the cell behavior as aging progresses. These data have been summarized in an earlier section, but some noteworthy features are worth repeating:

- The positive electrode is the dominant contributor to cell impedance rise. The electrode impedance rise appears to result from two distinct, and maybe independent, mechanisms that become prominent in different stages of the cell's life.
- The cell capacity fade includes contributions from (a) lithium-consuming side reactions at the negative electrode, and (b) impedance rise that reduces the ability of the positive electrode to deliver and accept lithium at the C/1 and C/25 rates.

The various mechanistic postulates will now be discussed in light of the above observations. These postulates are geared toward explaining the positive electrode impedance rise; the role of the negative electrode is indicated, when appropriate. Note that these postulates are not mutually exclusive, i.e., the mechanisms may be interrelated and cell performance degradation may be influenced by each of these factors to varying degrees.

8.1 POLYMER FORMATION/CO_2 REDUCTION HYPOTHESIS

This hypothesis is based on the GPC observations of high-molecular-weight polymers on both the positive and negative electrodes. Ring opening of the EC molecule, induced by PF_5, produces oligo-ethercarbonates in the electrolyte. The ceiling temperature for this reaction is 170°C, which means it is reversible and does not favor polymerization unless the CO_2 is removed from the polymer to form oligo-ethylene oxides. The evolution of CO_2 from the oligo-ethercarbonates to form oligo-ethylene oxides is also a reversible reaction and will stop if the solution is saturated with CO_2. The CO_2 can be removed from solution by reduction at the negative electrode to form CO, Li_2CO_3, and lithium oxalate, observed in the gas analysis and CE data. The CO_2 removal from the cell induces formation of more oligo-ethylene oxides. Base-induced EC ring opening, followed by CO_2 extrusion, generates oligo-ethylene oxides at the negative electrode.

The oligo-ethylene oxide chains can oxidize at the positive electrode to generate cations and protons according to the following reaction:

$$\text{-}CH_2CH_2\text{-}O\text{-}CH_2CH_2\text{-} \rightarrow CH_2CH^+\text{-}O\text{-}CH_2CH_2\text{-} + H^+ + 2e^- \qquad (6)$$

The rate of oxidation, and thus proton generation, depends on the positive electrode potential. The more positive the electrode potential, i.e., the higher the cell SOC, the greater the oxidation of the ethylene oxide chains. The protons would catalyze cross-linking reactions of the ethylene oxide chains, generating higher-molecular-weight products that could increase electrolyte viscosity adjacent to the oxide particles, leading to higher charge transfer impedances. The oligo-ethylene oxides may also react with PF_5 to form organo-fluorophosphates, which may be the fluorescent compounds observed on the separator. These long-chain phosphate compounds, which are similar to commercially available surfactants, could strongly interact with the nano-sized carbon black particles to produce a colloidial dispersion in the positive electrode, which may lead to increased viscosity, lower salt diffusion coefficients, and increased tortuosity, all of which could impact the electrode impedance.

The main weakness of this hypothesis is that the oligomers/polymers observed by the GPC experiments may be an artifact of the sample extraction process; appropriate “control” experiments are needed to exclude this possibility. Note that FTIR, XPS, and Raman measurements have not detected significant quantities of polymers on the electrode surfaces. Furthermore, there does not appear to be a correlation between the oligomer quantities and positive electrode impedance rise. In addition, although small quantities of oligomeric species have been detected in the electrolyte, there is no evidence of electrolyte viscosity changes with cell power fade.

8.2 CARBON RETREAT/REDISTRIBUTION HYPOTHESIS

The carbon retreat hypothesis is based on Raman microscopy/spectroscopy observations of carbon black moving away from, and/or carbon black redistribution on, the positive electrode surfaces. This carbon retreat/redistribution exposes small crystallites within the oxide particle agglomerates. If these particles were originally in poor electronic contact with their neighbors, then the consequent loss of a direct electronic path to the current collector through the receding carbon matrix will lead to an increased resistance within the composite coating and, eventually, to total isolation of some particles. The intergranular electronic contact within agglomerates may deteriorate further during cell aging/cycling due to mechanical stresses, thin film formation, gas evolution, etc. The combination of carbon retreat/rearrangement, along with degradation of the intrinsic electronic properties of the $LiNi_{0.8}Co_{0.15}Al_{0.05}O_2$ particles, is thus responsible for the observed cell power and capacity fade. An electrical circuit model based on a distributed resistance network has shown that the above described scenario can lead to a significant shift of the low-frequency minimum in the EIS spectra, with minimal effect on the position of the high-frequency minimum.

One weakness of this hypothesis lies in the SEM and TEM images that show carbon black in intimate contact with the oxide particles in cathodes from even highly aged cells. Another weakness lies in the assumption that the increase in cathode surface resistance with electrode age, observed in CSAFM measurements, arises from the retreat of carbon away from the oxide particles—insulating films on the electrode surface could produce similar results. Furthermore, the physical mechanism that induces carbon movement in the electrode, and the influence of cycling, temperature, SOC, and oxide composition on this movement, remains unclear. In addition, the low-rate and high-temperature cycling data have indicated that the electronic isolation of particles may be a significant contributor only in the mid- to late-life cells.

8.3 OXYGEN LOSS/OXIDE PARTICLE SHRINKING HYPOTHESIS

This hypothesis is based on TEM observations of gradual oxygen loss from the oxide particles, and on in-situ FTIR-ATR experiments that show the formation of an oxidation product on Gen 2 cathodes at 4.2 V and higher in a Gen 2 electrolyte. The reaction involves oxygen transfer from the oxide lattice to the solvent at the point where x in $Li_{(1-x)}Ni_{0.8}Co_{0.15}Al_{0.05}O_2$ is greater than 0.6, and may be represented by the following equation:

$$C_5H_{10}O_3 + O_2 \rightarrow C_4H_6O_3 + CO + 2H_2O \qquad (7)$$

The reaction products are a dicarboxylic acid anhydride (maleic anhydride being a model), CO, and water. The anhydrides are not expected to cause clogging of the electrode pores, i.e., they do not contribute directly to impedance rise. Rather, these phenomena may contribute to the 18650 cell power and capacity fade, as described below.

During aging, the cell SOC is 60%, corresponding (initially) to a nominal $x = 0.5$ in the oxide, using the relation $x = 0.15 + 0.55$ (SOC). We know from the XRD and Raman data that the oxide particles are not utilized uniformly, and that the nominal state of charge represents the average of high and low states of charge, i.e., some oxide particles may be at $x = 0.7$ and an equal number are at $x = 0.3$. Hence, some particles will react with electrolyte even when the nominal cell SOC is 60%. As the cell ages and Li is consumed at the anode, the mean value of x in the cathode will increase with time. At a loss of ~20% of the initial cyclable Li, the nominal value of x in the cathode active material at 3.7 V would increase to above the critical value of 0.6. It seems possible that close to $x = 0.6$ and at 45–55 °C, there is a slow loss of oxygen, on a time scale of 10^3 hours, from the oxide particles. This oxygen loss causes a shrinking of oxide particles away from the adjacent carbon matrix, resulting in particle isolation.

One weakness of this hypothesis lies in the lack of evidence that indicates that oxide particles shrink because of oxygen loss. Furthermore, the mechanism cannot explain impedance rise early in the cell life because the oxide particles are known to equilibrate rapidly, especially at the 45–55 °C aging temperatures. However, oxide particles at different SOC may be present in the cathode in late-life cells, even at the higher aging temperatures.

8.4 OXYGEN LOSS/SURFACE FILMS HYPOTHESIS

This hypothesis is based on the correlation observed between electrode impedance rise and composition changes in the electrode surface films observed with XPS, along with TEM observations of changes at the oxide particle surfaces. As mentioned previously, we know that the oxide particles in the composite coating contribute and accept Li ions at different rates. The particles that initially contribute and accept Li ions at high rates may also be more prone to gradually losing surface oxygen, which creates a $Li_xNi_{1-x}O$ layer that hinders Li-ion motion in and out of these particles. In addition, the evolved oxygen reacts with the adjacent electrolyte to form organic/inorganic compounds that coat the various particles and degrade the oxide particle-electrolyte interface. The inorganic compounds may not be the only contributors to interface degradation; similar compounds are also observed in the negative electrode, which shows minimal impedance rise. The continuing changes in the oxide surface films and surface structure with age affect the mid-frequency arc and Warburg tail, respectively. PF_5-induced corrosion of the oxide particle interfaces may also be partially responsible for the greater Warburg impedance observed in highly aged electrodes.

The cumulative loss of oxygen from the oxide particles would increase with time, thus influencing the surface structure and surface films on the oxide particles. Furthermore, the tendency of the oxide to lose oxygen would be enhanced by cell cycling, higher aging temperatures, higher SOC, and lower Al content in the oxide, i.e., the Gen 2 oxide is more prone to oxygen loss than the Var C oxide.

One weakness of this hypothesis lies in the lack of direct evidence for oxide oxygen loss under the conditions of cell aging (3.72 V, 55°C), especially early in cell life. Furthermore, the oxide particle surface films observed in the TEM appear to be relatively thin and discontinuous. TEM imaging conditions are, however, significantly different from those inside a working cell, and appropriate diagnostic tools must be developed/utilized to image the cathode surface films. In addition, the corrosive effect of PF_5 on the oxide primary particles needs to be verified.

9 CONCLUSIONS

Diagnostic examination of components harvested from high-power lithium-ion cells was conducted to determine the causes of capacity fade and impedance rise exhibited by the cells during accelerated aging. This report reflects our current understanding of the complex phenomena occurring in the cells. Our data show that the positive electrode is the dominant contributor to impedance rise in these cells. The electrode impedance rise appears to result from at least two distinct and maybe independent processes that become prominent in different stages of the cell life—degradation of the electrode-electrolyte interface in early- and mid-life cells, and degradation of lithium-ion diffusion characteristics within the composite electrode in late-life cells. The various mechanisms postulated to explain cell performance degradation behavior focus on the positive electrode and include (1) polymer formation and viscosity changes in the electrode pores, (2) retreat or redistribution of carbon away from the oxide particles, (3) oxide particle shrinking resulting from oxygen loss, and (4) oxide particle surface changes as a consequence of oxygen loss. These postulates may be modified as our experiments continue to yield relevant information. A phenomenological model, based on concentrated solution theory, has indicated that a general degradation of the ionic pathway is probably the most significant contributor to the positive electrode interfacial impedance increase.

We hope that this report will provide battery developers with insight into the process for diagnostic evaluation of a generic lithium-ion battery technology. The data presented herein indicate the type of information that can be obtained by the various diagnostic techniques. The level of understanding required by developers will dictate the type of tools used for the evaluation. This report may be used as a guide for appropriate tool selection. We welcome questions and comments on test methodology and data interpretation. Additional observations and feedback to the various contributing authors are encouraged and greatly appreciated.

REFERENCES

1. Anderman, M., J. Power Sources **127**, 2 (2004).

2. Bloom, I., B. W. Cole, J. J. Sohn, S. A. Jones, E. G. Polzin, V. S. Battaglia, G. L. Henriksen, C. Motlock, and R. Richardson, J. Power Sources **101**, 238 (2001).

3. Bloom, I., S. A. Jones, E. G. Polzin, V. S. Battaglia, G. L. Henriksen, C. G. Motlock, R. B. Wright, R. G. Jungst, H. L. Case, and D. H. Doughty, J. Power Sources **111**, 152 (2002).

4. Bloom, I., S. A. Jones, V. S. Battaglia, G. L. Henriksen, J. P. Christophersen, R. B. Wright, C. D. Ho, J. Belt, and C. G. Motloch, J. Power Sources **124**, 538 (2003).

5. Balasubramanian, M., X. Sun, X. Q. Yang, and J. Mcbreen, J. Power Sources **92**, 1 (2000).

6. Balasubramanian, M., X Sun, X. Q. Yang, and J. McBreen, J. Electrochem. Soc. **147**, 2903 (2000).

7. Balasubramanian, M., H. S. Lee, X. Sun, X. Q. Yang, A. R. Moodenbaugh, J. McBreen, D. A. Fischer, and Z. Fu, Electrochem. Solid-State Lett. **5**, A22 (2002).

8. Zhang, X., P. N. Ross, Jr., R. Kostecki, F. Kong, S. Sloop, J. B. Kerr, K. Striebel, E. Cairns, and F. McLarnon, J. Electrochem. Soc. **148**, A463 (2001).

9. Kostecki, R., and F. McLarnon, Electrochem Solid-State Lett. **5**, A164 (2002).

10. Norin, L., R. Kostecki, and F. McLarnon, Electrochem. Solid-State Lett. **5**, A67 (2002).

11. Sloop, S. E., J. B. Kerr, and K. Kinoshita, J. Power Sources **119–121**, 330 (2003).

12. Zhang, G. V., and P. N. Ross, Jr., Electrochem Solid-State Lett. **6**(7), A136 (2003).

13. Song, S.-W., G. V. Zhuang, and P. N. Ross, Jr., J. Electrochem. Soc. **151**(8), A1162 (2004).

14. Kostecki, R., L. Norin, X. Song, and F. McLarnon, J. Electrochem. Soc. **151**, A522 (2004).

15. Lei, J., F. McLarnon, and R. Kostecki, J. Phys. Chem. B **109**(2), 952 (2005).

16. Andersson, A. M., D. P. Abraham, R. Haasch, S. MacLaren, J. Liu, and K. Amine, J. Electrochem. Soc. **149**, A1358 (2002).

17. Abraham, D. P., J. Liu, C. H. Chen, Y. E. Hyung, M. Stoll, N. Elsen, S. MacLaren, R. Twesten, R. Haasch, E. Sammann, I. Petrov, K. Amine, and G. Henriksen, J. Power Sources **119-121**, 511 (2003).

18. Abraham, D. P., R. D. Twesten, M. Balasubramanian, J. Kropf, D. Fischer, J. McBreen, I. Petrov, and K. Amine, J. Electrochem. Soc. **150**, A1450 (2003).

19. Abraham, D. P., S. D. Poppen, A. N. Jansen, J. Liu, and D. W. Dees, Electrochim. Acta **49** 4763 (2004).

20. Herstedt, M., D. P. Abraham, J. B. Kerr, and K. Edstrom, Electrochim. Acta **49**, 5097 (2004).

21. Bloom, I., A. N. Jansen, D. P. Abraham, J. Knuth, S. A. Jones, V. S. Battaglia, and G. L. Henriksen, J. Power Sources **139**, 295 (2005).

22. Bloom, I., J. Christopherson, and K. Gehring, J. Power Sources **139**, 304 (2005).

23. Chen, C. H., J. Liu, and K. Amine, J. Power Sources **96** 321 (2001).

24. Amine, K., C. H. Chen, J. Liu, M. Hammond, A. Jansen, D. Dees, I. Bloom, D. Vissers, and G. Henriksen, J. Power Sources **97-98**, 684 (2001).

25. Dees, D., E. Gunen, D. Abraham, A. Jansen, and J. Prakash, J. Electrochem. Soc. **152**, A1409 (2005).

26. Battery Technology Life Verification Test Manual, Draft Report (June 2004). Available at http://www.uscar.org/consortia&teams/techteamhomepages/BATTERY.html.

27. PNGV Battery Test Manual, Revision 3, INL (2001).

28. Campion, C. L., W. Li, W. B. Euler, B. L. Lucht, B. Ravdel, J. F. DiCarlo, R. Gitzendanner, and K. M. Abraham, Electrochem. Solid-State Lett. **7**, A194 (2004).

29. Winter, M., J. O. Besenhard, M. E. Spahr, and P. Novak, Ad. Mater. **10**, 725 (1998).

30. Handbook of Diagnostic Techniques, Advanced Technology Program for Lithium-Ion Batteries, Lawrence Berkeley National Laboratory Report LBID-2464 (2003).

APPENDIX A. DIAGNOSTIC EVALUATION OF LITHIUM-ION BATTERY TECHNOLOGY

A.1 DIAGNOSTIC EVALUATION OF A LITHIUM-ION BATTERY TECHNOLOGY

Dennis Dees and Daniel Abraham

The description that follows is intended to supplement the information in the accompanying diagram (Fig. A-1). Its purpose is to illustrate the overall process involved in the diagnostic evaluation of a generic lithium-ion battery technology. While the approach presented here can be applied to any lithium-ion battery technology, the specific approach taken and level of effort needed for the various steps are highly dependent on the type of electrolyte used in the technology (i.e., liquid, plasticized, or polymer). As an example, the electrochemical characterization of aged laminate electrodes readily lends itself to liquid electrolyte systems for which the electrodes can more easily be extracted.

In the diagram, each of the numbered (lower right corner) boxes represents a piece of diagnostic process. The arrows show the order of studies and the flow of materials, components, or cells needed to accomplish the task and/or conduct the study. In general, the diagram can be broken down into four groups, shown as layers. The topmost layer (Boxes 1–4) contains the activities required to enable the diagnostic studies to be conducted. The second layer (Boxes 5–7) includes the electrochemical diagnostic studies and the initial physicochemical diagnostic studies. The third layer (Boxes 8–10) contains the more in-depth physicochemical diagnostic studies. The bottom layer (Boxes 11–16) is a short list of optional diagnostic studies that could be carried out if warranted by any of the suggested studies. This list is not meant to be all-inclusive, but merely illustrative of the types of studies that have been found to be useful in previous lithium-ion diagnostic studies. The same may be said of the specific studies listed in parentheses in some of the boxes.

The first requirement of any diagnostic evaluation of a technology is to establish access to the technology (Box 1). It is assumed here that an adequate number of test cells are available that can be aged in a controlled manner under appropriate stress factors (Box 2). The appropriate stress factors will obviously depend on the specific battery technology, but typically time, temperature, and state of charge are the primary factors for a lithium-ion technology. To a somewhat lesser extent, cycling protocols (e.g., pulsed or continuous, controlled current or power, and rate) can also affect life. It is important to have test cells aged to various states of life (from fresh through end-of-life) at reasonable increments, such as every 10 to 25% degradation. It is just as important to have available sufficient cell materials (e.g., active materials, binders, conductive additives, electrolyte salts, electrolyte solvents, electrolyte additives, separators, and current collectors) and components (e.g., positive and negative laminates and cell hardware) from each phase of cell manufacturing.

Electrochemical characterization of the individual cell components at the various states of life is a critical part of the diagnostic evaluation of the battery technology (Box 7). To accomplish this, a methodology must be developed for opening and disassembling the cells (Box 3) without significant degradation of the components (see Fig. A-2). Further, a methodology must be developed for studying the aged and fresh components in specially designed electrochemical cells (Box 4). These special cells would include, but certainly would not be limited to, full cells with a reference electrode, symmetric cells made with either the positive or negative electrodes, and half cells made with either the positive or negative electrode while using lithium as the counter electrode. A broad range of common electrochemical techniques can be used to characterize a lithium-ion technology. Types of techniques that have been particularly useful include AC impedance, current pulse studies developed for hybrid applications, and cycling at various rates.

Visual examination of all components during disassembly that is later supplemented by a series of SEM studies is often critical in focusing the diagnostic effort (Box 5). As an example, significant delamination or powdering of an electrode may suggest that a more in-depth examination of laminate adhesion and the binder be undertaken (Box 12). This may also suggest that the electronic conductivity of the electrodes needs to be measured (Box 13). The initial and in-depth physicochemical studies are geared to addressing areas of concern that are common to most lithium-ion battery technologies, but that may not be the life limiting issues with a specific battery technology. The electrochemical diagnostic studies would also be useful in directing the physicochemical studies.

Solid-state diffusion of lithium into and out of the active materials occurs in all lithium-ion battery technologies. This movement of lithium exerts stresses on the structural lattice and particles. Therefore, once the initial screening of the cell components has been completed, a close examination of the electrode’s active materials is the next step (Box 6). Scanning electron microscopy (SEM) and X-ray diffraction (XRD) can be used to determine if any major physical and structural changes have occurred in the active particles. These studies should detect such problems as particle cracking, primary particle separation, or changes in the materials’ structural lattice that could lead to performance losses.

All known organic electrolyte lithium battery technologies are thermodynamically unstable. This instability manifests itself as side reactions at the interfaces between the electrode materials and the electrolyte. The side reactions can consume usable lithium and generate thin films of products at the solid electrolyte interface (SEI). The SEI would also include any surface layers on the active materials that could be present from synthesis or may have developed during aging. Typically, the side reactions and resulting SEI are more evident on the negative active material than the positive, but reaction products are found on both materials. Impedance increases in lithium-ion cells have been associated with the SEI. Therefore, an in-depth examination of these surface films could provide key insights to the cell’s aging process (Box 9). Unfortunately, the thickness of the SEI and the composite electrode structure make them very difficult to examine. Typically, a number of different techniques need to be employed to gain a clear picture of the SEI. In a parallel effort, it is also possible to develop planar electrodes made of the active material on a conductive substrate, which could be used to better elucidate the SEI (Box 15).

The interfacial side reactions are generally greatest during the cell’s formation process, but can continue to occur throughout the life of the cell. Because the electrolyte is involved in the side reactions, its stability is an issue that gives rise to the need to examine the electrolyte for any changes in composition (Box 10). The presence of soluble contaminates from the electrodes that could react at the opposite electrode should also be explored. Significant changes in composition could also affect the electrolyte's transport properties, which may also need to be examined (Box 14). Electrolyte instability can generate gases and low molecular weight hydrocarbons (e.g., H_2, CO, CO_2, CH_4, C_2H_4, C_2H_6, etc.). Analyzing the changes in gas volume and composition may provide insight into degradation rates and mechanisms (Box 11). Finally, the electrolyte can react with all conductive materials in the cell that are at the electrode potentials, including the current collectors. If, for example, an initial examination of the current collectors shows evidence of significant pitting, then a more complete corrosion study may be needed (Box 16).

A lithium-ion battery tends to be a coated and rolled technology, creating a high geometric surface area device. The current in the cells is distributed by relatively thin metal foil current collectors. Uniformity of current distribution depends on many factors including cell impedance, temperature, current collector thickness, and the number and position of the current tabs on the foil. Because of the composite electrode structure, current uniformity is not only an issue across the face, but also through the thickness of the electrodes and from one active particle to another. Variations in electrode coating thickness and attack by contaminates (e.g., H_2O), especially along the edge of the cell, can also impact the current distribution. This suggests that multiple samples at various positions may need to be used for the electrochemical characterization work and other diagnostic studies.

The possibility of compositional changes occurring in the electrodes as they age should be examined (Box 8). As discussed in the previous paragraph, the state of charge of the active material may change with position, which can affect cell performance if the distribution becomes less uniform over time. Ideally, this study could form the basis for a lithium inventory of the cell, but that may require more effort than is warranted. Further, fundamental changes in the bulk composition of the electrodes should be investigated. As an example, the positive electrode's carbon-to-oxide ratio may change with time.

What has been described here is an extensive set of diagnostics for a generic lithium-ion battery technology. The first two layers on the diagram (Boxes 1–7) constitute a basic set of diagnostic studies. They will establish the technology's performance degradation rate and isolate each component's contribution. Depending on the severity and source of the performance loss, it may be possible to determine the mechanisms. In any case, these studies will provide a basis for proposing a hypothesis and could be crucial in determining the future direction of the diagnostic studies.

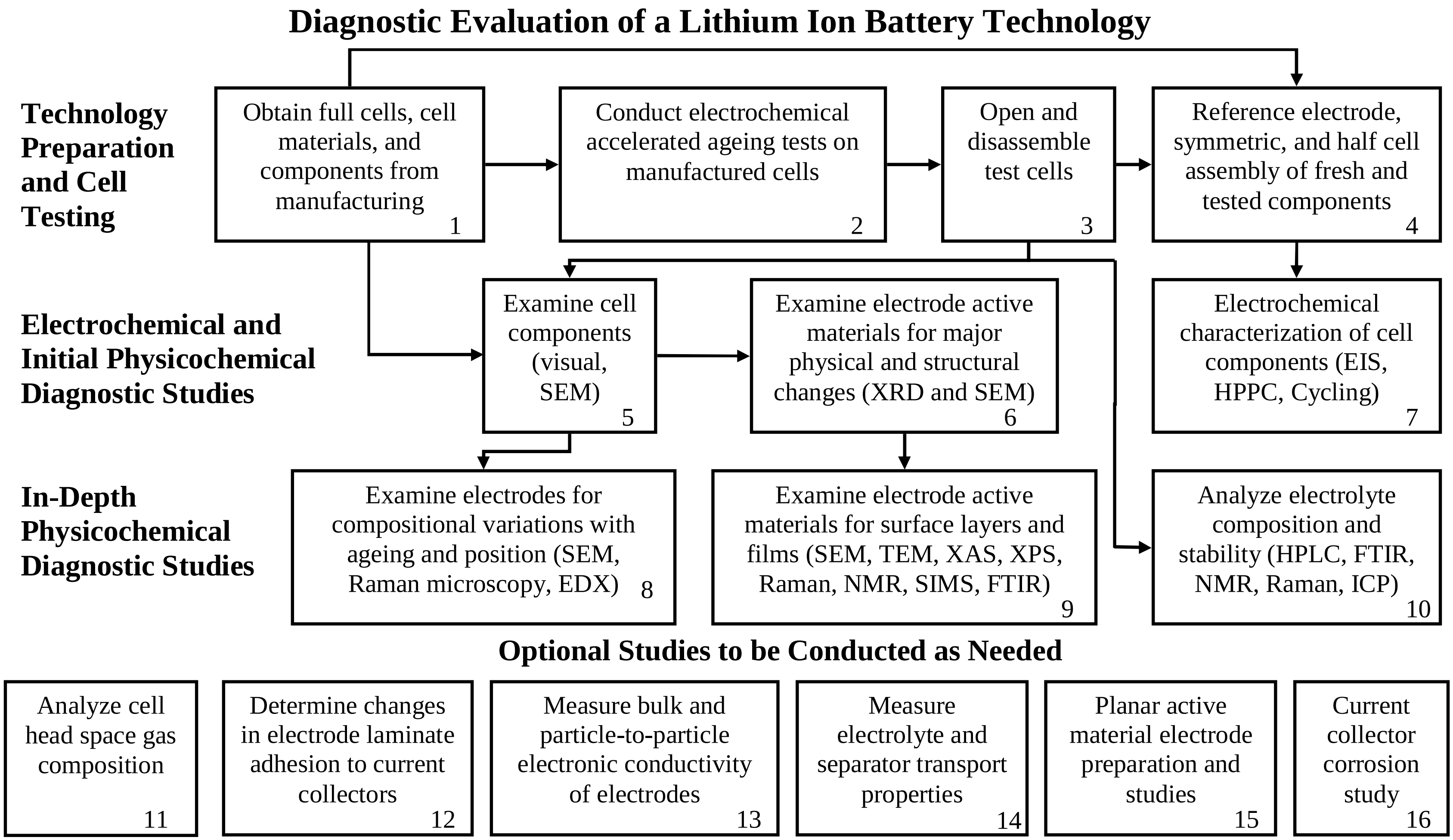

Fig. A-1. Overall Process Involved in Diagnostic Evaluation of a Generic Lithium-Ion Battery Technology.

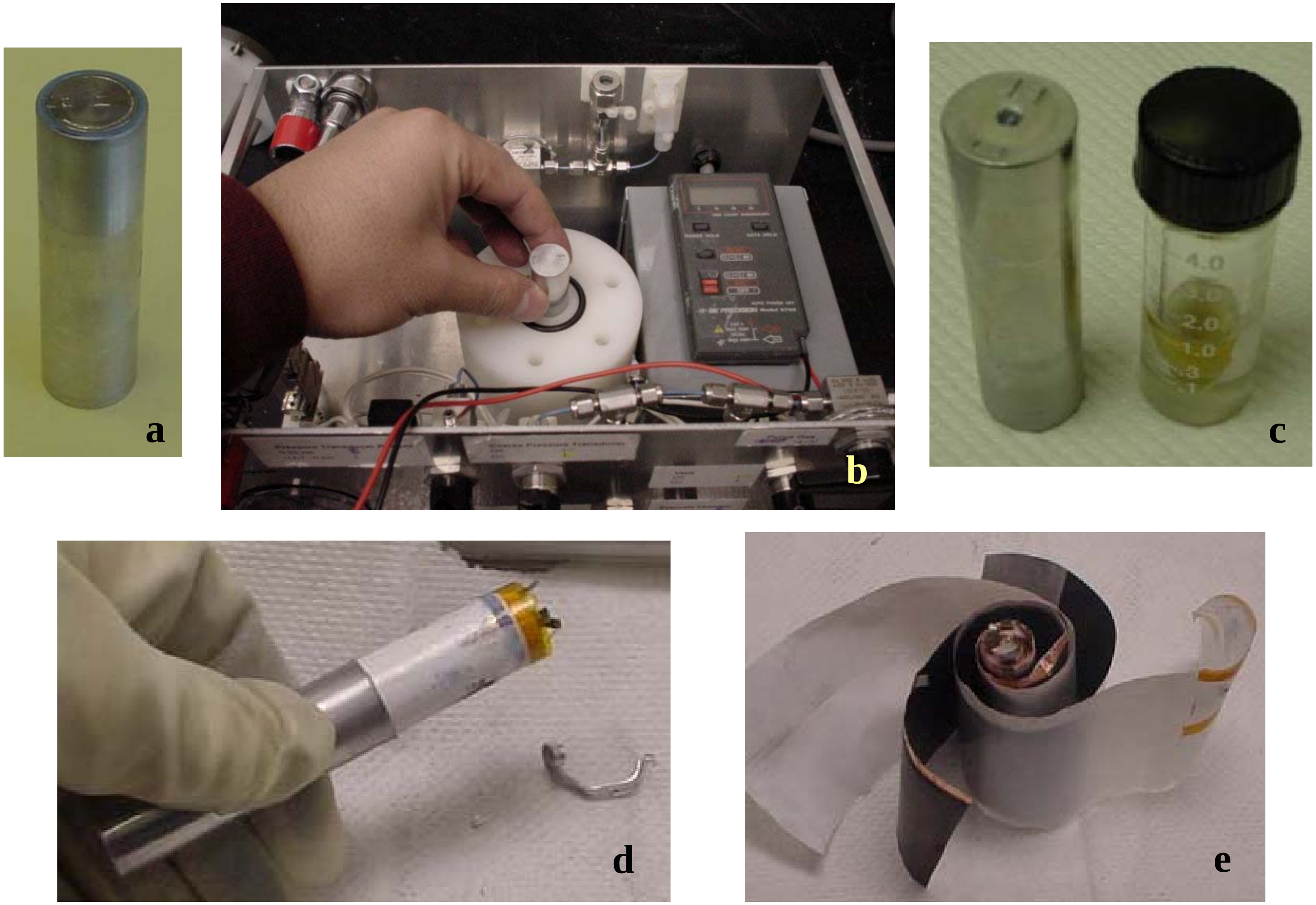

Fig. A-2. Portions of the Cell Disassembly Process: (a) 18650 Cell, (b) Cell Puncturing Device, (c) Centrifuged Electrolyte, (d) Extricating the Cell Innards, (e) Unraveling the Cell Components.

APPENDIX B. ANALYSIS OF GASES FROM 18650 CELLS

B.1 18650 CELL GAS ANALYSIS

Daniel Abraham and Yoo-Eup Hyung

B.1.1 Experiments Conducted

Gas composition was determined using He carrier gas with a Hewlett-Packard (HP) 6890 series gas chromatograph. A thermal conductivity detector was used to study noncombustible gases, such as CO and CO_2, and a HP 5973 mass-selective detector was used to study hydrocarbon gases, such as CH_4, C_2H_6, and C_2H_4. Inert gas species, such as He and Ar, were also present in the gas mixture.

B.1.2 Summary of Results

Figures B-1, B-2, and B-3 show the gas composition changes induced by aging the Gen 2 cells at 55°C and 45°C and Var C cells at 45°C, respectively. Hydrocarbons appear to be the dominant species after formation cycling. In all cases, CO content shows an increasing trend with cell age; the concentration appears to be enhanced by higher testing temperatures. The CO_2 content appears to increase in the initial weeks of aging, but then shows a decreasing trend. The hydrocarbon (CH_4, C_2H_6, and C_2H_4) content in the cells also appears to increase somewhat with cell age.

B.1.3 Conclusions

- Hydrocarbons appear to be the dominant species after formation cycling. The presence of these species is consistent with electrolyte reduction in forming the graphite SEI layer.
- The main trend for cell aging is the increase in cell CO content. Hydrocarbon content also appears to increase, although very gradually.

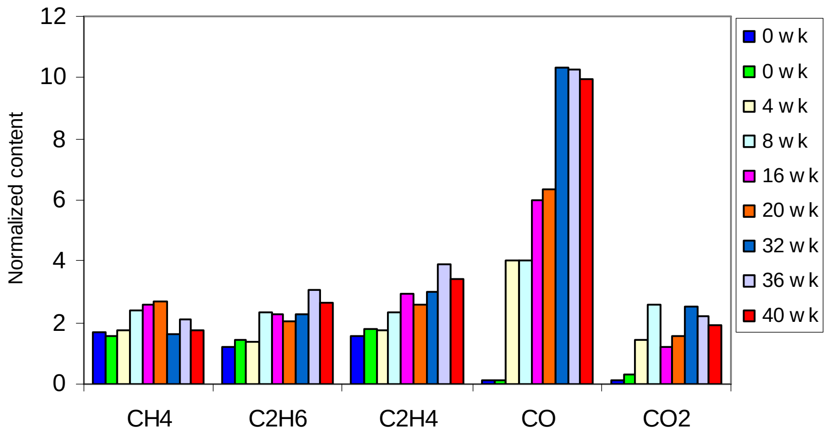

Fig. B-1. Gas Analysis Data from Gen 2 Calendar-Life Cells Aged at 55°C up to 40 Weeks. The 0-week cells were “formed” but not aged.

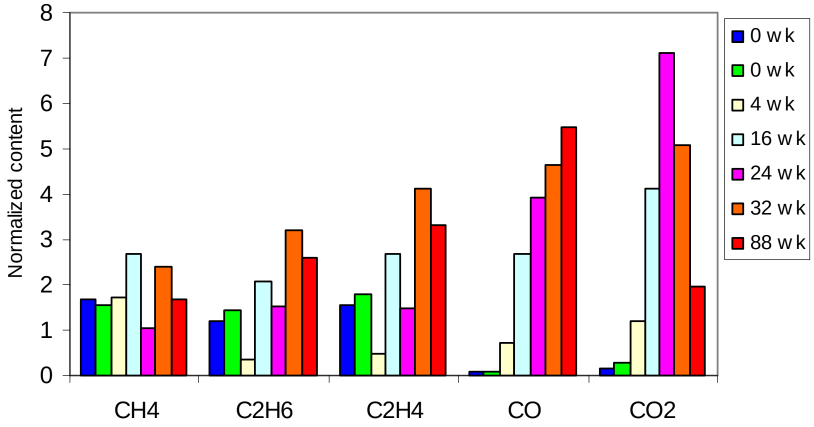

Fig. B-2. Gas Analysis Data from Gen 2 Cells Aged at 45°C up to 88 Weeks. The 0-week cells were "formed" but not aged. All data are from cycle-life cells, except for the 88-week data, which is from a calendar-life cell.

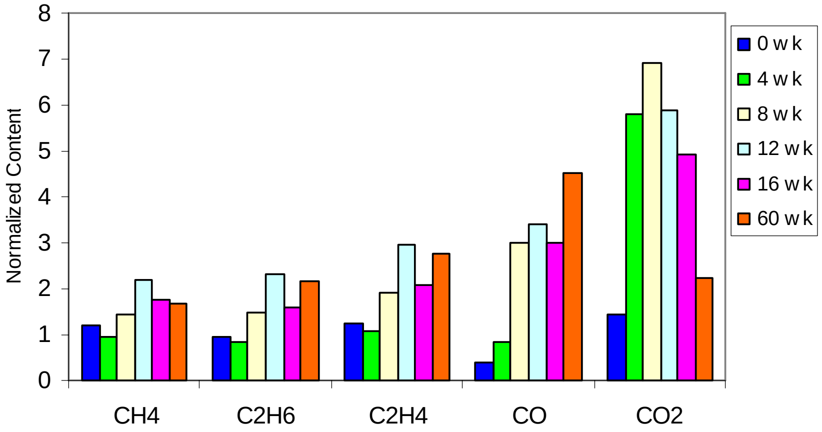

Fig. B-3. Gas Analysis Data from Var-C Cells Calendar- and Cycle-Life Aged at 45°C up to 60 Weeks. The 0-week cells were "formed" but not aged.

APPENDIX C. ANALYSIS OF ELECTROLYTES FROM 18650 CELLS

C.1 HIGH-PERFORMANCE LIQUID CHROMATOGRAPHY ANALYSIS

Daniel Abraham and Michael Stoll

C.1.1 Experiments Conducted

High-performance liquid chromatography (HPLC) uses a liquid mobile phase to separate the components of a mixture. These components are first dissolved in a solvent, and then forced to flow through a chromatographic column under a high pressure, where the mixture is resolved into its components. HPLC analysis was used to identify and quantify organic electrolytic constituents in electrolytes extracted from 18650 cells. The punctured cells were centrifuged to extract the electrolyte, which was analyzed with a refractive index detector on a Hitachi D-7000 high-performance liquid chromatograph. About 100 µL of the electrolyte solution was diluted with a water:acetonitrile (60:40 vol%) mobile phase for the analysis. Control experiments were conducted on fresh Gen 2 electrolyte samples.

C.1.2 Summary of Results

Figure C-1 shows the changes in the Gen 2 electrolyte induced by formation cycling. It is apparent that the electrolyte solvent changes from a binary (EC-EMC) mixture to a multi-component mixture that contains EC, EMC, DEC, DMC, EMDOHC, DEDOHC, and DMDOHC. These additional solvent components are not observed when the electrolyte is simply heated to 55°C; they are observed only in cycled cells, which suggests that the transesterification reactions that produce the additional components are electrochemically induced.

Figure C-2 shows data from a series of Gen 2 cells that were calendar-life aged at 55°C up to 40 weeks. Figure 3 shows data from Gen 2 and Var C cells that were aged at 45°C up to 32 weeks. Both data sets show that cell aging does not measurably alter the bulk electrolyte composition beyond that induced by the formation cycling process.

C.1.3 Conclusions

- Formation cycling induces transesterification reactions in the Gen 2 electrolyte that convert it from a binary solvent to a multi-component mixture.
- The compositions of the bulk solvents from the various cells were very similar, which suggests that (a) cell aging does not alter the solvent, or (b) the HPLC technique is not sensitive enough to detect subtle changes in the electrolyte that are induced by the aging process.

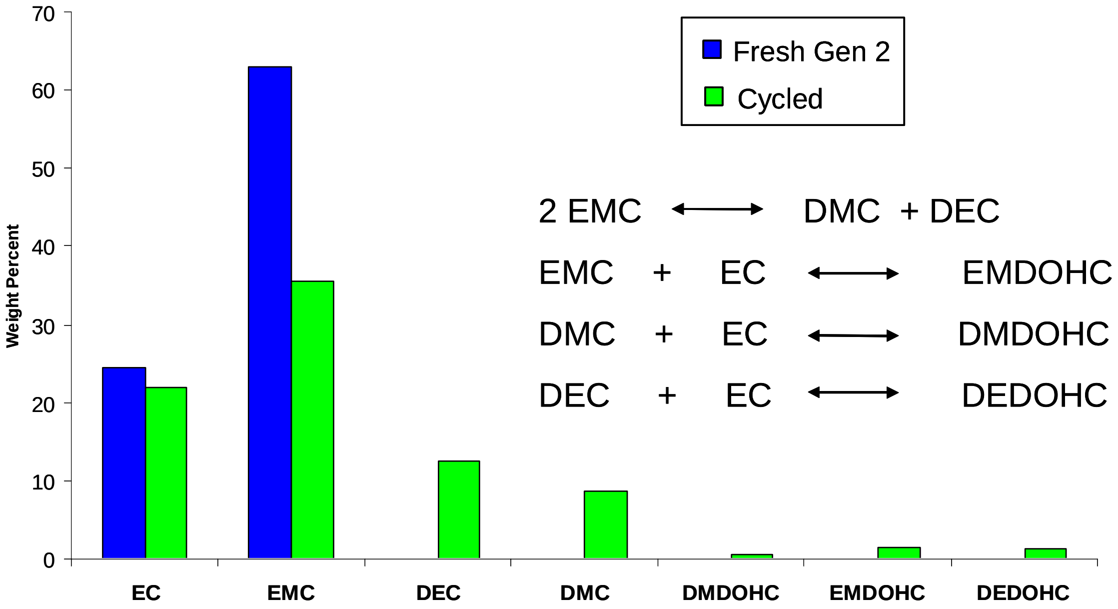

Fig. C-1. Electrolyte Constituents Quantified by HPLC before (Fresh Gen 2) and after Cell Formation. Chemical reactions that produce additional electrolyte components during cell cycling are shown.

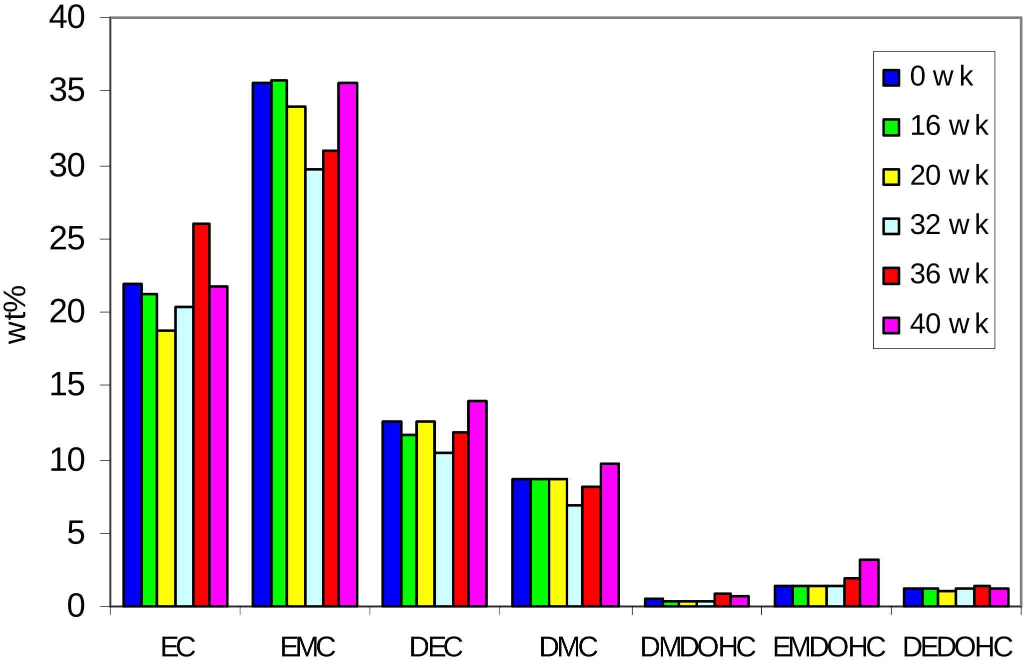

Fig. C-2. Electrolyte Solvent Data from Gen 2 Cells Calendar-Life Aged at 55°C up to 40 Weeks. The 0-week cell was “formed” but not aged.

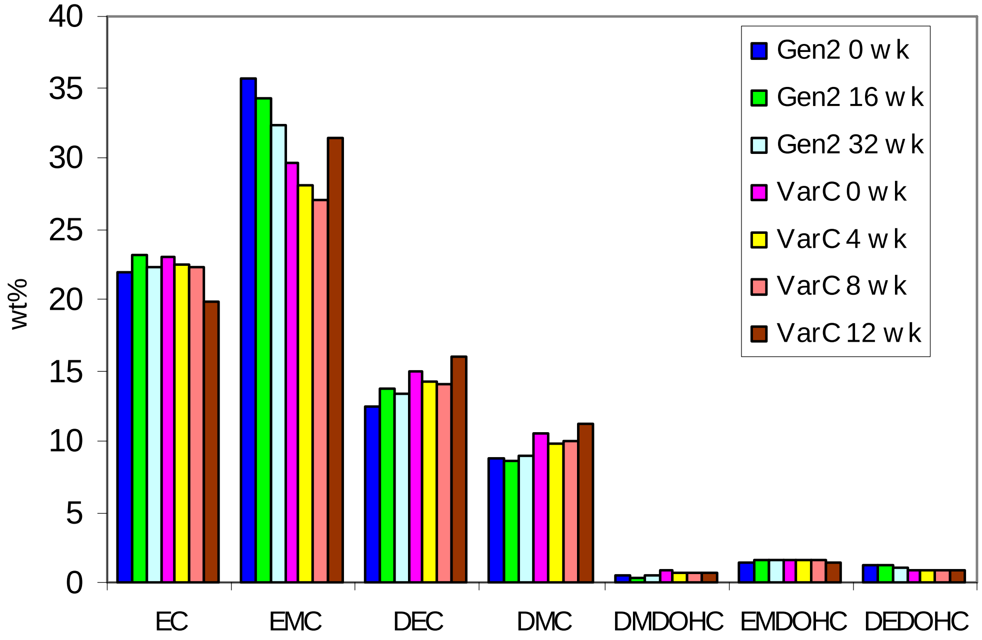

Fig.C-3. Electrolyte Solvent Data from Gen 2 and Var C Cells That Were Aged at 45°C to 32 Weeks. The 0-week cells were "formed" but not aged.

C.2 FOURIER TRANSFORM INFRARED SPECTROSCOPY ELECTROLYTE ANALYSIS

Vera Zhuang and PhilipRoss

Fourier transform infrared (FTIR) spectroscopy data were obtained on a liquid electrolyte sample in the attenuated total reflection (ATR) mode. All spectra were acquired with a spectral resolution of 4 cm^{-1} and summed over 512 scans. The probe size was 2 mm in diameter, and probing depth was estimated to be ca. 500 nm. The spectra were corrected for light penetration depth as a function of wavelength, and a linear background correction was applied. None of the spectra were subjected to a smoothing algorithm.

C.2.1 Experiments Conducted

Diethyl carbonate (DEC) and dimethyl carbonate (DMC) were added into fresh Gen 2 electrolyte (EC(3):EMC(7)/1.2 M $LiPF_6$) to form a reference mixture containing EC:EMC:DMC:DEC = 1:2.33:0.58:0.58. A FTIR spectrum of the mixture was obtained and with that of an electrolyte from a cell.

FTIR measurements were performed on electrolyte extracted from an aged cell, which had the following ATD identifier number: G2.60C55.A211.30.40.31.G.L. This cell was calendar-life aged at 55°C for 40 weeks and showed ~31% power fade.

C.2.2 Summary of Results

DMC and DEC, which are not Gen 2 electrolyte components, were found in the electrolyte from the aged cell (see Fig. C-4).

C.2.3 Conclusions

By comparing the FTIR spectrum of a Gen 2 electrolyte mixed with DMC and DEC with that of an electrolyte from an aged cell, we found evidence of electrolyte transesterification, which was consistent with the HPLC data.

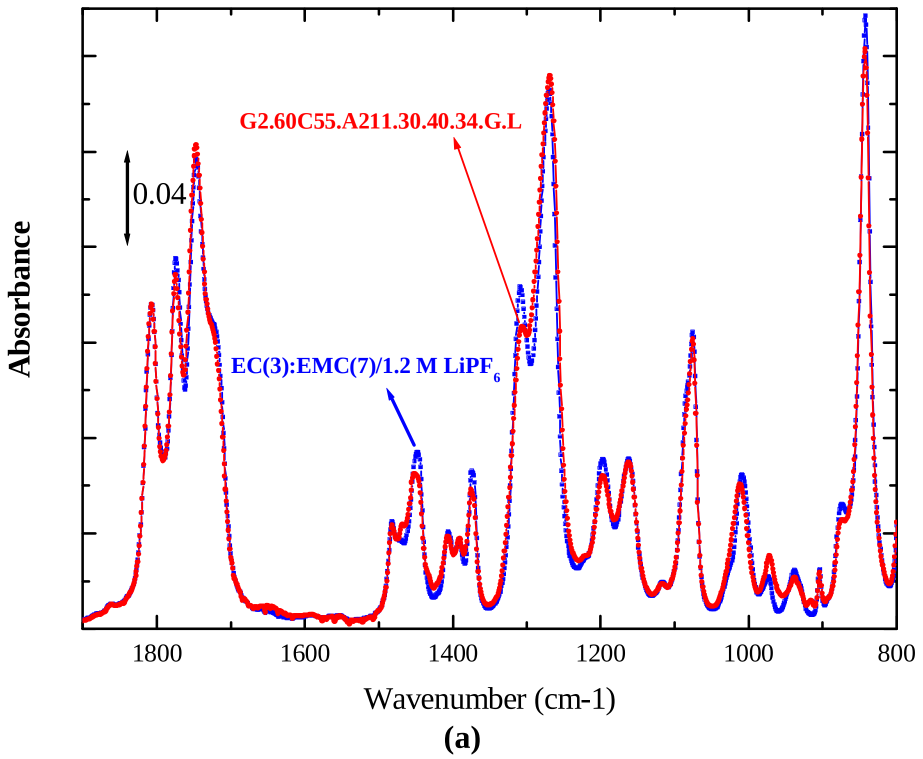

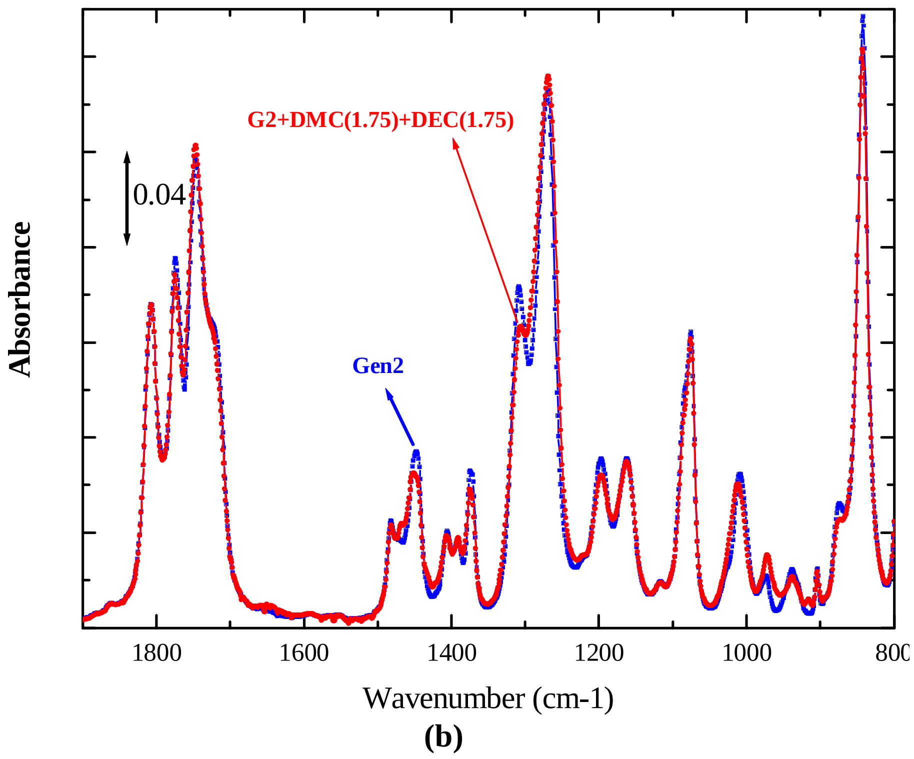

Fig. C-4. FTIR Data on (a) Electrolyte Extracted from an Aged Cell Compared with the Gen 2 Electrolyte, and (b) Reference Electrolyte Mixture Compared with the Gen 2 Electrolyte.

C.3 PROTON NUCLEAR MAGNETIC RESONANCE ELECTROLYTE ANALYSIS

Daniel Abraham and Rex. E. Gerald II

C.3.1 Experiments Conducted

High-resolution proton nuclear magnetic resonance (NMR) analyses were conducted to examine the possible presence of polyethylene oxide (PEO) in an electrolyte extracted from an 18650 cell (see Table C-1). Control experiments were simultaneously conducted on a fresh Gen 2 electrolyte.

Table C-1. Characteristics of 18650 Cell Studied

18650 Cell IT	Aging T, Period	Capacity Fade, %	Power Fade, %
SNL 325	45°C, 40 weeks	31.0	51.3

C.3.2 Summary of Results

The experimental observations are listed in Table C-2.

Table C-2. Summary of Experimental Observations

Solution	Comments
Fresh Gen 2 electrolyte	No PEO peaks in spectra.
Fresh Gen 2 electrolyte + 6 drops of polyethylene glycol (PEG300)	PEO peaks observed. Spectra served as reference.
SNL 325 electrolyte	Weak peaks in spectra are consistent with PEO/oligo-ethylene oxide presence. C13 satellite peaks not observed. Changing experimental conditions (long pulses, acetonitrile addition) did not change data.
SNL 325 electrolyte, long-pulse experiment to enhance PEO peak intensity	
SNL 325 electrolyte + acetonitrile, long-pulse experiment	

C.3.3 Conclusions

- While absent in the fresh Gen 2 electrolyte, small quantities of oligo-ethylene oxides are present in electrolyte from the aged cell.
- The oligo-ethylene oxides could have been produced during cell formation and/or during cell aging; information from a 0% PF cell electrolyte is needed to draw definitive conclusions.

C.4 NUCLEAR MAGNETIC RESONANCE (^{19}F AND ^{31}P) ELECTROLYTE ANALYSIS

Marie Kerlau, Jeffrey Reimer, and Elton Cairns

C.4.1 Experiments Conducted

Nuclear magnetic resonance (NMR) spectroscopy was used to investigate the electrolyte decomposition products because solvent decomposition might be an important factor in the capacity fading. ^{19}F and ^{31}P NMR measurements were carried out on a Gen 2 cell electrolyte (1.2 M $LiPF_6$ in EC:EMC 3:7). The cell exhibited 50% power fade after 72 weeks of storage at 45˚C and 60% state of charge (SOC); the ATD identifier number for the cell was G2.60C45.A217.50.72.50.G.L.

C.4.2 Summary of Results

Figure C-5 presents the ^{19}F and ^{31}P NMR spectra obtained from the electrolyte of the Gen 2 cell. The ^{19}F NMR spectrum exhibits a doublet at –73 ppm relative to PF_6^-, which is consistent with data presented in other studies. Fluorophosphate species were also observed in the electrolyte in the chemical shift range –79 ppm to –91 ppm. These species correspond to mono ($OPF(OR)_2$) and difluorophospates ($OPF_2(OR)$), thereby indicating the relative instability of $LiPF_6$ in EC:EMC under the cell testing conditions (60% SOC, 45°C). The ^{31}P NMR spectrum exhibits a septet at –145 ppm corresponding to PF_6^-. The fluorophospates are observed in the chemical range of 0 to –25 ppm.

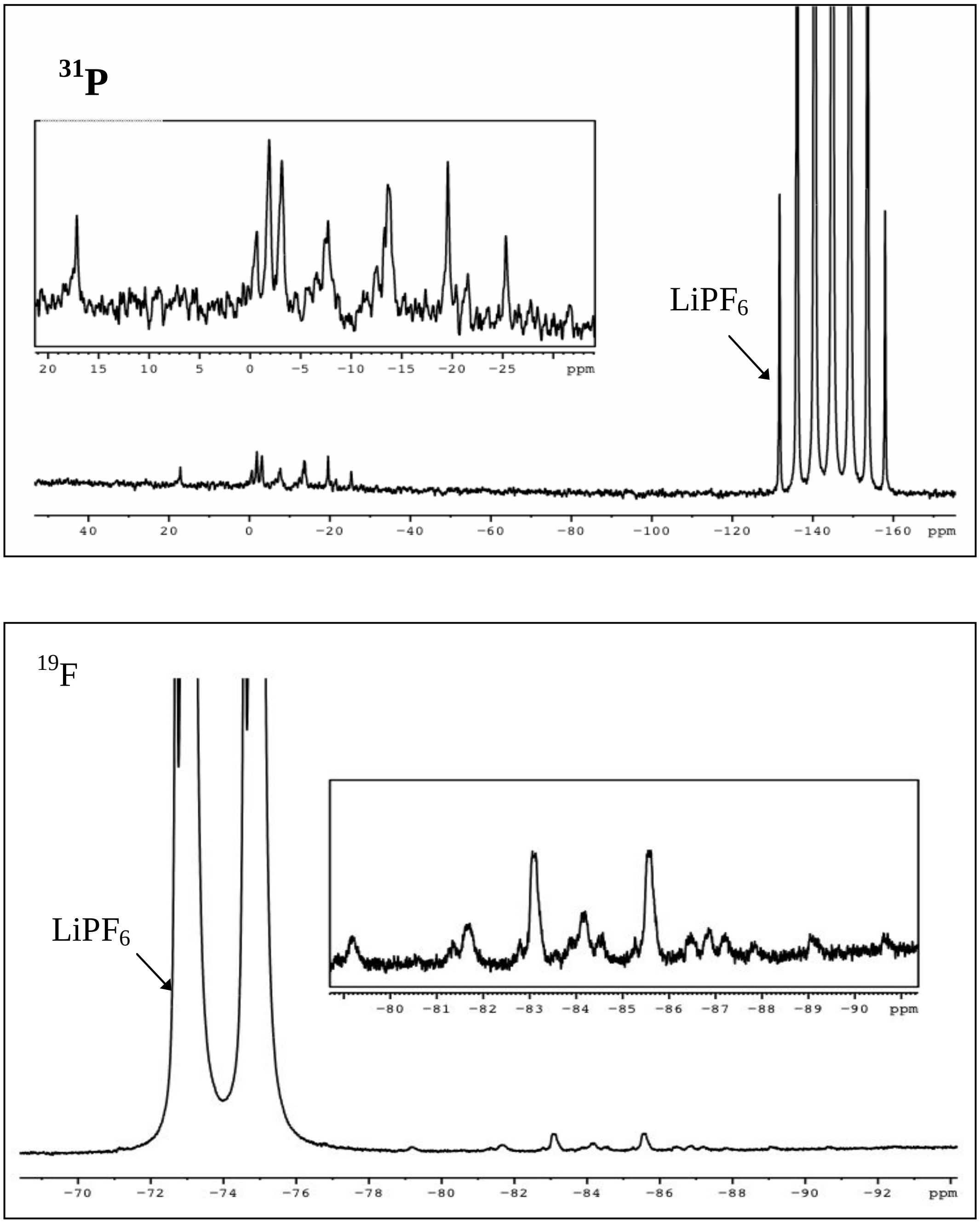

Fig. C-5. ^{31}P and ^{19}F NMR Spectra of Aged Electrolyte. The fluorophosphates species NMR shifts are shown in inset, and the much larger LiPF$_6$ shifts are also shown.

C.5 INDUCTIVELY COUPLED-PLASMA MASS SPECTROMETRY ELECTROLYTE ANALYSIS

Daniel Abraham

C.5.1 Experiments Conducted

Inductively coupled plasma mass spectroscopy (ICP-MS) analyses were conducted to examine the concentrations of Ni, Co, and Al in electrolytes extracted from the18650 cells. The analyses were conducted with a FISON ICP-MS PQII Turbo® used by the Analytical Chemistry Laboratory at Argonne National Laboratory. About 20 μL of the sample was diluted with 2% HNO_3 (in ultra-pure deionized water) so that the total sample volume was 2 mL, i.e., a dilution factor of 100. Control experiments were simultaneously conducted on a fresh Gen 2 electrolyte.

C.5.2 Summary of results

The experimental observations are listed in Table C-3.

Table C-3. Summary of Experimental Observations

ID	Cell Aging Conditions	Element Concentration, ppm		
		Ni, ±10%	Co, ±10%	Al, ±20%
Fresh	Fresh Gen 2 electrolyte	<0.2	<0.004	1.6
I134	Formation only, 0% PF	2.9	0.05	4.5
2-074	Cycle life, 45°C, 16 wk, 16.3% PF	2.8	0.06	3.9
2-070	Cycle life, 45°C, 40 wk, 29.3% PF	2.3	< 0.004	1.3
2-014	Cal life, 55°C, 20 wk, 24.1% PF	1.7	0.02	1.5
2-026	Cal life, 45°C, 88 wk, 50.9% PF	<0.2	<0.004	2.1

C.5.3 Conclusions

- In the fresh Gen 2 electrolyte, the Ni and Co are below the detection limit of the instrument, as expected; however, there appears to be some Al contamination in the fresh electrolyte, originating from some unidentified source.
- Small amounts of Ni (ppm level), Co (sub-ppm level), and Al (ppm level) are detected in the electrolyte from the cell that saw only formation cycling. We do not know whether these elements were released into solution as a consequence of voltage cycling, or whether such release occurs when the positive electrode is simply immersed in the electrolyte. The Ni:Co ratio is roughly an order of magnitude higher than 5.33, which is the ratio expected if the oxide were to corrode uniformly; the higher ratio may indicate (a) preferential leaching of Ni from the oxide, or (b) an alternate source of Ni in the cell, such as the Ni-based negative electrode tap on the copper current collector. The higher-than-expected Al levels probably indicate an alternative source, such as the positive electrode current collector.
- The Ni, Co, and Al contents in the electrolyte show a decreasing trend with cell age, which suggests that (a) oxide corrosion, if any, is most prevalent during formation

cycling; (b) the elements precipitate out of solution onto some solid surface in the cell, which may include the negative electrode surface; (c) the Al current collector does not corrode further on aging.

C.6 ANALYSIS OF GEN 2 ELECTROLYTES AND SAMPLES EXTRACTED FROM GEN 2 CELL COMPONENTS

John Kerr and Steven Sloop

C.6.1 Introduction

Gen 2 electrolytes and samples extracted from Gen 2 cell components (anode, cathode, and separator) have been analyzed (Table C-4) by conventional wet-chemistry analytical procedures that include gas chromatography (GC), GC coupled with mass spectroscopy (GC-MS) for detection and measurement of volatile organic compounds, high-pressure liquid chromatography (HPLC) configured for gel permeation chromatography (GPC) for measurement of nonvolatile compounds and polymeric materials, and capillary electrophoresis (CE) for measurement of nonvolatile ionic materials. Details of these techniques are described in the ATD Diagnostics Handbook [1]. Samples were either introduced directly into the analysis equipment if they were of the appropriate form, or they were converted through some form of quenching reaction and extraction to produce samples that could be analyzed appropriately in the equipment.

Electrolyte samples centrifuged from Gen 2 cells were analyzed directly with only a small dilution with an appropriate solvent—dichloromethane or pentane for GC and GC/MS, water for GPC and CE, or DMF for GPC.

Samples from the solid cell components were extracted with solvents such as dichloromethane, dimethylcarbonate, acetonitrile, or water. Treatment with water was followed by extraction with dichloromethane to obtain the products in a form that would chromatograph—for example, lithium salts of alkoxides such as lithium methoxide or ethoxide were converted to methanol or ethanol, which could be separated, identified and measured by GC and GC/MS. For the solid components, the electrolytes were not removed by centrifugation; instead, the volatile solvents were allowed to evaporate in the glove box, leaving the nonvolatiles and higher boilers adsorbed on the solid surfaces. These solids were then extracted as described.

Table C-4. Identification of 18650 Cells from which Components Were Extracted for Analysis

Cell ID	Cell Component Analyzed			
	Electrolyte	Anode	Cathode	Separator
G2.60C55.A205.16.08.13.G.L		X	X	
G2.60C55.A212.24.28.24.G.L		X	X	X
G2.60C55.A214.33.40.34.G.L		X	X	X
G2.60C45.A217.50.72.50.G.L			X (rinse)	
G2C.60C45.A221.25.40.26.G.L	X			
G2.60L25.I103.02.04.02.G.L		X	X	
G2.60L45.I116.00.CC.00.G.L			X	
G2.60L45.I118.10.04.10.G.L		X	X	
G2.60L45.I130.50.68.52.G.L.	X			

C.6.2 GC and GC-MS Analysis

C.6.2.1 Analysis of Centrifuged Electrolyte Samples

The gas chromatograms of electrolyte samples removed from a Gen 2 baseline and a Var C cell are shown in Figures C-6 and C-7, respectively; summary comments are provided next to each chromatogram. The electrolyte samples were diluted with dichloromethane to lessen the effect of $LiPF_6$ on the chromatographic columns. The samples were placed directly on the GC columns at temperatures below –15°C to lessen thermal degradation upon injection. However, the presence of the salt leads to degradation of column performance unless diluted with a solvent (such as dichloromethane).

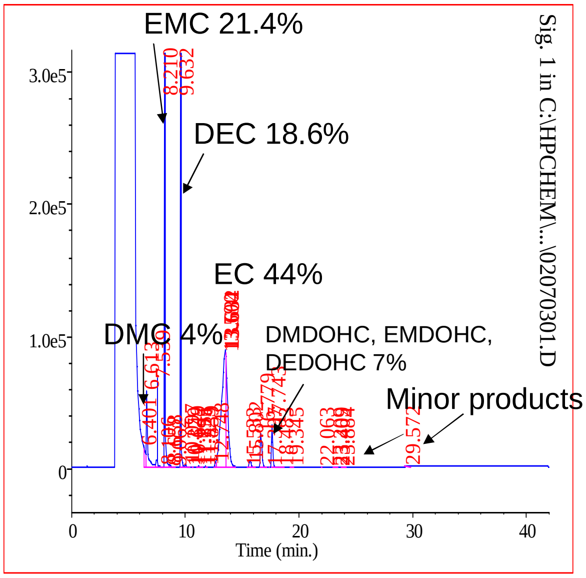

Cell ID #G2.60L45.I130.50.68.52.G.L

Fig. C-6. GC Analysis of Electrolyte from I130, a Gen 2 Baseline Cell.

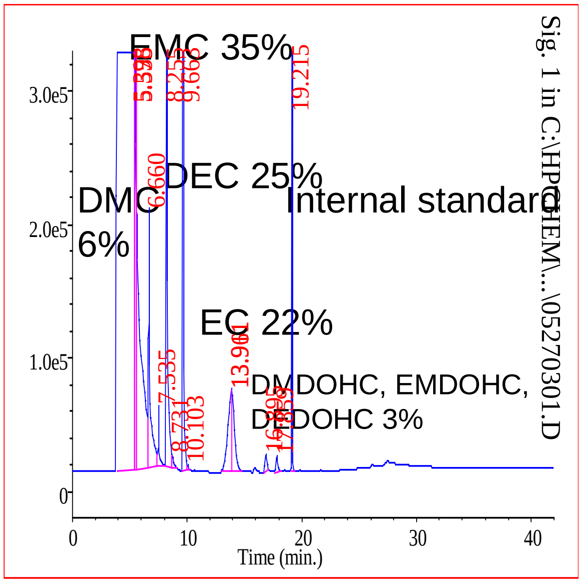

Fig. C-7. GC Analysis of Electrolyte from Cell A221, a Variant C Cell.

Summary of Results

Analysis of fresh Gen 2 electrolyte shows (in area%) EMC 68% and EC 24.5%.

In I130, we observed the following:

- Large loss of linear carbonate solvent relative to EC.
- Considerable transesterification according to the reaction EMC ⇔ DEC + DMC.
- Dimer formation (EMDOHC, etc.) consistent with previous ANL analyses.
- GPC analysis of water-quenched electrolyte showed presence of high-molecular-weight material (>5,000). In contrast, control analysis of fresh electrolyte showed a much lower quantity (<1%) of high-molecular-weight material.
- CE analysis of water quenched sample indicated presence of oxalate and formate.

Data from A221 showed the following:

- Loss of linear carbonate less than in Gen 2 baseline cell.
- Transesterification similar to Gen 2 baseline cell, EMC ⇔ DEC + DMC.
- Dimer formation (DMDOHC, etc.) about half that of Gen 2 cell.
- GPC analysis (water added) of electrolyte/separator showed some oligomers 1–5k mol wt. Very little polymer was observed in anode and cathode extracts.

Additional observations from the data are as follows:

- In the Gen 2 and Var C cells, the loss of DMC may be attributed to evaporation. Loss of linear carbonate is less in Figure C-7 than Figure C-6.
- The dimer formation appears to be less in Figure C-7 than it is in Figure C-6, but relative to the EC found, the amount is similar in both samples.
- At longer retention times, a small series of three peaks are observed that are consistent with the formation of higher molecular weight oligomers that are capped with two methyl groups, two ethyl groups, and an unsymmetrical methyl and ethyl group. The amounts of these products are very small, but they are detectable and their presence implies the presence of a polymerization reaction.

C.6.2.2 Analysis of Extracts from Solid Cell Components

Figure C-8 shows an example of results obtained by extracting cell components, such as the cathode of cell I118 (10% PF). The chromatogram was obtained on a sample that was prepared by water extraction of the cathode followed by extraction of the water with dichloromethane. A sample obtained by direct extraction of the electrode by dichloromethane gave a very similar result. It can be seen that linear carbonates are mostly absent due to evaporation. Higher molecular weight product peaks seen imply the formation of oligomers or polymers.

Quantitative analysis was carried out by adding the extracting solvent to a known weight of electrode: these data are listed in Table C-5. A standard (diethylene glycol dibutyl ether) was added to the dichloromethane to allow quantitative estimates of the amounts of materials that were found. It can be noted that, except for one cell, the amount of dimer formed (transesterification product) is much less on the anode than on the cathode.

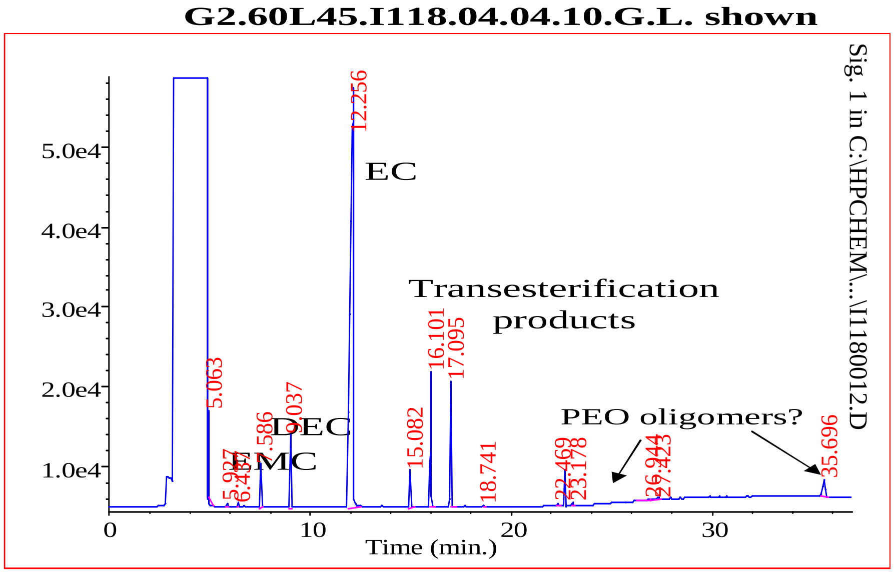

Fig. C-8. GC Analysis of Cathode Extract from Cell I118.

Table C-5. Quantitative Measurements of Transesterification Products in Cathodes and Anodes

Electrode	I118 (+)	I118 (–)	A205 (+)	A205 (–)	A212 (+)	A212 (–)	A214 (+)	A214 (–)
µmole/gm electrode	11.5	1.01	11.7	15	5.52	Trace	6.49	None

C.6.2.3 Analyses of DMC Washes of Sonicated Cathodes

The DMC solutions obtained after sonically washing a cathode from A217 (>50% PF) were analyzed by GC and GC-MS. The GC trace is shown in Figure C-9. The DMC solutions were concentrated first and then diluted with dichloromethane for injection on the GC-MS using a cold on-column inlet at –15 °C. The samples were briefly exposed to atmosphere during injection; no water was added.

Summary of Results

- Mass spectra show presence of species that correspond to ethylene oxide-type and ether carbonate-type oligomers.
- Spectra show evidence of F_xPO groups.
- GPC analysis using DMF as solvent indicated the presence of high molecular weight material. Response of RI detector was consistent with a material that contained fluorine, which suggests that these materials are organofluorphosphates.

Additional observations were as follows:

- The presence of organofluorphosphates is consistent with NMR measurements on this particular sample (see Appendix G).
- These results are consistent with the formation of PEO or ethercarbonate oligomers that react with PF_5 to form organofluorophosphates.
- The organofluorophosphate species fluoresce, which is consistent with the Raman studies.
- The use of the sonication wash illustrates that the surface species on the composite electrode may be different from those formed in the interior, and some of the chemistry may be different within the composite electrode.

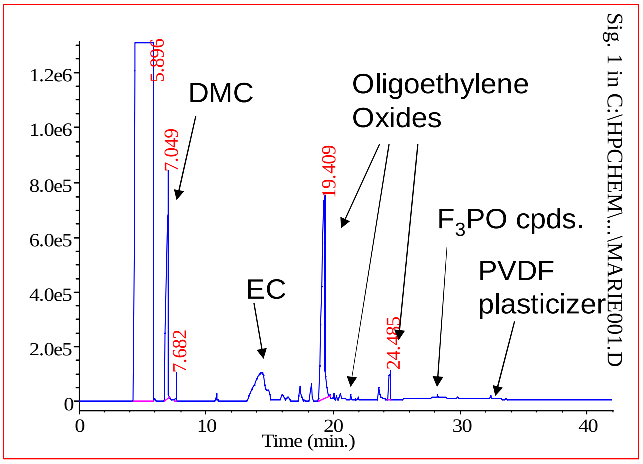

Fig. C-9. GC Analysis of DMC Solution from Ultrasonic Wash of A217 Cathode.

C.6.3 GPC Analysis of Extracts from Solid Cell Components (Anode, Cathode, Separator)

GPC analysis is a method of estimating the molecular weight of polymers. Its accuracy depends on the similarity of sample components with known standards. Typically, polystyrene standards of known molecular weight are used; these would be inappropriate for comparison with the polar products expected from Gen 2 cells. We used PEO standards, which are more polar, but note that these will not be accurate for materials with greater polarity, particularly for low molecular weight products.

An example of the GPC data is shown in Figure C-10 for anodes and cathodes from cell A212 (24% PF), which were extracted with water. The water was then injected on the column for analysis using a refractive index (RI) detector. Comparison of the chromatograms of the anode and cathode extracts with that of a 10k mol wt PEO standard shows that there are species present in the extracts that have molecular weights larger than the starting electrolyte materials. In fact, the cathode trace shows evidence for species with molecular weight around 100k by comparison with a PEO standard. However, the majority of the material has molecular weights in the 500 to 5,000 range.

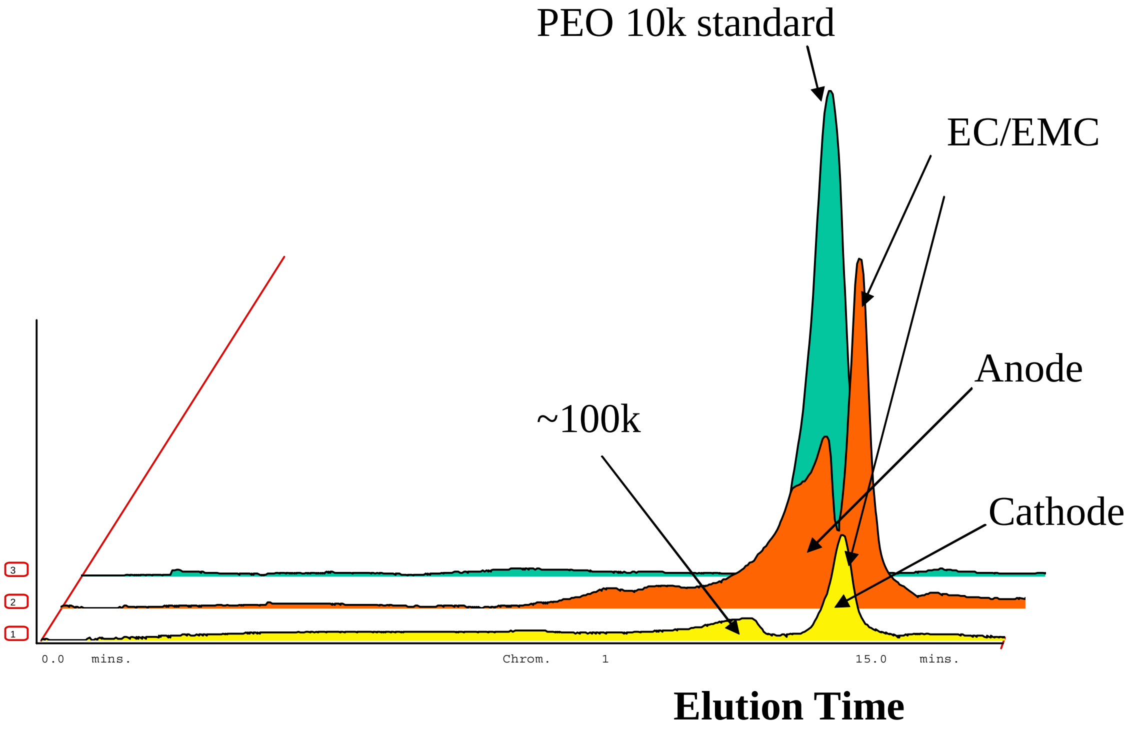

Fig. C-10. GPC Analyses of Water Extracts from Cell A212 Anode and Cathode Compared with 10k mol wt PEO Standard.

Quantitative estimates of the higher molecular weight materials on the cell components are obtained by peak-area integration and comparison with the response of known amounts of PEO standards. Figure C-11 shows GPC traces for electrodes harvested from the 18650 cells; the amounts of polymer found per gram of cell component are shown in Table C-6.

The amounts detected are consistent with those found for the low-molecular-weight dimers by GC (Figure C-8). The majority of the material detected has low molecular weights with only very small amounts at high molecular weights. This is significant because PEO-type polymers with molecular weights <20,000 are quite soluble in the Gen 2 electrolyte and its components (e.g., DMC). Therefore, any washing of electrodes during sample preparation for spectroscopic or microscopic analysis will remove these materials.

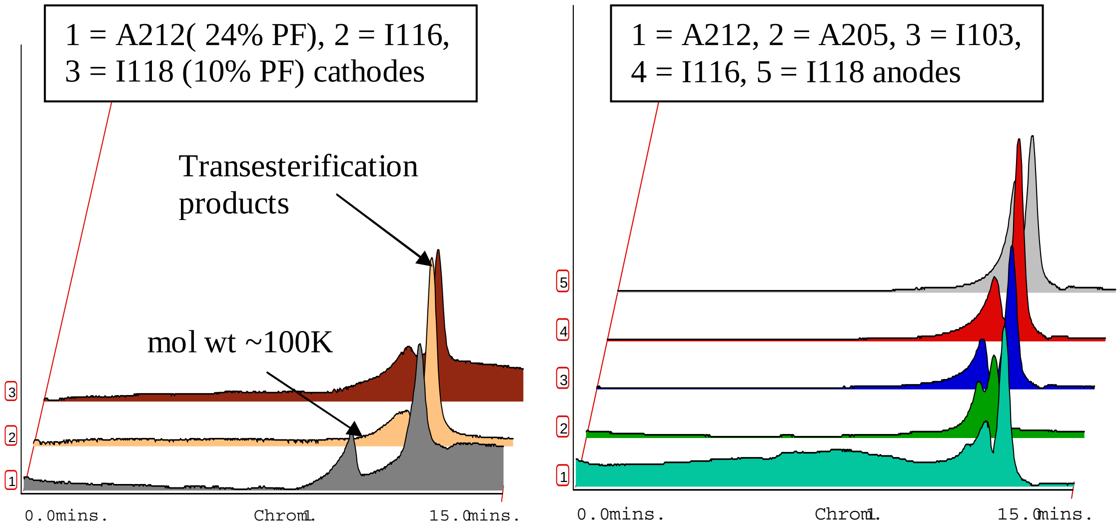

Fig. C-11. GPC Analyses of Water Extracts of Cell Components.

Table C-6. Amounts of Polymer Extracted with Water from Cell Components

Cell ID	Cathode, mg polymer/gm cathode[a]	Anode, mg polymer/gm anode[a]	Separator, mg polymer/gm separator[a]
A212	0.33(100k), 1.23(10k), 10(300)	0.1(1–2k), 0.4(300)	0.76(20k), 21.8(300)
A214	0.24(100k), 0.84(10k)	0.6(100k), 2.3(2–4k)	0.81(40k), 11.4(300)

[a] Numbers in parentheses refer to the molecular weight of the extracted polymers.

No significant polymer formation was detected by GPC in control experiments where water was added to fresh electrolyte samples. However, it is more difficult to perform true control experiments on the anodes and cathodes because they are sources of bases and acids, respectively. It is known that acids and bases catalyze polymer formation through ring opening of the EC ring. Nevertheless, it may be noted that high molecular weight materials were detected even on the separators, which is not a source of acids or bases. It should be noted that $LiPF_6$ is completely stable in water and our extraction process uses enough water to ensure stability under the extraction conditions. However, acids and bases that may be present in the electrodes could catalyze polymer formation reactions.

Data from the GPC experiments indicate the following:

- Higher-molecular-weight materials are produced in the cell during cycling and aging. For the most part, however, these materials have oligomeric molecular weights in the range of 300 to 5,000 and they are mostly soluble in the electrolyte.
- The observed oligomers are unlikely to form an SEI-like film on the cathode and may be washed off by rinsing during sample preparation for spectroscopic analysis. This may partially explain why PEO signals are not observed in vibrational spectroscopy of the electrodes.

- Extraction of the same electrodes after storage in the glove box for six months did not produce the same results. Virtually no high-molecular-weight material was observed in these analyses. This may indicate either that the polymers are an artifact from reaction with EC and the extraction solvent (not borne out by controls) or that further reaction occurred over time to produce materials that could not be extracted or broke down to form volatile products that evaporated.

C.6.4 Capillary Electrophoresis Analysis of Cell Components

The same aqueous extracts used for GPC analysis can also be analyzed by capillary electrophoresis (CE). Typical electropherograms of aqueous extracts of cell A212 components are shown in Figure C-12. The observations from the data are as follows:

- Lithium carbonate, oxalate, and formate were detected on the cell components by comparison with migration times of standard samples. Oxalate and formate appeared to be present throughout the cell, whereas carbonate was mostly concentrated on the anode.
- The oxalate, formate, and carbonate products are consistent with products of CO_2 reduction. Analysis of gases produced by Gen 2 cells confirms the production of CO, methane, and ethylene, which are also products of CO_2 reduction.
- The data showed the presence of PF_6 and fluoride.
- Quantitation proved to be very difficult due to the large PF_6 background.
- The data also showed the presence of a number of other products, some of which may be carboxylic acids that result from electrolyte solvent reduction reactions.

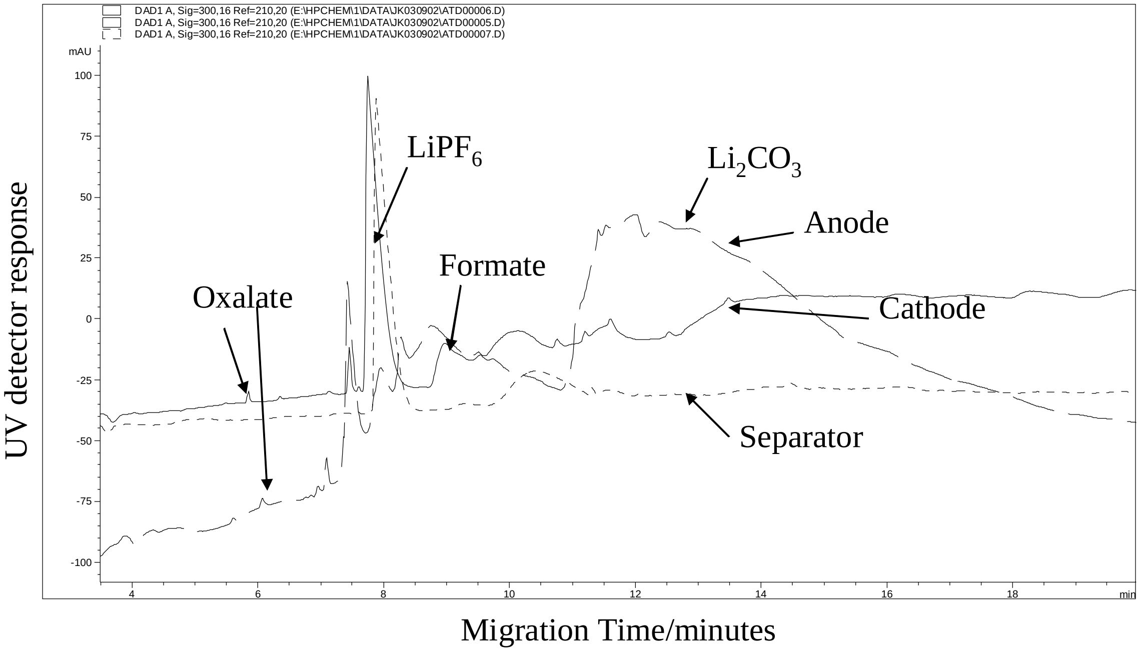

Fig. C-12. CE Analysis of Water Extracts from Cell A212 Anode, Cathode, and Separator.

References, Section C.6

1. Handbook of Diagnostic Techniques, Advanced Technology Program for Lithium-Ion Batteries, Lawrence Berkeley National Laboratory Report LBID-2464 (2003).

C.7 FUNDAMENTAL STUDIES OF THE CHEMISTRY OF ELECTROLYTE COMPONENTS

John Kerr and Steven Sloop

C.7.1 Effect of Heating on the Gen 2 Electrolyte

The complex chemistry of the electrolyte components leads to a diversity of results that is quite confusing. It is therefore appropriate to study thermal reactions of the electrolyte outside the cell in order to provide background for the diagnostics effort. Rates of disappearance of EC and of production of transesterification products have been measured for EC/EMC/$LiPF_6$ solutions as a function of temperature. Figure C-13 shows the concentrations of EMC and DEC (transesterification product) plotted against time for four different temperatures. One may observe that the rates of reaction are quite low for 50 and 60°C; however, at 70°C the reaction rates are significant.

The rates of EC and EMC disappearance and of the appearance of DEC and DEDOHC transesterification products are shown as an Arrhenius plot in Figure C-14. The rates for the DEDOHC compounds are multiplied by 4 to enhance the graph. It is clear that DEDOHC dimer formation is slowest, while the transesterification reaction is fastest. It is noted that these reactions occur also with $LiBF_4$ but not with LiTFSI or with the electrolyte solvents on their own. It is further noted that the loss of EMC can be mostly accounted for by the production of DMC and DEC. However, the loss of EC cannot be accounted for by the production of the dimers (DEDOHC, etc.), which indicates that a product (polymeric or ionic) is formed that the gas chromatograph does not detect.

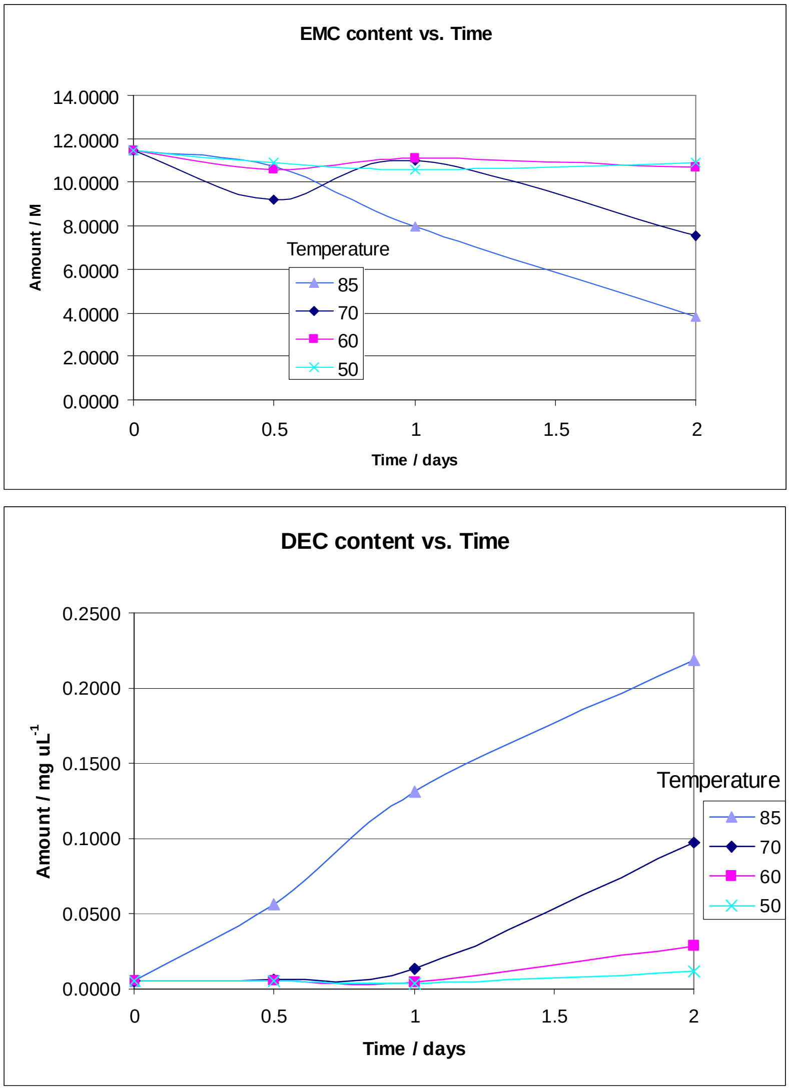

Fig. C-13. Disappearance of EMC and Appearance of DEC (Transesterification Product) with Time at Different Temperatures.

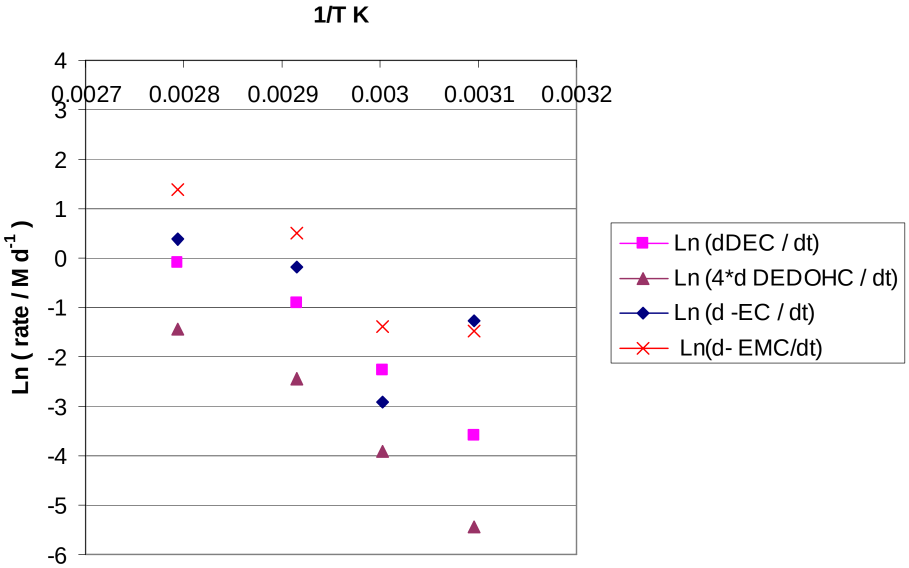

Fig. C-14. Arrhenius Plot of EC and EMC Disappearance and Appearance of DEC (Transesterification Product) with Time at Different Temperatures.

C.7.2 $LiPF_6$ Salt – LiF Solubility and Its Relation to PF_5 Reactivity

During the experiments described above, a control experiment was carried out in which 10% water was added to the Gen 2 electrolyte and the sample was heated at 85°C. The glass vial containing the solution exploded violently after two hours, and there was clear evidence of glass etching, indicating the production of HF. By contrast, a 1 M $LiPF_6$ solution in water that was treated identically did not react at all and showed no evidence of glass etching. This demonstrates that $LiPF_6$ is quite stable in water. It is noted that both PF_6 and BF_4 are available in acid form as 50% solutions in water and are quite stable. It appears, however, that a small amount of water in an organic solvent leads to HF production and reactions. Thus, any aqueous extractions that are carried out should be done with an excess of water.

We have previously reported on the reaction of solvent components with PF_5 [1]. PF_5 was produced by heating $LiPF_6$ in a Schlenk line, and the PF_5 gas was allowed to dissolve in a mixture of EC/DMC at liquid nitrogen temperature. The mixture was brought to room temperature, and the solution was observed to gain color. GC analysis showed similar products as that found in a heated Gen 2 electrolyte. This indicates that PF_5 can react with the solvent components at room temperature, but the concentration of PF_5 is low under normal conditions in the presence of PF_6 salts. This is because the PF_6 anion exists in equilibrium with LiF and PF_5:

$$LiPF_{6\,(sol)} \quad \leftrightarrow \quad LiF_{\,(s)} + PF_{5\,(sol)}$$

The lifetime of PF_5 is limited by the rate of the back reaction with LiF. If LiF is insoluble, then the back reaction will be slow and the PF_5 will have more time to react with other species. If the LiF is soluble and available, then the back reaction is favored and the PF_5 is not free long enough to react with other species such as water, EC, or EMC.

It is interesting to note that simple solubility tests show that LiF is soluble in EC, so one would expect little reaction of $LiPF_6$ in pure EC. However, LiF is insoluble in EMC, so PF_5 reactions with other substrates are favored. The dielectric constant of the medium must play a role here. In the 10% water-added experiment, the PF_5 must exist long enough to react with water to generate HF, whereas in pure water the LiF is so soluble that it keeps the PF_5 bound and unreactive.

Another example is shown in Figure C-15, where GC traces of PEGDME 250 are shown before and two weeks after addition of $LiPF_6$. The solution was not heated at all, yet significant reaction occurred. Note the relative increase in the concentration of shorter-chain oligomers after $LiPF_6$ addition. In the PEGDME 250 solution, the dielectric constant of the solvent is low, so LiF is not soluble. The PF_5 therefore has ample time to react with the PEGDME. In contrast, in a gel electrolyte that contains EC, DMC, and PEO-type polymers, the degradation of the polymer is significantly slower. This can be rationalized by the higher dielectric constant of the gel that limits the availability of PF_5.

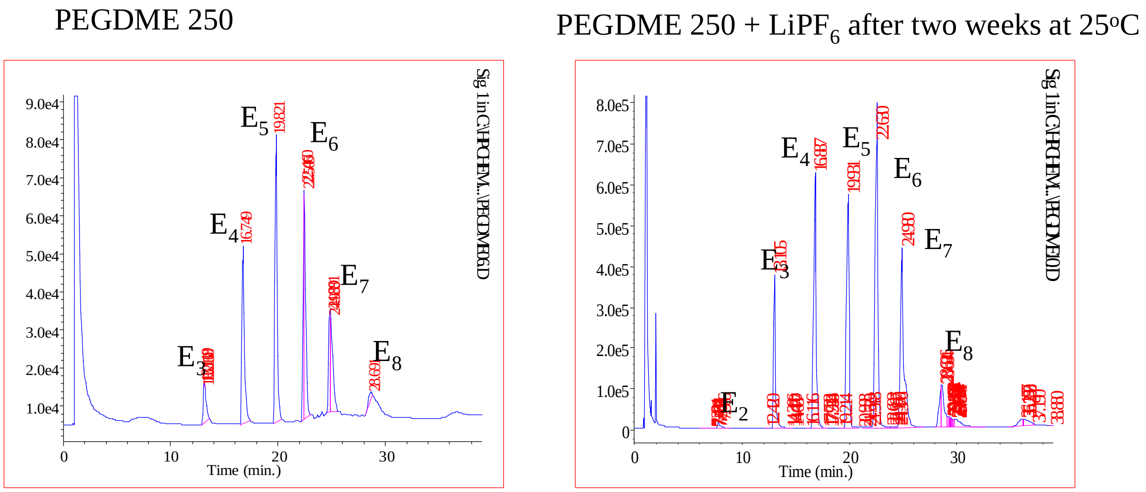
PEGDME 250

PEGDME 250 + $LiPF_6$ after two weeks at 25°C

Fig. C-15. GC Analyses of PEGDME250 and PEGDME250/$LiPF_6$ at 25°C. E_x = x units of ethylene oxide.

These observations concerning PF_5 reactivity as a function of solvent polarity are intriguing. It has been known for some time that the dielectric constant and polarity of solvents next to surfaces undergoes some changes. It may be quite possible that a lowering of polarity occurs next to electrode surfaces (e.g., carbon black, cracks and crevices in oxide particles) that encourages the precipitation of LiF, thereby increasing the effective concentration of PF_5. The reaction of PF_5 with electrolyte components could then lead to some of the observed particle isolation through precipitation of these products. If this hypothesis is correct, one can stop the isolation of active material particles by limiting the formation of PEO-type materials and other components that PF_5 reacts rapidly with.

C.7.3 Conclusions

- Degradation of the Gen 2 electrolyte is low at 50 and 60°C, but is substantial at temperatures greater than 70°C.
- Transesterification reactions occur in $LiPF_6$ and $LiBF_4$ electrolytes, but are not are observed in LiTFSI electrolytes or when electrolyte solvents are heated on their own.
- Reaction of PF_5 with cell components appears to be governed by LiF solubility in the solution: the lower the LiF solubility, the greater the PF_5 reactivity.

References, Section C.7

1. Sloop, S. E., J. B. Kerr, and K. Kinoshita, J. Power Sources **330,** 119–121 (2003).

APPENDIX D. ELECTROCHEMICAL TESTING OF HARVESTED ELECTRODES

D.1 EFFECT OF 18650 CELL AGING ON POSITIVE ELECTRODE CAPACITY

Daniel Abraham and Jamie Knuth

D.1.1 Experiments Conducted

Coin cells (2032-type) were assembled with 1.6-cm^2 area samples punched from positive electrodes harvested from 18650 cells (see Table D-1), lithium-metal counter electrode, fresh Celgard 2325 separator, and fresh Gen 2 electrolyte, to determine the effect on aging on electrode capacity. The cells were cycled from 3 to 4.3 V with a 0.064 mA current.

Table D-1. Characteristics of 18650 Cells Studied

Cell ID	Aging T, Period, Type	C/1 Capacity Fade, %	Power Fade, %
Gen 2, 2-034	0 wks	0	0
Gen 2, 2-006	55°C, 4 weeks, calendar	3.7	15.4
Gen 2, 2-017	55°C, 32 weeks, calendar	14	27.4
Gen 2, 2-009	55°C, 40 weeks, calendar	18.3	32.3
Gen 2, 2-026	45°C, 88 weeks, calendar	34.4	50.9
Gen 2, 2-076	45°C, 32 weeks, cycle	10	22.9
Gen 2, 2-078	45°C, 68 weeks, cycle	30	48.4
Var C, C-022	0 weeks	0	0
Var C, C-035	45°C, 4 weeks, cycle	1.8	14.6
Var C, C-031	45°C, 40 weeks, cycle	3.8	20.8
Var C, C-010	45°C, 40 weeks, calendar	1.8	20
Var C, C-004	45°C, 60 weeks, calendar	2.7	30.5

D.1.2 Summary of Results

The experimental data are summarized in Figures D-1 and D-2 for the Gen 2 and Var C cells, respectively.

D.1.3 Conclusions

- Positive electrode capacity decreases with 18650 cell age. Because the counter electrode is an infinite source of lithium, the coin cell capacity variations indicate significant changes in the positive electrode during accelerated aging of the 18650 cells.
- Cycling hysteresis becomes more prominent with the age of the 18650 cells. Such hysteresis results from the inability of the material to attain thermodynamic equilibrium during the constant-current cycling. The presence of cycling hysteresis indicates that the positive electrode "slows down" on aging; i.e., as it ages, the positive electrode is unable to deliver or accept lithium at rates that were previously possible.
- The capacity of the 0% CF Var C electrodes is lower than those of the 0% CF Gen 2 electrodes; also, unlike the Gen 2 electrode, the Var C electrode shows some cycling

hysteresis. Apparently, the extra Al content in the Var C oxide makes it difficult to extract/insert Li ions.

- In Table D-1, note that the power fade to capacity fade ratio for Var C cells is much larger than that for the Gen 2 cells. That is, the capacity fade displayed by the aged Var C samples in Figure D-2 is probably more influenced by the impedance rise in the electrodes.

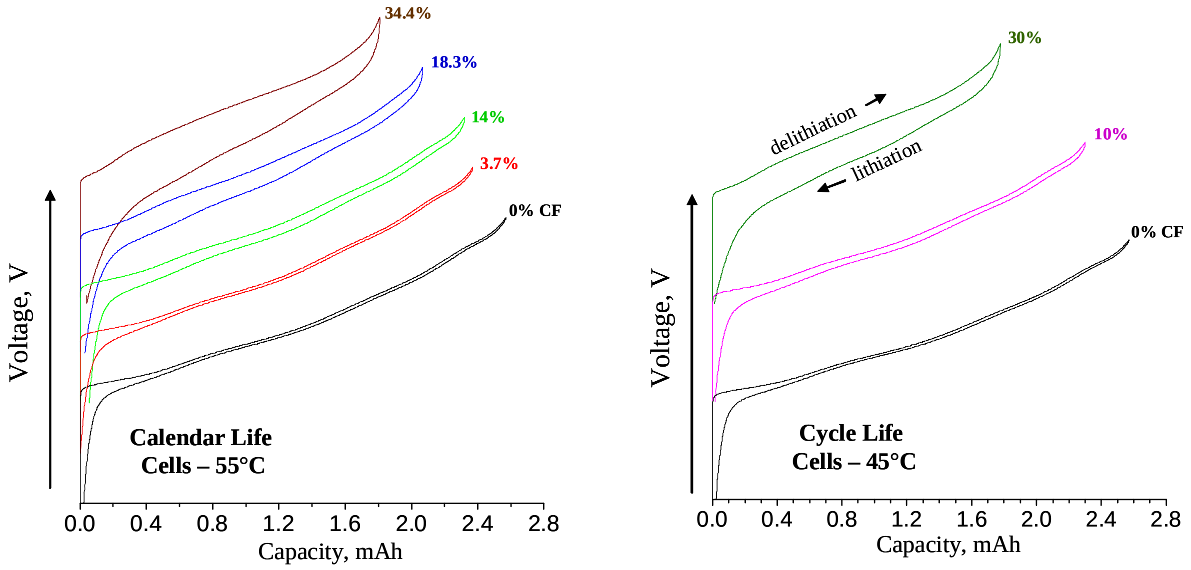

Fig. D-1. Cycling Data from Positive Electrodes (vs. Li) Harvested from Gen 2 Cells, in the 3 to 4.3 V Range, Obtained with a 0.064-mA Current. The C/1capacity fade (CF) of the 18650 cells is shown in the figures. Curves have been offset vertically for clarity.

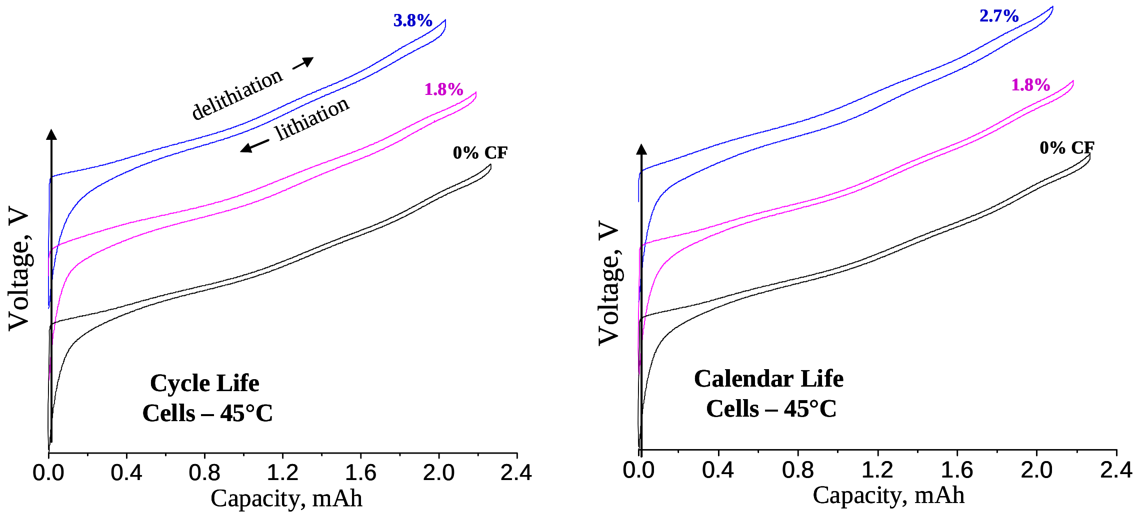

Fig. D-2. Cycling Data from Positive Electrodes (vs. Li) Harvested from Calendar-Life Var C Cells, in the 3 to 4.3 V Range, Obtained with a 0.064-mA Current. The C/1 capacity fade (CF) of the 18650 cells is shown in the figures.

D.2 EFFECT OF CYCLING RATE ON POSITIVE ELECTRODE CAPACITY

Daniel Abraham and Jamie Knuth

D.2.1 Experiments Conducted

Coin cells (2032-type) were assembled with 1.6-cm^2 area samples punched from positive electrodes harvested from 18650 cells (see Table D-2), lithium-metal counter electrode, fresh Celgard 2325 separator, and fresh Gen 2 electrolyte to determine the effect of cycling rate on positive electrode capacity. The cells were cycled from 3 to 4.3 V with 0.064-, 0.032-, and 0.008-mA currents.

Table D-2. Characteristics of 18650 Cells Studied

Cell ID	Aging T, Period, Type	C/1 Capacity Fade, %	Power Fade, %
Gen 2, 2-034	0 weeks	0	0
Gen 2, 2-076	45°C, 32 weeks, cycle	10	22.9
Gen 2, 2-078	45°C, 68 weeks, cycle	30	48.4
Var C, C-022	0 weeks	0	0
Var C, C-004	45°C, 60 weeks, calendar	2.7	30.5

D.2.2 Summary of Results

The experimental data are summarized in Figures D-3 and D-4 for the Gen 2 and Var C cells, respectively.

D.2.3 Conclusions

- The positive electrode capacity shows a strong dependence on cycling currents.
- For the Gen 2 electrodes:
  - Capacity gains and cycling hysteresis improvements are observed at the lower currents. The 2-076 electrode cell shows 2.28-, 2.34-, and 2.36-mAh capacities when cycled with 0.064-, 0.032-, and 0.008-mA currents, respectively.
  - Significant capacity gains and improvements in cycling hysteresis are observed when electrodes from highly aged (late-life) cells are cycled at slower rates. For example, the 2-078 electrode cell shows 1.77-, 1.91-, and 2.05-mAh capacities when cycled with 0.064-, 0.032-, and 0.008-mA currents, respectively. However, even at the lower cycling currents, the capacities of cells containing the aged electrodes are lower than those of the cell containing the 0% CF electrode.
- Cycling the Var C electrode with a lower current also results in a capacity gain and improvements in cycling hysteresis. When cycled with a 0.008 mA current, the C-004 electrode cell has a capacity that is comparable to that of the 0% CF Var C electrode—the oxide particles can be accessed at slower cycling rates, which indicates that the electrode capacity loss is a manifestation of impedance rise, i.e., the particles are not electronically isolated.

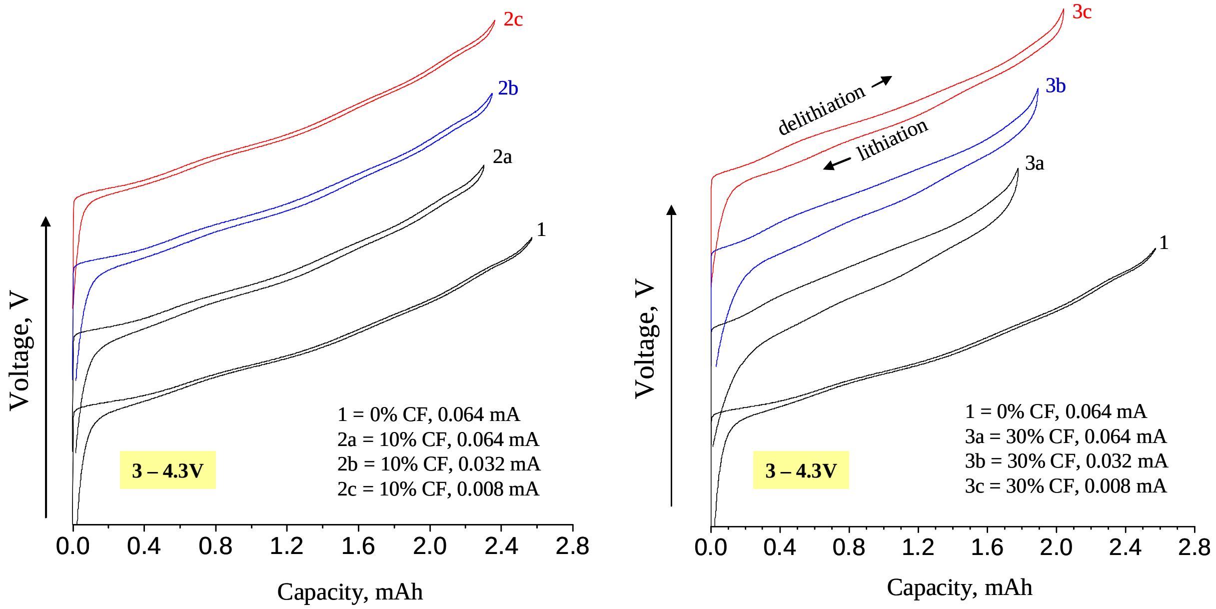

Fig. D-3. Cycling Rate Effect on Capacity Data for Positive Electrodes (vs. Li) Harvested from Gen 2 Cells, in the 3 to 4.3 V Range. The C/1 capacity fade (CF) of the 18650 cells and the cycling currents employed for testing are shown in the figures. Data from a 0% capacity fade cell are shown for comparison. Curves have been offset vertically for clarity.

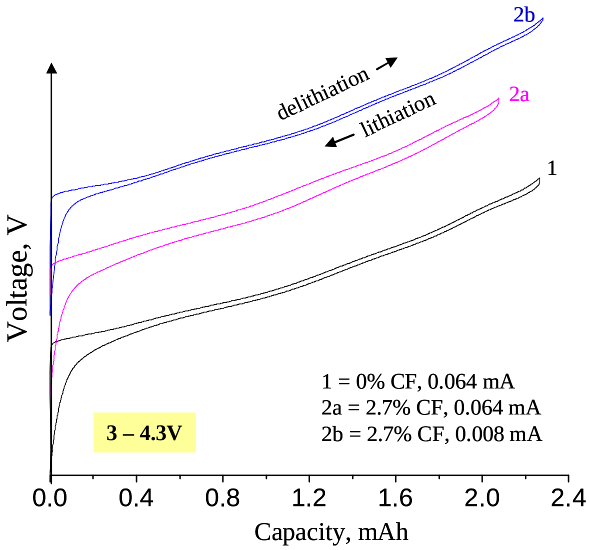

Fig. D-4. Cycling Rate Effect on Capacity Data for Positive Electrodes (vs. Li) Harvested from Var C Cells, in the 3 to 4.3 V Range. The C/1 capacity fade of the 18650 cell and the cycling currents employed to obtain the data are shown in the figure.

D.3 EFFECT OF RINSING ON POSITIVE ELECTRODE CAPACITY

Daniel Abraham, Jamie Knuth, and Evangeline Reynolds

D.3.1 Experiments Conducted

In an attempt to regain their “original” capacity, positive electrodes from aged cells were gently “rinsed” in various solvents (see Table D-3). The procedure involved immersing the samples in the rinse solvents for ~48 hours; the solvent was replaced twice with a “fresher version” during this period. H_2O rinsing was conducted to remove PEO-type oligomers that may be present on the electrode samples: after rinsing; the samples were dried in a 110°C vacuum oven for 24 h. Supercritical CO_2 rinsing was conducted by Dr. Steven Sloop, OnTo Technology LLC (Bend, Oregon). Coin cells (2032-type) were then assembled with 1.6-cm^2 area samples punched from these rinsed electrodes, lithium-metal counter electrode, fresh Celgard 2325 separator, and fresh Gen 2 electrolyte. The cells were cycled from 3 to 4.3 V with a 0.064-mA current.

Table D-3. Solvent Rinse of 18650 Cell Electrodes

Cell	Rinse Solvent				
	None	DMC	EC:EMC (3:7)	H_2O	CO_2
2-034, 0% CF, 0% PF	X	X	X		
2-017, 55°C, cal, 14% CF, 27.4% PF	X	X			
2-078, 45°C, cyc, 29.6% CF, 48.4% PF	X	X			
2-026, 45°C, cal, 34.4% CF, 50.9% PF	X		X	X	X

D.3.2 Summary of Results

The experimental data are summarized in Figure D-5:

- DMC rinsing and EC:EMC rinsing of 0% CF electrode samples do not affect cathode cycling performance (within limits of experimental uncertainty). These data are as expected, since the rinse solvents do not damage the cathode laminate, i.e., affect the PVDF binder, etc.
- DMC rinsing of the 14% CF and 29.6% CF electrode samples significantly degrades sample cycling performance. The rinsed samples have lower capacities and show greater polarization both on charge and discharge.
- H_2O rinsing and EC:EMC rinsing of the 34.4% CF electrode samples do not affect cathode cycling performance (within limits of experimental uncertainty). However, samples rinsed with supercritical CO_2 show a significantly lower capacity — we do not know whether these data are influenced by the rinsing protocol.

D.3.3 Conclusions

- Our rinse experiments have not, so far, succeeded in regaining original electrode capacity.
- Instead of improving electrode capacity, the rinsing solvents are either ineffective (EC:EMC, H_2O) or degrade material performance (DMC, supercritical CO_2). The data suggest that the more non-polar the rinse solvent, the greater the material degradation.

- The variations in electrode capacities with the rinsing conditions indicate that electrode capacity can be altered by causes that are strictly external to the oxide crystals (the rinse protocol is far too gentle to produce oxide particle damage).
- The influence of rinse solvent polarity on sample capacity indicates that the “structure” of the cathode surface films is apparently more important than its composition. This surface film structure apparently contains charged species that are bound to the oxide particles and interfere with the motion of Li ions, i.e., electrode capacity is lowered by increasing the impedance at the oxide surface. We speculate that the DMC rinse alters this surface-film structure by removing the components (such as EC) that may be responsible for the structure—EC:EMC and H_2O apparently do not alter the structure.
- The ineffectiveness of H_2O rinsing suggests that PEO-type oligomers (if present) are not responsible for the capacity fade, which is apparently a manifestation of the impedance rise displayed by the aged samples.

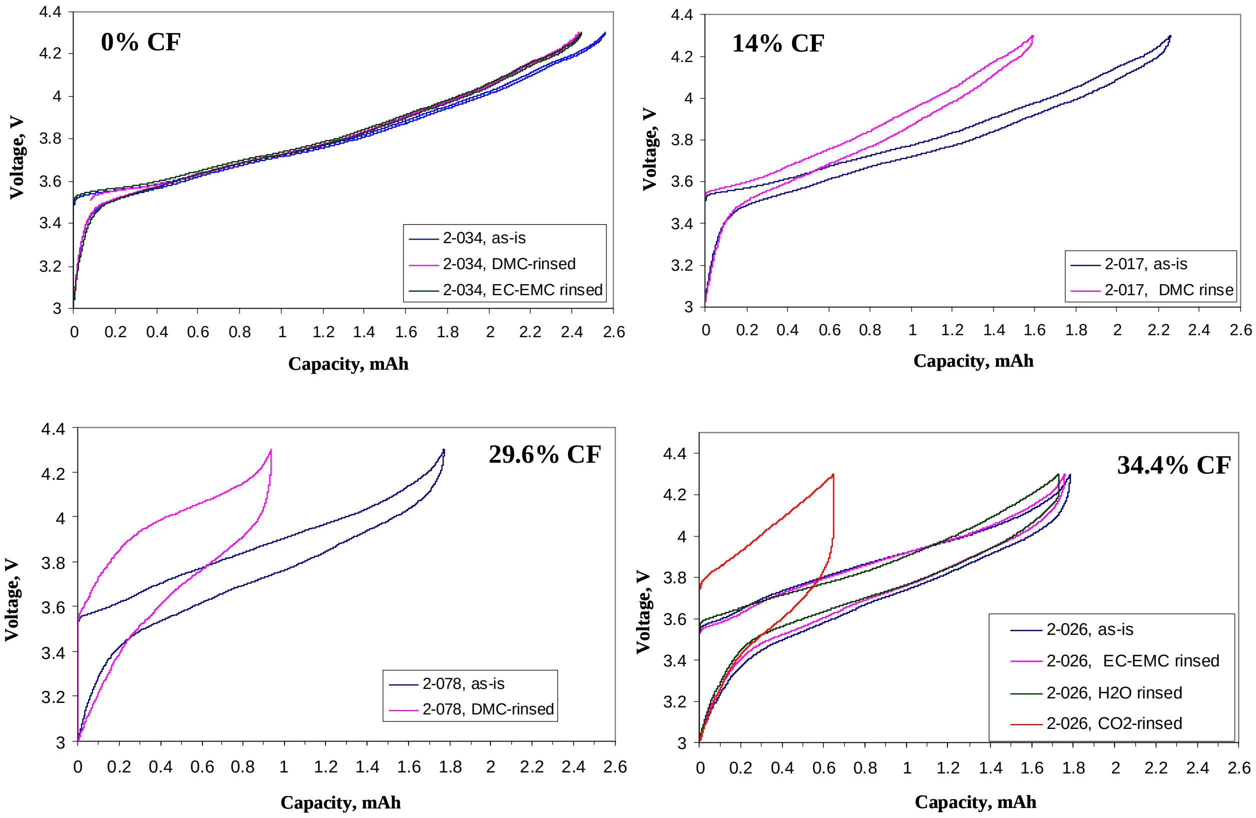

Fig. D-5. Effect of Rinsing on Capacity Data for Positive Electrodes Harvested from Gen 2 Cells.

D.4 EFFECT OF TESTING TEMPERATURE ON POSITIVE ELECTRODE CAPACITY

Daniel Abraham and Evangeline Reynolds

D.4.1 Experiments Conducted

Coin cells (2032-type) were assembled with 1.6-cm^2 area samples punched from positive electrodes harvested from 18650 cells (see Table D-4), lithium-metal counter electrode, fresh Celgard 2325 separator, and fresh Gen 2 electrolyte. The cells were cycled from 3 to 4.3 V with a 0.064-mA current at room temperature and at 55°C. The high-temperature cycling was conducted in an attempt to regain the "original" capacity of the aged positive electrodes; the higher temperature is known to reduce positive electrode impedance and improve cell kinetics. Note that the high-temperature cycling may have produced additional aging of the electrodes.

Table D-4. Characteristics of 18650 Cells Studied

Cell ID	Aging T, Period, Type	C/1 Capacity Fade, %	Power Fade, %
Gen 2, 2-057	25°C, 52 weeks, cycle	9.8	20.0
Gen 2, 2-026	45°C, 88 weeks, cycle	34.4	50.9

D.4.2 Summary of Results

The observations based on the experimental data shown in Figure D-6 are as follows:

- Electrodes from 2-057, which is a mid-life cell, have a lower capacity than that of the 0% CF cell when the measurement is conducted at RT. When tested at 55°C, however, the 2-057 electrode capacity is only slightly smaller than that of the 0% CF electrode, i.e., the capacity approaches that of the starting electrode. Significant capacity gains and improvements in cycling hysteresis result from the higher temperature test.
- Electrodes from 2-026, which is a highly aged (late-life) cell, have a significantly lower capacity and display significantly greater cycling hysteresis than the 0% CF electrodes when the measurement is conducted at RT. When tested at 55°C, however, the 2-026 data show lesser cycling hysteresis than the RT data, and electrode capacity improves; however, the 55°C capacity is still much smaller than that of the 0% CF electrode.

D.4.3 Conclusions

- When tested at elevated temperatures, electrodes from mid-life cells show capacities that are comparable to those of the starting electrodes. Therefore, the capacity loss measured at room temperature is mostly a manifestation of the impedance rise that reduces electrode rate capability.
- Electrodes from late-life (Region 3) Gen 2 cells show significant cycling hysteresis even at 55°C, which indicates that the cycling is not under equilibrium conditions. This suggests that a significant portion of the apparent capacity fade arises from the electrode impedance; a small portion of the capacity fade may be from inaccessible charge storage that could result from electronically isolated particles.

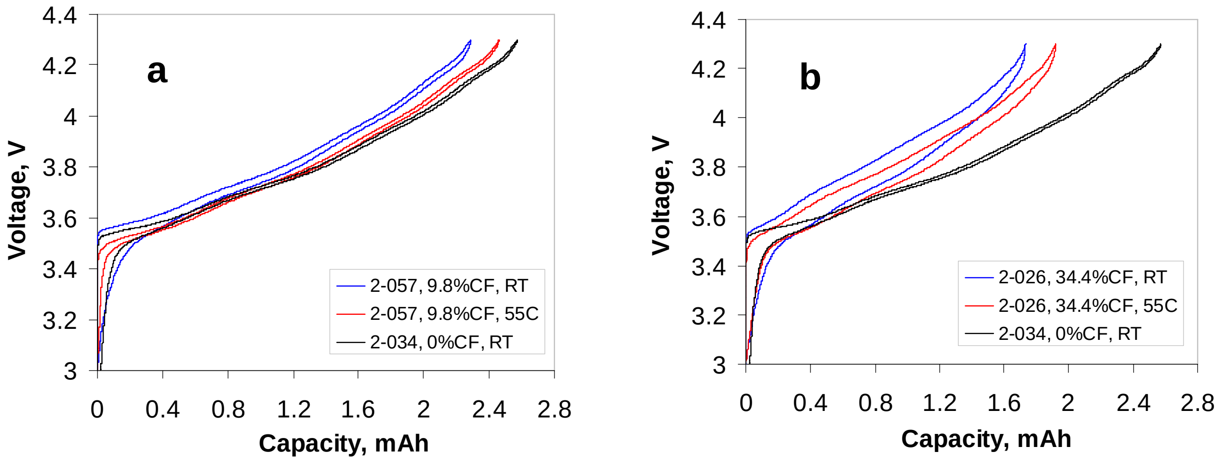

Fig. D-6. Effect of Testing Temperature on Capacity Data for Positive Electrodes Harvested from Gen 2 Cells. Data from cells 2-057 and 2-026 are shown in (a) and (b), respectively. The 0% CF electrode RT data are shown for comparison.

D.5 ROOM-TEMPERATURE IMPEDANCE MEASUREMENTS ON HARVESTED ELECTRODES

Daniel Abraham, Jamie Knuth, and Evangeline Reynolds

D.5.1 Experiments Conducted

Reference electrode cells were prepared to determine the relative contributions of the positive and negative electrodes to impedance rise. The reference electrode cells were assembled with 15.5-cm^2 area harvested electrodes (see Table D-5), two Celgard 2325 separators enveloping a Li-Sn reference electrode, and fresh Gen 2 electrolyte. Details on the Li-Sn reference electrode, cell assembly, test equipment, and test procedures are discussed elsewhere [1].

Table D-5. Characteristics of 18650 Cells Studied

Cell ID	Aging T, Period	C/1 Fade, %	Power Fade, %	ASI Rise, %
Gen 2, 2-034	0 weeks	0	0	0
Gen 2, 2-076	45°C, 32 weeks	10	22.9	25
Gen 2, 2-017	55°C, 32 weeks	14	27.4	31
Gen 2, 2-078	45°C, 68 weeks	30	48.4	77
Var C, C-022	0 weeks	0	0	0
Var C, C-031	45°C, 12 weeks	3.8	20.8	18.8
Var C, C-004	45°C, 60 weeks	2.7	30.5	39.1
Var C, C-023	45°C, 124 weeks	2.7	30.5	84.2

D.5.2 Summary of Results

- Representative HPPC data obtained by applying an 18-s, ~6C discharge pulse at different open circuit voltages of the cell are shown in Figure D-7.
    - The full-cell data are consistent with those measured on the corresponding 18650 cells.
    - The sharp full-cell impedance increase observed at lower full-cell voltages (<3.55 V) are associated with the positive electrode.
    - The positive electrode is the dominant contributor to cell impedance rise on aging.
- Representative EIS data obtained on the full cell and on individual electrodes are shown in Figure D-8.
    - The 0% PF data contain (a) a high-frequency tail, which is a measurement artifact; (b) a depressed semicircular arc at mid-frequencies (to ~1 Hz), which is also known as the mid-frequency arc; and a low-frequency (typically <1 Hz) tail.
    - The positive electrode is the main contributor to the full-cell impedance on aging, which is mainly reflected as an increase in the mid-frequency arc width. Electrodes from late-life cells also show significant changes in the Warburg impedance tail.

D.5.3 Conclusions

The positive electrode is the dominant impedance contributor on cell aging.

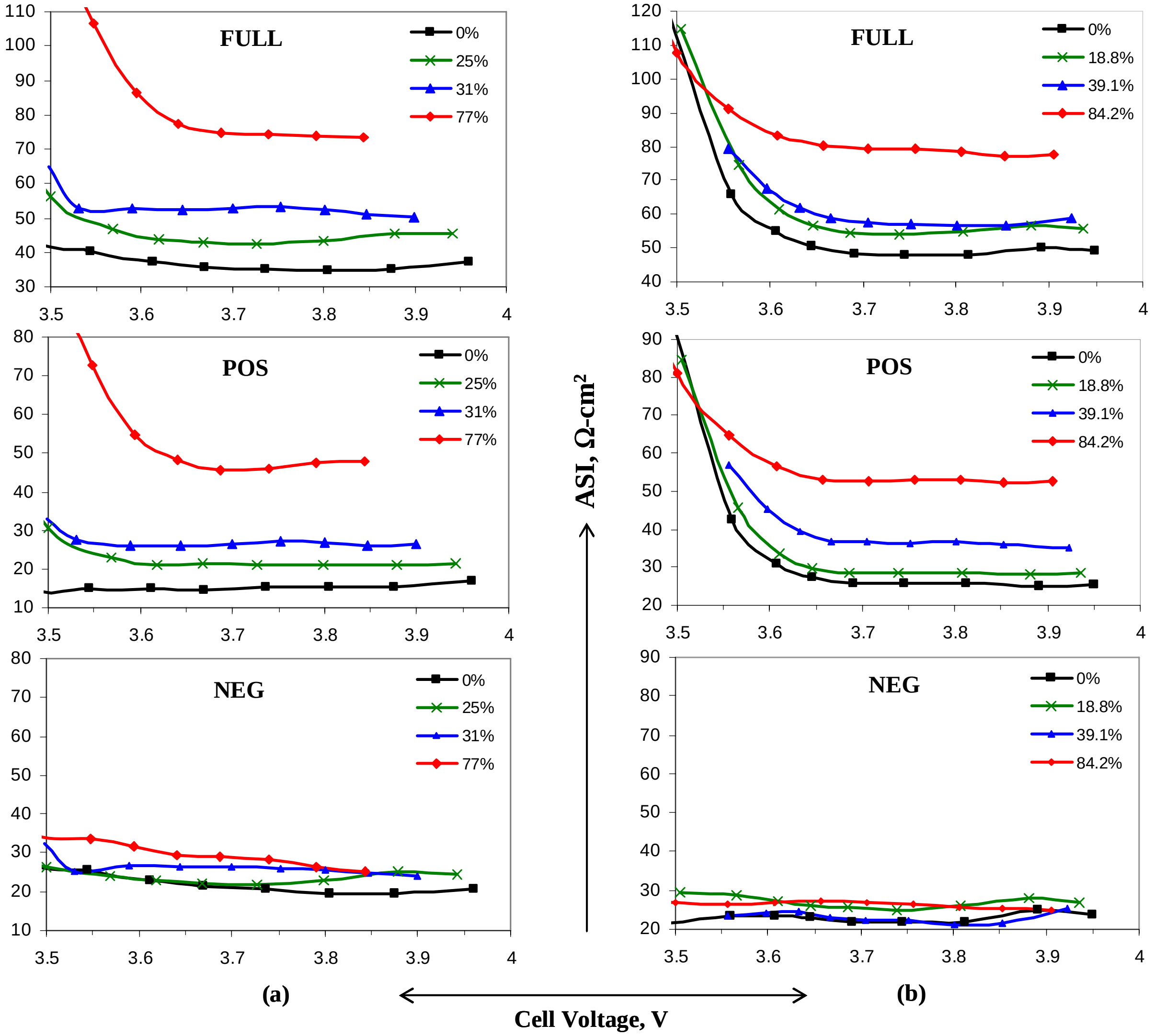

Fig. D-7. Results from the HPPC Test (18-s Discharge Pulse) Conducted on Electrodes Harvested from (a) Gen 2 and (b) Var C Cells.

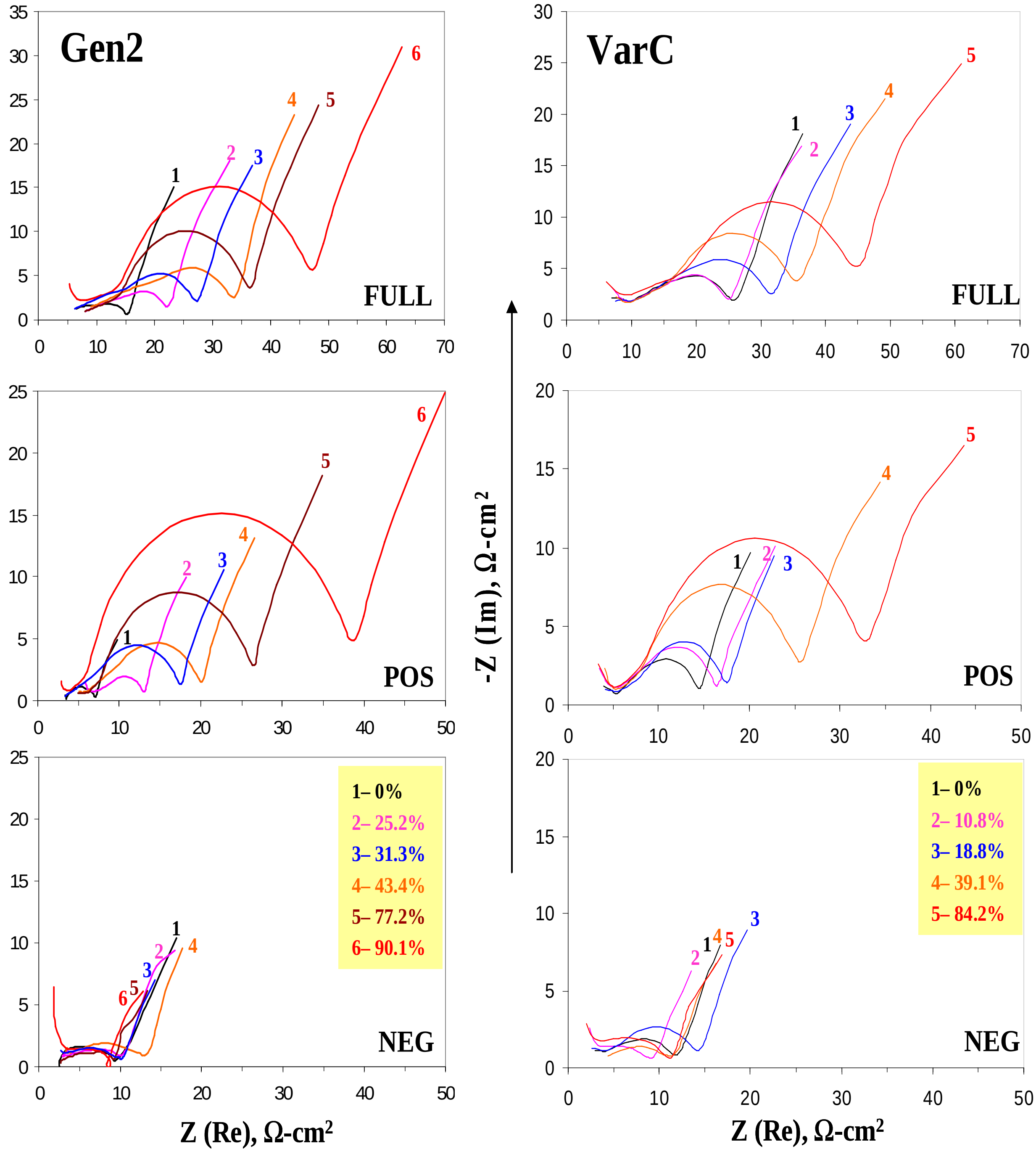

Fig. D-8. EIS Data Obtained on Electrodes Harvested from Gen 2 and Var C Cells. These room-temperature data were obtained at a full-cell voltage of 3.72 V, in the 10 kHz–0.01 Hz frequency range.

References, Section D.5

1. Abraham, D. P., S. D. Poppen, A. N. Jansen, J. Liu, D. and W. Dees, Electrochim. Acta **49**, 4763 (2004).

D.6 TESTING TEMPERATURE EFFECTS ON POSITIVE ELECTRODE IMPEDANCE

Daniel Abraham and Evangeline Reynolds

D.6.1 Experiments Conducted

These experiments with conducted in Li-Sn reference electrode cells containing 15.5-cm^2 positive and negative electrodes harvested from 18650 cells, two Celgard 2325 separators enveloping the reference electrode, and fresh Gen 2 electrolyte. EIS data were measured at various testing temperatures to determine the effect on positive electrode impedance. Control experiments were conducted to ensure that the testing protocol did not irreversibly damage the electrodes/cell.

D.6.2 Summary of Results

Figure D-9 shows data for a highly aged electrode sample (2-026, 34.4% CF, 50.9% PF).

- The mid-frequency arc width decreases with increasing temperature. The mid-frequency arc maximum and minimum occur at higher frequencies at the higher temperatures.
- The testing temperature effects are reversible. The EIS data depend only on the test temperature, and are independent of the process (cell heating, cooling) by which the temperature is attained.

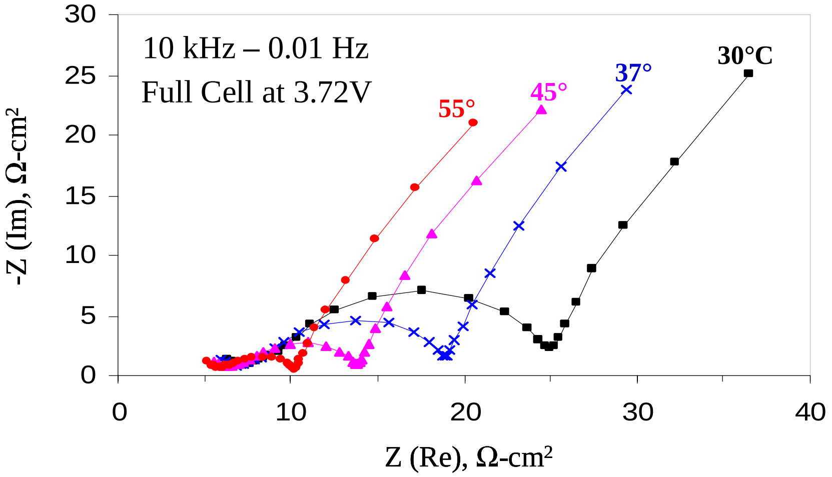

Fig. D-9. Effect of Testing Temperature on Positive Electrode Impedance.

Figure D-10 shows low-frequency data for a highly aged electrode sample (2-026, 34.4% CF, 50.9% PF) that were obtained at 30°C and 45°C. Room-temperature data from a 0% PF cell are shown for comparison.

- Cell aging has a significant effect on the Warburg impedance tail that reflects diffusion processes within the positive electrode.

- For the 0% PF sample, the electrochemical processes below 1 mHz are mainly capacitive. The 50.9% PF sample data is significantly different, and shows both resistive and capacitive components.
- The Warburg impedance tail is not affected to any significant degree when the EIS measurements are conducted at the higher test temperature.

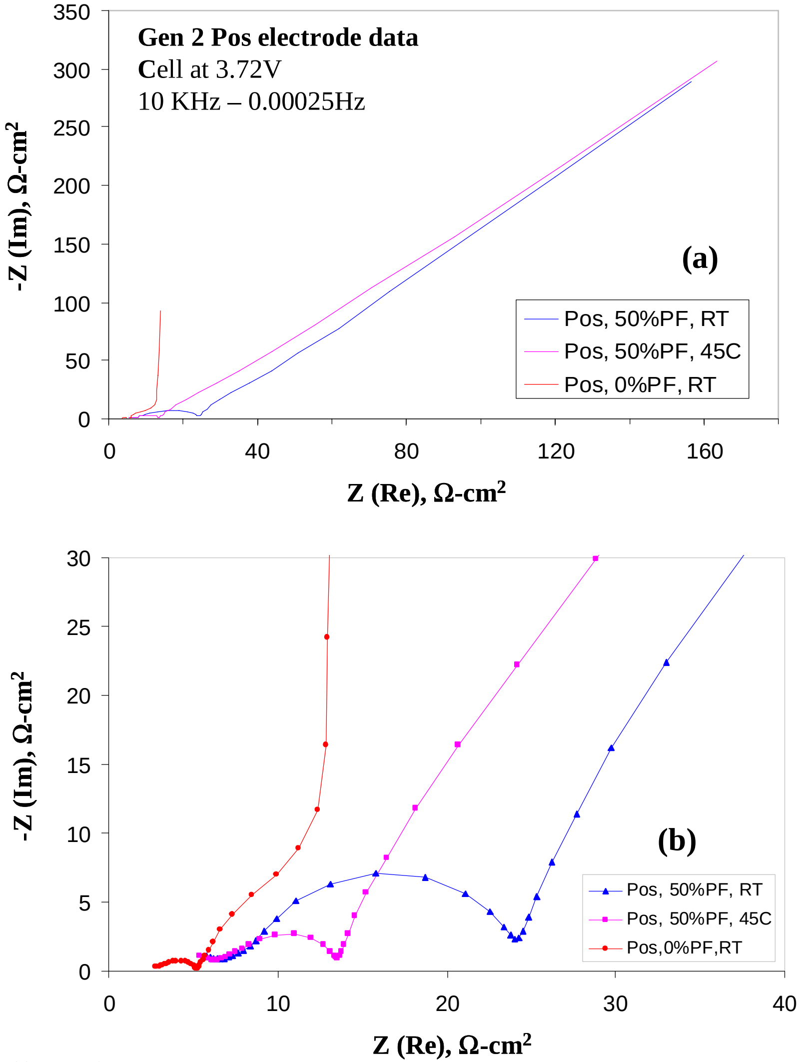

Fig. D-10. (a) Effect of Testing Temperature on Positive Electrode EIS Data Measured to Low Frequencies and (b) Enlarged View, to Show Aging- and Temperature-Related Changes in the Mid-frequency Arc.

D.6.3 Conclusions

- The higher the test temperature, the lower the cell impedance.
- The increase in the positive electrode mid-frequency arc width suggests that the oxide particle-electrolyte interface degrades on cell aging. The interfacial feature (oxide particle surface films, etc.) responsible for this degradation is sensitive to the testing temperature—the higher the test temperature, the less the effect of this interfacial feature.

- The shape of the Warburg impedance tail is not affected by the higher temperature testing, i.e., the feature that produces the Warburg tail is not sensitive to temperature in the 25–55°C range. The tail is most likely associated with diffusion processes at interfaces between the oxide particles.

D.7 RINSING EFFECTS ON POSITIVE ELECTRODE IMPEDANCE

Daniel Abraham and Jamie Knuth

D.7.1 Experiments Conducted

These experiments with conducted in Li-Sn reference electrode cells [1] containing 15.5-cm^2 positive and negative electrodes harvested from 18650 cells, two Celgard 2325 separators enveloping the reference electrode, and fresh Gen 2 electrolyte. The positive electrodes were immersed in DMC solvent (for ~48 hours before cell assembly) in an attempt to regain "original" electrode performance.

D.7.2 Summary of Results

Figure D-11 shows data for a highly aged electrode sample (2-026, 34.4% CF, 50.9% PF). The DMC rinse increases the mid-frequency arc width, but does not significantly affect the Warburg impedance tail. The mid-frequency arc maximum and minimum occur at similar frequencies for both samples.

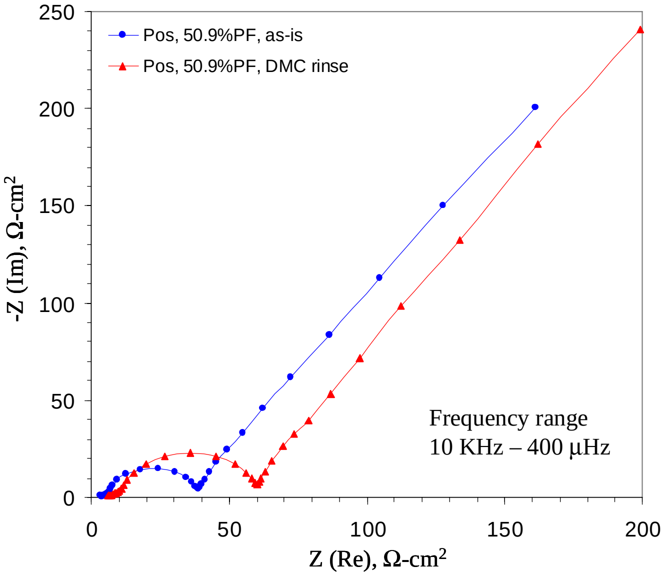

Fig. D-11. Effect of DMC Rinse on the Impedance of a Positive Electrode from a Highly Aged Cell.

D.7.3 Conclusions

- Electrode impedance is increased by the DMC rinse.

- A simple manipulation of the electrolyte environment can thus mimic the effects of additional aging (because the rinsing protocol is far too gentle to damage the oxide material). The DMC rinse may have increased impedance by altering the structure of the surface films on the oxide particles.
- The feature that produces the Warburg impedance tail is relatively insensitive to gentle electrode rinsing, which again suggests that the tail is most likely associated with diffusion processes at interfaces between the oxide particles.

References, Section D.7

1. Abraham, D. P., S. D. Poppen, A. N. Jansen, J. Liu, and D. W. Dees, Electrochim. Acta **49**, 4763 (2004).

D.8 ELECTROCHEMICAL STUDIES OF GEN 2 POSITIVE ELECTRODES

Marie Kerlau, Jeffrey Reimer, and Elton Cairns

D.8.1 Capacity Measurements

Swagelok cells were assembled with samples of Gen 2 cathodes in order to investigate mechanical and contact issues that might contribute to cell capacity and power fade.

D.8.1.1 Experiments Performed

The cells consisted of a $LiNi_{0.8}Co_{0.15}Al_{0.05}O_2$ cathode sample harvested from an aged cell, a Li metal anode, and a separator. The electrolyte solution was 1 M $LiPF_6$ in 1:1 mixture (by weight) of ethylene carbonate (EC) and diethyl carbonate (DEC).

Three different treatments (ultrasonically washing with DMC, pressing, and ultrasonically washing and pressing) were carried out on three cathode samples before assembling them into cells.

D.8.1.2 Summary of Results

The treatments improved the capacity of the cells (Fig. D-12). The greatest improvement was obtained with the washed and pressed cathode, and the capacity of this cell was nearly equal to that of a fresh cell; the capacity, however, decreased rapidly on cell cycling.

D.8.2 Electrochemical Impedance Spectroscopy Measurements

Electrochemical impedance spectroscopy (EIS) measurements were performed on reassembled Swagelock cells containing Gen 2 cathode samples obtained from cell G2.60C45.A217.50.72.50.G.L. (50% PF cell) and a Li counter electrode. The measurements were carried out at an open-circuit voltage (OCV) of about 2.5 V with an AC oscillation of 10 mV over the frequency range from 100 kHz to 1 mHz.

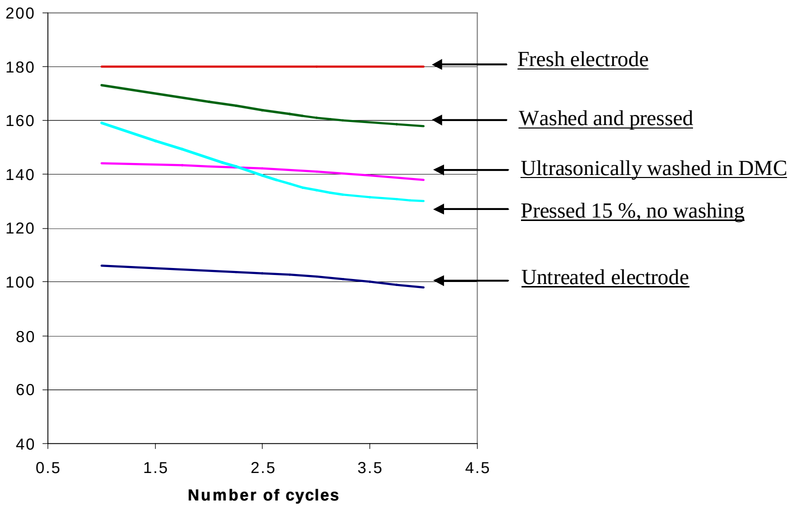

Fig. D-12. Effect of Electrode Treatment on Capacity of Positive Electrode Harvested from a Highly Aged (~50% Power Fade) 18650 Cell. Cells were cycled between 2.5 and 4.2 V at a ~C/20 rate.

D.8.2.1 Summary of Results

The EIS experimental data of three cells assembled with untreated, pressed, and washed and pressed electrode samples are shown in Figure D-13. For the treated electrodes, two semicircles and a diffusion straight line appeared, as also reported in various studies on $LiNi_{0.8}Co_{0.2}O_2$ electrodes. The semicircle at high frequency (left part of the graph) indicates the solid-state interface layer resistance, and the second semicircle at medium frequency represents charge transfer resistance at the $LiNi_{0.8}Co_{0.15}Al_{0.05}O_2$ electrode surface. The straight sloping line is due to the diffusion process of lithium ions at the interface between the active material particles and electrolyte. It can be clearly seen that the treatments of the electrodes dramatically decreased the impedance of the cells at low frequency. Moreover, the charge transfer resistance is much smaller in the case of the washed electrode. For the untreated electrode, the semicircle at medium frequency was not observed, due to a very high charge transfer resistance.

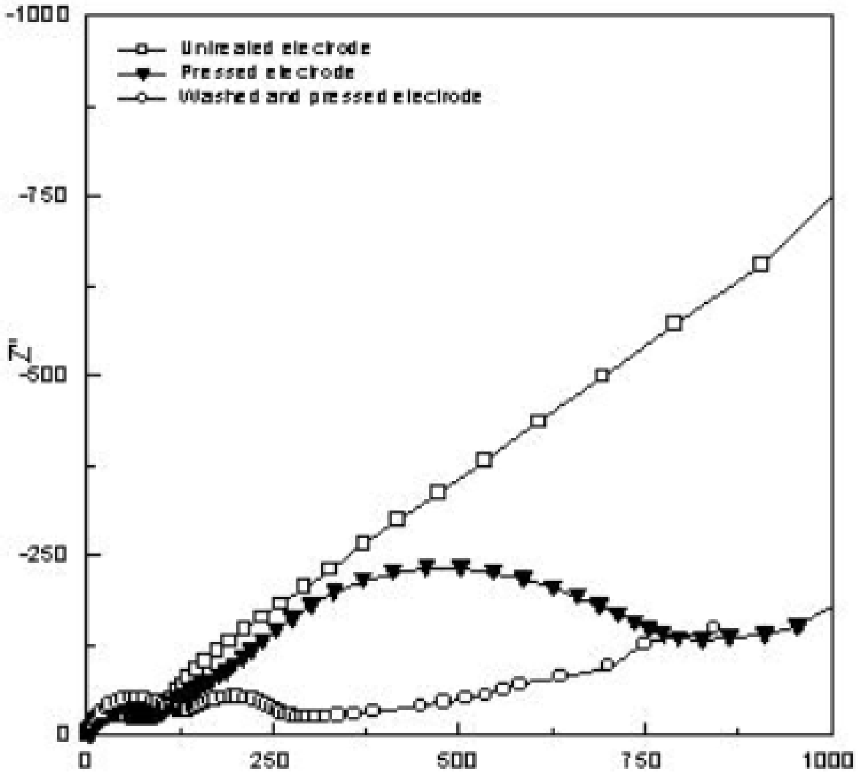

Fig. D-13. Nyquist Plots of Swagelok Cells Assembled with $LiNi_{0.8}Co_{0.15}Al_{0.05}O_2$ Positive Electrodes in the Discharged State (about 2.5 V vs. Li).

D.9 CAPACITY MEASUREMENTS ON NEGATIVE ELECTRODE HARVESTED FROM 18650 CELLS

Daniel Abraham and Jamie Knuth

D.9.1 Experiments Conducted

Coin cells (2032-type) were assembled with 1.6-cm^2 area samples punched from negative electrodes harvested from 18650 cells (see Table D-6), lithium-metal counter electrode, fresh Celgard 2325 separator, and fresh Gen 2 electrolyte, to determine the effect of aging on electrode capacity. The cells were cycled from 1.5 to 0 V with a 0.064 mA current.

Table D-6. Characteristics of 18650 Cells Studied

Cell ID	Aging T, Period, Type	C/1 Capacity Fade, %	Power Fade, %
Gen 2, 2-034	0 weeks	0	0
Gen 2, 2-006	55°C, 4 weeks, calendar	3.7	15.4
Gen 2, 2-009	55°C, 40 weeks, calendar	18.3	32.3
Gen 2, 2-026	45°C, 88 weeks, calendar	34.4	50.9

D.9.2 Summary of Results

The experimental data are summarized in Figures D-14, D-15, and D-16:

- All curves display the staging effects expected during lithium intercalation-deintercalation into graphite materials.
- Figures D-14a and D-14b show:
    - The electrode capacity decreases with increasing age of the 18650 cell.
    - The 0%, 3.7%, 18.3%, and 34.4% CF samples have capacities of 2.94, 2.82, 2.68, and 2.30 mAh, respectively. The corresponding positive electrodes had capacities of 2.56, 2.36, 2.03, and 1.8 mAh, respectively, when cycled vs. Li. Therefore, in spite of the capacity decrease, the graphite electrode has sufficient capacity to accept lithium ions from the positive electrode even for the late-life cells.
    - Cycling hysteresis is observed even for samples from cells that were not aged. In addition, except for the highly aged samples, the hysteresis effects are quite similar.
- Figure D-14c shows the voltage-capacity curves for the various electrode samples after normalizing out the cell capacity variations. The similarity of the various curves indicates that the graphite particles that contribute to electrode capacity behave very similarly. That is, the graphite particles are not damaged during cell aging.
- Data acquired at various cycling rates are shown in Figure D-15. The capacity gain from cycling at slower rates is very small.
- The effect of electrode rinsing in DMC solvent is shown in Figure D-16. Rinsed samples, even from late-life cell samples, show capacities that are comparable to 0% CF electrodes, which indicates that the graphite structure is unchanged on cell aging.

D.9.3 Conclusions

The negative electrode capacity loss on aging most likely results from pore clogging or isolation of graphite particle by electronically insulating surface films that can be washed off in solvents such as DMC.

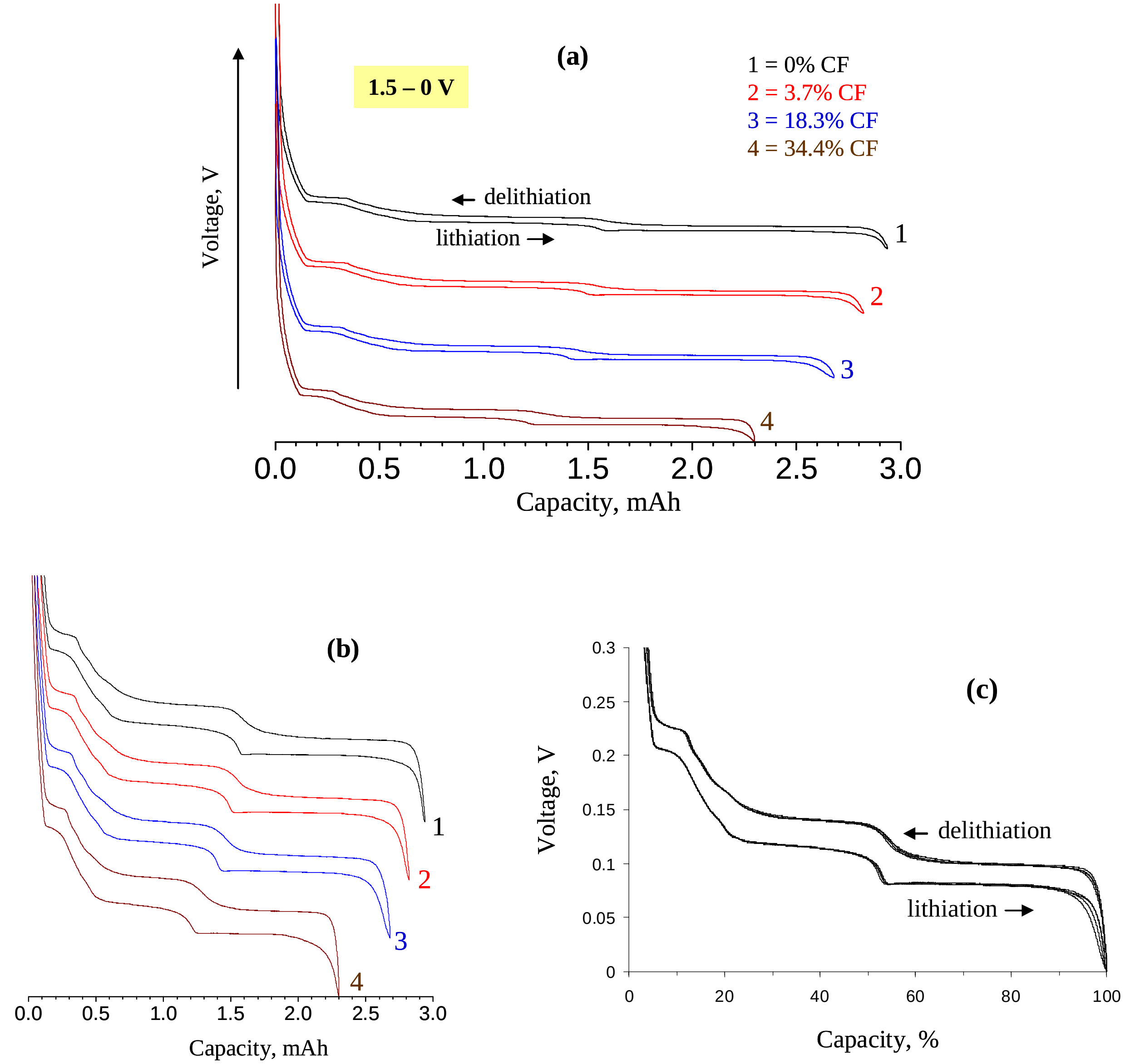

Fig. D-14. Cycling Data (vs. Li) from Harvested Anodes. (a) Obtained with a 0.064-mA current in the 1.5 to 0 V Range; (b) same data as (a), but showing data in the 0.3 to 0 V range; (c) same data as in (b), but after normalizing for cell capacity variations. In (a) and (b), curves have been offset for clarity.

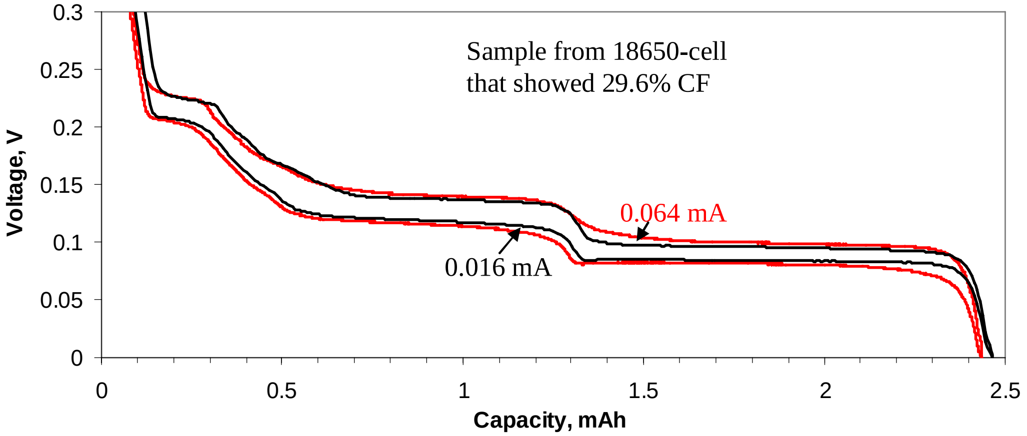

Fig. D-15. Representative Data Showing Cycling Rate Effect on Negative Electrode Capacity Data. The cycling currents are 0.064 mA and 0.016 mA. Only data in the 0.3 to 0 V range are shown.

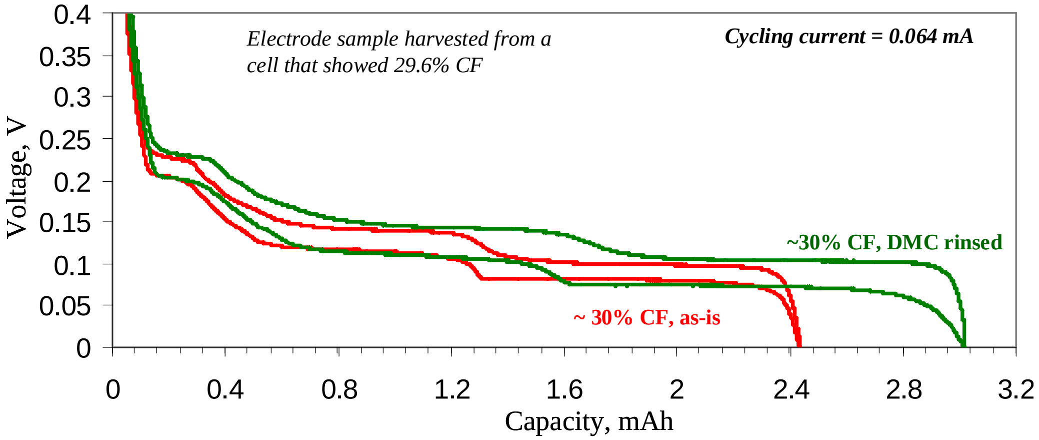

Fig. D-16. Representative Data Showing the Effect of DMC Rinse on Negative Electrode Capacity.

APPENDIX E. SEPARATOR STUDIES

E.1 STUDY OF MEMBRANE DEGRADATION IN GEN 2 HIGH-POWER LI-ION CELLS

Robert Kostecki, Frank McLarnon, and Laura Norin

The Gen 2 high-power Li-ion cells included a Celgard 2300 membrane separator. In this study, we carried out a comparative study of separators removed from control cells that underwent only formation cycles at room temperature (control separator) with separators of cells that were aged at 55°C for up to 50 weeks, losing up to 52% of their initial power (aged separators). The membranes of these cells were compared with unused samples of Celgard 2300.

E.1.1 Electrochemical Impedance Measurements of Fresh/Aged Separators

E.1.1.1 Experiments Conducted

Impedance spectra of separators soaked in the electrolyte were recorded inside an argon-filled glove box using an impedance phase analyzer and a potentiostat. Each sample had been soaked in electrolyte for 30 minutes prior to being placed between two identical nickel electrodes. During each test, the membrane was held between the electrodes at constant force. Impedance spectra were recorded at $U_{ac} = 5$ mV for ~12 different locations on the membrane.

E.1.1.2 Summary of Results

- All impedance spectra displayed features characteristic of a series RC circuit at high frequencies (Fig. E-1).
- The high-frequency end of the impedance spectrum, which corresponds to the separator ionic resistance, shifts continuously toward higher resistances with increasing cell storage time (Fig. E-2).
- The local membrane resistance became more nonuniform as the cells aged.

E.1.1.3 Conclusions

The membrane impedance increases significantly upon cycling and/or aging of lithium-ion cells and accounts for ~15% of the total cell impedance rise.

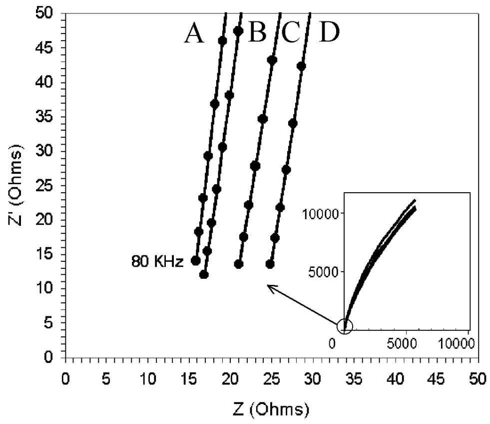

Fig. E-1. Impedance Spectra of Separators Removed from (A) Fresh Cell, and Cells Stored at 55°C for (B) 8 Weeks, (C) 24 Weeks, and (D) 40 Weeks.

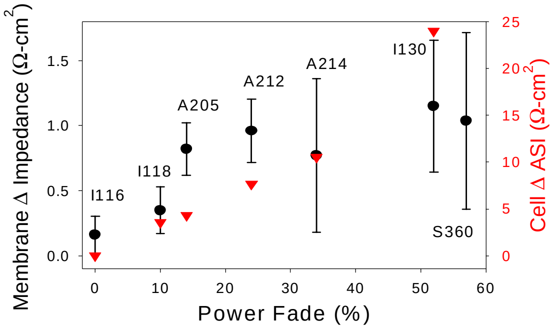

Fig. E-2. Change of Celgard 2300 Membrane Area-Specific Impedance, Measured at 80 kHz (left ordinate and circles) and Change of Li-Ion Cell Area-Specific Impedance, Measured at 3.6 V after Cell Testing (right ordinate and triangles).

E.1.2 Scanning Electron Microscopy (SEM) and Atomic Force Microscopy (AFM) Studies of Surface Morphology of Fresh/Aged Separators

E.1.2.1 Experiments Conducted

All separators were soaked in dimethyl carbonate (DMC) for 30 minutes after removal from Li-ion cells inside an argon-filled glove box. This eliminated all electrolyte salt from the separator (as verified with infrared spectroscopy) to prevent its reaction with air and moisture. AFM images were produced in contact mode inside a He-filled glove box. Prior to SEM measurements, all samples were rinsed in ethyl methyl carbonate (EMC) in order to remove dust or other contaminants.

E.1.2.2 Summary of Results

- The membranes removed from cycled and aged cells display dramatic changes in surface morphology (Fig. E-3).
- The increased fiber thickness and their swollen appearance, which were observed in separators aged for shorter periods of time, are due to the deposition of a residue from the electrolyte (Fig. E-4).
- The distribution of the deposit in the separator is highly nonuniform and exhibits a patchy pattern.

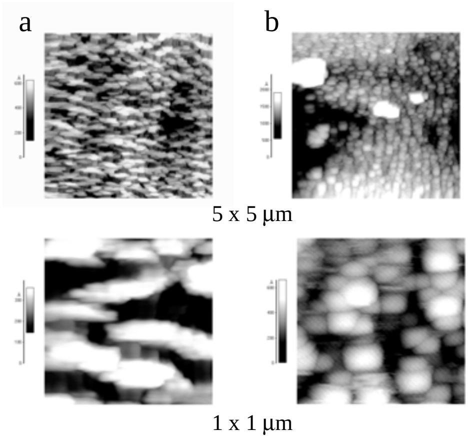

Fig. E-3. AFM Images of Separators Extracted from (a) Fresh Cell, (b) Cell Stored at 55°C for 40 Weeks.

E.1.2.3 Conclusions

- Morphology changes may result in a nonuniform current distribution across the cell and consequent accelerated electrode degradation at high-current locations. Membrane swelling could also increase mechanical stress in the cell, which may degrade electrode integrity.
- The compounds covering the fibers significantly reduce both the size of the pores and the homogeneity of the separator, thereby increasing the mean path length of the ions, and consequently increasing the potential drop across the separator.

E.1.3 Fluorescence Spectroscopy and Microscopy of Fresh/Aged Separators

E.1.3.1 Experiments Conducted

All separators were soaked in dimethyl carbonate (DMC) for 30 minutes after removal from Li-ion cells inside an argon-filled glove box. This eliminated all electrolyte salt from the separator (as verified with infrared spectroscopy) to prevent its reaction with air and moisture. Prior to all measurements, samples were rinsed in ethyl methyl carbonate (EMC) in order to remove dust or other contaminants. Fluorescence images of the separators were obtained in the 350- to 580-nm spectral range. Fluorescence spectra of the separators were recorded using a 325-nm UV laser at 2 mW/cm^2.

E.1.3.2 Summary of Results

- Fluorescence images of a separator removed from aged Li-ion cells display a nonuniform patchy pattern of fluorescent and non-fluorescent spots (Fig. E-5).

- Parts of the Li-ion cell separator that extended beyond the edges of the electrodes in the cell show uniform and strong fluorescence (Fig. E-6).
- Fluorescence imaging of the cathode and anode harvested from the aged cell reveal some areas of low-intensity fluorescence emission.
- Parts of the separator that were in contact with electrodes show a completely different spectral characteristic.

E.1.2.3 Conclusions

- Strongly fluorescent $LiPO_x$:MeF fluorophosphates precipitate from the electrolyte and form 25–100 nm films on all Gen 2 cell components.
- The film impedes Li^+ transport through the pores and contributes to surface chemistries on both electrodes, e.g., SEI (re)formation.

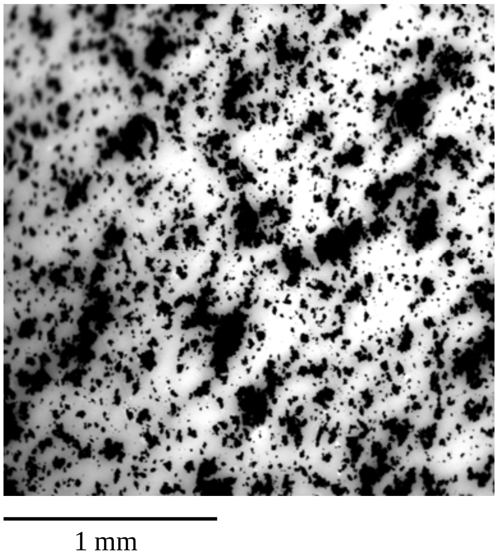

Fig. E-5. 2.5 × 2.5 mm Fluorescence Image Obtained in the 350–580 nm Spectral Range of a Separator Aged in a Cell for 40 Weeks at 55°C. Bright areas correspond to intense fluorescence emission; dark patches are non-fluorescent.

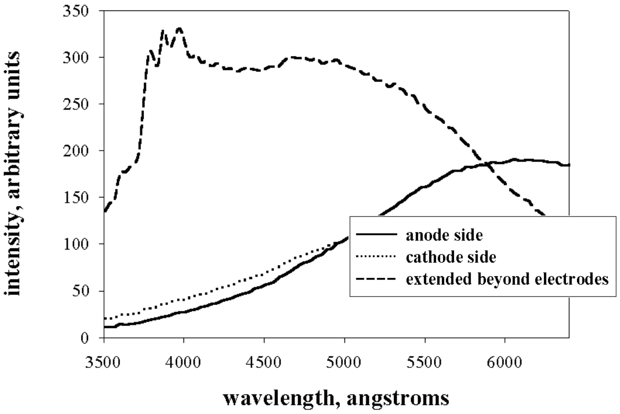

Fig. E-6. Fluorescence Spectra of Three Parts of the Separator: Two Sections That Were in Contact with the Anode or Cathode inside the Cell and a Section That Was Not in Contact with the Electrodes. Excitation light source: 325 nm UV laser at 2 mW/cm^2.

Publications on Related Subjects, Section E.1

Kostecki, R., L. Norin, X. Song, and F. McLarnon, “Diagnostic Studies of Polyolefin Separators in High-Power Lithium-Ion Cells,” J. Electrochem. Soc. **151**, A522 (2004).

Norin, L., R. Kostecki, and F. McLarnon, “Study of Membrane Degradation in High-Power Lithium-Ion Cells,” Electrochem. Solid-State Lett. **5**, A67 (2002).

E.2 EXAMINATION OF SEPARATORS HARVESTED FROM 18650 CELLS

Daniel Abraham and Scott MacLaren

E.2.1 Electrochemical Measurements

EIS measurements were conducted on separator samples harvested from 18650 cells (see Table E-1) to examine the effect of cell aging on separator degradation. The 1.6-cm^2 area samples were sandwiched between two stainless steel plates within 2032-type coin cells containing the Gen 2 electrolyte. Some of the samples were studied “as harvested” from the 18650 cells. Other samples were ultrasonically washed in a DMC-water mixture, then dried in a vacuum oven at 80°C. Control experiments were conducted on a fresh separator sample. EIS data were collected between 100 kHz and 0.01 Hz with a 10-mV perturbation about the open-circuit voltage; only the high-frequency portion is needed to determine the ohmic resistance of the separator.

Table E-1. Characteristics of the 18650 Cells Studied

Cell ID	Aging T, Period, Type	C/1 Capacity Fade, %	Power Fade, %
Gen 2, 2-032	0 weeks	0	0
Gen 2, 2-011	55°C, 8 weeks, calendar	6.8	13.4
Gen 2, 2-014	55°C, 20 weeks, calendar	9.6	24.1
Gen 2, 2-074	45°C, 16 weeks, cycle	7.6	16.3

E.2.1.1 Summary of Results

- Scattered data were obtained from the “as harvested” samples, which indicated that the resistance was nonuniform along the length and width of the separators. The data showed no obvious trends with 18650 cell age.
- Relatively consistent data were obtained from the ultrasonically washed separator samples. Furthermore, the data from all samples (see Fig. E-7) appeared to be within the bounds of experimental uncertainty; no obvious trends with aging were observed.

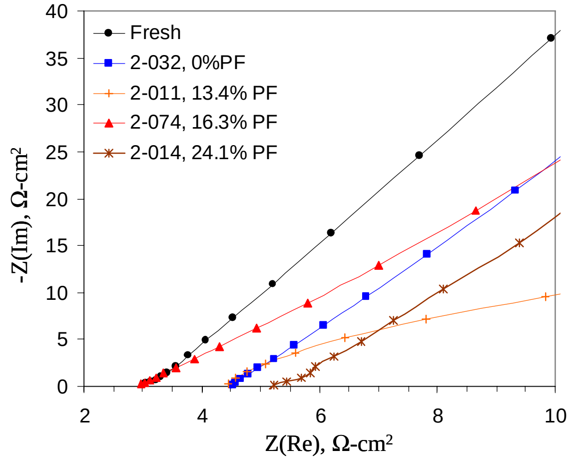

Fig. E-7. EIS Data from Fresh and Aged Separators. Only the high-frequency portion is shown.

E.2.2 Visual and SEM Examination

SEM images of separator samples harvested from 18650 cells (see Table E-2) were obtained with a Hitachi S-4700 scanning electron microscope (SEM) operating at 20 keV; these samples saw brief (<1 min) air exposure during loading into the microscope. Both "as harvested" samples and samples ultrasonically washed in a DMC-water mixture were studied.

Table E-2. Characteristics of 18650 Cells Studied

Cell ID	Aging T, Period, Type	C/1 Capacity Fade, %	Power Fade, %
Gen 2, 2-032	0 weeks	0	0
Gen 2, 2-021	55°C, 36 weeks, calendar	14	35
SNL321	55°C, 36 weeks, 80% SOC	32	54
Gen 2, 2-026	45°C, 88 weeks, 60% SOC	34.4	50.9

E.2.2.1 Summary of Results

Visual examination showed the following:

- Separator samples from the 0% PF sample were white in color.
- The samples showed increasing discoloration with increasing age of the 18650 cells. The separator side adjacent to the positive electrode was observed to have a different coloration from the side adjacent to the negative electrode.
- The original (white) color of the separator sample on the anode side was regained after the ultrasonic wash, which indicated that the separator discoloration was produced by surface deposits. The cathode side retained a light yellowish-brown tinge even after the ultrasonic wash, i.e., the polypropylene separator material was irreversibly discolored by cell aging.
- The separator material appeared to be "stickier" with cell age, i.e., portions of the electrode coatings stuck to the separator during cell disassembly, especially for mid-life and late-life cells.

- Separator areas near the electrode edges were darker. However, only a few millimeters away from the edge, the separator coloration was relatively uniform.

Observations from the SEM studies are as follows:

- All "as harvested" samples showed surface deposits, which include electrolyte residue and remnants of electrode surface films that adhered to the separator during cell disassembly. Separators from highly aged cells also showed some $LiNi_{0.8}Co_{0.15}Al_{0.05}O_2$ and graphite particles on the cathode and anode sides, respectively (Fig. E-8).
- The portions in contact with the electrode edges showed heavier residue relative to the rest of the separator.
- Separators from mid-life cells showed pores that were relatively open, not swollen shut by electrolyte residue. Some areas of these aged samples had fewer pores, but these were also observed in the 0% PF samples; this pore closing appears to be a mechanical effect caused by a smearing of the upper layer onto the pores (Fig. E-9).
- The as-harvested separator material from SNL321 (36 weeks, 54% PF) showed relative open pores (Fig. E-10). However, heavy surface residue that obscured the pores was observed all over the 2-026 (88 weeks, 50.9% PF) separator material (Fig. E-11a). These data suggest that the obstruction of separator pores by electrolyte residue/surface films may be an impedance contributor in high-power-fade cells, which are aged gradually.
- The DMC-water ultrasonic wash removed surface residue on both sides of the separator (Fig. E-11b). Rinsed separator samples, even from highly aged cells, showed morphologies that were comparable to those in the 0% PF cells.

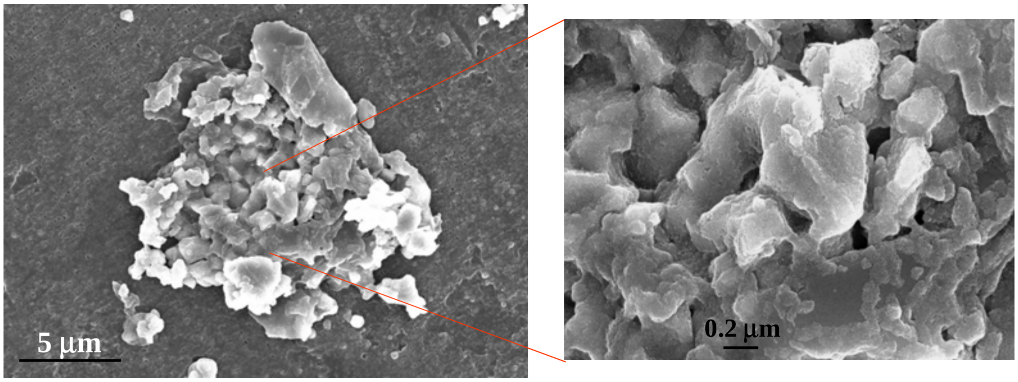

Fig. E-8. Oxide Particles on Cathode Side of "as Harvested" 2-026 Separator. Magnified view shows deposits on these particles that may include electrolyte residue.

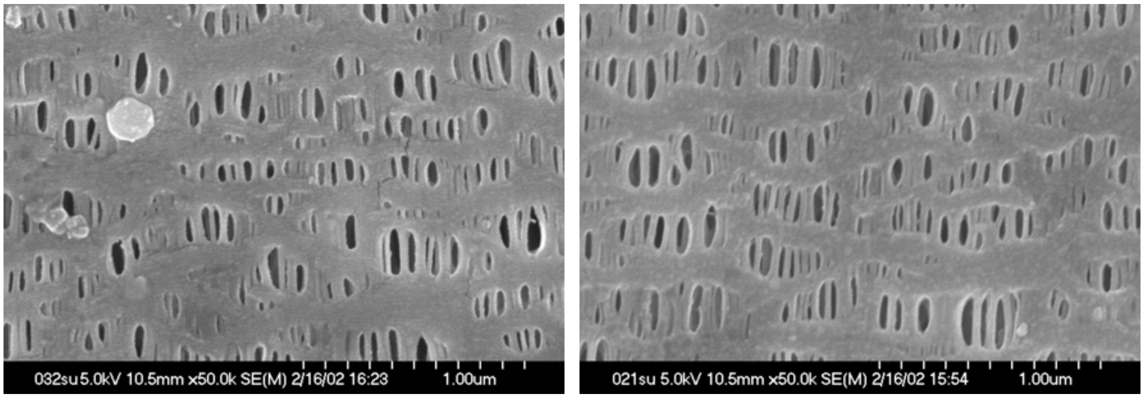

(a) (b)

Fig. E-9. SEM Images from “as Harvested” (a) 0% PF Sample and (b) 35% PF Sample.

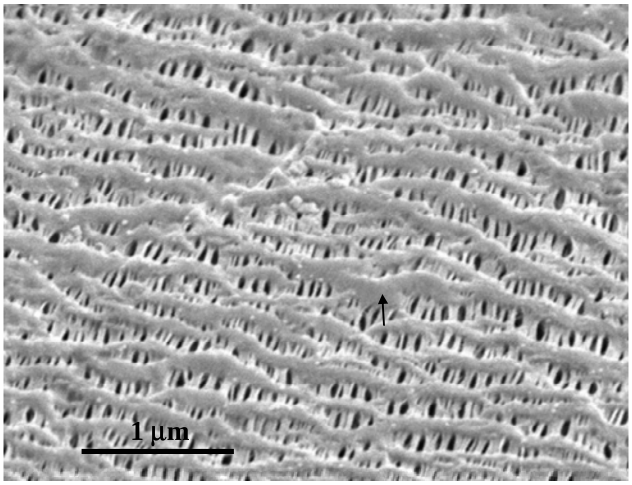

Fig. E-10. SEM Image from “as Harvested” SNL321 Sample, Showing Open Pores. The raised areas are intrinsic features of the separator; some surface residue is also seen.

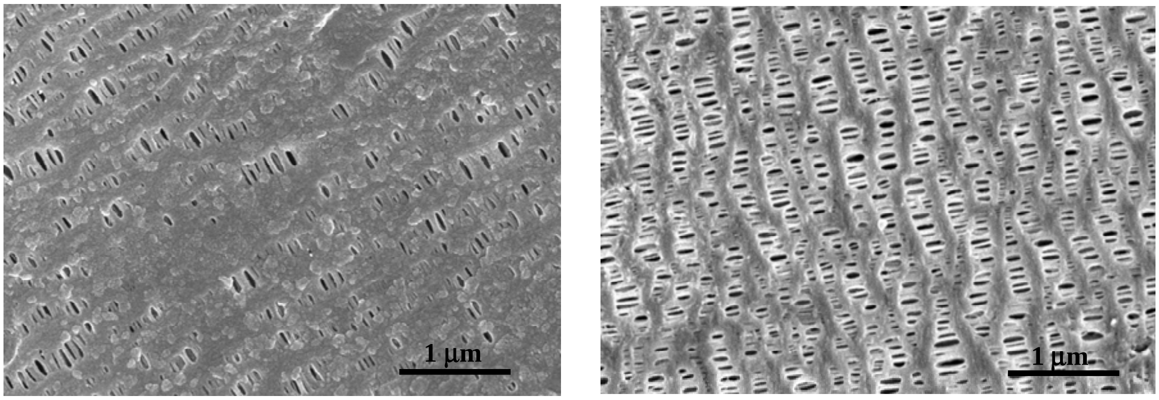

(a) (b)

Fig. E-11. SEM Images from 2-026 (a)“as Harvested” and (b) Rinsed Separator Samples. In (a), a large portion of the pores appear to be obscured by surface films that may include electrolyte residue. Image (b) shows that the surface films can be rinsed away.

E.2.2.2 Conclusions

- The separator material, even from high-power cells, does not appeared to be damaged by the cell aging protocol.
- The different discolorations indicate that the separator material is affected differently by the oxidizing conditions prevalent on the cathode and reducing conditions prevalent on the anode side during cell aging.
- The clogging of separator pores by electrode surface films could be an impedance contributor in high-power-fade cells, especially those that are aged gradually.

APPENDIX F. NEGATIVE ELECTRODE STUDIES

F.1 SCANNING ELECTRON MICROSCOPY EXAMINATION OF NEGATIVE ELECTRODE SAMPLES

Daniel Abraham and Scott MacLaren

F.1.1 Experiments Conducted

Micrographs of “as harvested” negative electrode samples (see Table F-1) were obtained with a Hitachi S-4700 scanning electron microscope (SEM) operating at 20 keV; these samples saw brief (<1 min) air exposure during loading into the microscope. Images from fresh negative electrode samples that had never been exposed to the electrolyte were obtained for comparison.

Table F-1. Characteristics of 18650 Cells Studied

Cell ID	Aging T, Period	Capacity Fade, %	Power Fade, %
Gen 2 fresh	None	NA	NA
Gen 2-023	0	0	0
Gen 2 SNL321	55°C, 20 weeks, 80% SOC	32	54
Gen 2 SNL325	45°C, 40 weeks, 80% SOC	31	51.3
2-026	45°C, 88 weeks	34.4	50.9
Var C-031	45°C, 12 weeks	3.8	20.8

[a] SNL321 cell was disassembled at 3.9 V. All other cells were discharged to less than 3.2 V.

F.1.2 Summary of Results

- A typical image of the fresh laminate (see Fig. F-1a) showed the characteristic plate-like particles of Mag-10 graphite that are ~5- to 10-µm wide with well-defined active edges; portions of the graphite that flaked off the surface are visible in the figure.
- Micrographs of the 0% power fade sample (Fig. F-1b) showed some rounding of the graphite images, which indicated the presence of a surface film (SEI) had formed. Electrolyte residue and the PVDF binder were apparent in some micrographs.
- Micrographs of samples from high-power-fade cells (Fig. F-1c) showed a distinct rounding of the graphite edges. The surface flakes apparent in the fresh laminate were indistinct in these samples, suggesting the presence of a layer that covered both the graphite surface and edges; the PVDF binder was never observed in these images.
- Micrographs of samples that were soaked in DMC (rinsed) were mostly comparable to that of the 0% PF samples (Fig. F-1d). The graphite particles, even from highly aged cells, had well-defined edges, which indicated that most of the electrode surface films had been washed off. In some images, surface deposits, presumably electrolyte residue, were observed.

F.1.3 Conclusions

- Formation cycling produces a SEI layer on the graphite particles. The SEI layer grows thicker with aging and covers both the active material and the PVDF binder.
- DMC rinsing appears to remove most of the electrode surface films that include the SEI layer and residual electrolyte.

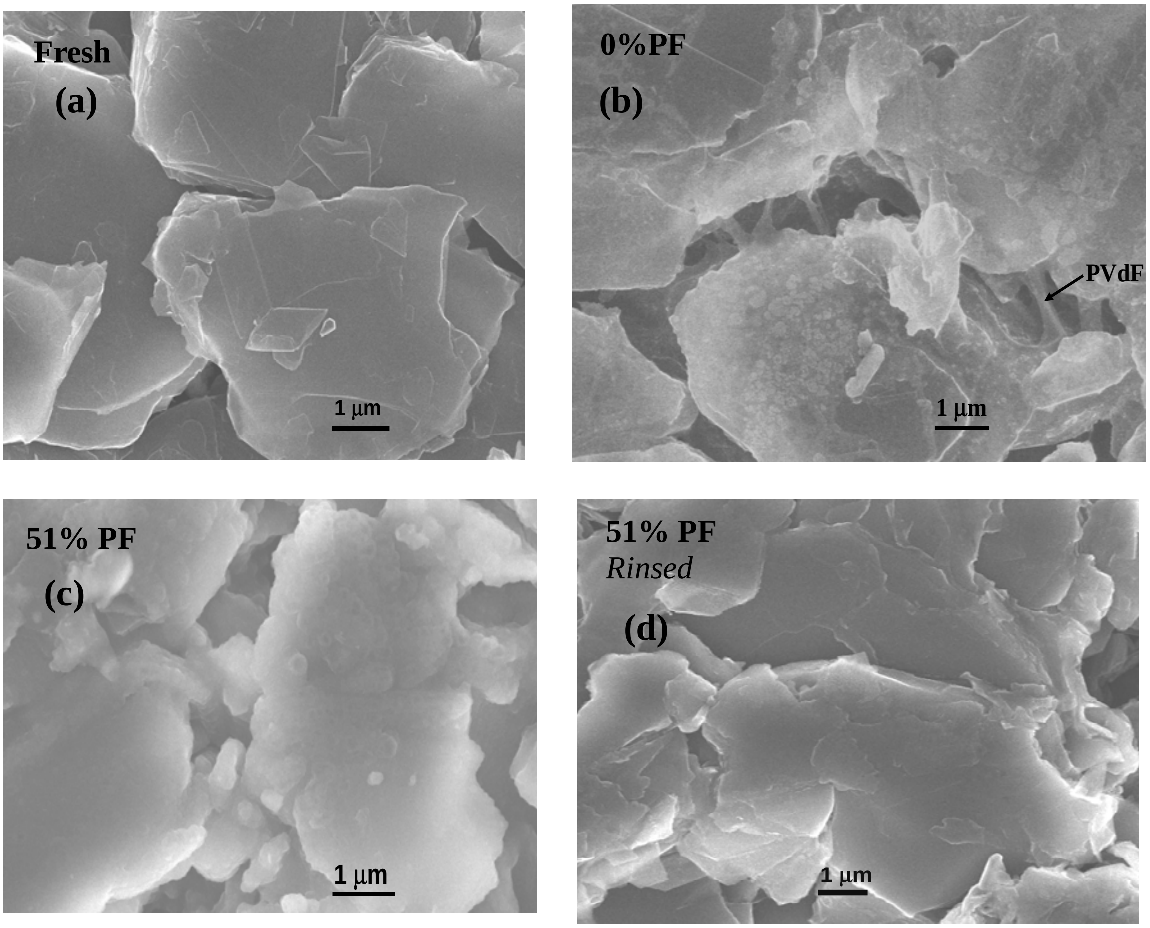

Fig. F-1. SEM Images of Negative Electrode Samples Harvested from Gen 2 Cells. (a) fresh, (b) 0% power fade, (c) 51% power fade, and (d) DMC rinsed, 51% power fade.

F.2 X-RAY DIFFRACTION STUDIES OF NEGATIVE ELECTRODES

Daniel Abraham and Mauro Sardela

F.2.1 Experiments Conducted

X-ray diffraction studies were conducted on negative electrode samples harvested from 18650 cells (see Table F-2) to examine the effect of cell aging on graphite degradation. The samples were examined in a specially designed, hermetically sealed container to avoid any incidental exposure to air. The data were collected on a Philips powder diffractometer using CuK_α radiation for two-theta values of 20 to 80°. Control experiments were conducted on fresh negative electrode samples that had never been exposed to the electrolyte.

Table F-2. Characteristics of 18650 Cells Studied

Cell ID	Aging T, Period	Capacity Fade, %	Power Fade, %
Fresh	None	NA	NA
2-023	0	0	0
2-021	55C, 36 weeks	17.5	35
SNL321[a]	55°C, 20 weeks, 80% SOC	32	54
SNL325	45°C, 40 weeks, 80% SOC	31	51.3

[a] SNL321 cell was disassembled at 3.9 V. All other cells were discharged to less than 3.2 V.

F.2.2 Summary of Results

- Strong graphite diffraction peaks were observed for electrode samples from even the highly aged cells, which indicated that the graphite structure was not damaged.
- Figure F-2 shows (002) the strongest graphite diffraction peak.
  - The lower peak intensities of the harvested electrodes, relative to that of the fresh electrode, may reflect the presence of the SEI layer.
  - The (002) and (004) peaks showed a slight decrease with increasing cell age. This difference, however, may not be statistically significant.
  - The larger interplanar spacing of the SNL321 sample reflects the lattice expansion induced by lithium remaining in the graphite layers. The diffraction pattern was consistent with the presence of LiC_{12} in the sample.
- Peaks corresponding to LiF and Li_2CO_3 were not observed in the diffraction patterns. These compounds, if present, are below the detection limits of the instrument.
- Figure F-3 shows extra peaks, not observed in the fresh sample, between 20 and 25 degrees. These peaks may arise from diffracting compounds in the SEI layer. The intensities of these peaks cannot be correlated with cell age.

F.2.3 Conclusions

- The graphite structure is not damaged by the cell aging process.
- The diffraction patterns are indicative of a SEI layer on the harvested electrodes. The compounds in the SEI layer, however, cannot be conclusively identified.
- The hermetically sealed holder provided a reliable method to study the lithiated graphite electrodes.

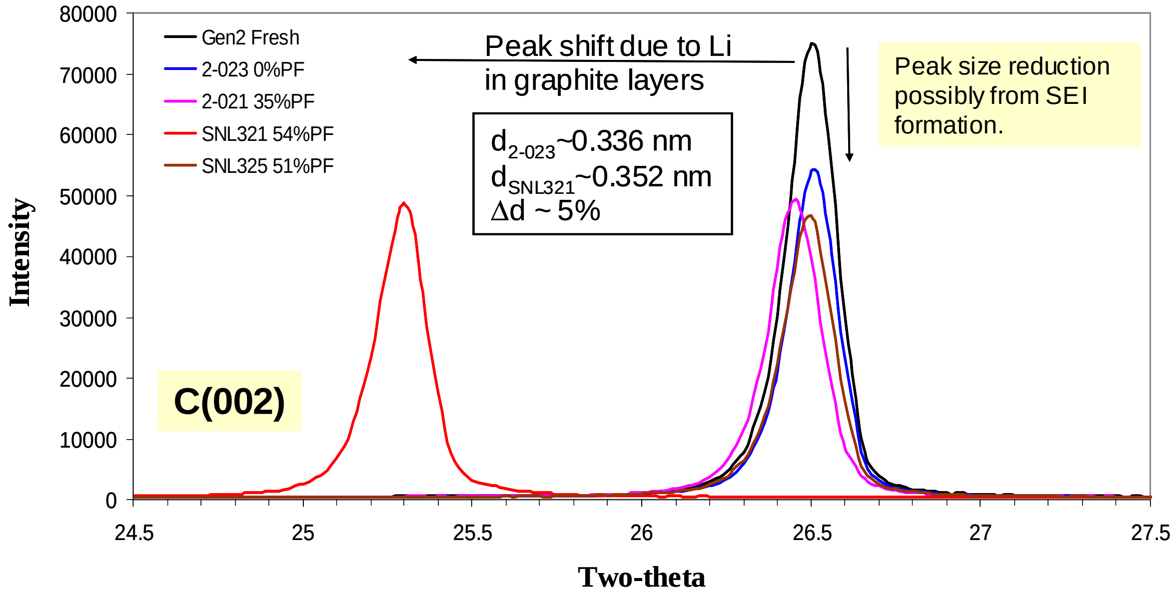

Fig. F-2. The (002) Graphite Peak from Fresh and Harvested Negative Electrode Samples.

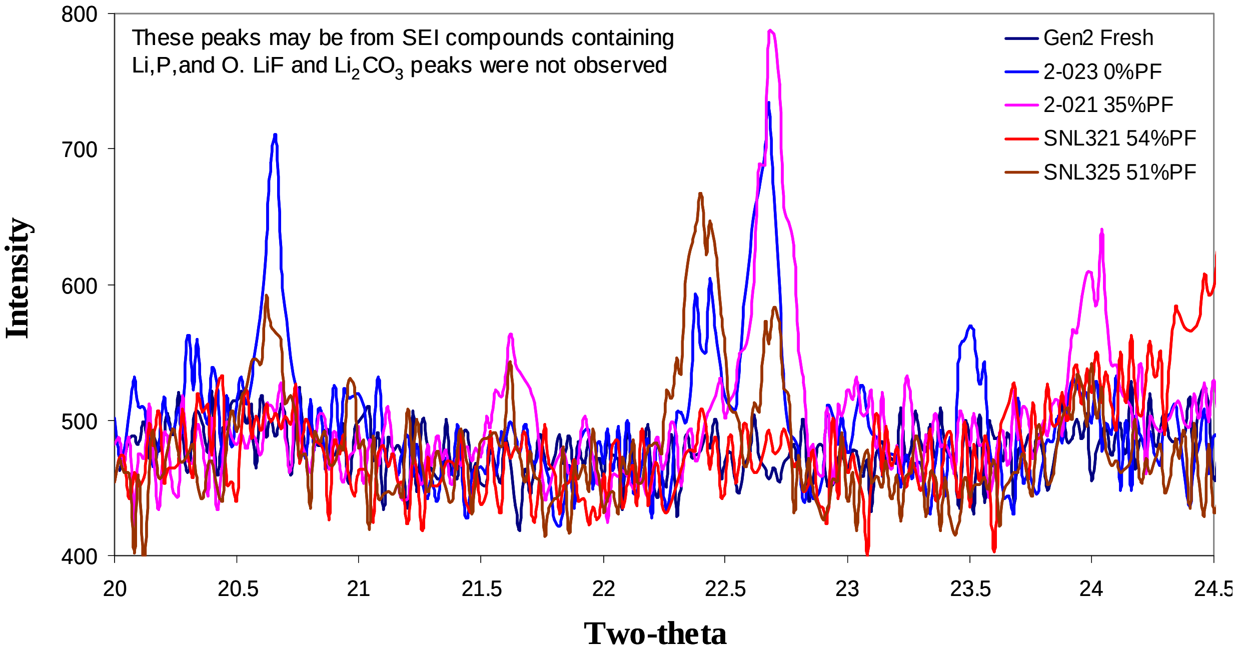

Fig. F-3. Diffraction Peaks in the 20 to 25 Degree Range That Are Not Observed in the Fresh Sample.

F.3 STUDY OF NEGATIVE ELECTRODE DEGRADATION BY SPECTROSCOPY AND MICROSCOPY TECHNIQUES

Robert Kostecki, Kathryn McCarthy, and Frank McLarnon

The Gen 2 high-power Li-ion cells included a composite anode that consists of 96 wt% MAG-10 synthetic graphite and 4wt% PVDF binder. We carried out a comparative study of anodes removed from control cells that underwent only formation cycles at room temperature (control anodes) with anodes of cells that were aged at 55°C for up to 68 weeks, losing up to 52% of their initial power (aged cells). The anodes of these cells were compared with fresh samples of Gen 2 composite anode.

F.3.1. Raman Spectroscopy and Microscopy Measurements of Fresh/Aged Anodes

F.3.1.1 Experiments Conducted

All anodes were soaked in dimethyl carbonate (DMC) for 30 minutes after removal from Li-ion cells inside an argon-filled glove box. This procedure removed electrolyte salt from the electrode to prevent its reaction with air and moisture. The excitation source was a He-Ne (632-nm) 10-mW laser. The power of the laser beam was adjusted to 0.1 mW with neutral filters of various optical densities. The size of the laser beam at the sample was ~1.2 µm, which is one order of magnitude smaller than the size of an average MAG-10 graphite particle.

A typical Raman spectrum of graphite consists of the E_{2g} active mode, or (G) band at ~1,582 cm^{-1}, and the A_{1g} mode, or (D) band at ~1,360 cm^{-1}, which is associated with the breakage of symmetry occurring at the edges of graphite sheets. The relative intensity of the D band vs. G band is attributed to carbon crystalline structure, for example, in microcrystalline graphite. The ratio of D/G integrated peak intensities is inversely proportional to the intra-planar microcrystallite distance L_a. and to the size of graphene domains. It increases with the extent of carbon disorder.

A semi-quantitative surface analysis of the anode structure and composition was carried out by deconvoluting thousands of Raman spectra that were collected systematically from 40 × 62 µm sections of anode surfaces at 0.7 µm resolution into two carbon bands.

F.3.1.2 Summary of Results

- The relative D and G peak heights change noticeably for the anodes from aged/cycled cells. The D band intensity increases substantially, the G band broadens significantly, and a new band at ~1,620 cm^{-1}, which is typical of “severely disordered” carbonaceous materials, appears in the spectrum (Figs. F-4, F-5, and F-6).
- Accumulation of inorganic compounds, i.e., $LiPO_x$, Li_2CO_3, LiF, and traces of NiO_x and CoO_x, on the surface of tested anodes was observed in aged/cycled cells.
- The SEI is more evident on regions of disordered carbon. The increased thickness of the SEI is directly correlated with an increasing concentration of graphite edges, lattice defects, etc.

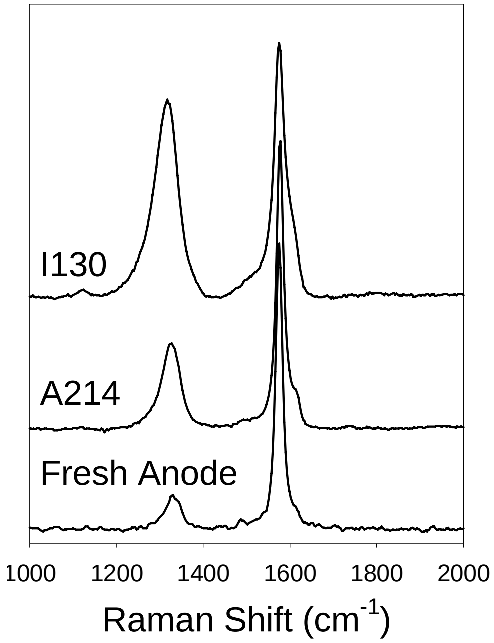

Fig. F-4. Average Raman Spectra of Gen 2 Graphite Anodes from Fresh and Aged Gen 2 Cells.

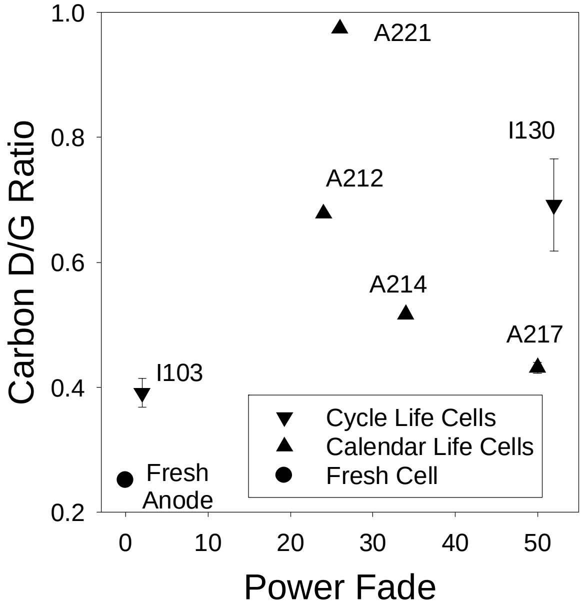

Fig. F-5. Average Carbon D/G Ratio Calculated from Raman Microscopy Images of Anodes Extracted from Gen 2 Cells.

Fig. F-6. Raman Microscope Spectra Collected from Various Locations at the Anode Removed from the I130 Cell. The bands <1,200 cm^{-1} correspond to $LiPO_x$, Li_2CO_3, LiF, and traces of NiO_x and CoO_x.

F.3.1.3 Conclusions

- Micro Raman spectroscopic surface analyses of Gen 2 anodes revealed increased amounts of amorphous carbon in anodes taken from tested cells (Fig. F-7).
- The concentration of amorphous carbon depended strongly upon location on the electrode surface and in its bulk, at both microscopic and macroscopic scales.
- Raman mapping of an anode cross section showed that the concentration of amorphous carbon is greater at the anode/electrolyte interface and smaller at the copper/anode interface.
- Inorganic reaction products, such as the carbonates and polyphosphates contained in the anode SEI layer, were found at locations where there are greater amounts of disordered carbon.
- Accumulation of inorganic products at graphite particles create a barrier to Li-ion diffusion and thereby reduce cell power capabilities.
- The gradual transfer of lithium from the cathode to the anode SEI prevents full discharge of the cathode and thereby limits the Li-ion cell capacity.

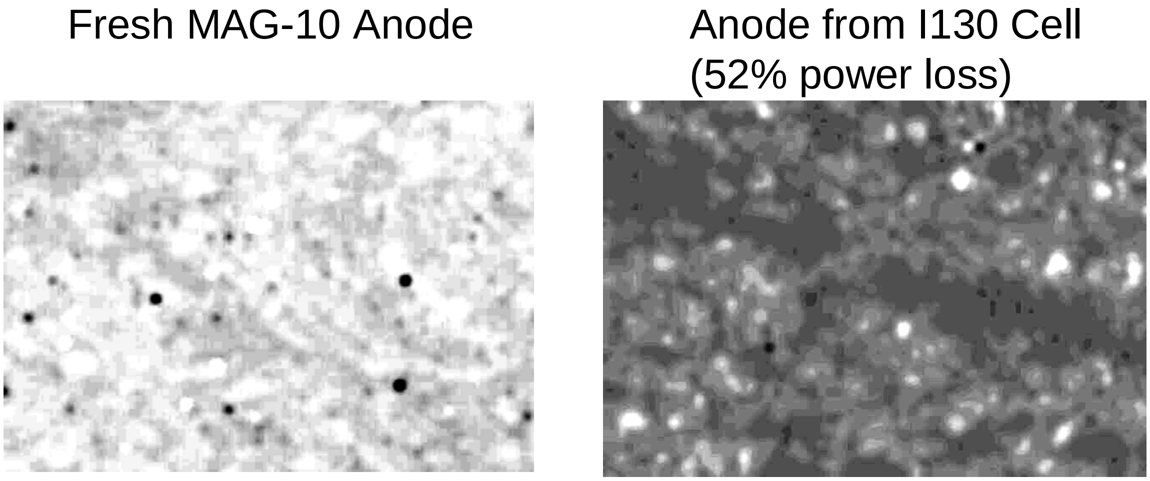

Fig. F-7. Raman Microscopy Images of Graphite Anodes. White areas represent pure graphite, and dark gray areas indicate structural disorder. The small, black round spots visible on the left panel are artifacts. The image size is 40 × 60 µm.

F.3.2 Scanning Electron Microscopy (SEM) and Atomic Force Microscopy (AFM) Studies of Surface Morphology of Fresh/Aged Anodes

F.3.2.1 Experiments Conducted

All anodes were soaked in dimethyl carbonate (DMC) for 30 minutes after removal from Li-ion cells inside an argon-filled glove box. This procedure removed electrolyte salt from the electrode to prevent its reaction with air and moisture. All AFM experiments were performed in constant-force mode with a controlled oxide-tip voltage difference under a controlled dry N_2 atmosphere.

F.3.2.2 Summary of Results

- AFM surface images revealed significant changes in electrode topography (Fig. F-8).
- Nanocrystalline deposits accumulated preferentially on graphite flake cross sections, plane steps, and edges. There is no clear evidence of such nanocrystalline deposits on the graphitic planes.
- The increased thickness of the SEI is directly correlated with temperature and the duration of electrochemical test.

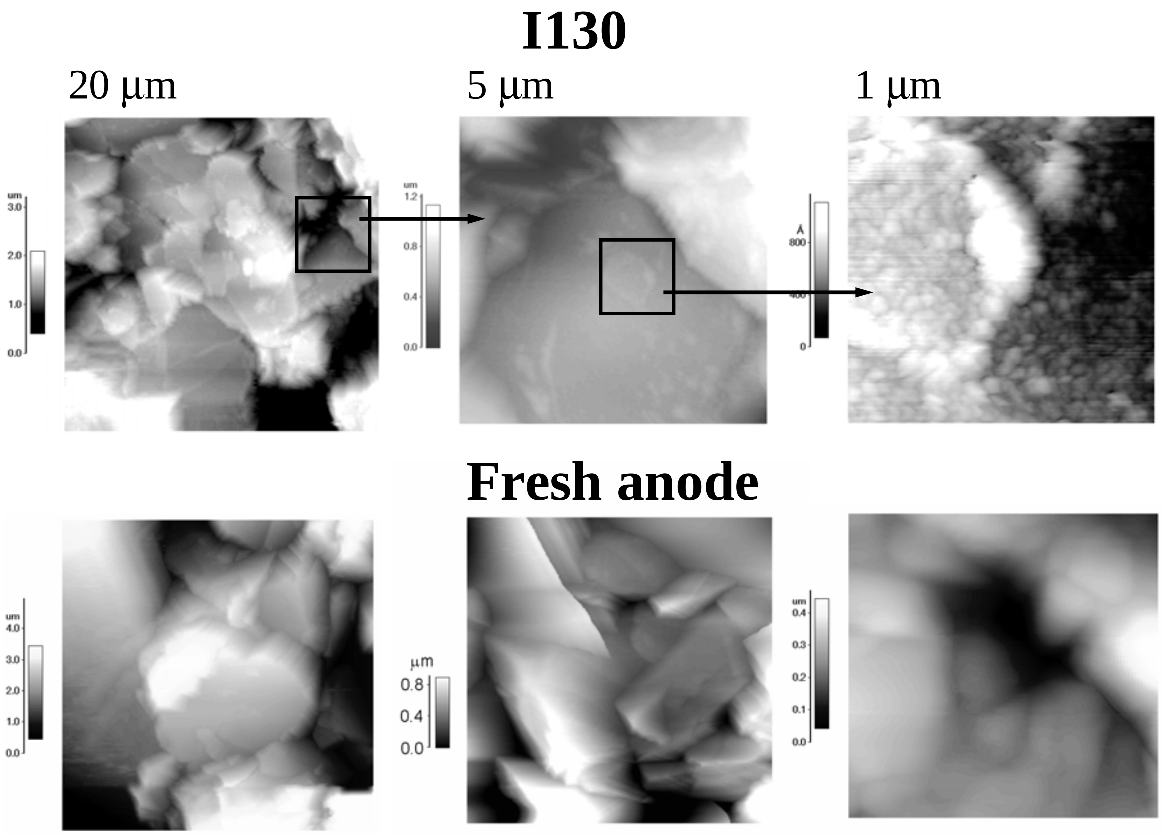

Fig. F-8. AFM Images of a Fresh Graphite Anode and the Anode from the I130 Cell (52% Power Loss).

Publications on Related Subjects, Section F.3

Striebel, K. A., J. Shim, E. J. Cairns, R. Kostecki, Y.-J. Lee, J. Reimer, T. J. Richardson, P. N. Ross, X. Song, and G. V. Zhuang, "Diagnostic Analysis of Electrodes from High-Power Lithium-Ion Cells Cycled under Different Conditions," J. Electrochem. Soc. **151**, A857 (2004).

Kostecki, R., and F. McLarnon, "MicroProbe Study of the Effect of Li Intercalation on the Structure of Graphite," J. Power Sources **119-121**, 550 (2003). (LBNL-52890)

Shim, J., R. Kostecki, T. Richardson, X. Song, and K. A. Striebel, "Electrochemical and Physical Analysis of a Li-Ion Cell Cycled at Elevated Temperature," J. Power Sources **112**, 222 (2002).

F.4 ANODE EXAMINATION BY FOURIER TRANSFORM INFRARED SPECTROSCOPY

Vera Zhuang and Phil Ross

Fourier transform infrared (FTIR) spectroscopy data were obtained directly from electrode surfaces in the attenuated total reflection (ATR) mode. All spectra were acquired with a spectral resolution of 4 cm^{-1} and summed over 512 scans. The probe size was 2 mm in diameter; sample and probing depth was estimated to be ca. 500 nm. The spectra were corrected for light penetration depth as a function of wavelength, and a linear background correction was applied. None of the spectra were subjected to a smoothing algorithm.

FTIR was used to analyze the chemical composition of the solid electrolyte interface (SEI) on Gen 2 anodes. An anode harvested from a fresh cell only subject to formation cycles and from two aged cells, G2.60C55.A211.30.40.31.G.L and G2.60C55.A214.34.40.34.G.L, were analyzed. The more detailed summary of this work has been published in Electrochemical and Solid-State Letters, **6**(7), A136–139 (2003).

F.4.1 Experiments Conducted

- All anodes were harvested from the cells in a glove box and transferred from the glove box to the He-purged spectrometer sample chamber using a portable vacuum-sealed container.
- Measurements were performed directly on anode surface without any preparation, or with light "washing" in dimethyl carbonate (DMC) to remove residual electrolyte.

F.4.2 Summary of Results

- No significant variation of chemical composition of the SEI layer with position on the electrode was measured for the fresh anode.
- The chemical composition of SEI layer on the aged anodes is less uniform than that on the fresh anode, but there was no systematic variation with position on the electrode.
- The SEI layer is composed of lithium alkyl carbonate, lithium oxalate, lithium carboxylate, and lithium alkoxide. Highly localized amounts of lithium hydroxide and

methanol were also found on anodes from aged cells. Formation of the latter two compounds is probably from reaction of the primary SEI components with water over time, e.g., lithium methoxide plus water goes to lithium hydroxide plus methanol. The source of water is unclear.

F.4.3 Conclusions

SEI composition changes with aging forming mostly “inorganic” compounds, i.e., general loss of $-CH_2-$ or $-CH_3$ functionalities, with some evidence for thermal hydrolysis reactions in the cell. However, no obvious increase in the thickness of the SEI layer that might cause an increase in anode impedance.

F.5 PROTON NUCLEAR MAGNETIC RESONANCE ANODE EXAMINATION

Daniel Abraham and Rex E. Gerald II

F.5.1 Experiments Conducted

High-resolution proton NMR analyses were conducted to examine the possible presence of polyethylene oxide (PEO) or its oligomers in surface films on anodes harvested from 18650 cells (see Table F-3). The surface films were extracted by washing the samples several times with acetonitrile solvent. The PEO content of each sample was quantified by summing the PEO contents determined for each wash solution. Control experiments conducted on fresh ethylene carbonate (EC) samples are described in Appendix G.

Table F-3. Characteristics of 18650 Cells Studied

Cell ID	Aging T, Period	Capacity Fade, %	Power Fade, %
2-034	None	0	0
2-078	45°C, 68 weeks	29.6	48.4

F.5.2 Summary of Results

The experimental observations are listed in Table F-4.

Table F-4. Summary of Experimental Observations

Sample	Comments
2-034 (acetonitrile extraction) 2-078 (acetonitrile extraction)	Very weak PEO peaks in spectra. C13 satellites not observed. **PEO peak intensities/quantities were similar in both solutions.**

F.5.3 Conclusions

- Small amounts of PEO (polyethylene oxide) may be present in surface films extracted from the anode samples. However, no increase in PEO content with cell (electrode) age was observed.
- The PEO peaks observed in the spectra could be an artifact of the extraction process, although acetonitrile addition to EC did not produce these peaks.

F.6 X-RAY PHOTOELECTRON SPECTROSCOPY EXAMINATION OF NEGATIVE ELECTRODE SAMPLES

Daniel Abraham

F.6.1 Experiments Conducted

X-ray photoelectron spectroscopy (XPS) experiments were conducted to determine aging-related changes in negative electrode samples from 18650 cells (see Table F-5). The XPS measurements were conducted on a PHI 5500 instrument using monochromatized AlK_{α} radiation. High-resolution C1s, O1s, F1s, P2p, and Li1s spectra were obtained with a pass energy of 23.5 eV. Depth profile data were obtained by Ar^+ ion sputtering (3 kV). Details of this work have been published in Electrochim. Acta, **49**, 5097 (2003).

Table F-5. Source of Negative Electrode Samples Studied by XPS

Sample Description	CF%[a]	PF%[b]
Fresh electrode laminate, no electrolyte contact	–	–
Formed cell, no 55°C aging	0	0
Cell aged 4 weeks at 55°C, 3.72 V	3.7	15.4
Cell aged 40 weeks at 55°C, 3.72 V	17.5	35

[a] C/1 capacity fade (CF).

[b] Power fade percentage.

F.6.2 Summary of Results

- Figure F-9 shows that the constitution of the SEI layer varies with cell aging.
    - EC- and EMC-reduction products are dominant in the SEI layer of anodes harvested from low-power-fade cells. $LiPF_6$ reaction products are dominant in the SEI layer of anodes harvested from high-power-fade cells.
    - Our data are consistent with the absence of lithium alkyl carbonates ($ROCO_2Li$) and Li_2CO_3 in the SEI layer. The dominant solvent reduction product appears to be a carboxylate-based compound.
    - Samples from the higher-capacity-fade cells showed larger quantities of LiF, Li_xPF_y, and $Li_xPF_yO_z$.

- Figure F-10 indicates that the relative thickness of the SEI layer is greater on samples from cells showing higher power fade.
- Rinsing appeared to be effective in removing electrolyte residue. The Li_xPF_y and carbonate species observed after rinsing are inherent to the SEI layer.
- Air exposure produces significant changes to the SEI layer, which underlines the importance of conducting the anode XPS studies without air or moisture exposure.

F.6.3 Conclusions

The SEI layer changes with aging do not affect cell impedance. However, cell capacity fade may be associated with the increasing SEI layer thickness by side reactions that consume cycleable lithium in the cell.

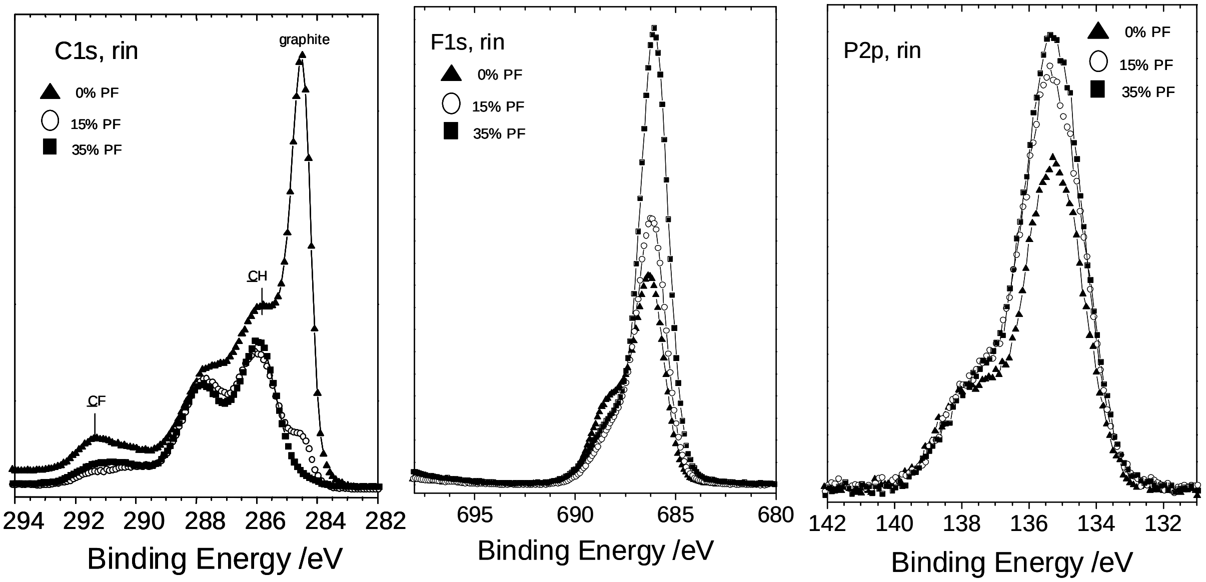

Fig. F-9. XPS Spectra from Harvested Electrodes That Were Immersed in DMC before Study.

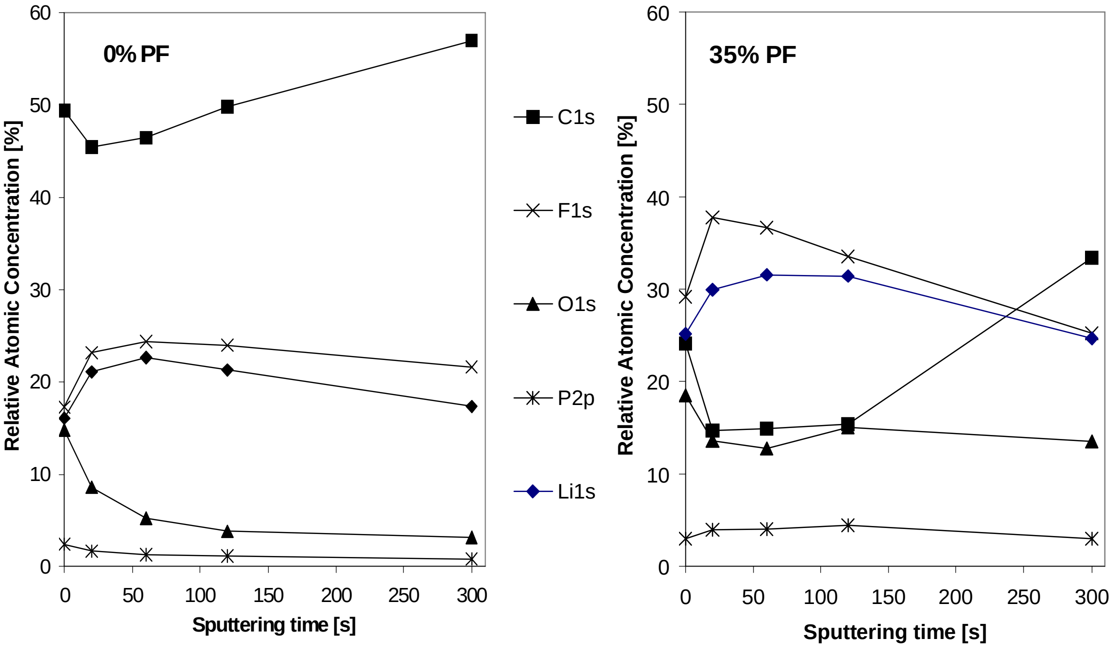

Fig. F-10. Relative Atomic Concentration for (a) Rinsed 0% PF and (b) Rinsed 35% PF Electrodes before and after Ar-Ion Sputtering for 20 s, 60 s, 120 s, and 240 s.

APPENDIX G. POSITIVE ELECTRODE STUDIES

G.1 SCANNING ELECTRON MICROSCOPY EXAMINATION OF POSITIVE ELECTRODE SAMPLES

Daniel Abraham and Scott MacLaren

G.1.1 Experiments Conducted

Micrographs of positive electrode samples were obtained with a Hitachi S-4700 scanning electron microscope (SEM) operating at 20 KeV; these samples saw brief (<1 min) air exposure during loading into the microscope. Images from the oxide power and fresh positive electrode samples, which had never been exposed to the electrolyte, were obtained for comparison.

G.1.2 Summary of Results

- The Gen 2 oxide comprised ~5- to 10-µm-size secondary particles, which were made of ~0.2- to 0.5-µm-size faceted primary particles.
- The Gen 2 fresh electrode micrographs showed oxide particles, graphite, and the acetylene black (Fig. G-1). The plate-like graphite was ~5–10 µm in size. The acetylene black was <100 nm, irregularly shaped with rounded edges and was continuous. The oxide particles were coated with a thin film, which was apparently the PVDF binder. In areas between the oxide and graphite particles, the binder showed a thin "chewing gum" type morphology.
- Micrographs of the 0% power fade Gen 2 sample (Fig. G-2a) were similar to those of the fresh electrodes, except for the presence of "surface films" on the oxide particles that may include electrolyte residue and the PVDF binder.
- Micrographs of the aged Gen 2 samples (Fig. G-2b) were mostly similar to those of the 0% power fade sample. In highly aged (~50% PF) samples, however, oxide particle debris was occasionally observed. We do not know whether these debris resulted from oxide particle fracture or were a result of the cell disassembly process; the separators from the high power-fade cells were "stickier" than those from cells that were not aged.
- Micrographs from the Variant C samples were also similar to those from the Gen 2 samples. Features that could obviously be correlated with power fade were not observed.

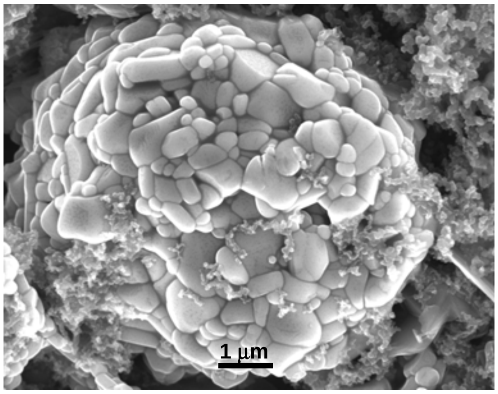

Fig. G-1. Image of a Fresh Gen 2 Electrode.

G.1.3 Conclusions

- Aging-related changes are not obviously apparent in the SEM micrographs.
- There is plenty of carbon adjacent to the oxide, even in highly aged electrodes.
- The binder morphology appeared unchanged by the cell aging process.
- Oxide particle debris was occasionally observed in highly aged samples.

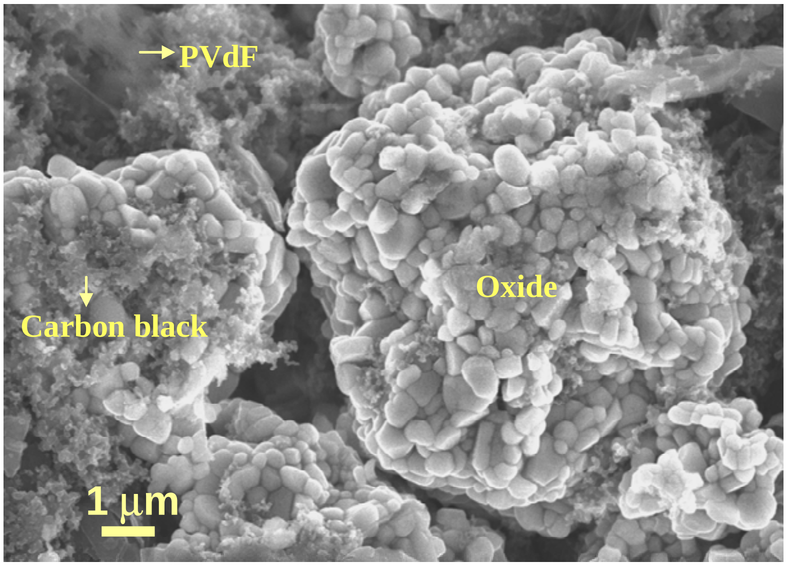

(a)

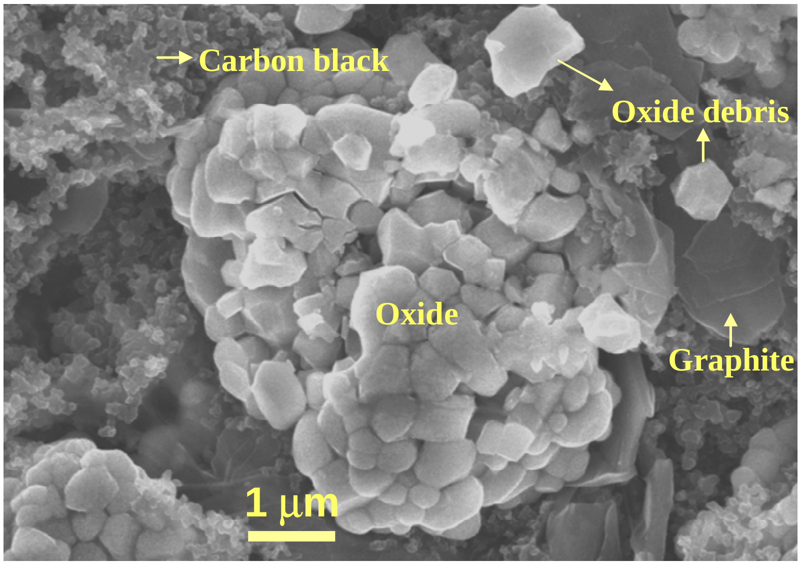

(b)

Fig. G-2. Electrode Images from (a) 0% and (b) 50.9% Power Fade Gen 2 Cells.

G.2 CRYSTAL STRUCTURE DETERMINATION BY X-RAY DIFFRACTION

Daniel Abraham, Mauro Sardela, and Ilias Belharouak

G.2.1 Experiments Conducted

X-ray diffraction (XRD) studies were conducted on positive electrode samples harvested from Gen 2 18650 cells (see Table G-1) to examine the effect of cell aging on electrode degradation. The data were obtained from air-exposed samples on a Philips X'pert diffractometer using CuK_α radiation for two-theta values from 10 to 80°. Control experiments were conducted on fresh electrode samples.

Table G-1. XRD Study Results

18650 Cell	Aging T, Period	Capacity Fade, %	Power Fade, %	$LiNi_{0.8}Co_{0.15}Al_{0.05}O_2$ Lattice Parameters, nm
Fresh	None	NA	NA	a= 0.2862, c= 1.4170
2-034[a]	0	0	0	a= 0.2858, c= 1.4210
2-014[a]	55°C, 20 weeks	9.6	24.1	a= 0.2862, c= 1.4228
2-017[a]	55°C, 32 weeks	14.0	27.4	a= 0.2858, c= 1.4263
2-009[a]	55°C, 40 weeks	18.3	32.3	a= 0.2855, c= 1.4274
2-078[b]	45°C, 68 weeks	29.6	48.4	a= 0.2858, c= 1.4218
2-026[b]	45°C, 88 weeks	34.4	50.9	a= 0.2857, c= 1.4224

[a] Cells were discharged to 3.1 V at C/1 rate before disassembly.

[b] Cells were discharged to 3.1 V at C/1 rate, followed by constant voltage hold at 3.1 V for 24 h before disassembly.

G.2.2 Summary of Results

The X-ray diffraction patterns for the various samples were very similar. Representative data are shown in Figure G-3. The following were observed in the data:

- The (003)/(104) peak area ratios for $LiNi_{0.8}Co_{0.15}Al_{0.05}O_2$ were similar for all samples studied, which indicates that no significant disorder was induced in the oxide bulk by cell aging.
- For electrodes from cells that were discharged to 3.1 V at a C/1 rate, the *c* dimension of the $LiNi_{0.8}Co_{0.15}Al_{0.05}O_2$ hexagonal unit cell increased with capacity fade, which indicated that the oxide lithium content was smaller for the higher-capacity-fade electrodes. However, electrodes from cells that were held at 3.1 V for 24 h showed a much smaller increase in the *c* dimension, which indicates that the apparent lithium loss is mostly a manifestation of electrode impedance.
- The C(002) graphite peak was similar for the various samples (see Fig. G-4) studied. Calculations showed that the graphite lattice parameters (and hence the structures) were not altered by cell aging.

G.2.3 Conclusions

The bulk crystal structures of the $LiNi_{0.8}Co_{0.15}Al_{0.05}O_2$ and the graphite in the positive electrode are little changed by cell aging.

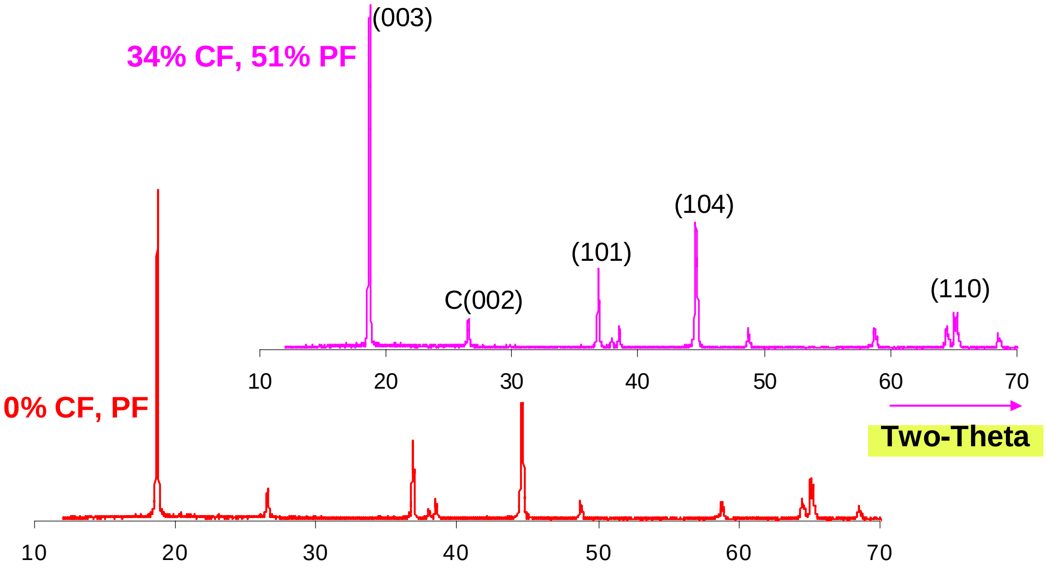

Fig. G-3. Representative X-ray Diffraction Data from Positive Electrode Samples Harvested from 18650 Cells 2-034 and 2-026.

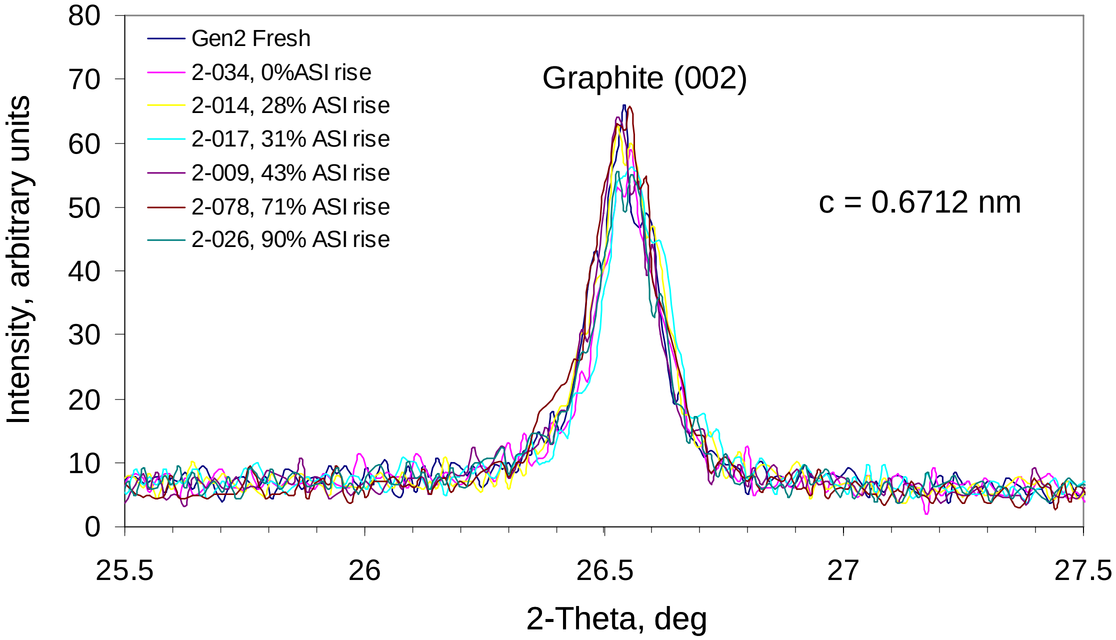

Fig. G-4. Graphite(002) Peak from the Various Positive Electrode Samples.

G.3 EX-SITU X-RAY DIFFRACTION OF POSITIVE ELECTRODE SAMPLES

Thomas Richardson

G.3.1 Crystal Chemistry

Cathodes harvested from Gen 2 cells with varying levels of power fade were examined. Analyses of the diffraction patterns provided information on active phase composition, impurities, and reaction production, state of charge (SOC), and crystallite sizes. Some evidence for bulk compositional changes comes from an examination of the lattice parameters of cycled cathodes. In stoichiometric $LiNi_{0.8}Co_{0.15}Al_{0.05}O_2$, both the a and c dimensions of the hexagonal unit cell vary approximately linearly with SOC. By determining the cell parameters in electrodes from cells that have been cycled for short times at 25°C, it is possible to obtain the SOC using either a or c. For high-power-fade cathodes that have been maintained at elevated temperatures, however, a different SOC is found using the a value vs. that calculated from the c value. A plot of c vs. a (Fig. G-5) shows the deviation from the expected linear relationship. This suggests that a small but significant change in composition or structure has taken place. No evidence was found in the pattern refinements for migration of transition metal ions into lithium sites. The shift of the c/a ratios is generally in the direction of increasing Co content for the dominant phase (no other phases were detected). This is consistent with segregation of nickel to form a reduced oxide species at the particle surfaces.

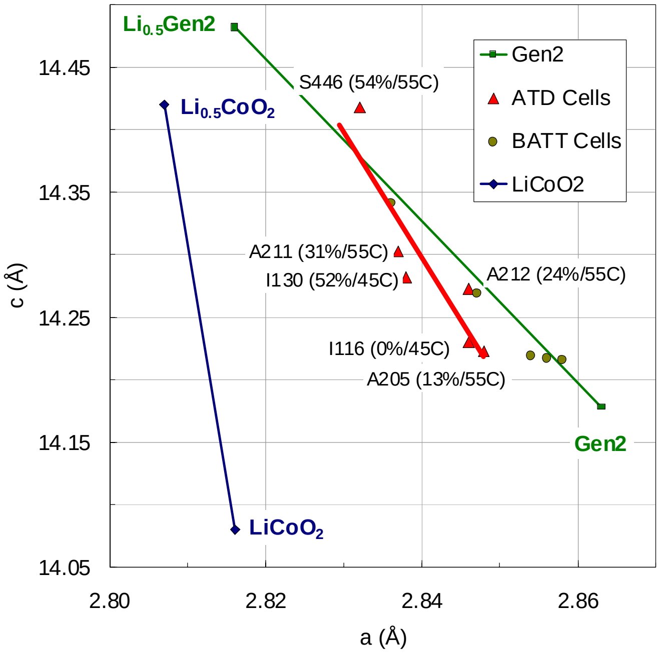

Fig. G-5. c vs. a in Cycled Gen 2 Cathodes. S446 was disassembled at 3.8 V; all other ATD cells were disassembled at 3.1 V.

G.3.1.1 Summary of Results

- No major impurity phases or degradation/decomposition products were found.
- There were small but significant changes in stoichiometry or structure after high-temperature cycling/storage.

G.3.2 Particle Isolation

Cathodes were polarized at 4.1 V until a certain amount of charge had been passed and then quickly removed and rinsed to remove the electrolyte. Particles isolated by poor electronic or ionic conduction paths are "frozen" in the state of charge that existed at the end of the test. High-resolution XRD patterns (Fig. G-6) show the presence of particles at very different states of charge after fast charging of cathodes harvested from high-power-fade cells. In this case, about one-third of the material did not participate in charging. The rest was at a nearly uniform SOC. This bimodal distribution of states of charge between well-connected and poorly connected particles in these cathodes is similar to, but less dramatic than, that in fresh cathodes exposed to air for long periods of time, during which a thick film of Li_2CO_3 forms on the particle surfaces.

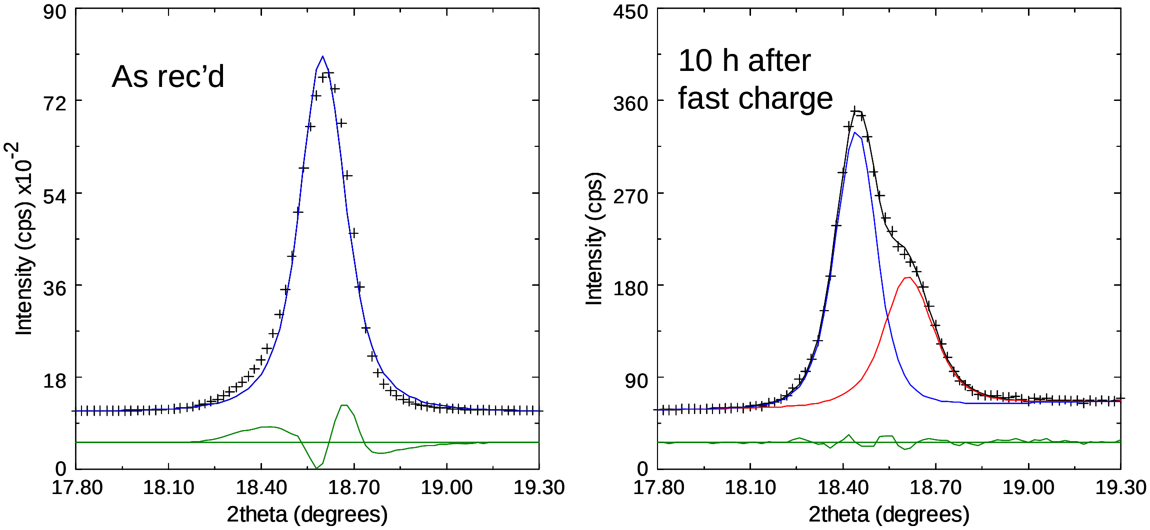

Fig. G-6. XRD of Fast-Charged I130 Gen 2 Cathode.

Some SOC distribution is found even in fresh, unexposed cathodes (Fig. G-7), but in this case, there is fairly rapid relaxation to a uniform SOC. This effect is attributed to redistribution of charge within large, agglomerated secondary particles, perhaps assisted by residual electrolyte within the pores of the agglomerates. Since the SOC of smaller, less agglomerated particles is nearly homogeneous at the end of the test, they do not exhibit this redistribution. The result is a broad XRD peak after relaxation due to the presence of particles with a range of SOC.

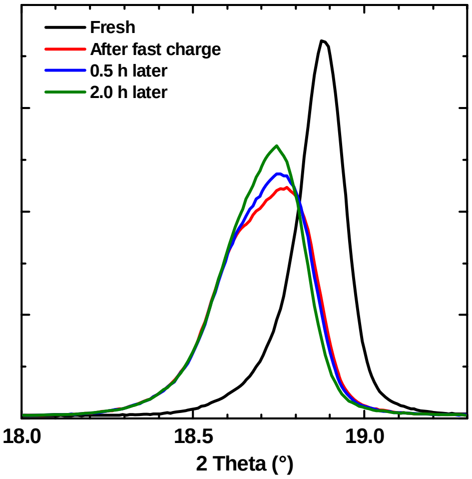

Fig. G-7. XRD of Fast-Charged Fresh Gen 2 Cathode.

G.3.2.1 Summary of Results

- Particle isolation exists in high-power-fade cathodes, not in fresh ones.
- Power fade may be due to the same mechanism that causes particle isolation. Significance of direct contribution of particle isolation to power fade is unclear.

G.4 IN-SITU X-RAY DIFFRACTION STUDIES OF POWER FADE OF GEN 2 CATHODE DURING CYCLING

Xing Qing Yang, Won-Sub Yoon, Mahalingam Balasubramanian, Kyung-Yoon Chung, and James McBreen

G.4.1 Experiments Conducted

In-situ X-ray diffraction (XRD) studies were carried out on the Gen 2 electrodes from LBNL and ANL. The following procedures were used for doing high-resolution XRD on samples from cycled and abused cells. Discs (1.8 cm diameter) were punched from the anodes and cathodes of disassembled cells. The active material was removed from one side of the current collector prior to assembly in the cell. The cell pack consisted of the anode, cathode, a fresh Celgard separator, and electrolyte. The cell was housed between two machined blocks of aluminum. The aluminum blocks were machined to provide X-ray windows and holes for bolts. The windows were sheets of 250-µm Mylar. A rubber gasket was used to make a hermetic seal. Provisions were made for current collection by using thin strips of copper and aluminum. In-situ XRD studies were done in the transmission mode at beamlines X7A and X18A at the National Synchrotron Light Source (NSLS). The XRD facilities at these two beamlines are suitable for collecting data at fast rates with high resolution. This is due to the use of a position-sensitive detector (PSD) developed at BNL.

During data collection in the transmission mode, the X-ray beam has to pass through the cathode and the 15-µm Cu foil anode current collector. Co, Ni, and Cu are adjacent first-row transition metals with their respective K absorption edges at 7,709, 8,333, and 8,979 eV. To minimize absorption, the X-rays should have an energy that is either below the Co K edge or a higher energy beyond the Cu K edge, where the absorption is equally low. The X-ray absorption by the cathode is almost identical at 7.5 and 17 keV. At beamline X7A, the beam energy is 17.7 keV, and at X18A, it is 10.375 keV.

Figure G-8 shows a typical XRD pattern for a spectroelectrochemical cell assembled with electrodes harvested from a fresh Gen 2 cathode during first charge. The pattern was recorded at beamline X7A during the first charge up to 5.2 V at the C/9 rate with the scan numbers marked in it. Scan 19 was recorded at resting after cutting off the charge current. Figure G-9 is the exploded plot of Fig. G-8 in the 2θ angle range near the (003) reflection. The phase transitions from H1 to H2 and finally to H3 were clearly observed from the position change of the (003) reflection. It can be seen that the structural changes closely track the charge curve. However, the structural changes have quite different behavior after significant power fading during cycling. This can be seen in Figure G-10, where the same (003) reflection region of the in situ XRD data collected on ANL G-2 cathode with 50% power fade during charge up to 4.1 V are plotted. It is interesting to see that at the 4.1 V current cutoff (indicated by the red curve), the cathode was at the H1 and H2 two-phase coexistent region, rather than at the H2 phase region, as in the fresh cell. During resting, it gradually moved to the H2 single-phase region but still has some residue of H1 structure. This indicates the power fade is mainly a loss of dynamic response due to the increase of impedance. Therefore, even the cathode still has some unused capacity if charged or discharged at very slow rate; this capacity cannot be utilized at a high rate.

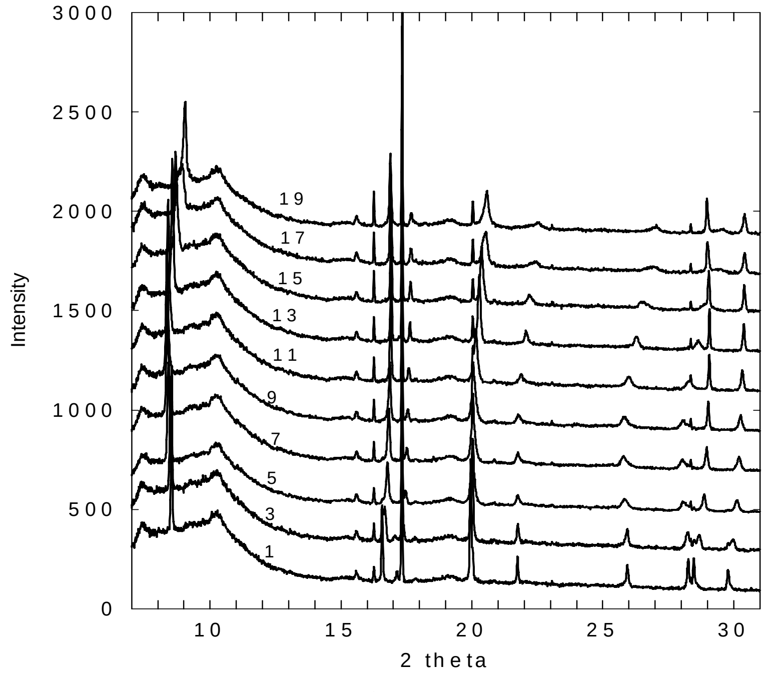

Fig. G-8. In Situ XRD Spectra for a Fresh G-2 Cathode during First Charge at C/9 Rate from 3 V to 5.2 V. The 19th scan was collected at rest after the 5.2 V limit was reached and the charge current was cut off.

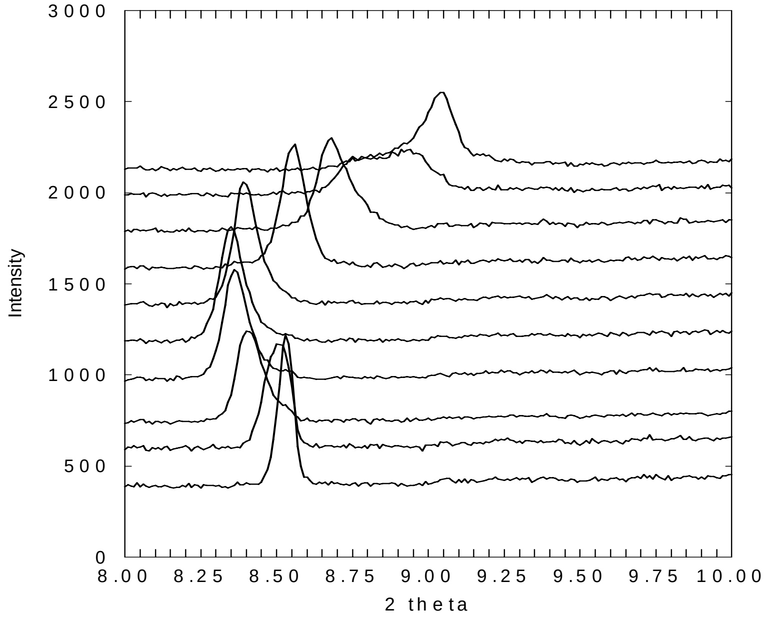

Fig. G-9. In Situ XRD Spectra near (003) Region for a Fresh G-2 Cathode during First Charge at C/9 Rate from 3 V to 5.2 V. The last scan is scan 19, which was collected at rest after the 5.2 V limit was reached and the charge current was cut off. Data were collected at X-7a with a wavelength of λ=0.8 Å.

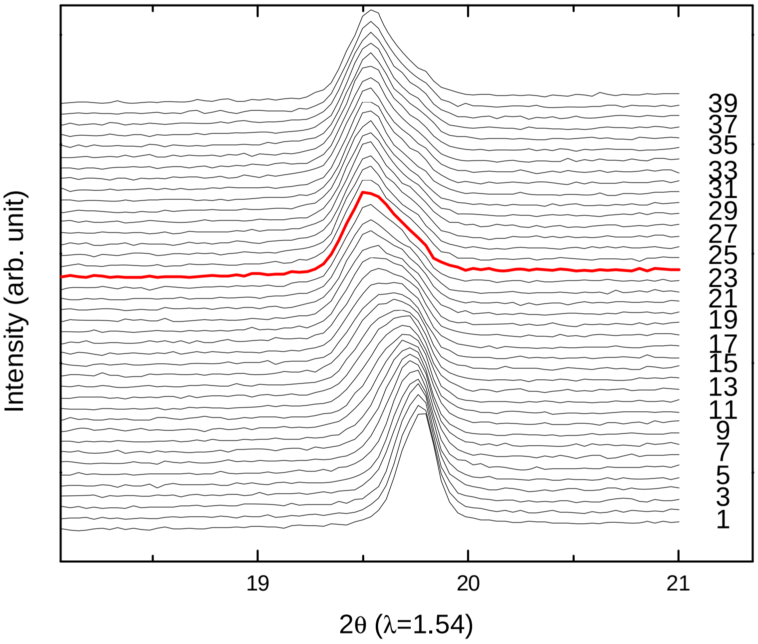

Fig. G-10. XRD Patterns near (003) Reflection Region of G-2 Cathode (ANL) with >51% Power Fade during Charge from 3.5 V to 4.1 V. Data were collected at X7b at the NSLS. The 2θ angles were converted to the wavelength corresponding to CuK_α for easy comparison.

Publications and Invited Presentations on Related Subjects, Section G.4

Balasubramanian, M., X. Sun, X. Q. Yang, and J. McBreen, "In Situ X-ray Diffraction and X-ray Absorption Studies of High-Rate Lithium-Ion Batteries," J. Power Sources **92**, 1–8 (2000).

Balasubramanian, M., X. Sun, X. Q. Yang, and J. McBreen, "Studies of High-Rate Lithium Batteries Using Synchrotron Techniques," Electrochemical Society Proceedings **2000–21**, 533 (2000).

McBreen, J., M. Balasubramanian, X. Q. Yang, and X. Sun, "Synchrotron X-ray Studies of Lithium-Ion Battery Materials," invited talk, presented at the 11th International Meeting on Lithium Batteries, June 23–28, 2002, Monterey, California.

G.5 ELECTRON MICROSCOPY OF POSITIVE ELECTRODE SAMPLES AT LAWRENCE BERKELEY NATIONAL LABORATORY

Thomas Richardson

Transmission electron microscopy (TEM) and scanning electron microscopy (SEM) were used to examine electrodes taken from Gen 2 cells, using energy dispersive X-ray analysis (EDX) for quantitative elemental analysis in combination with both techniques. Most of this work was carried out on electrodes from cells with the highest power fade. Fracturing of larger oxide particles into smaller ones with the same composition was observed in some cathodes (Fig. G-11). The crystallinity of all oxide particles was degraded relative to that in fresh electrodes. Elemental analysis and line profiles by EDX showed small variations in metal content in fresh electrodes, and greater variations after cycling. This technique is most sensitive to surface composition, especially for lighter elements such as oxygen. Significant decreases in total oxygen, O/Ni ratios, and Co/Ni ratios were found in high-power-fade cathodes, with a fairly strong correlation between oxygen loss and power fade (Fig. G-12). Phosphorus was detected in measurable amounts on oxide particles, but not on carbon particles in cathodes. Small amounts of iron and magnesium were also found, presumably originating from the aluminum current collector. Evidence for corrosion of cathode active material was found in the presence of small amounts of Ni and Co on anodes.

Very thin layers were sometimes seen on oxide particle surfaces in TEM images (Fig. G-13). The thickness and composition were quite variable. In many cases, they were not continuous or conformal. Some were identified as lithium carbonate, while others contain mainly nickel oxide, with small amounts of phosphorus and fluorine.

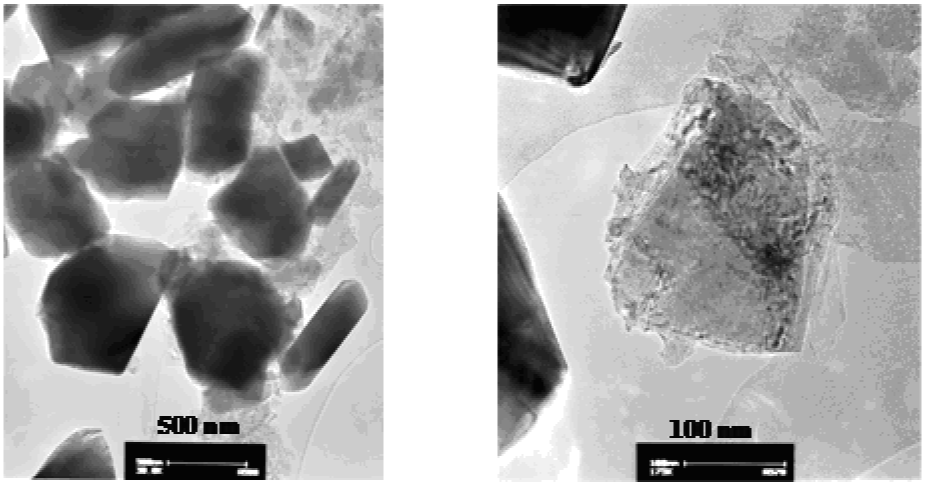

Fig. G-11. Small Particle Debris Is $LiNi_{0.8}Co_{0.15}Al_{0.05}O_2$, Fractured and Poorly Crystalline.

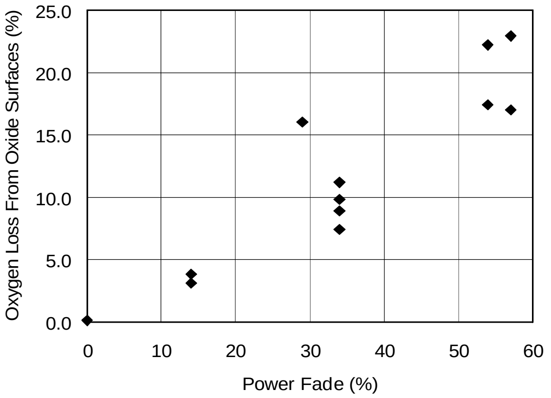

Fig. G-12. Correlation of Oxygen Loss from Cathode Surfaces.

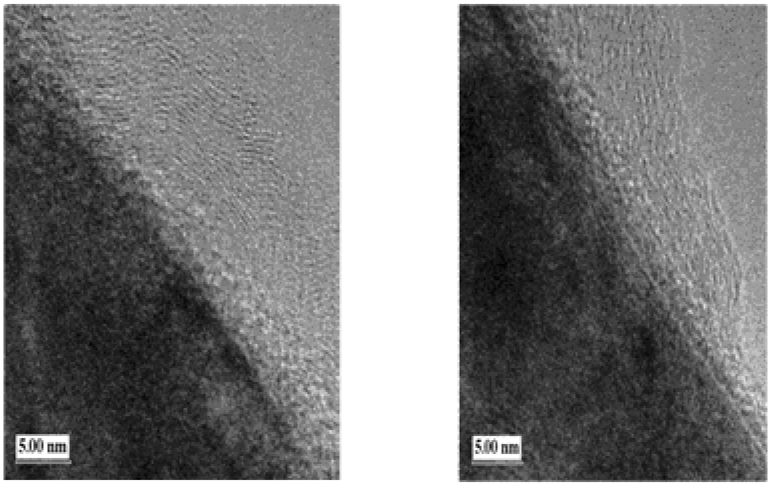

Fig. G-13. Thin, Nonuniform Layers on Oxide Particles Contain Some P and F.

G.5.1 Summary of Results

- Active material in fresh cathodes has a uniform composition, consistent with that of the fresh powder from which they were prepared.
- Metal-metal and metal-oxygen ratios change with cell power fade.
- A much greater scatter in compositions among particles is found in electrodes from cells with high power fade.
- There was a slight enrichment of Ni and a decrease in oxygen content in cycled electrodes.
- Phosphorus accumulates on oxide particles (but not on carbon).
- A thin (~5 nm) irregular SEI was detected via TEM.
- Some contamination (Fe, Mg) detected in cathodes from cells with high power fade (source is probably current-collector corrosion).

G.6 ELECTRON MICROSCOPY OF POSITIVE ELECTRODE SAMPLES AT ARGONNE NATIONAL LABORATORY

Daniel Abraham and Ray Twesten

G.6.1 Experiments Conducted

Transmission electron microscopy (TEM) studies on several positive electrode samples (Table G-2) were carried out with a JEOL 2010F operating at 200 kV. Compositional analyses of particles were conducted with an energy dispersive spectrometer equipped with a Oxford INCA thin-window Si(Li) detector and with a Gatan Image Filter (GIF) 2001 that filtered both images and diffraction patterns and served as an electron energy-loss spectrometer. TEM samples were prepared using a variety of techniques, which included binder removal and oxide particle dispersion, Ar-ion thinning, and focused ion beam milling; details of the sample preparation and analysis techniques are discussed in the referenced articles.

Table G-2. Characteristics of 18650 Cells Studied

Cell ID	Aging T, Period, Test Type, SOC	Capacity Fade, %	Power Fade, %
2-034	0	0	0
2-021	55°C, 36 weeks, calendar, 60% SOC	17.5	35
2-078	45°C, 68 weeks, cycle, 60% SOC	29.6	48.4
SNL325	45°C, 40 weeks, calendar, 80% SOC	31	51.3
SNL321[a]	55°C, 20 weeks, calendar, 80% SOC	32	54

[a] Cell was disassembled at 3.9 V (or 80% SOC).

G.6.2 Summary of Results

- Structural differences (Figs. G-14 and G-15) were observed between the surface and bulk of the $LiNi_{0.8}Co_{0.15}Al_{0.05}O_2$ primary particles. The particle bulk has the expected ordered R-3m structure, whereas the particle surface has the Fm-3m structure. Elemental analysis data indicated that the particle surfaces had higher Ni:O and Co:O ratios than the bulk, which apparently results from oxygen loss at the particle surface.

- The thickness of the oxide particle surface layer ranged from 0 to 15 nm in the 0% PF samples; particles from aged electrodes showed thicknesses from ~5 to 20 nm. Our data suggest that more oxide particles in the highly aged samples display this surface layer compared with those in the 0% PF samples.
- Oxygen loss was observed in oxide particles from Gen 2 fresh samples subjected to high electron current densities, which suggests that the particles can lose oxygen under appropriate conditions. The Ni EELS spectra remained unchanged during the experiment.
- P enrichment was observed at the oxide primary particle grain boundaries (see Fig. G-16). This enrichment was observed in samples from both the 0% PF and the aged cells.
- Surface films were observed on oxide particles that were in contact with the electrolyte (see Fig. G-17). These films may include the electrolyte residue and binder, in addition to the inorganic and organic species that are known to form on these electrodes. In general, the surface films were nonuniform and varied widely in thickness.
- Samples from highly aged cells showed increased separation of the primary particles relative to samples from 0% PF cells (see Fig. G-18).
- Oxide particle damage was occasionally observed in samples from high-power-fade cells (see Fig. G-19).

G.6.3 Conclusions

- Under appropriate conditions, a $LiNi_{0.8}Co_{0.15}Al_{0.05}O_2$ particle can lose oxygen from its surface, creating a $Li_xNi_{1-x}O$ surface layer that has a lower Li ion conductivity (higher impedance) than the particle bulk.
- Cell aging appears to induce subtle but significant changes at the interfaces between primary particles. Increased primary particle separation may result from the weakening of these interfaces by an electrolyte-induced corrosion process.
- Extended defects such as dislocations, stacking faults, and twin faults were rarely observed in oxide particles, even from highly aged cells. Except for samples from cells that showed very rapid aging, the oxide particles appeared free of obvious defects such as particle fractures.

Publications on Related Subjects, Section G.6

Abraham, D. P., R. D. Twesten, M. Balasubramanian, I. Petrov, J. McBreen, and K. Amine, Electrochem. Comm. **4**, 620–625 (2002).

Abraham, D. P., R. D. Twesten, M. Balasubramanian, J. Kropf, D. Fischer, J. McBreen, I. Petrov, and K. Amine, J. Electrochem. Soc. **150**, A1450–A1456 (2003).

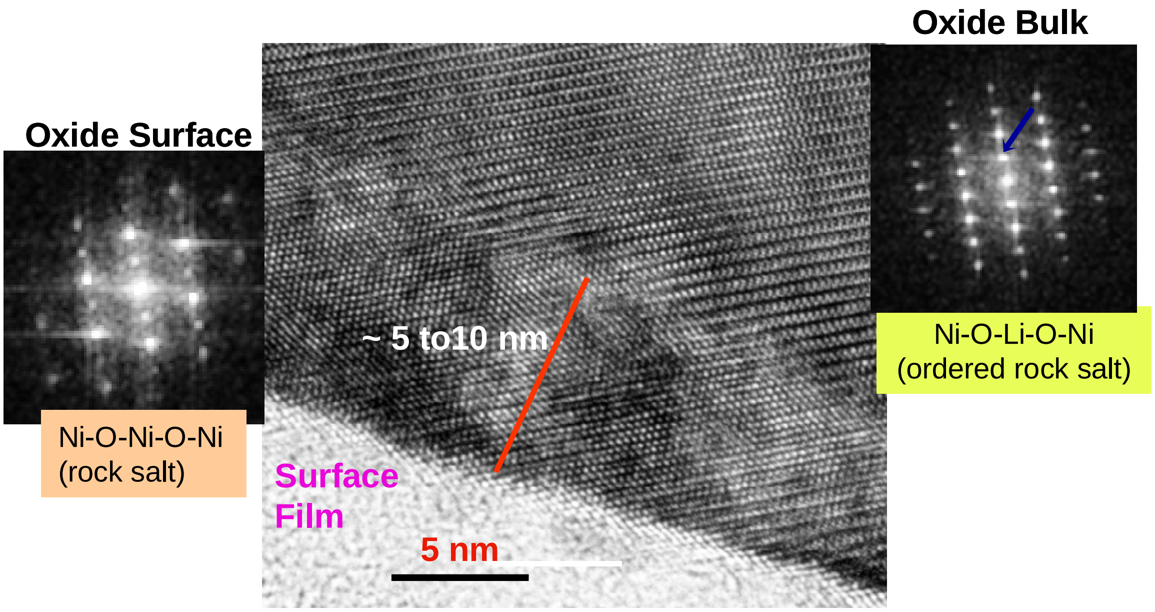

Fig. G-14. High-Resolution TEM Image and Fast Fourier Transform Patterns Showing Structural Differences between the Surface and Bulk of $LiNi_{0.8}Co_{0.15}Al_{0.05}O_2$ Primary Particles.

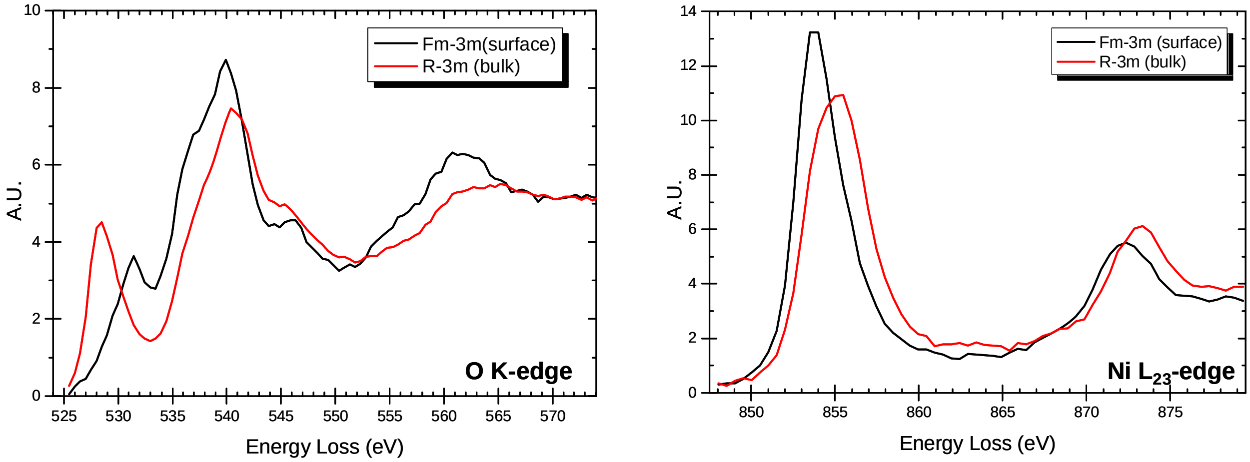

Fig. G-15. EELS Data Showing Differences between the Surface and Bulk of $LiNi_{0.8}Co_{0.15}Al_{0.05}O_2$ Primary Particles.

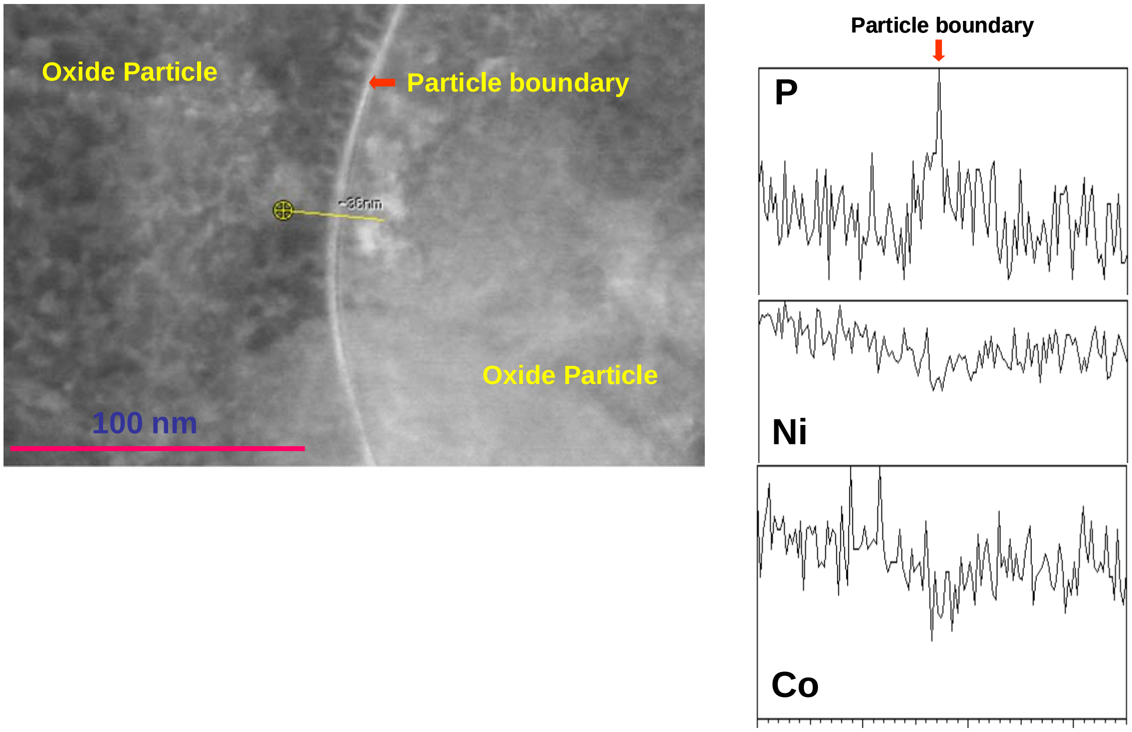

Fig. G-16. Phosphorous Enrichment at the Boundaries between $LiNi_{0.8}Co_{0.15}Al_{0.05}O_2$ Primary Particles.

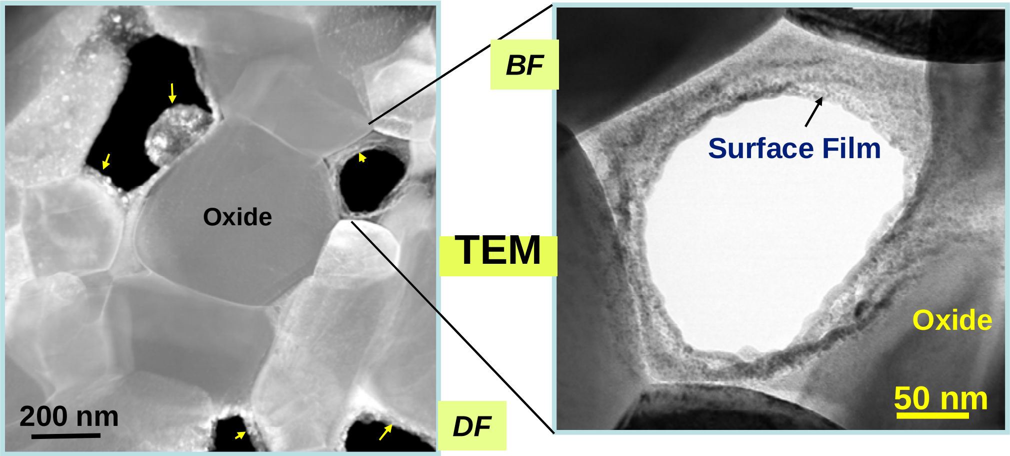

Fig. G-17. Surface Films Observed in the Pores between $LiNi_{0.8}Co_{0.15}Al_{0.05}O_2$ Primary Particles from an “as Harvested” Electrode. These films may also include the electrolyte residue.

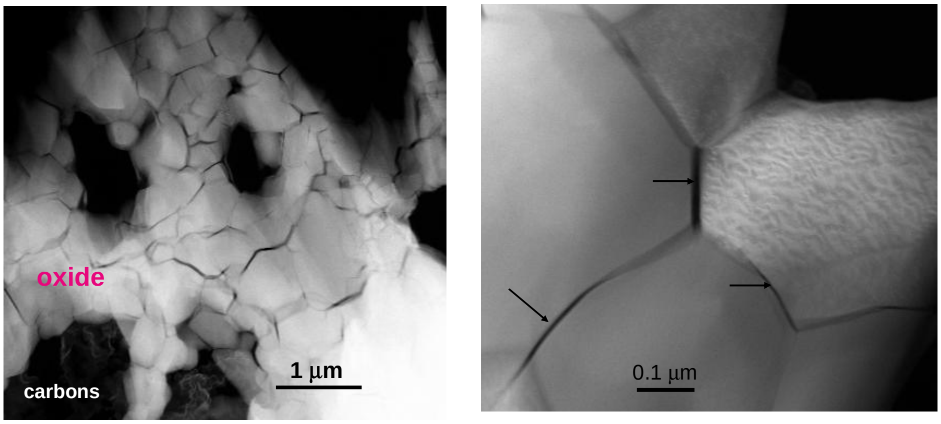

Fig. G-18. Primary Particle Separation Observed in Samples from High-Power-Fade Cells.

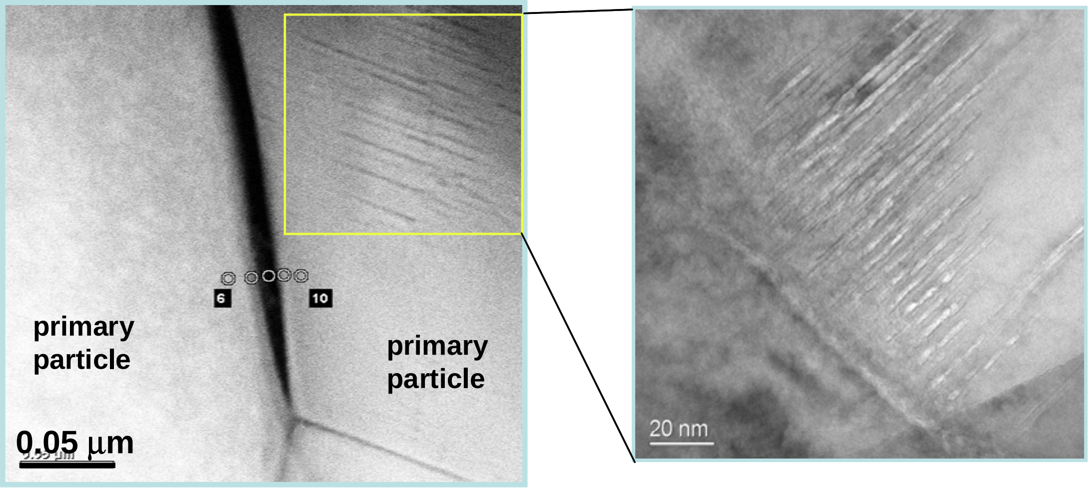

Fig. G-19. Defects/Damage Observed in Primary Particles from High-Power-Fade Cells.

G.7 STUDY OF CATHODE DEGRADATION IN GEN 2 HIGH-POWER LITHIUM-ION CELLS

Robert Kostecki, Jinglei Lei, Kathryn McCarthy, and Frank McLarnon

The Gen 2 high-power Li-ion cells included a composite cathode that consists of 84 wt% $LiNi_{0.8}Co_{0.15}Al_{0.05}O_2$, 4 wt% acetylene black, 4 wt% SFG-6 graphite, and 4wt% PVDF binder. In this study, we carried out a comparative study of cathodes removed from control cells that underwent only formation cycles at room temperature (control cathodes) with cathodes of cells that were aged at 55°C for up to 68 weeks, losing up to 52% of their initial power (aged cells). The cathodes of these cells were compared with fresh samples of Gen 2 composite cathode.

G.7.1 Raman Spectroscopy and Microscopy Measurements of Fresh/Aged Cathodes

G.7.1.1 Experiments Conducted

All cathodes were soaked in dimethyl carbonate (DMC) for 30 minutes after removal from Li-ion cells inside an argon-filled glove box. This procedure removed electrolyte salt from the electrode to prevent its reaction with air and moisture. The Raman excitation source was a He-Ne (632-nm) 10-mW laser. The power of the laser beam was adjusted to 0.1 mW. The size of the laser beam at the sample was ~1.2 µm, which was one order of magnitude smaller than the size of an average $LiNi_{0.8}Co_{0.15}Al_{0.05}O_2$ particle.

A semi-quantitative analysis of the cathode surface composition was carried out by deconvoluting thousands of Raman spectra, which were collected systematically from 52 × 75 µm sections of cathode surfaces at 0.7 µm resolution into three electrode components. The Raman spectra of the fresh cathodes is dominated by two groups of bands: a broad maximum centered at ~510 cm^{-1}, characteristic for $LiNi_{0.8}Co_{0.15}Al_{0.05}O_2$ oxide, and two peaks at ~1,350 and ~1,600 cm^{-1}, which correspond to the D and G bands of elemental carbon, respectively. These three major bands were integrated for each spectrum that was recorded at a given location on the cathode surface and expressed by red, blue, and green colors (trace [c] in Fig. G-20). The saturation of each color is proportional to the integrated area under the respective Raman band for each location on the cathode surface. Thus, the resultant color corresponds to the local surface concentration of the $LiNi_{0.8}Co_{0.15}Al_{0.05}O_2$ active material (red), acetylene black (bright blue), and graphite (green) (Fig. G-21).

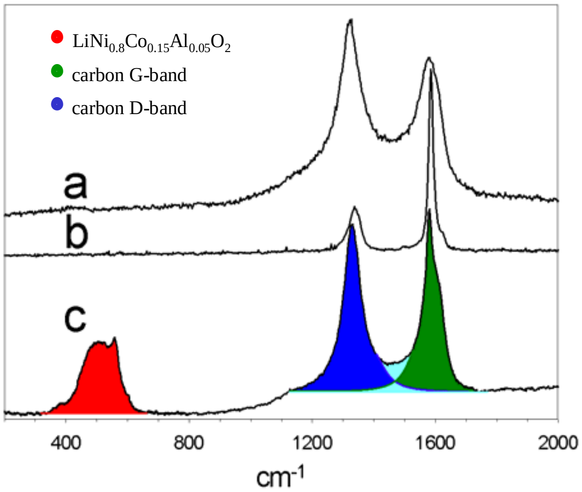

Fig. G-20. Typical Raman Microscope Spectra of the Fresh Composite $LiNi_{0.8}Co_{0.15}Al_{0.05}O_2$ Cathode Recorded at Different Surface Locations. Spectra (a), (b), and (c) correspond to surface regions dominated by acetylene black, graphite, and oxide, respectively. The color-coding analysis scheme is illustrated by spectrum (c).

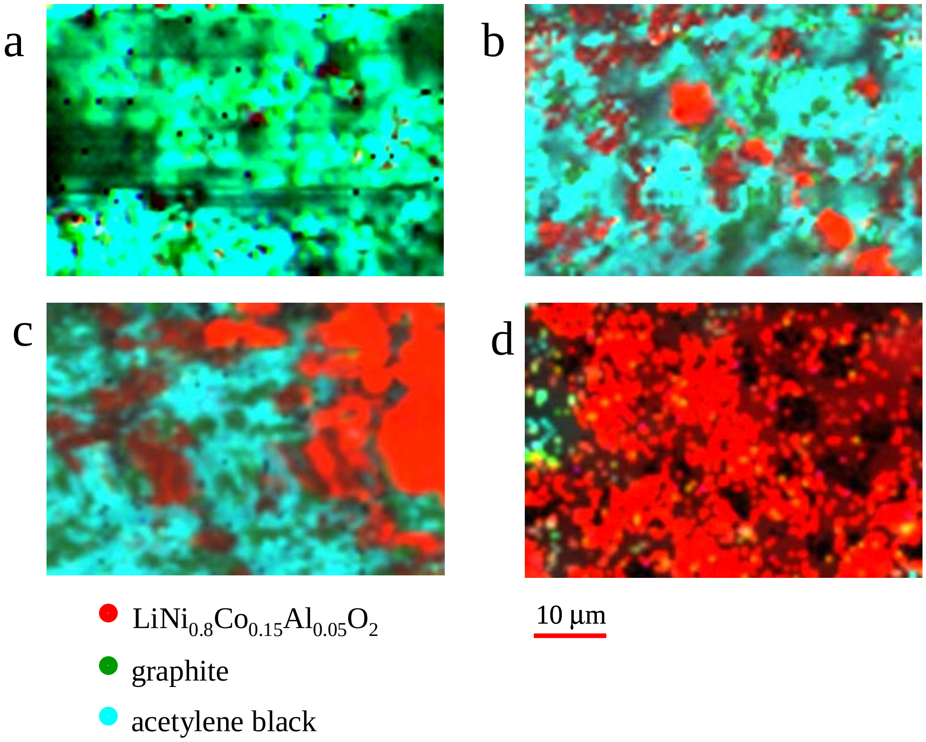

Fig. G-21. 52 × 75 µm Raman Microscope Images of the Composite $LiNi_{0.8}Co_{0.15}Al_{0.05}O_2$ Cathodes. The images consist of Raman spectra collected at 0.7 µm resolution. The intensity of red, blue, and green color corresponds to the integrated band intensity of $LiNi_{0.8}Co_{0.15}Al_{0.05}O_2$, and D and G carbon bands of each spectrum, respectively for (a) fresh cathode and (b), (c), and (d) cathodes from cells that lost 10, 34, and 52% of power, respectively.

G.7.1.2 Results

- The Raman composition maps clearly indicate that the fresh cathode surface is almost fully coated by acetylene black and graphite.
- Cathode surface composition changed significantly in tested cells, which display much higher oxide/carbon surface concentration ratios (Fig. G-22)
- Raman microscopy shows that the extent of carbon retreat correlates with power fade.
- Raman spectra display the presence of lithium fluorophosphates, which originated from the thermal decomposition of the $LiPF_6$ salt in the electrolyte (see Appendix D).
- The cathode surface SOC varies between individual grains of active material from (a) fully discharged through (b) partially charged to (c) fully charged, even though the cell was fully discharged at the end of cell testing (Fig. G-23).
- In situ spectral monitoring of the SOC of selected oxide particles in a composite cathode harvested from a tested cell revealed that the rate at which particles deintercalate-interalate Li ions changes with time and location.

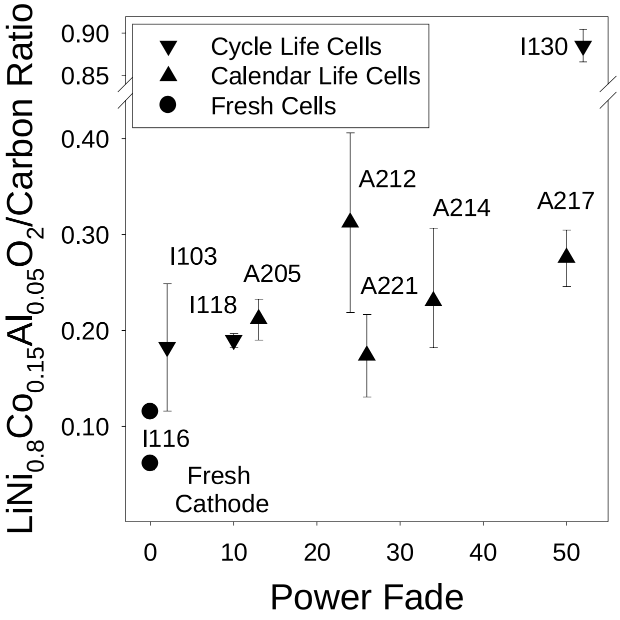

Fig.G-22. Average Ratio of Surface Concentration of $LiNi_{0.8}Co_{0.15}Al_{0.05}O_2$ Active Material to Carbon Additive Calculated from the Raman Microscopy Images of Composite Cathodes Removed from Gen 2 Cells.

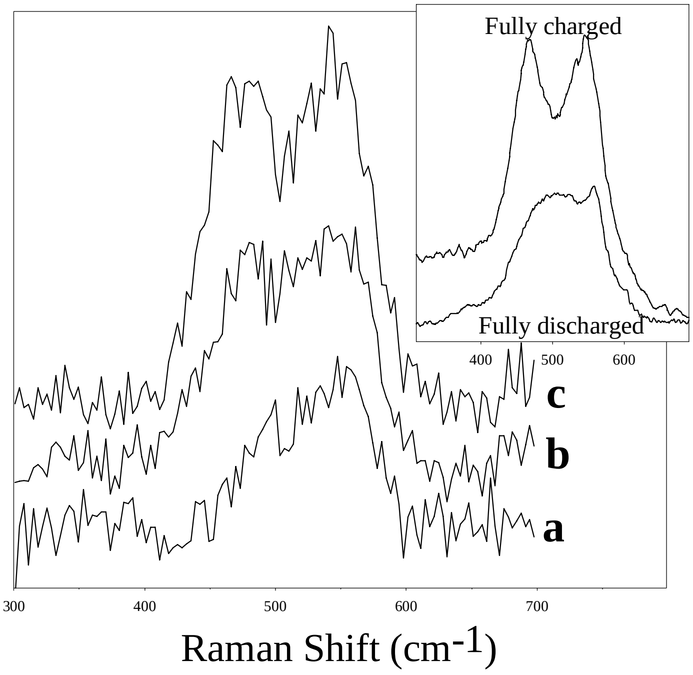

Fig. G-23. Raman Microscope Spectra of Three Individual $LiNi_{0.8}Co_{0.15}Al_{0.05}O_2$ Particles in the I130 (52% Power Loss) Tested Cathode. The band at 510 cm^{-1} consists of two Raman active vibrations characteristic for $LiNi_{0.8}Co_{0.15}Al_{0.05}O_2$ oxide. The insert shows Raman spectra of fully charged and fully discharged $Li_xNi_{0.8}Co_{0.15}Al_{0.05}O_2$.

G.7.1.3 Conclusions

- The Raman microscopy data provide evidence for carbon retreat (or redistribution) from the cathode surface, a phenomenon that has escaped detection in prior diagnostic studies of Li-ion cells.
- Nonuniform performance at the micro-scale of the $LiNi_{0.8}Co_{0.15}Al_{0.05}O_2$ particles in composite cathodes is one of the key signatures of degradation. The nonuniform charge-discharge rate directly implies that the electrode local current distribution is also highly nonhomogeneous.

- Carbon additive retreat or rearrangement in portions of the tested $LiNi_{0.8}Co_{0.15}Al_{0.05}O_2$ cathodes is closely linked with reduction in local electronic conductance (see Sec. G.7.2) and is mainly responsible for the observed isolation of oxide active material.

G.7.2 Scanning Electron Microscopy (SEM) and Atomic Force Microscopy (AFM) Studies of Surface Morphology of Fresh/Aged Cathodes

G.7.2.1 Experiments Conducted

All cathodes were soaked in dimethyl carbonate (DMC) for 30 minutes after removal from Li-ion cells inside an argon-filled glove box. This procedure removed electrolyte salt from the electrode to prevent its reaction with air and moisture. Prior to SEM measurements, all samples were rinsed in EMC in order to remove dust or other contaminants.

Current-sensing atomic force microscopy (CSAFM) was used to test and image the electronic conductivity of Gen 2 composite cathodes and individual grains of $LiNi_{0.8}Co_{0.15}Al_{0.05}O_2$ powder (Fuji Chemical). The powder was pressed into a gold foil to produce randomly scattered particles of $LiNi_{0.8}Co_{0.15}Al_{0.05}O_2$ in good electronic contact with the Au substrate. The Si atomic force microscope (AFM) tips were coated with a thin conductive layer of W_2C. All CSAFM experiments were performed in the constant-force mode with a controlled oxide-tip voltage difference under a controlled dry N_2 atmosphere. A single scan of the tip over the sample surface simultaneously produced two images: a topographic image and a conductance image; the latter represents Au/$LiNi_{0.8}Co_{0.15}Al_{0.05}O_2$-tip current variations during scanning at a given sample-tip voltage difference.

G.7.2.2 Summary of Results

- SEM images appear to confirm micro-Raman observations, but cannot resolve cathode surface composition (Fig. G-24).
- The surface conductance image of the cathode from a fresh cell exhibits areas of mostly high electronic conductance, due to the presence of highly conductive graphite and acetylene black (Fig. G-25).
- The conductance images of cathodes tested at elevated temperatures show a dramatic increase of surface resistance.
- The conductance image of pristine 10- to 20-μm agglomerates of $LiNi_{0.8}Co_{0.15}Al_{0.05}O_2$ embedded into a gold foil revealed that the agglomerate crystallites were not uniformly conductive (Fig. G-26).
- The intergranular electronic contact within agglomerates deteriorates even further during cell cycling/aging. Secondary particle decrepitation upon cycling/ageing is observed.

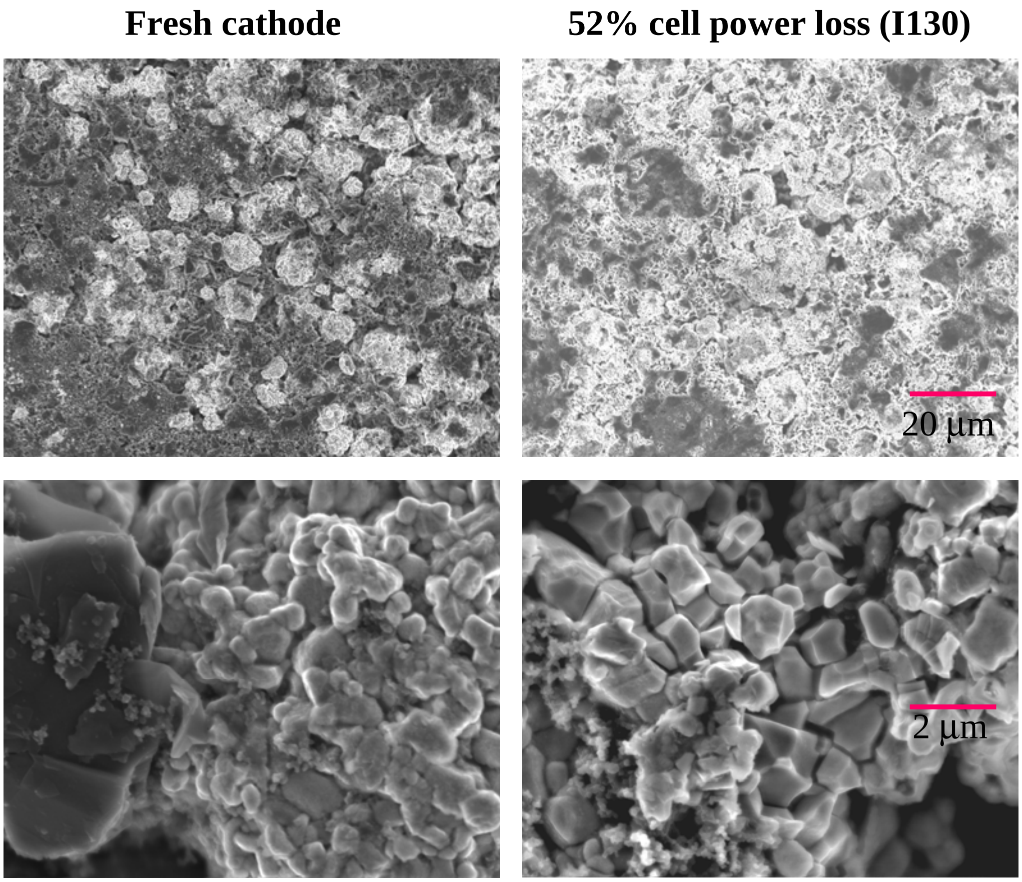
Fresh cathode

52% cell power loss (I130)

Fig.G-24. SEM Images of Separators Extracted from (a) Fresh Cell and (b) Cell Stored at 45°C for 68 Weeks.

G.7.2.3 Conclusions

- Partial or complete loss of electronic contact between primary particles of $LiNi_{0.8}Co_{0.15}Al_{0.05}O_2$ is most likely the origin of the observed electrode impedance increase and nonuniform electrochemical performance of the active material at the micro-scale.
- The observed carbon retreat (or redistribution) at the cathode surfaces of tested cells can “expose” crystallites that are in poor electronic contact with their neighbors. The consequent loss of a direct electronic path through the receding carbon matrix will lead to an increased resistance within the agglomerate and, eventually, total isolation of some particles.
- The combination of carbon retreat (or rearrangement) and the electronic properties of the $LiNi_{0.8}Co_{0.15}Al_{0.05}O_2$ agglomerates is responsible for the observed cell power and capacity fade.

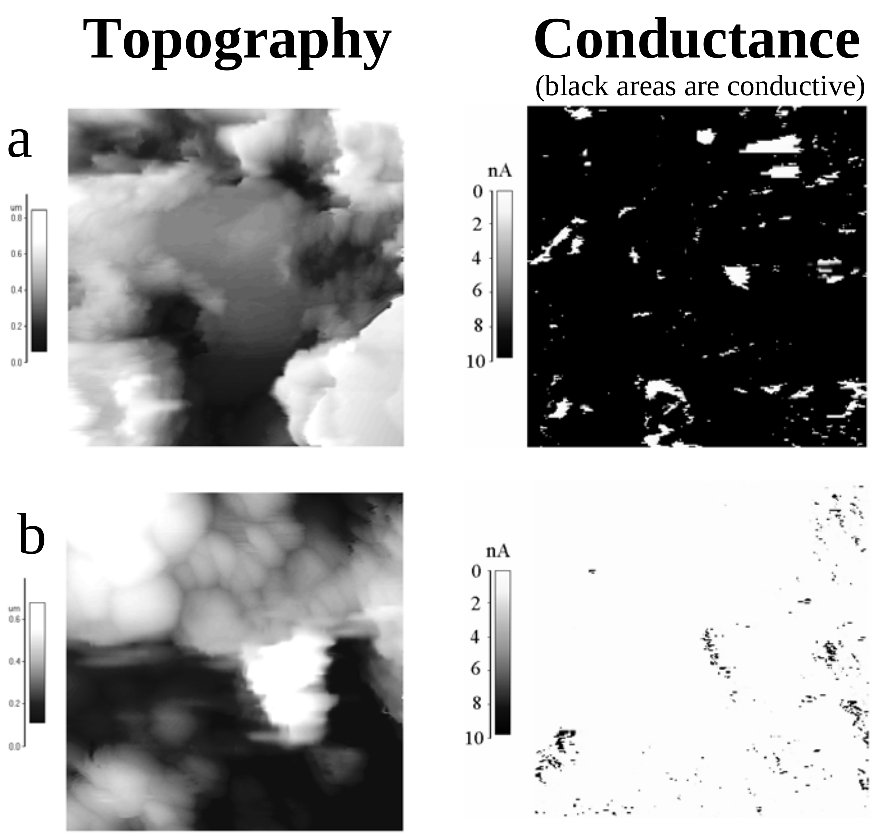

Fig. G-25. CSAFM Images of Surface Conductance (right panel) and Topography (left panel) of a 5 × 5 μm Region of the Composite $LiNi_{0.8}Co_{0.15}Al_{0.05}O_2$ Cathode Surface at 1.0 V Tip-Sample Voltage Difference: (a) Virgin Cell; (b) Cathode from the Cell that Lost 34% of Power (A214).

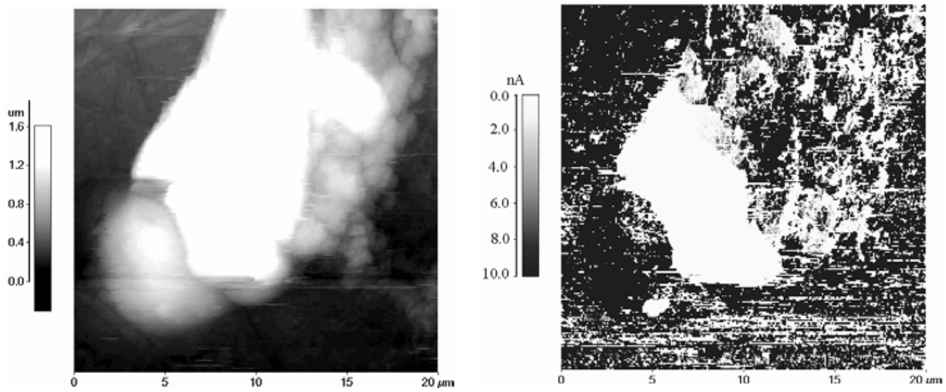

Fig. G-26. 20 × 20 μm CSAFM Images of Surface Conductance and Topography of a Single Particle of $LiNi_{0.8}Co_{0.15}Al_{0.05}O_2$ Embedded into a Au Foil at 1.0 V Tip-Sample Voltage Difference.

Publications on Related Subjects, Section G.7

Lei, J., F. McLarnon, and R. Kostecki, "In-situ Raman Microscopy of Individual $LiNi_{0.8}Co_{0.15}Al_{0.05}O_2$ Particles in the Li-Ion Battery Composite Cathode," J. Phys. Chem. B **109**(2), 952–957 (2005).

Kostecki, R., and F. McLarnon, "Local-Probe Studies of Degradation of Composite $LiNi_{0.8}Co_{0.15}Al_{0.05}O_2$ Cathodes in High-Power Lithium-Ion Cells," Electrochem. Solid-State Lett. **7**, A380 (2004).

Striebel, K. A., J. Shim, E. J. Cairns, R. Kostecki, Y.-J. Lee, J. Reimer, T. J. Richardson, P. N. Ross, X. Song, and G. V. Zhuang, "Diagnostic Analysis of Electrodes from High-Power Lithium-Ion Cells Cycled under Different Conditions," J. Electrochem. Soc. **151**, A857 (2004).

Shim, J., R. Kostecki, T. Richardson, X. Song, and K. A. Striebel, "Electrochemical and Physical Analysis of a Li-Ion Cell Cycled at Elevated Temperature," J. Power Sources **112**, 222 (2002).

Kostecki, R., and F. McLarnon, "Degradation of $LiNi_{0.8}Co_{0.2}O_2$ Cathode Surfaces in High-Power Lithium-Ion Batteries," Electrochem. Solid-State Lett. **5**, A164 (2002).

Zhang, X., P. N. Ross, Jr., R. Kostecki, F. Kong, S. Sloop, J. B. Kerr, K. Striebel, E. Cairns, and F. McLarnon, "Diagnostic Characterization of High-Power Lithium-Ion Batteries for Use in Hybrid Electric Vehicles," J. Electrochem. Soc. **148**, A463 (2001).

G.8 IN-SITU X-RAY ABSORPTION STUDIES OF POWER FADE OF GEN 2 CATHODE DURING CYCLING

Won-Sub Yoon, Mahalingam Balasubramanian, Kyung-Yoon Chung, Xuai Qing Yang, and James McBreen

G.8.1 Experiments Conducted

In-situ X-ray absorption (XAS) studies were carried out on the Gen 2 electrodes from LBNL and ANL.

XAS is simply the accurate determination of the X-ray absorption coefficient of a material as a function of photon energy, in an energy range that is below and above the absorption edge of one of the elements in the material. Absorption edges are due to the X-ray having sufficient energy to eject a photoelectron from a core shell in the atom. Absorption measurements are usually done a K or L3 edge, as absorption at the L3 edge is much higher than at the other L edges. The K edge is due to absorption by a 1s state and the L3 to absorption by a 2p3/2 core state. Measurements at the K edge are most suitable for elements of low atomic number (low Z) and for first- and second-row transition metal elements. In-situ measurements can easily be done at the K edges of first row transition metals in the same spectroelectrochemical cell that is used for the in-situ XRD measurements. Measurements are done in the transmission mode, and ionization chambers are used to measure X-ray beam intensity before and after it goes through the cell. XAS spectra consist of two parts. One is called the X-ray absorption near edge structure (XANES), and the other the extended X-ray absorption fine structure (EXAFS). XANES typically covers a region from –50 eV below the edge to 50 eV above the edge. XANES features are due to bound state transitions to empty states in the vicinity of the Fermi level and multiple electron scattering effects. XANES gives chemical information such as oxidation state and coordination symmetry. EXAFS is due to interference between the outgoing photoelectron wave from the excited atom and backscattering of a small portion of the wave by surrounding atoms. EXAFS extends from about 50 eV to about 1,000 eV above the edge. This modulates the absorption and gives rise to ripples in the absorption vs. energy plot. EXAFS gives short-range structural information out to about 8 Å from the excited atom. It gives quantitative information on bond distances and coordination numbers.

X-ray absorption: Examples of typical XAS data for Gen 2 cathodes are given below. The measurements were done at beamline X11A at NSLS. XAS scans covering both the Co and Ni K edges were taken while charging the cell at the C/2 rate. A third ionization chamber was used in conjunction with Co and Ni foils to provide internal calibration for the alignment of the edge positions. A total of seven scans were taken during charge.

XANES: Figure G-27a shows the XANES at the Ni K edge. During charge, the edge position of the first five scans shifts to higher energies, indicating the oxidation of Ni(III) to Ni(IV) as charging progresses. There is no further shift in edge position during the last two scans. The number labeled for each scan corresponds to the x value in $Li_{1-x}Ni_{0.8}Co_{0.15}Al_{0.05}O_2$, and EOC means the end of charge. Figure G-27b shows the XANES at the Co K edge. There is very little shift in the Co edge. This indicates that either the Co(III) is not oxidized during charge or that charge compensation occurs via holes on the O atoms associated with Co.

EXAFS: Figure G-28a shows Fourier transforms of the Ni EXAFS. The Fourier transforms are uncorrected for photoelectron phase shifts; thus, the bond distances are 0.3–0.4 Å shorter than the actual bond distances. The peaks at ~1.5 Å are due to the Ni-O interactions of the first coordination shell. The amplitude of these peaks increases with the degree of charge. This is due to a dynamic Jahn-Teller distortion for Ni(III). When Ni is oxidized to Ni(IV) during charge, the oxygen coordination around the Ni becomes symmetrical and the peak magnitude increases. The second set of peaks, at ~2.6 Å, is due to the first Ni-metal coordination shell in the basal plane. The shifts to lower R values during charge are due to a contraction in the Ni-metal bond distances. The peaks at ~5.4 Å are also due to backscattering by Ni-metal coordination shells that are aligned with the metal atoms of the first Ni-metal shell and are at double the distance of the first shell. This alignment produces a forward scattering effect that yields peaks in the Fourier transform at large R. The Fourier transformed spectra of the Co EXAFS plotted in Figure G-28b have similar features corresponding to Co-O interactions and Co-metal (Ni/Co) interactions, except for the absence of the Jahn-Teller effects.

In situ XANES of Gen-2 material

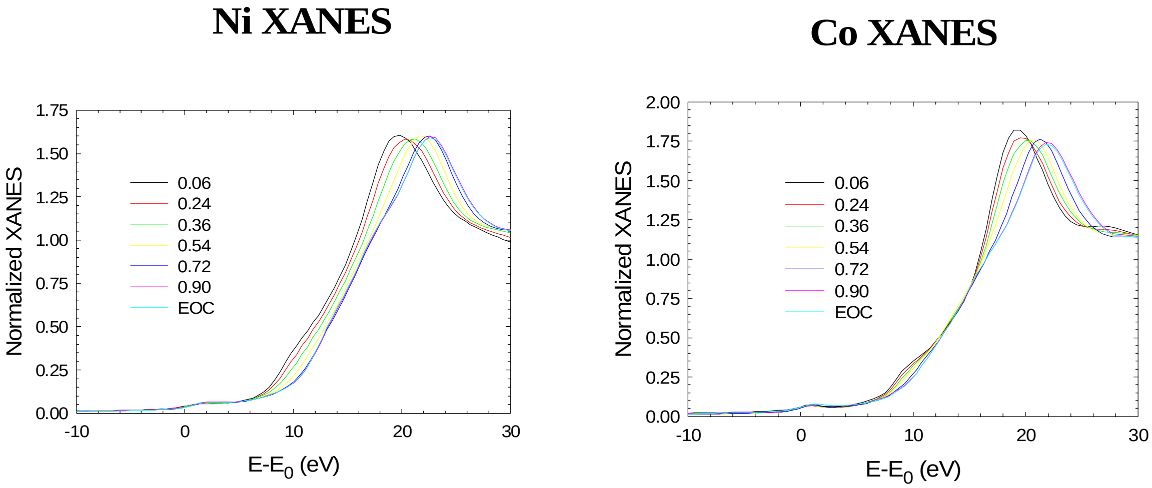

(a) (b)

Fig. G-27. In Situ XANES of Gen 2 Cathode at (a) Ni and (b) Co K Edge. The numbers labeling the curves correspond to the x values in $Li_{1-x}Ni_{0.8}Co_{0.15}Al_{0.05}O_2$, and EOC means the end of charge.

Ni and Co EXAFS for Gen-2 material

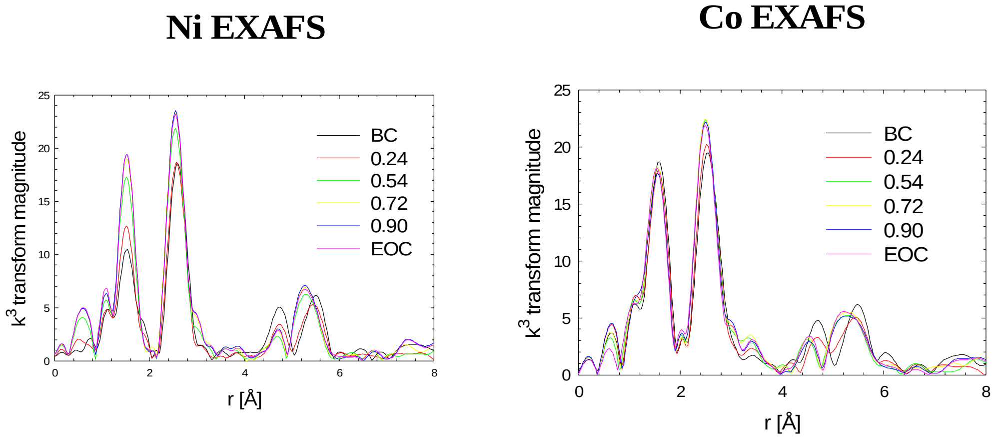

(a) (b)

Fig. G-28. Fourier Transformed In-Situ EXAFS of Gen 2 Cathode for (a) Ni and (b) Co K Edge. The numbers labeling the curves correspond to the x values in $Li_{1-x}Ni_{0.8}Co_{0.15}Al_{0.05}O_2$, and EOC means the end of charge.

Publications and Invited Presentations on Related Subjects, Section G.8

Balasubramanian, M., X. Sun, X. Q. Yang, and J. McBreen, "In Situ X-ray Diffraction and X-ray Absorption Studies of High-Rate Lithium-Ion Batteries," J. Power Sources **92**, 1–8 (2000).

Balasubramanian, M., X. Sun, X. Q. Yang, and J. McBreen, "In Situ X-Ray Absorption Studies of a High-Rate $LiNi_{0.85}Co_{0.15}O_2$ Cathode Material," J. Electrochem. Soc. **147**, 2903 (2000).

McBreen, J., M. Balasubramanian, X. Q. Yang, and X. Sun, "Synchrotron X-ray Studies of Lithium-Ion Battery Materials," invited talk, presented at the 11th International Meeting on Lithium Batteries, June 23–28, 2002, Monterey, California.

G.9 TIME-RESOLVED X-RAY DIFFRACTION STUDIES OF THERMAL STABILITY OF GEN 2 CATHODE

Won-Sub Yoon, Mahalingam Balasubramanian, Kyung-Yoon Chung, James McBreen, and Xiao Qing Yang

G.9.1 Experiments Conducted

XRD studies were conducted of the thermal decomposition of Gen 2 cathodes at various charged states as affected by the presence of electrolyte. The structural changes of the cathode material under the thermal abuse condition and the interaction between cathode and electrolyte are two important factors for understanding thermal abuse. Time-resolved XRD analysis has been developed at BNL to investigate thermal behavior of $Li_{1-x}Ni_{0.8}Co_{0.15}Al_{0.05}O_2$ cathodes (Gen 2 cathode material). Cathode materials electrochemically charged to various charged states were sealed in quartz capillaries with or without electrolyte. These capillaries could withstand the pressure generated on heating. Time-resolved XRD patterns were continuously collected when these capillaries were heated from 25°C to 450°C.

Figure G-29 shows that the thermal decomposition was not observed at 450°C for the sample at 0% state of charge (SOC) without electrolyte. However, for the sample charged to 50% SOC without electrolyte, the thermal decomposition was observed at a temperature of about 280°C (Fig. G-30). With a higher percentage of SOC, the decomposition was lowered further. The effects of the electrolyte on the thermal decomposition of the cathode were also studied. The electrolyte accelerated the thermal decomposition of the charged cathode material. The presence of the electrolyte changes the paths of the structural changes and lowers the temperatures for the onset of the reactions. In the presence of electrolyte, the solvent acts as a reducing agent and reacts with lithium extracted from the structure, resulting in the formation of Li_2CO_3.

As shown in Fig. G-31, the time-resolved XRD patterns for $Li_{0.27}Ni_{0.8}Co_{0.15}Al_{0.05}O_2$ (100% SOC) in the presence of electrolyte indicate that decomposition of the layered structure starts at about 200˚C. In the interval between 200˚C and 250˚C, the coalescence of the (108) and (110) peaks in the layered structure was observed, suggesting the formation of a disordered spinel phase. Based on a $2 \times 2 \times 2$ cubic rock salt lattice, this merged peak corresponds to the (440) peak in the cubic structure with space group Fd3m. At above 290˚C, a rock salt structure was observed, which is consistent with the formation of NiO-like phase. The disordered spinel phase transforms progressively to the NiO-like phase by a first order phase transition as the temperature increases. During the conversion from a spinel to a rock salt phase, lithium and nickel ions move randomly to other layers, and there is no difference between the cation layers in the resulting structure. Therefore, the resulting rock salt phase has a unit cell with a lattice parameter, one-half that of the spinel phase. The transformation of the spinel phase to NiO-like rock salt phase is completed at the end of heating. The remaining peaks could be indexed, assuming a cubic cell with a space group of Fm3m.

The effects of chemical compositions on the thermal decomposition of layer-structured cathode materials are shown in Figure G-32. For cathode materials charged to the same level, the thermal decomposition temperature for $Li_{0.33}Ni_{0.5}Mn_{0.5}O_2$ (100% SOC) was the highest (265 ºC), compared with 200ºC for the Gen 2 cathode ($Li_{0.33}Ni_{0.8}Co_{0.15}Al_{0.05}O_2$), which is still better than the 170ºC for $Li_{0.33}NiO_2$.

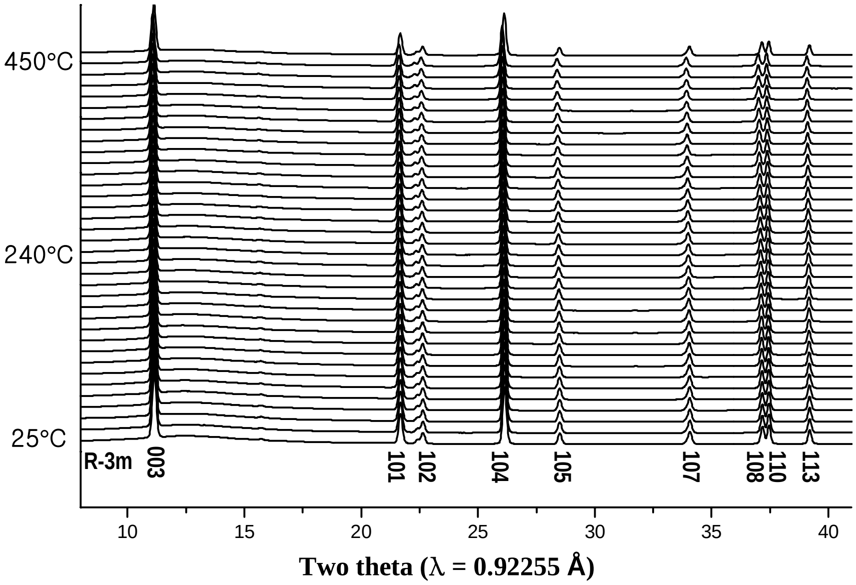

Fig. G-29. In-Situ Time-Resolved XRD Patterns of Gen 2 Cathode $Li_{1.0}Ni_{0.8}Co_{0.15}Al_{0.05}O_2$ (0%SOC) without Electrolyte.

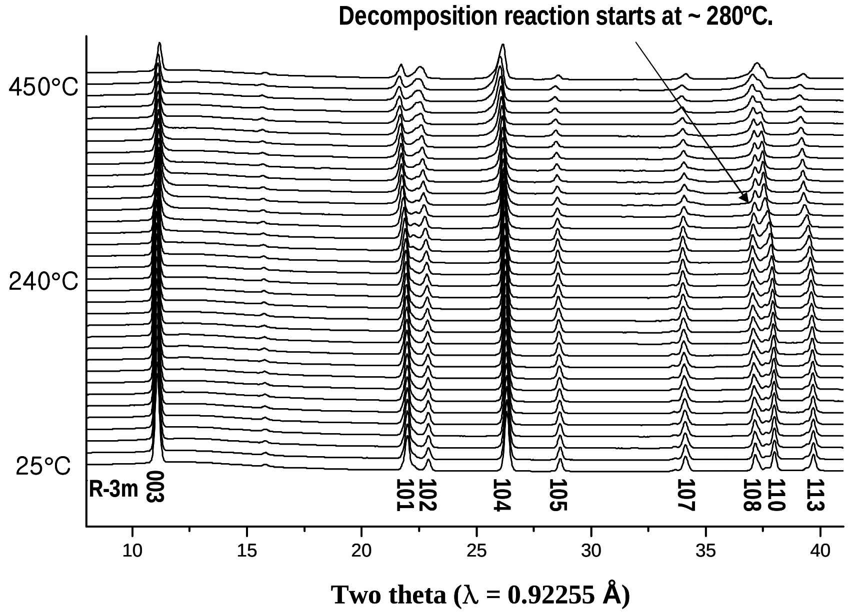

Fig. G-30. In-Situ Time-Resolved XRD Patterns of Gen 2 Cathode $Li_{0.67}Ni_{0.8}Co_{0.15}Al_{0.05}O_2$ (50%SOC) without Electrolyte.

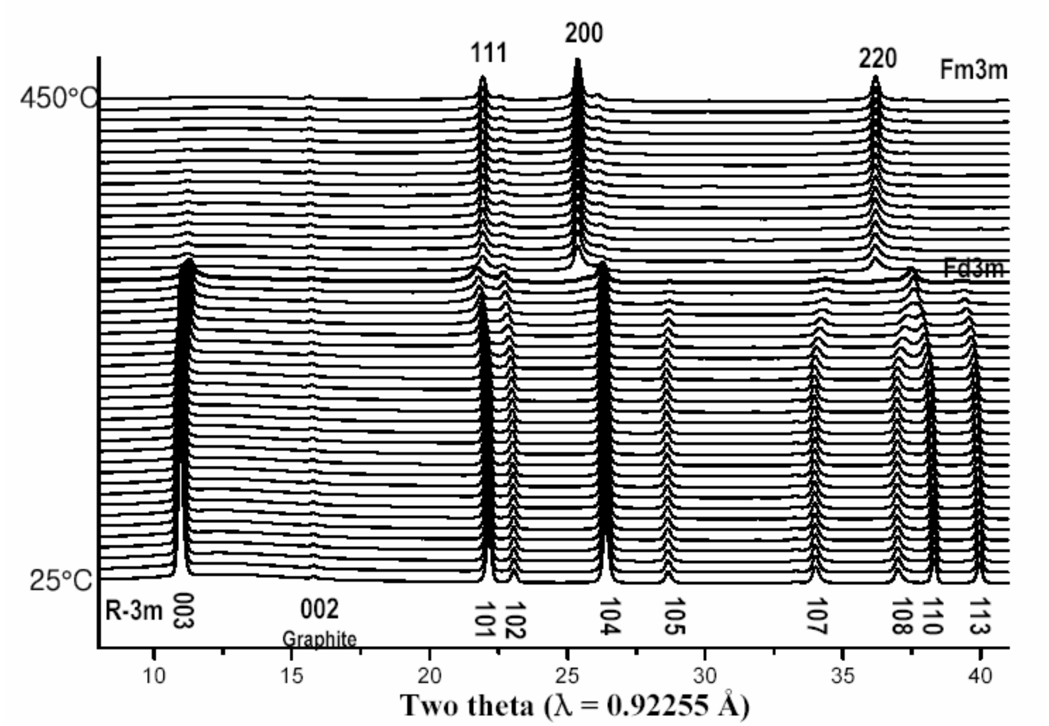

Fig. G-31. Time-Resolved XRD Patterns for Gen 2 Cathode $Li_{0.27}Ni_{0.8}Co_{0.15}Al_{0.05}O_2$ in the Presence of Electrolyte When Heated from 25°C to 450°C.

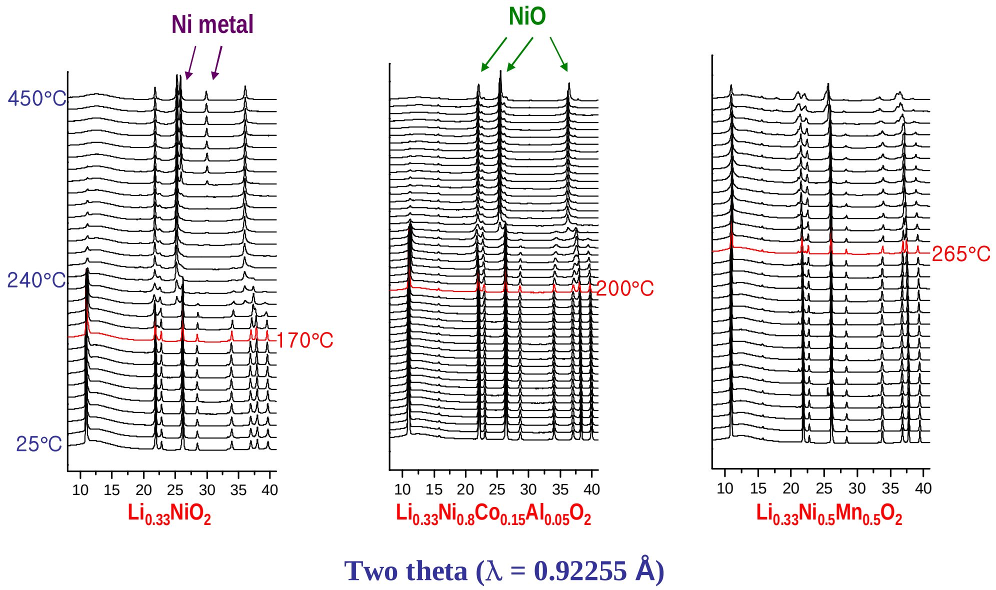

Fig. G-32. Time-Resolved XRD Spectra for Cathode Material $Li_{0.33}Ni_{0.5}Mn_{0.5}O_2$ Charged to 100% SOC, in Comparison with $Li_{0.33}NiO_2$ and Gen 2 Cathode $Li_{0.33}Ni_{0.8}Co_{0.15}Al_{0.05}O_2$ When Heated from 25°C to 450°C.

Publications and Invited Presentations on Related Subjects, Section G.9

Yoon, W.-S., M. Balasubramanian, X.-Q. Yang, J. McBreen, and J. Hanson, "Time Resolved XRD Study on the Thermal Decomposition of $Li_{1-x}Ni_{0.8}Co_{0.15}Al_{0.05}O_2$ Cathode Materials for Li-Ion Batteries," Electrochemical and Solid-State Letters **8**(2), A83 (2005).

Yoon, W.-S., M. Balasubramanian, K. Y. Chung, X.-Q. Yang, J. McBreen, and J. Hanson, "Time Resolved XRD Study on the Thermal Decomposition of $Li_{1-x}Ni_{0.8}Co_{0.15}Al_{0.05}O_2$ Cathode Materials for Li-Ion Batteries," 12th International Meeting on Lithium Batteries, Nara, Japan (2004).

Balasubramanian, M., W. S. Yoon, X. Q. Yang, J. McBreen, and J. Hanson, "Time Resolved X-ray Diffraction Study of the Thermal Degradation of Cathode Materials Used in Li-Ion Batteries," Electrochemical Society Proceedings, accepted.

G.10 X-RAY PHOTOELECTRON SPECTROSCOPY EXAMINATION OF POSITIVE ELECTRODE SAMPLES

Daniel Abraham and Richard Haasch

G.10.1 Experiments Conducted

X-ray photoelectron spectroscopy experiments were conducted on positive electrodes harvested from 14 Gen 2 and 6 Var C 18650 cells that showed from 0% to 54% power fade, to determine changes associated with cell aging. Several samples from each electrode were studied to examine data variability along the electrode's width and length. Data were acquired on "as harvested" samples and on samples that were rinsed in DMC. The rinsing procedure involved immersing the samples in DMC for ~48 hours; the solvent was replaced twice with a "fresher version" during this period. Control data were obtained on fresh electrode samples. The XPS spectra were obtained on a Kratos Axis ULTRA X-ray photoelectron spectrometer under UHV (10^{-9} torr) conditions. Most elements were analyzed using monochromatic Al Kα (1,486.6 eV) radiation as the primary excitation source; the Ni 2*p* and Co 2*p* data were collected using Mg Kα radiation (1,253.6 eV). The energy scale was adjusted based on the graphite peak in the C 1*s* spectrum at 2,84.5 eV. Details of the experimental technique and analysis are provided in J. Electrochemical Soc., **149**(10), A1358 (2002).

G.10.2 Summary of Results

- XPS spectra from samples that were always handled in an inert atmosphere were compared with those from samples that were exposed to air for a brief period (less than 30 minutes). Unlike the anode samples, air exposure had little effect on the XPS data.
- The data acquired along various portions of an electrode were mostly within the bounds of experimental uncertainty. Data from electrodes subjected to various levels of aging showed distinct differences.
- XPS spectra from rinsed positive electrodes harvested from Gen 2 and Var C cells are shown in Figure G-33. The trends observed in the various spectra on aging are as follows:
  - The C 1*s* spectra of fresh electrode samples indicate the locations of the graphite and PVDF binder peaks. With increasing age, the intensity of the graphite and PVDF peaks decreased. However, the total surface carbon content for the variously aged samples showed little change, which indicates that new carbon-bearing compounds build up on the electrode surface with increasing cell age.
  - The O 1*s* spectra of fresh samples showed strong Li_2CO_3 peaks in addition to the oxide peaks, which indicated that the oxide particles were partially covered by Li_2CO_3. Neither oxide nor Li_2CO_3 peaks were observed in the 0% PF sample, probably because the oxide was buried under the surface films that include electrolyte residue and new compounds that result from formation cycling; the Li_2CO_3 probably decomposed during cycling. On cell aging, the total surface oxygen content of the electrodes increased, which indicates that the new aging-related compounds also contain oxygen.
  - The F 1*s* spectra of fresh samples show peaks arising from the PVDF binder and weak LiF peaks. The PVDF and LiF peak intensities decrease, probably because they are buried by the new compounds formed on aging.
  - The P 2*p* spectra contain contributions from P-F bonds, probably from Li_xPF_y compounds in the electrolyte residue; these show no trends on aging. On the other hand, the intensity of P-O bonds that may be either from $Li_xPF_yO_z$ or from organophosphate compounds increases with cell age.
- Representative XPS spectra depicting the effect of the DMC rinse are shown in Figure G-34. The observations from the various spectra are as follows:
  - In the C 1*s* spectra, rinsing partially removes the compounds that cover the graphite and binder peaks; this is especially evident for the 48% PF sample.

  - The P 2*p* spectra shows a clear P-F bond intensity decrease, which indicates that the $LiPF_6$ electrolyte residue is at least partially removed by the rinse protocol. The P-O bond intensity, on the other hand, appears unaffected.
  - In the F 1*s* spectra, the LiF peak intensity decreases, indicating that the rinsing removes some of this compound. The PVDF peak intensity, on the other hand, is unaffected, which indicates that the immersion rinse does not remove the compound(s) covering the binder.
  - In the O 1*s* spectra, rinsing appears to lower the peak intensities of the higher binding energy compounds in the electrode surface films. The peak associated with oxygen in $LiNi_{0.8}Co_{0.15}Al_{0.05}O_2$ is not visible in the rinsed samples, which indicates that the oxide is still covered by the surface film compounds.
- XPS spectra corresponding to "scraped" positive electrodes are compared with those from as-harvested electrodes in Figure G-35. The scraping was conducted with a razor blade in a He glove box; it removed some of the composite coating but did not expose the Al current collector. The observations from these electrodes are as follows:
  - The C 1*s* spectra showed that scraping uncovers the graphite and PVDF binder; this is especially evident for the 48% PF sample.
  - The O 1*s* spectra showed $LiNi_{0.8}Co_{0.15}Al_{0.05}O_2$ peaks, which indicated that the surface films covering the oxide were at least partially removed. The ~531 eV binding energy is similar to that of LiOH. In polyamide compounds, the O 1*s* peak also has a ~531 eV binding energy. However, the N present in these compounds was not observed in the XPS spectra.
  - The P 2*p* spectral intensity was significantly reduced, which indicated that the P-bearing compounds that probably covered the oxide and carbons were removed by the scraping.
  - The F 1*s* spectra (not shown) indicated that scraping removed the LiF and LiP_xF_y electrode residue that was present on the electrode samples.
  - Co peaks, which are rarely observed in the XPS spectra, were observed in the scraped samples, which again indicated that the oxide was exposed.
- Ar-ion sputtering data showed a similar surface film thickness for the 0% and 35% PF samples.

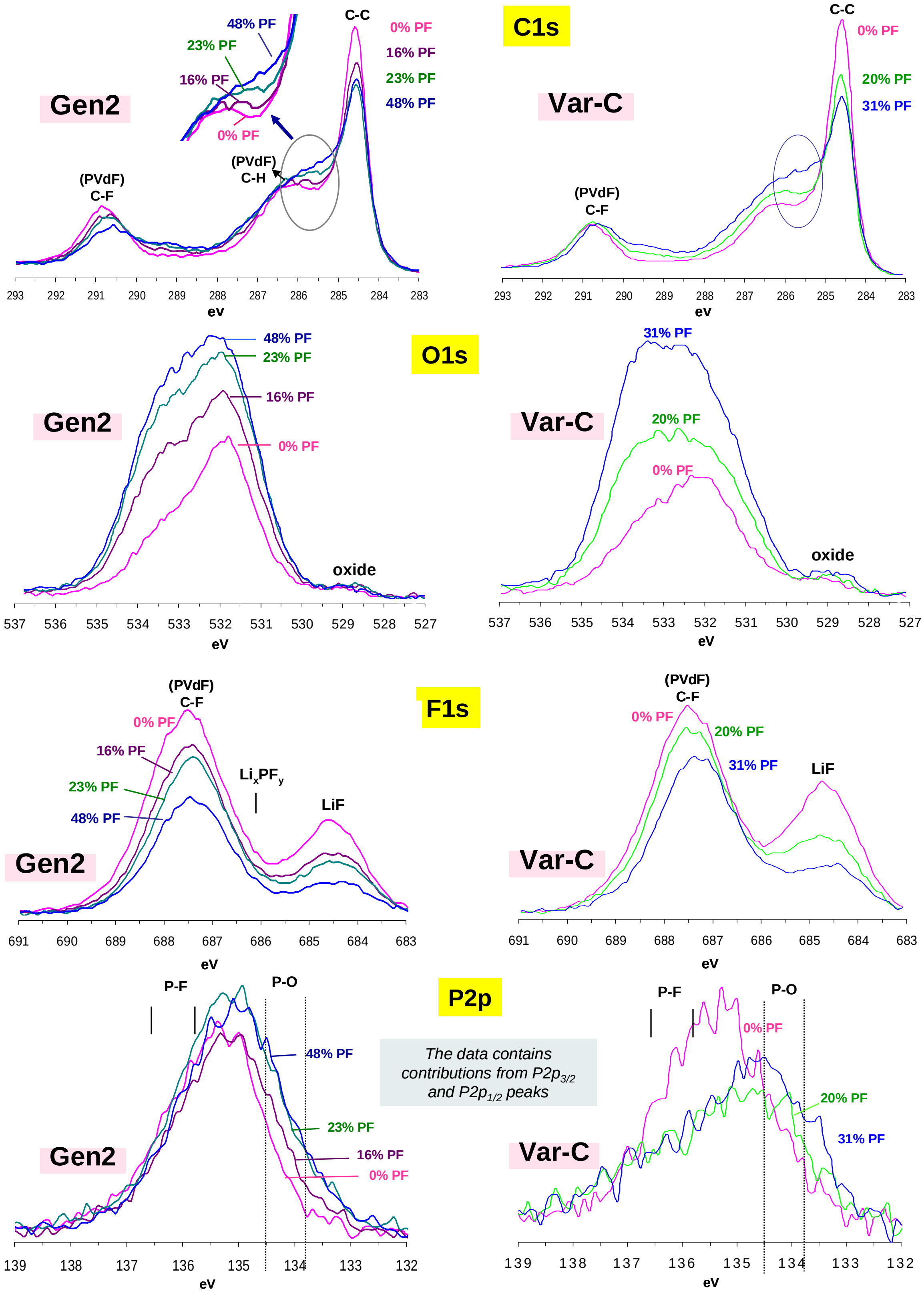

The data contains contributions from P2p$_{3/2}$ and P2p$_{1/2}$ peaks

Fig. G-33. XPS Spectra from Rinsed Positive Electrodes Harvested from Gen 2 and Var C Cells.

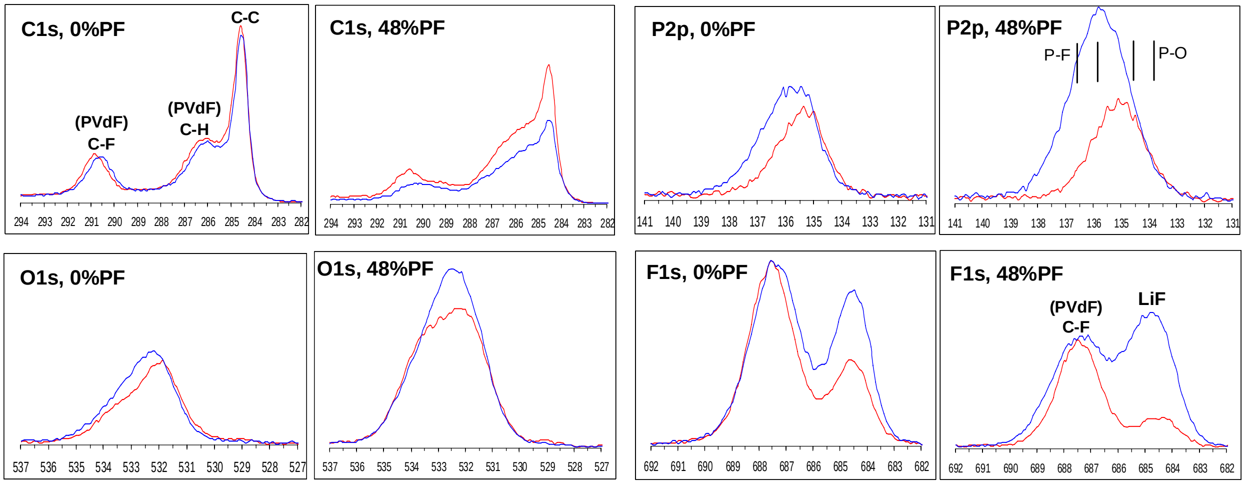

Fig. G-34. Effect of Rinsing on the XPS Spectra of a 0% PF and 48% PF (Highly Aged) Positive Electrodes Harvested from Gen 2 Cells. The intensity (vertical) scales are the same for each element, so that the data are directly comparable. The as-harvested and rinsed spectra are in blue and red, respectively.

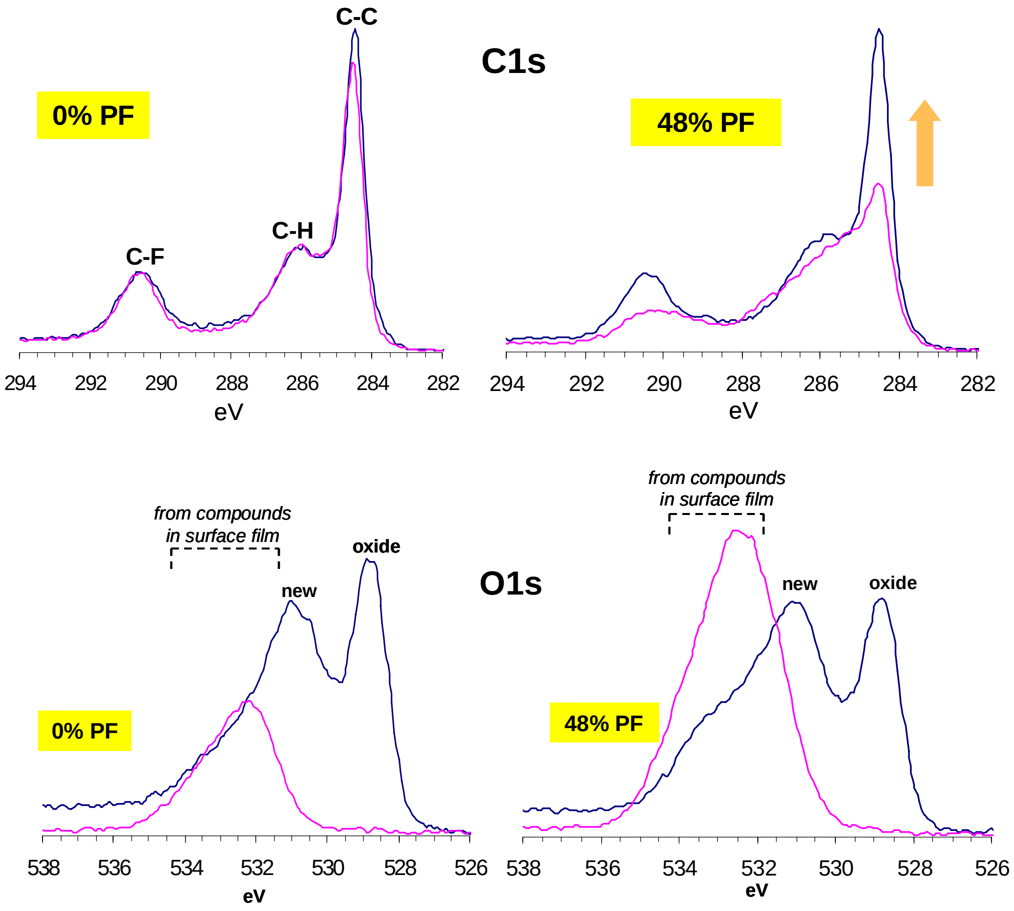

Fig. G-35. XPS Spectra of as-Harvested (pink) and Scraped (blue) Electrodes. The scraping process removes the surface films and exposes the underlying materials.

G.10.3 Conclusions

- The XPS spectra show that the composition of surface films present on the positive electrode samples changes with cell age.
- Comparisons with standard spectra showed that PEO (if present) is not a dominant species in the surface films.
- LiF and Li_xPF_y were observed on the electrode surface. Both compounds were at least partially rinsed off in DMC.
- The increases in the O, P, and C content may be associated with increases in the organophosphate content of the surface films.

G.11 CATHODE EXAMINATION BY FTIR

Vera Zhuang and Phil Ross

Fourier transform infrared spectroscopy (FTIR) was used to analyze the chemical composition of cathode material $LiNi_{0.8}Co_{0.15}Al_{0.05}O_2$ in a pristine Gen 2 cathode (not from a cell), in cathode from a fresh cell and the aged cell G2.60C55.A211.30.40.31.G.L. Measurements were performed directly on electrode surfaces without any preparation in the attenuated total reflection (ATR) mode. Generally, washing in dimethyl carbonate (DMC) was not necessary, as the cathodes retain much less residual electrolyte than the anodes. More detailed summaries of this work have been published in J. Electrochemical Soc., **151**(8), A1162–1167 (2004) and in J. Power Sources, **134**, 293–297 (2004).

G.11.1 Summary of Results

- There is a preexisting layer of lithium carbonate (Li_2CO_3) on the $LiNi_{0.8}Co_{0.15}Al_{0.05}O_2$ active in a pristine Gen 2 cathode. The thickness of the layer increases with air exposure, and is produced by reaction of the oxide with CO_2 in the air (Fig. G-36).
- No lithium carbonate was found on cathodes either from the fresh or aged cell. There was no lithium carbonate from a pristine cathode merely soaked in the Gen 2 electrolyte.
- No PEO or other polymeric species other than the PVDF binder could be detected on the cathode surface from the aged cell.

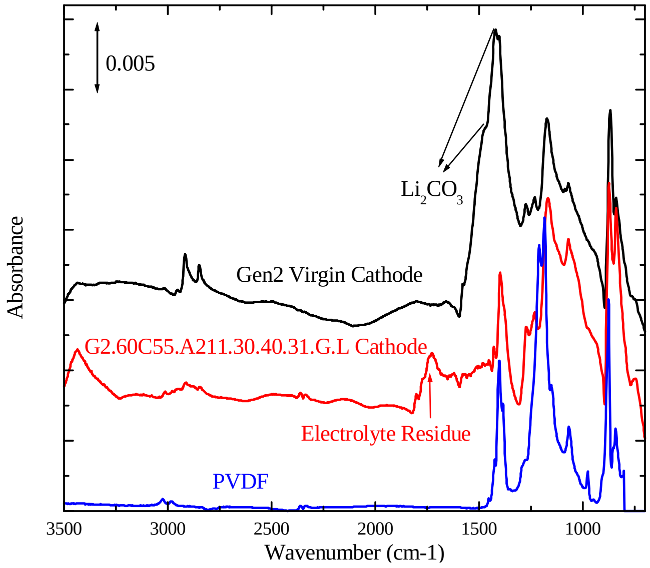

Fig. G-36. FTIR-ATR Data from Fresh and Aged Positive Electrode Samples. The spectrum from a PVDF sample is shown for comparison.

G.11.2 Conclusions

- The preexisting surface layer of Li_2CO_3 on the Gen 2 cathode material appears to react with the HF impurity in the Gen 2 electrolyte to form H_2O, CO_2, and LiF. The water from this reaction could be the source of water for the thermal hydrolysis reaction occurring with cell aging.
- No products of the reaction of electrolyte with the Gen 2 active material during aging could be detected by FTIR-ATR, e.g., no organic or polymeric compounds other than electrolyte and PVDF binder.

G.12 PROTON NUCLEAR MAGNETIC RESPONANCE CATHODE EXAMINATION

Daniel Abraham and Rex E. Gerald II

G.12.1 Experiments Conducted

High-resolution proton NMR analyses were conducted to examine the possible presence of polyethylene oxide (PEO) or its oligomers in surface films on cathodes harvested from 18650 cells (see Table G-3). The surface films were extracted by washing the samples several times with D_2O or acetonitrile solvent; typical data are shown in Figure G-37. The experiments showed that, even for highly aged samples, surface film extraction was essentially complete after 6 washes. The PEO content of each sample was quantified by summing the PEO contents determined for each wash solution. Control experiments were conducted on fresh ethylene carbonate (EC) samples.

Table G-3. Characteristics of 18650 Cells Studied

Cell ID	Aging T, Period	Capacity Fade, %	Power Fade, %
2-032	None	0	0
SNL 325	45°C, 40 weeks	31.0	51.3
2-078	45°C, 68 weeks	29.6	48.4

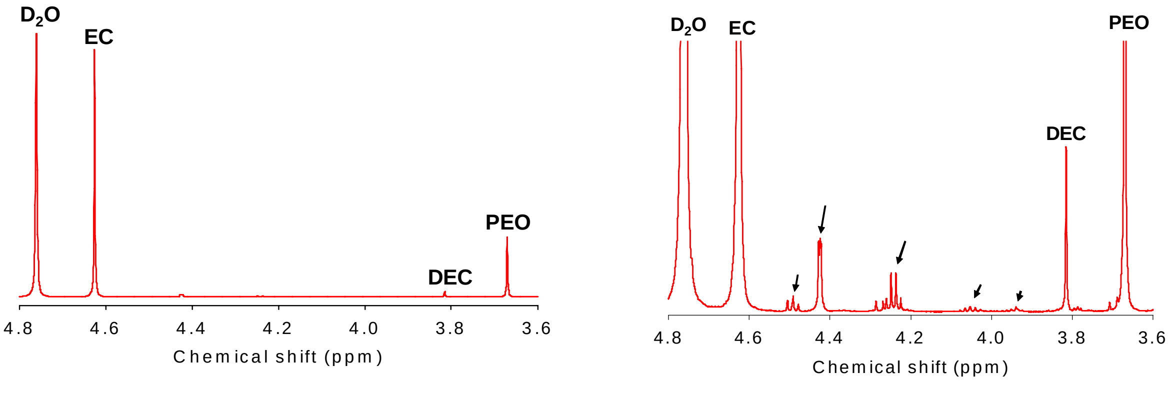

(a) (b)

Fig. G-37. (a) NMR Extraction Data Obtained on a Positive Electrode Laminate from a ~50% Power Fade Cell. (b) Y-axis Expanded to Show Minor Components (marked by arrows) in Data That Have Not Been Identified but Could Include DEDOHC, EMDODHC, and DMDOHC.

G.12.2 Summary of Results

The experimental observations are listed in Table G-4.

Table G-4. Summary of Experimental Observations

Sample	Comments
2-032 (D_2O extraction) SNL 325 (D_2O extraction)	**PEO peak intensities/quantities were similar in both D_2O-extraction solutions.**
2-032 (acetonitrile extraction) 2-078 (acetonitrile extraction)	Very weak PEO peaks in spectra. C13 satellites not observed. **PEO peak intensities/quantities were similar in both acetonitrile-extraction solutions.**
EC + acetonitrile (heated/sonicated)	No PEO peaks in spectra.
EC + 4 drops deionized H_2O (40°C)	No PEO peaks in spectra.
EC + deionized H_2O (40°C) + KOH	Strong PEO peaks in spectra.
H_2O or acetonitrile extraction to EC does not produce PEO, but KOH addition does.	

G.12.3 Conclusions

PEO (polyethylene oxide) peak intensities were very similar for all cathode samples studied. No increase in PEO content with cell (electrode) age was observed.
The PEO peaks observed in the spectra could be an artifact of the extraction process, although H_2O and acetonitrile addition to EC did not produce these peaks.
D_2O is a better extraction solvent for PEO than acetonitrile (if PEO is indeed present in the cathode samples).

G.13 NUCLEAR MAGNETIC RESONANCE (^{19}F AND ^{31}P) POSITIVE ELECTRODE ANALYSIS

Marie Kerlau, Jeffrey Reimer, and Elton Cairns

G.13.1 Experiments Conducted

^{31}P NMR experiments were performed on the Gen 2 cathode material obtained from cell G2.60C45.A217.50.72.50.G.L, which exhibited 50% power fade after 72 weeks of storage at 45˚C and 60% state of charge.

G.13.1 Summary of Results

Fluorophosphate decomposition products and the $LiPF_6$ salt were present on the surface of the electrode obtained from the aged cell, as shown in the ^{31}P NMR spectrum (Fig. G-38). It is thus clear that these compounds can interact with the electrode particles. We performed the same experiment with a cathode sample sonically washed in DMC. In this case, none of the phosphate species appeared in the ^{31}P NMR spectrum.

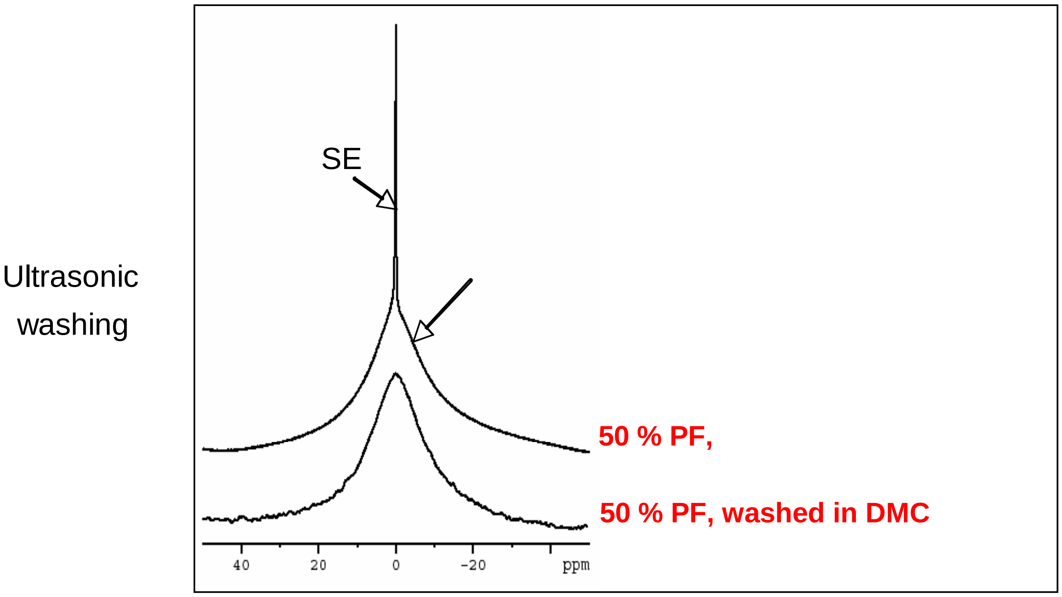

Fig. G-38. ^{31}P NMR Spectrum of a Cathode of a Gen 2 Cell Aged 72 Weeks at 45°C and Showing 50% Power Fade.

G.14 SOFT X-RAY ABSORPTION STUDIES OF GEN 2 CATHODE

Won-Sub Yoon, Mahalingam Balasubramanian, James McBreen, and Xiao Qing Yang

G.14.1 Experiments Conducted

Soft X-ray absorption spectroscopy (XAS) was used to study the mechanism of power fading of the Gen 2 cathode. Soft X-ray XAS measurements on elements with absorption edges between 200 and 1,000 eV (e.g., the K edges of O and F) made it possible to get both surface and bulk sensitivity. Figure G-39 shows a schematic of an ex-situ XAS experiment. Measurements of the absorption can be done in three ways: transmission, fluorescence (FY), and electron yield (EY). Transmission probes the bulk, and the measurements are done by simply measuring the intensity of the X-ray beam before (I_o) and after (I_t) it goes through the sample.

Figure G-39 summarizes, in schematic form, the phenomenology established from our ex-situ soft X-ray XAS studies of electrodes from cycled and abused cells.

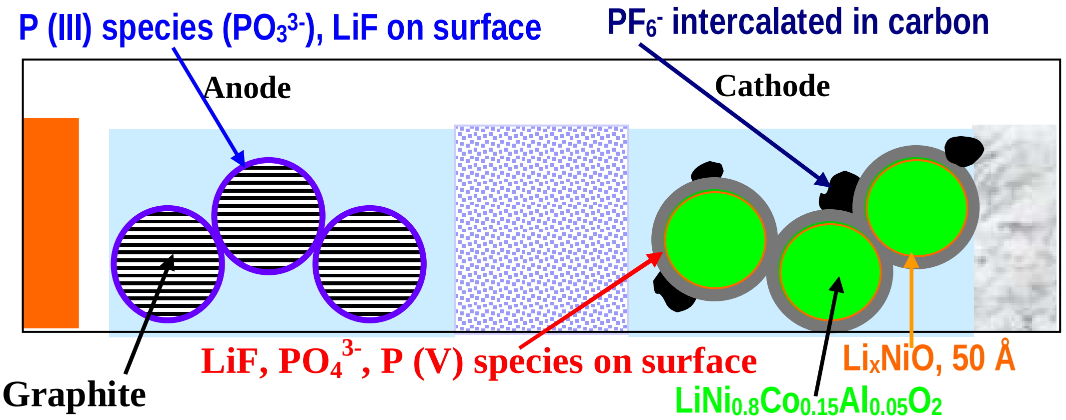

Fig. G-39. Schematic Representation of Precipitation Products from $LiPF_6$ Decomposition Identified by XAS Studies of the Surface of Electrodes from Cycled and Abused Cells. XAS also identified PF_6^- that could not be leached from the cathode. A comparison of O K edge XAS on the cathode in the FY and EY mode shows the presence of Ni(II) on the surface (outer 50 Å) of the cathode active material particles in both fresh and cycled cells.

Figure G-40 shows typical F K edge XAS data in the EY mode for fresh and cycled cathodes. The data for the fresh electrodes are those expected for the PVDF binder. The data for cycled electrodes indicate the precipitation of LiF on the surface of the cathodes. LiF has also been seen on the anodes from cycled cells. The amount of F associated with LiF is comparable to the F associated with the PVDF.

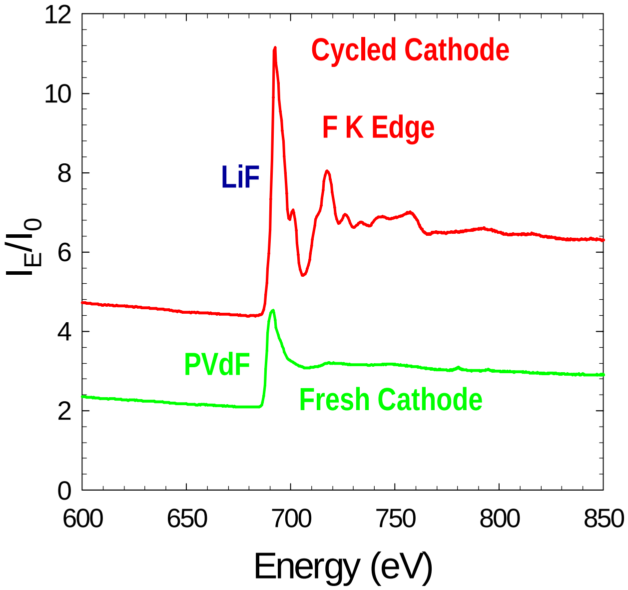

Fig. G-40. Typical F K Edge XAS Data in the EY Mode for Fresh and Cycled Cathodes.

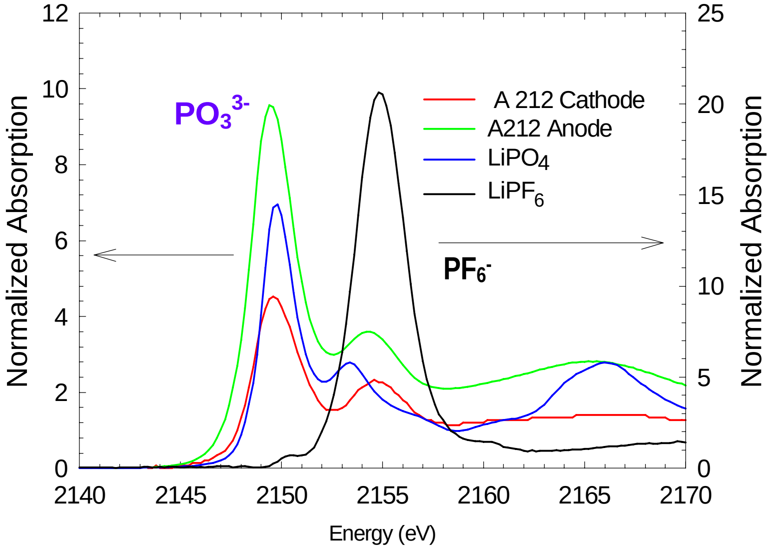

Fig. G-41. Typical P K Edge XAS for Electrodes from a Calendar-Life Cell. Data for Li_3PO_4 and 0.05 M $LiPF_6$ standards are also shown. Note the different scale for the $LiPF_6$ data. Also note the negative shift in anode data. No P spectra were observed on fresh electrodes.

Figure G-41 shows XANES spectra at the P K edge for an anode and cathode taken from a calendar-life cell from ANL, G2.50C55, A212.24.28.24.G. L. Also shown are spectra for Li_3PO_4 and 0.05 M $LiPF_6$ standards. No P spectra were observed on fresh electrodes. The only reason why we can see low levels of PF_6^- in cycled cathodes is that the method is very sensitive. This sensitivity is due to the unique electronic properties of PF_6^-. PF_6^- has a unique XANES spectrum because of its electronic structure. In PF_6^-, the electron-withdrawing F empties the P 3*s* and 3*p* states. The result is a more ionic bonding that shifts the edge to higher energies. This also causes an enormous increase in the intensity of the white line (the peak at 2,155 eV). The increase in the intensity is due to the fact that there are many empty 3*p* states for dipole-allowed bound state transitions of the excited 1s core electrons. The high degree of symmetry of PF_6^- also enhances multiple scattering of the electrons, further increasing the peak intensity. The unique position and intensity of this peak make it a very sensitive probe for the presence of PF_6^-. In the case of the cathode, we see a symmetric peak at 2,155 eV, indicating the presence of PF_6^-.

The P K edge XAS indicates the presence of pentavalent P species on the surface of cathodes from cycled and abused cells. The negative shift in the edge data for the anodes indicates the presence of trivalent P species such as PO_3^{3-}. This indicates electrochemical reduction of P(V) species to P(III) at anode potentials.

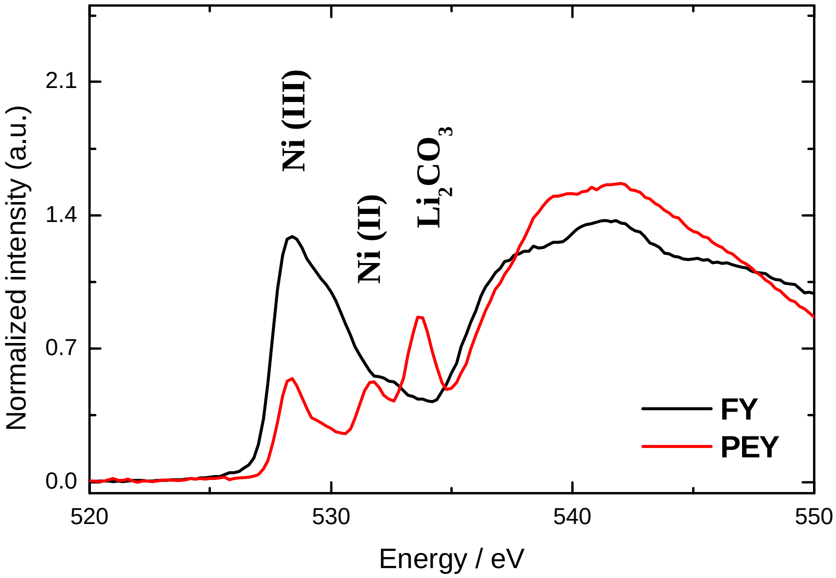

Fig. G-42. O K Edge XAS in the EY and FY Modes for the as Received Gen 2 Cathode Material. The results indicate that the surface composition of Ni-based cathode materials is different than the bulk. In the bulk of the material, the Ni exists as Ni(III), whereas on the surface, it is Ni(II).

Figure G-42 shows O K edge XAS in the EY and FY modes for the as received Gen 2 cathode material. The results are the same for materials from cycled and abused cells. When O is covalently bonded to low-Z elements, such as C, P, or Al, there are no features in the O XANES below 535 eV. However, if O is covalently bonded to a first-row transition metal, there can be mixing of O *p* states and transition metal *d* states. These empty mixed states with *p* character give rise to pre-edge peaks in the 525–535 eV region. The position of these peaks depends on the transition metal and its oxidation state. These results indicate that the surface composition of Ni-based cathode materials is different than the bulk. In the bulk of the material, the Ni exists as Ni(III), whereas on the surface, it is Ni(II). This apparently occurs because of a loss of O on the surface of the cathode material particles. Li_2CO_3 is also observed at the surface of fresh Gen 2 cathode material. In the case of $LiCoO_2$, the surface and bulk compositions are the same.

All of the data presented here are ex-situ data. In a typical experiment, cells were disassembled in an argon-filled glove box. The electrodes were washed with either DME or THF to remove the electrolyte and dried in the glove box. The soft X-ray XAS at the O and F K edges was done under vacuum (2×10^{-7} torr) at NSLS. In the case of the P K edge XAS, the samples were mounted in a helium-filled electron detector at atmospheric pressure. In all cases, FY and EY measurements were done simultaneously. Samples tested under identical conditions show very reproducible data. There is no beam damage from the X-rays.

G.14.2 Summary of Results

In summary, we have very convincing evidence for the decomposition of $LiPF_6$ in cycled and abused cells. This results in the precipitation of products on the electrode surfaces (LiF and phosphates) that are insoluble in conventional nonaqueous solvents. We also have convincing evidence that the surface of nickel-based cathodes differs from the bulk. Ni(II) species are found on the surface of the particles. This is true for both uncycled and cycled materials. This has been corroborated by TEM work at ANL. Because of the sensitivity of our technique, we can see small amounts of PF_6^- species that cannot be removed by repeated washing in nonaqueous solvents such as DME or THF. The XAS results indicate that 10–15% of the P in the cathode exists as PF_6^-. We have not been able to locate where the PF_6^- is entrained in the cathode.

Publications and Invited Presentations on Related Subjects, Section G.14

Balasubramanian, M., H. S. Lee, X. Sun, X. Q. Yang, A. R. Moodenbaugh, J. McBreen, D. A. Fischer, and Z. Fu, "Formation of SEI on Cycled Lithium-Ion Battery Cathodes: Soft X-Ray Absorption Study," Electrochem. Solid-State Lett. **5**, A22 (2002).

McBreen, J., M. Balasubramanian, X. Q. Yang, and X. Sun, "Synchrotron X-ray Studies of Lithium-Ion Battery Materials," invited talk, presented at the 11th International Meeting on Lithium Batteries, June 23–28, 2002, Monterey, California.

McBreen, J., X.-Q. Yang, M. Balasubramanian, H.-S. Lee, and X. Sun, "Synchrotron X-ray Studies of Lithium-Ion Battery Components," invited talk, presented at the 43rd Battery Symposium in Japan, October 12–14, 2002, Fukuoka, Japan.

G.15 ANALYSIS OF CARBON CONTENT IN GEN 2 POSITIVE ELECTRODES

Daniel Abraham

The carbon content of Gen 2 cathode samples was measured with a Leco Corporation Model C/S 300 carbon/sulfur determinator by the Analytical Chemistry Laboratory at Argonne National Laboratory. The instrument was calibrated, and calibration verified with carbon-in-steel samples that reference traceability to National Institute of Standards and Technology standards. For analysis, the cathode coating was scraped off the aluminum current collector and added to a ceramic crucible, along with a combustion accelerator. The crucible was placed in the instrument, where it was heated to about 2,000°C in a flowing stream of oxygen to produce carbon dioxide gases that were analyzed by solid state infrared absorption cells. The resulting data are shown in Table G-3. Low boiling point organic compounds do not contribute to the final result because they are volatilized during the early stages of heating.

Table G-3. Carbon Content (± 5%) of Gen 2 Cathode Samples

ID	Sample Description	Sample Wt, mg	C, wt%
Fresh Gen 2	Fresh sample, no electrolyte contact	9.650	11.8
2-023 C	From cell 2-023, 0% power fade	9.633	12.5
2-021 C	From cell 2-021, 35% power fade	9.642	12.6
SNL325 C	From cell SNL325, 54% power fade	12.449	12.6

The nominal composition of a fresh Gen 2 cathode laminate coating is 84 wt% $LiNi_{0.8}Co_{0.15}Al_{0.05}O_2$, 4 wt% graphite, 4 wt% acetylene black, and 8 wt% PVDF binder. The measured value for the fresh Gen 2 fresh sample is 11.8 wt%, which indicates that the PVDF contributes to the carbon content. Calculations using atomic weights show that 37.5 wt% of PVDF is carbon. Given the nominal electrode composition, the expected carbon content is 11 wt%, which is lower than the measured value. The higher measured value probably results from a graphite and/or acetylene black content that is larger than the nominal value.

The carbon content for the 0% power fade sample is 12.5 wt%, which is slightly larger than the value for the fresh sample; repeated measurements have indicated that this difference is statistically significant. The higher value for the 0% power fade sample may be related to surface film components on the sample that are oxidized on heating.

Table G-3 shows that the carbon content for the 0%, 35%, and 54% power fade samples are very similar. These data show that there is no reduction in the bulk cathode carbon content as a result of aging, even at 54% power fade. These data indicate that cathode carbon loss is not a likely power fade mechanism in Gen 2 cells.

APPENDIX H. ELECTROCHEMICAL MODELING

H.1 PHENOMENOLOGICAL MODEL

Dennis Dees

The phenomenological modeling effort is aimed at examining the impedance rise in Gen 2 technology cells. The overall goal of this work is to associate changes that are seen in the post-test diagnostic studies with the loss of electrochemical performance, as measured by the HPPC tests on 18650 cells. The approach taken in this effort is to develop a model based on the analytical diagnostic studies, establish the model parameters, and conduct parametric studies with the model. The parametric studies are conducted to gain confidence with the model, examine degradation mechanisms, and analyze cell limitations. To accomplish these tasks, two versions of the model have been developed. One version simulates the cell response from AC impedance studies, and another model version is utilized for examining HPPC tests. Both of these experimental techniques are extensively used in the program to quantify the cell's electrochemical performance and that of its components. The underlying basis for both models is the same, as well as their parameter set. The modeling effort has concentrated on the positive electrode because of its importance in the cell's overall impedance rise.

The general methodology for the phenomenological model follows the work of Professor Newman at Berkeley [1], and a detailed description of the development can be found elsewhere [2]. Concentrated solution theory is used to describe the transport of salt in the electrolyte. Volume-averaged transport equations account for the composite electrode geometry. Electrode kinetics, thermodynamics, and diffusion of lithium in the oxide active particles are also included. The detailed theoretical description of the oxide active material/electrolyte interface, commonly referred to as the solid electrolyte interface, or SEI, is based on post-test analytical diagnostic studies. The SEI region is assumed to be a film on the oxide and an oxide layer at the surface of the oxide. The film on the oxide is taken to be an ill-defined mixture of organic and inorganic material through which lithium ions from the electrolyte must diffuse and/or migrate across to react electrochemically at the surface of the oxide. The lithium is then assumed to diffuse through the oxide surface layer and into the bulk oxide material in the particle. A double-layer capacity is added in parallel with the Butler-Volmer kinetic expression. A localized electronic resistance between the current carrying carbon and the oxide interface can be added, and a secondary film capacitance can also be included.

In the AC impedance version of the model [3], the pertinent electrochemical-reaction, thermodynamic, and transport equations were linearized for a small sinusoidal perturbation. The resulting system of differential equations was solved numerically using a partial differential equation solver over the frequency range of interest. The level of complexity of the model made determining all of its approximately 35 parameters independently a challenge. More than half of the parameters were set by cell construction, obtained from the literature, or estimated. Electrode open circuit voltage curves were determined from the slow cycling of half-cells. Diffusion, Hittorf, and concentration cell studies were performed on the electrolyte to obtain a set of transport and thermodynamic parameters for the electrolyte. The remaining 10 parameters, most of which were associated with SEI phenomena, were determined from the reference electrode cell measurements. A comparison of the model simulation with the positive electrode experimental AC impedance is given in Figure H-1.

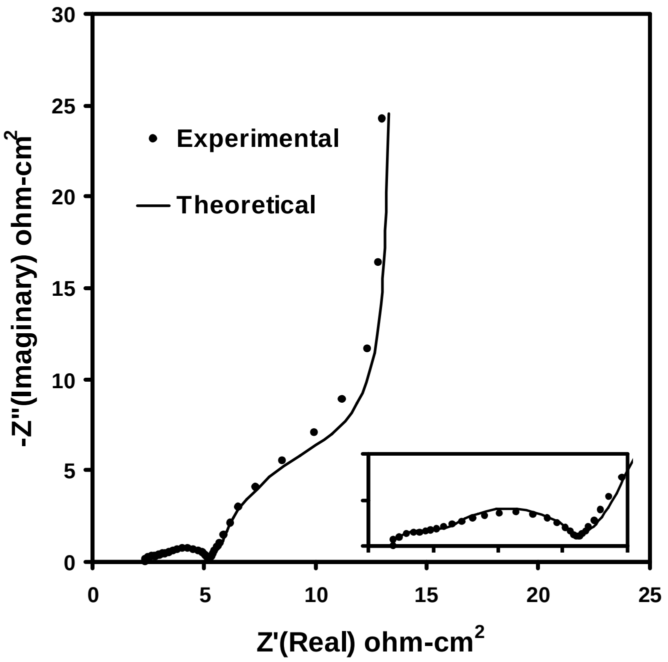

Fig. H-1. Comparison of Phenomenological Model and Experiment for the Positive Electrode AC Impedance (100 kHz–1 mHz) at 60% State of Charge.

In order to fit the low-frequency Warburg impedance for the positive electrode, a bimodal particle distribution of oxide particles in the electrode was assumed. These two particle sizes were further assumed to only differ in active area and lithium diffusion length in the bulk oxide. The fit of the low-frequency AC impedance data indicated that approximately 40% of the oxide had a characteristic lithium diffusion length of 1.0 μm and the remainder had a diffusion length of 2.6 μm. These two characteristic lengths are significantly greater than the oxide primary particle size and are indicative of the extent to which the electrochemical reaction penetrates into the secondary particles, as well as the amount of solid-state lithium diffusion occurring across oxide primary particle interfaces. Therefore, the lithium diffusion coefficient through the bulk oxide used in the model represents a weighted average of the diffusion of lithium through the primary particles and across primary particle interfaces.

EIS studies on the aging of Gen 2 18650 cells indicate that the interfacial impedance (i.e., the high-frequency arcs on the Nyquist plot) of the cells grows all through a cell's life. Furthermore, the low-frequency Warburg diffusional impedance tail also begins to increase late in life. The initiation of the increase in the cell's diffusional impedance roughly corresponds to a change in the impedance growth rate (i.e., from square-root of time to proportional in time) of the Gen 2 18650 cells as measured by the HPPC tests. The frequency dependence of the Gen 2 18650 cell's impedance increase can alternatively be represented in Figure H-2, where the change in the magnitude of the impedance in each frequency range is given as a function of time. The advantage of this method is that the time constant (i.e., as represented by frequency) of the impedance increase can be easily seen. While all six frequency ranges eventually exhibit an increase in impedance, most of the observed increases occur over three orders of magnitude of frequency.

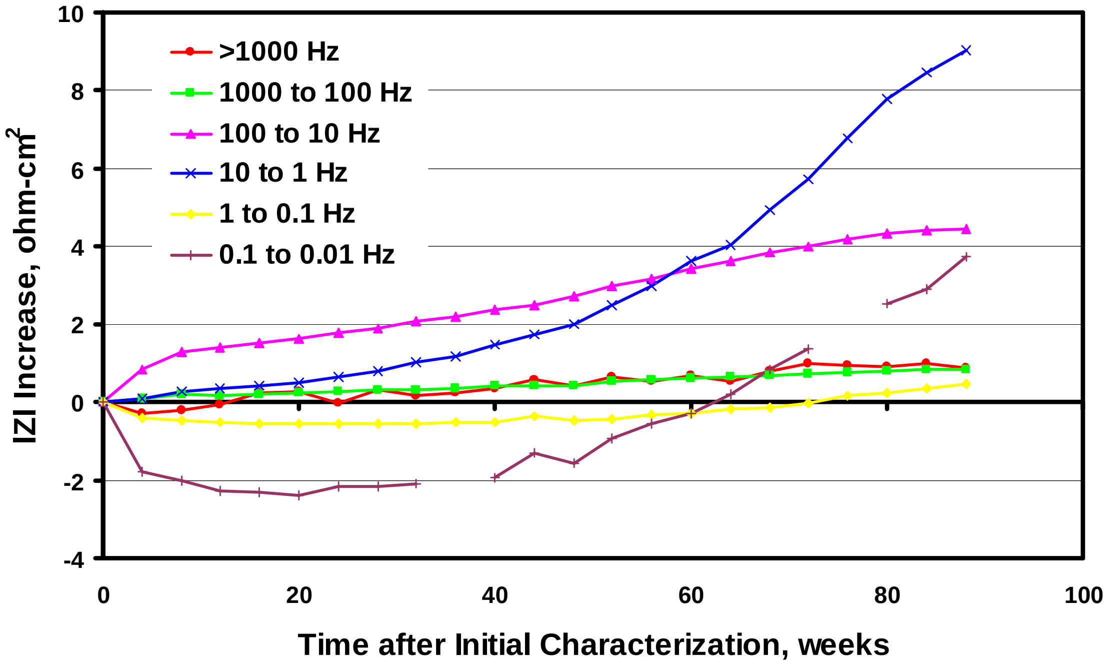

Fig. H-2. Increase in Magnitude of EIS Impedance after Initial Characterization during 45°C Calendar Aging of Gen 2 Technology 18650 Cell.

The major increase in interfacial impedance actually corresponds to impedance increases between 100 and 1 Hz. This roughly corresponds to phenomena with a time constant between 0.01 and 1 second. While somewhat arbitrary, the increase in interfacial impedance can be broken down in terms of orders of magnitude of frequency. The impedance between 100 and 10 Hz is continuously growing throughout the life of the cell, but in general goes through two steps: an initial step in the first 8 weeks that is responsible for most of the cell's initial impedance rise, and a second step at around 40 weeks that corresponds to major impedance increases in the 10 to 1 Hz and 0.1 to 0.01 Hz frequency ranges. Further, it is the impedance increase between 0.1 to 0.01 Hz that is responsible for the increase in diffusional impedance late in cell life, which appears to follow the interfacial impedance increases late in life. One apparent difference between the interfacial and diffusional impedance increases late in life is that the interfacial impedance increases appear to level off after 80 weeks.

The diffusional impedance between 0.1 to 0.01 Hz exhibits a significant drop between the initial characterization and the first reference performance test. This drop in impedance does not show up in the HPPC tests because the frequency range is too low. In fact, because of the significant changes in impedance that occur early in life, it is interesting to examine a similar plot, given in Figure H-3, where the reference impedance is taken at the 8 week reference performance test. In Figure H-3, it is easy to see that the two interfacial frequency ranges accounting for most of the increase in interfacial impedance (i.e., 100 to 10 Hz and 10 to 1 Hz) closely follow each other for about 30 weeks before the interfacial impedance in the lower frequency range increases dramatically.

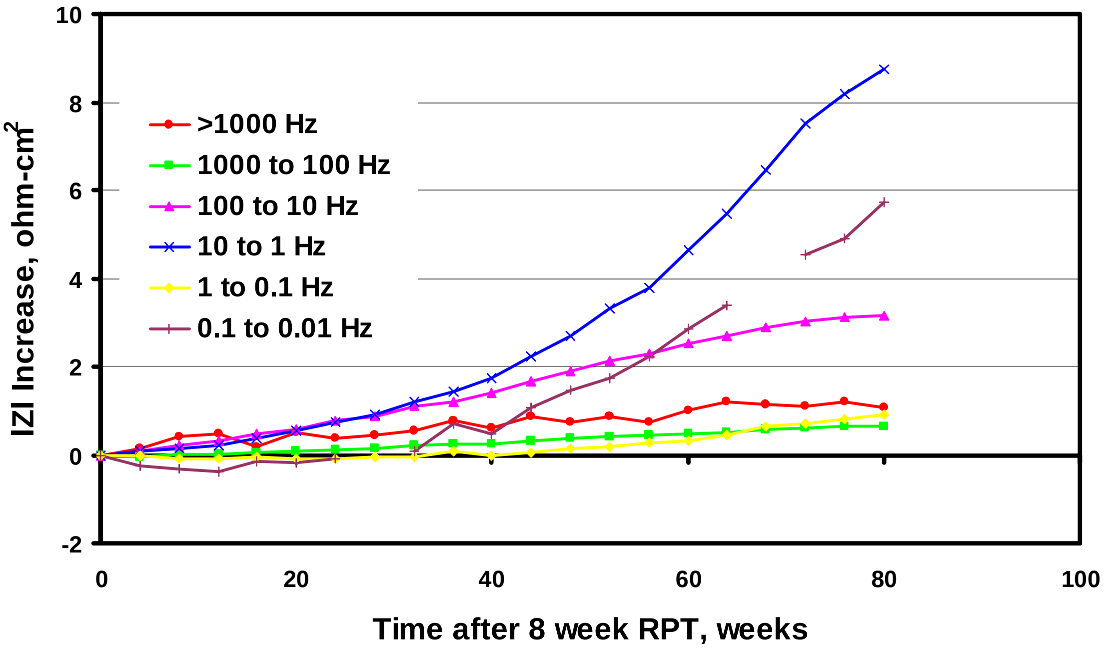

Fig. H-3. Increase in Magnitude of EIS Impedance after 8-Week RPT during 45°C Calendar Aging of Gen 2 Technology 18650 Cell.

The standard Gen 2 technology impedance increases can be compared to the aging of the Variant C 18650 cells, as shown in Figure H-4. Both types of cells exhibit significant increases in their interfacial impedance between 100 and 1 Hz, but the specific behavior is very different for each frequency range over the life of the cell. The impedance increase for the Variant C cell between 100 and 10 Hz occurs early in life, but, unlike that of the standard technology cell, levels off quickly. The 10 to 1 Hz Variant C data shows a significant increase early in life and then continues to increase linearly to the end of the test. The linear behavior of the 10 to 1 Hz Variant C impedance increase data is even clearer in Figure H-5, where, as in Figure H-3, the impedance at the 8-week reference performance test is used as the reference. It is also clear from Figure H-5 that there is no significant increase (maybe a slight upturn at around 50 weeks) in the impedance late in life, as was apparent in the standard technology.

Because of the complex nature of electrochemical systems, it is difficult to change only one variable, but the increase in aluminum doping of the positive electrode's active material used in Variant C cells probably comes very close. The significant differences in the 18650 cell aging characteristics are a strong indicator of the importance of the positive electrode's active material to the performance of the cell. This importance has also been confirmed through extensive reference electrode studies. The observed increases in the interfacial impedance during aging indicate that the surface of the oxide changes with time. Differences between the impedance aging behavior of the Variant C and the standard Gen 2 cells indicate that minor changes in the surface characteristics can have a significant impact on cell impedance.

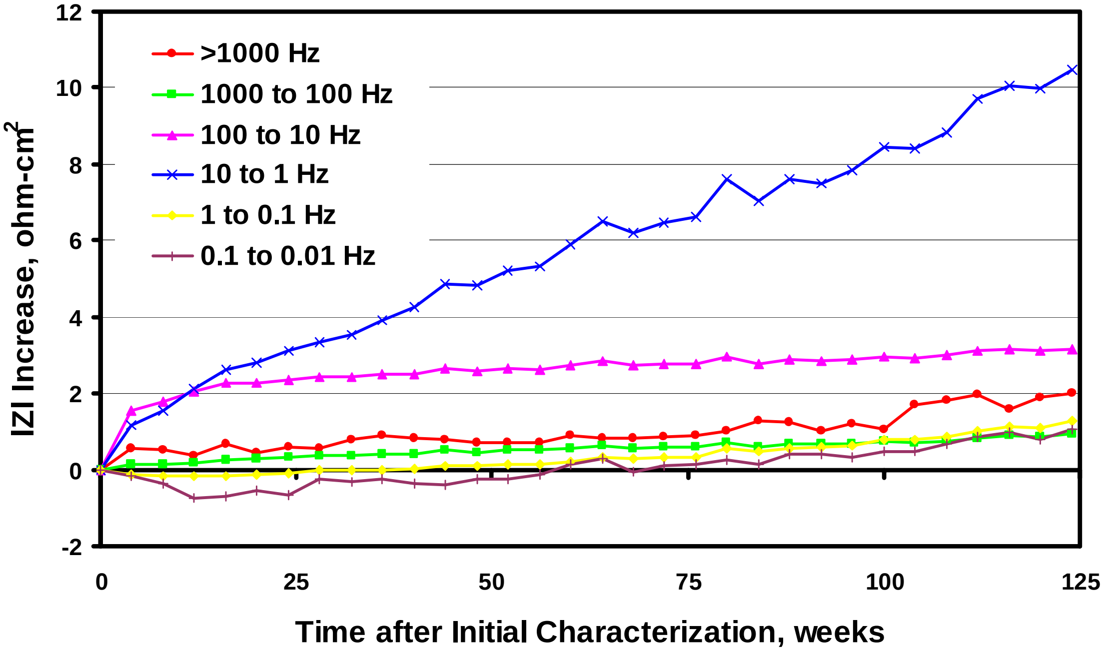

Fig. H-4. Increase in Magnitude of EIS Impedance after Initial Characterization during 45°C Calendar Aging of Variant C Technology 18650 Cell.

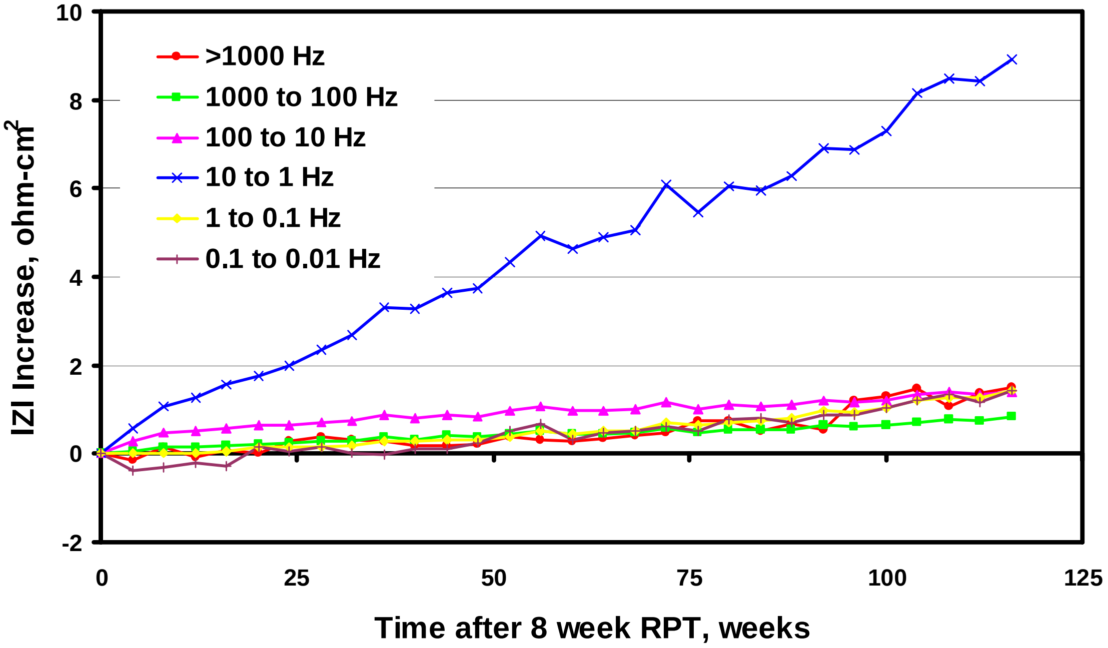

Fig. H-5. Increase in Magnitude of EIS Impedance after 8-Week RPT during 45°C Calendar Aging of Variant C Technology 18650 Cell.

As discussed above, reference electrode cell studies on harvested electrodes from Gen 2 18650 cells indicate that most of the cell impedance growth can be associated with the positive electrode. Therefore, during the majority of the Gen 2 technology cell's usable life, most of the impedance growth occurs in the positive electrode's interfacial impedance. During this time, one typically sees approximately 25% power fade and increases in the cell's interfacial arc in the range of 5–10 Ω cm^2 with a capacity fade of 10–15%. Late in life, the positive electrode's interfacial and diffusional impedances are the major contributors to the cell's impedance growth.

The phenomenological model was utilized to examine aging effects associated with the positive electrode when only its interfacial impedance increases. Three possible sources for the interfacial impedance increase were identified, which are consistent with at least some experimental observations. First, an interfacial impedance increase could result from a degradation of the ionic pathway for lithium ions between the electrolyte in the electrode pores and the bulk oxide active material. This could result from changes in the electrolyte/oxide interfacial structure, composition, and/or properties and would have a direct impact on the positive electrode's interfacial impedance. There are several parameters in the model that are associated with the interfacial phenomena that would have a direct impact on the interfacial impedance. Examples include the effects on the positive electrode impedance of changing the lithium diffusion coefficient through the oxide surface layer (see Figure H-6) and the kinetic exchange current density (see Figure H-7).

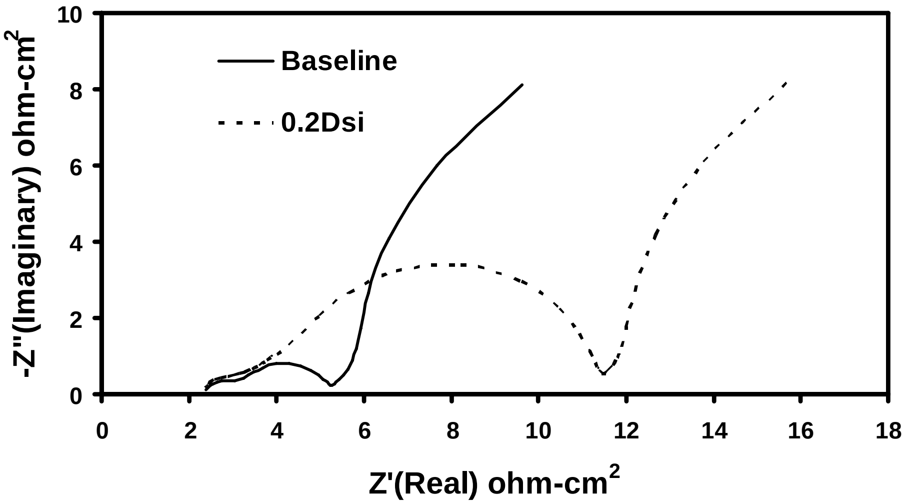

Fig. H-6. Simulation of the Positive Electrode AC Impedance (100 kHz–10 mHz) at 60% State of Charge, Showing the Effect of a Factor of 5 Reduction in the Lithium Diffusion Coefficient through the Oxide Surface Layer.

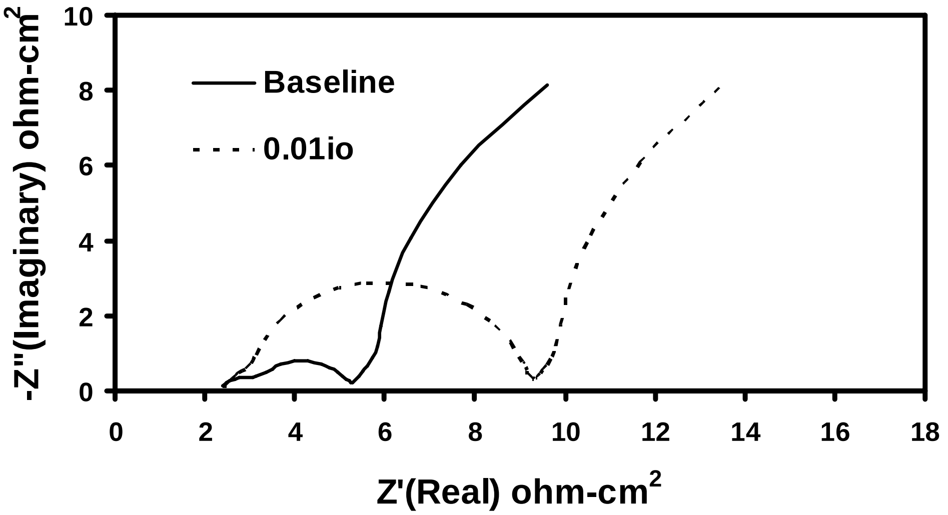

Fig. H-7. Simulation of the Positive Electrode AC Impedance (100 kHz–10 mHz) at 60% State of Charge, Showing the Effect of a Two Order of Magnitude Reduction in the Kinetic Exchange Current Density.

As demonstrated in the above examples, changing any of the interfacial parameters in the model can have an impact on the interfacial impedance of the positive electrode. However, a closer look at the frequency dependence of the parameter changes reveals a different conclusion. The frequency dependence of the positive electrode's impedance increase is given in Figure H-8, where the change in the magnitude of the impedance in each frequency range is given as a function of the relative change in oxide surface layer lithium diffusion coefficient. A similar plot is also given in Figure H-9 for the effect of changing the kinetic exchange current density. Comparing the two frequency dependence impedance plots to the observed impedance increases in Gen 2 18650 cells indicates that changes in the lithium diffusion coefficient through the oxide surface layer generate impedance changes corresponding to the observed frequency range, while changes in the kinetic exchange current density do not. Unfortunately no definitive conclusion as to which interfacial phenomena has the greatest impact the impedance can be drawn from these simulations because of the somewhat subjective nature of the assumptions made during the initial fitting of the interfacial parameters.

While the size of the relative change of the interfacial parameter needed to impact the impedance may vary, in all cases, a relatively large change is required to have a significant impact on the positive electrode's impedance. This can be attributed at least partially to the ratio of the electrochemically active area to the geometric area, which is estimated to be about ten. This fact, combined with the redistribution of current in the positive electrode, which occurs as the interfacial impedance increases, tends to dilute the effect of the interfacial parameter changes. It is generally a good thing that small changes in the interfacial parameters do not have a significant effect on electrode impedance. However, the size of the model parameter changes needed to account for the impedance increase suggests that there is a general degradation of the ionic pathway significantly affecting multiple interfacial parameters in the model.

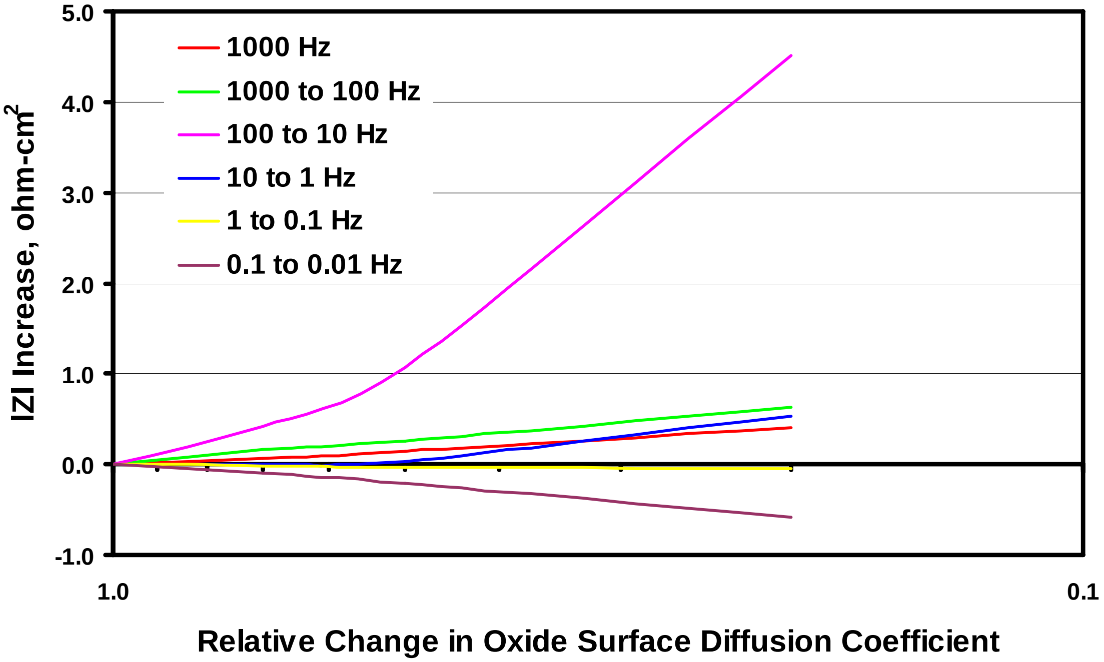

Fig. H-8. Simulation of the Change in Magnitude of EIS Impedance of the Positive Electrode, Showing the Effect of a Reduction in the Lithium Diffusion Coefficient through the Oxide Surface Layer.

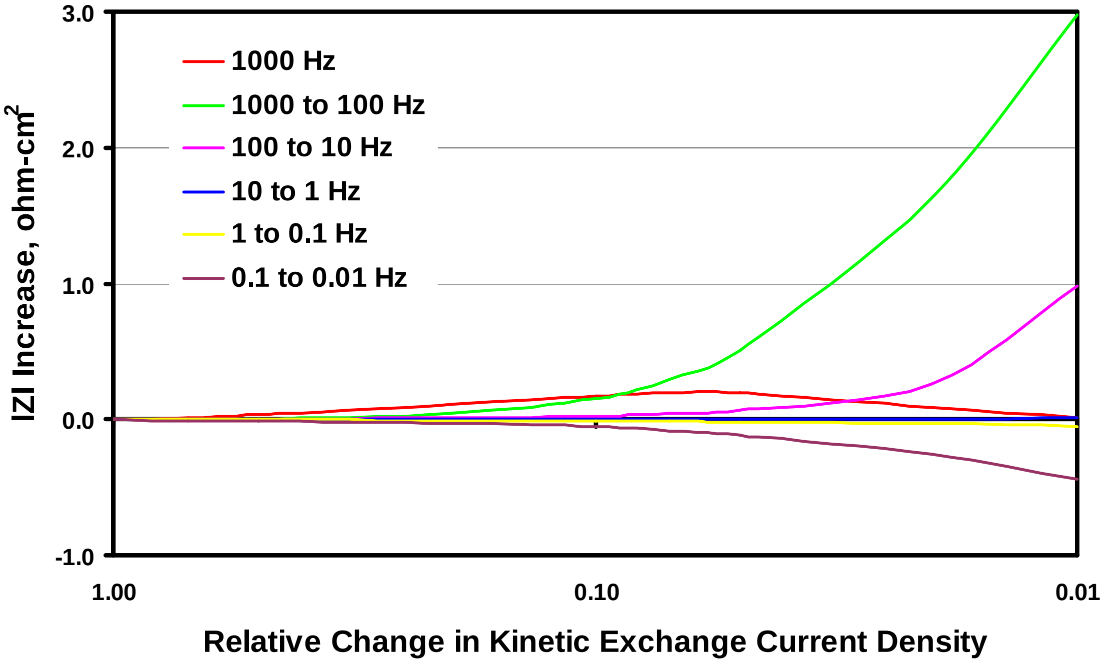

Fig. H-9. Simulation of the Change in Magnitude of EIS Impedance of the Positive Electrode, Showing the Effect of a Reduction in the Kinetic Exchange Current Density.

Another factor that could adversely affect the positive electrode's interfacial impedance is the isolation of some of the oxide from the electronically conducting carbon matrix. As discussed above, experimental studies indicate that there is some capacity loss associated with cell aging. Figure H-10 shows the simulation of the change in the impedance curve for a 20% loss of positive electrode capacity. Two cases are considered in Figure H-10, one in which the isolation of all oxide particles occurs equally, and the other for which only the finer oxide particles (i.e., the oxide particles with the shorter characteristic diffusion length) are isolated. As one may expect, isolation of the finer oxide particles exclusively has the greater impact on the interfacial impedance because of the higher surface area of the finer particles. Close examination of the impedance curves in Figure H-10 indicates that there will also be a corresponding small change in the low-frequency Warburg impedance, but this change may be difficult to discern experimentally. Both AC-impedance and HPPC simulations based on the measured cell capacity loss suggest that this effect can at best be only a minor contributor to the positive electrode's interfacial impedance increase.

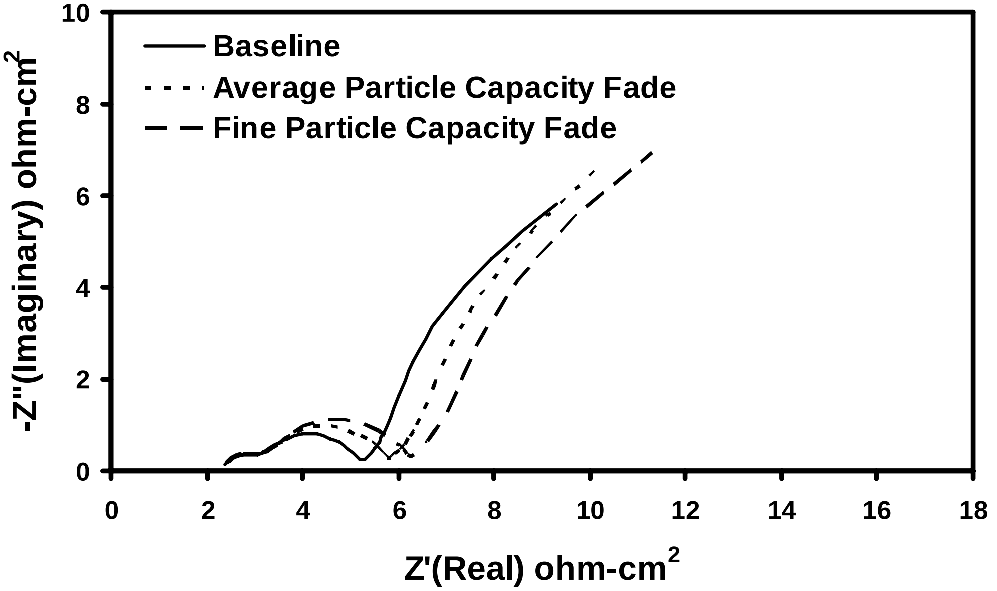

Fig. H-10. Simulation of the Positive Electrode AC Impedance (100 kHz–10 mHz) at 60% State of Charge, Showing the Effect of a 20% Capacity Fade Resulting from the Electronic Isolation of Fine and Average (i.e., both fine and coarse) Particles.

Finally, an interfacial impedance increase would result from a degradation of the electronic pathway between the carbon matrix and the oxide active material, provided the carbon matrix has a significant double-layer capacitance associated with it, which is possible. Degradation of the electronic pathway is simulated in the model by a large increase in the electronic resistance between the electronically conducting carbon matrix and oxide active material. As discussed below, experimental studies on symmetric cells with alumina-substituted Gen 2 positive electrodes indicate that most of the electrochemical activity of the carbon matrix in the positive electrode occurs at frequencies above 100 Hz. Since most of the impedance increases occur at lower frequencies, one can conclude that the positive electrode's electronic resistance does not have a significant impact on the cell's overall impedance increase. The same conclusion is also implied from differences in the aging of standard Gen 2 and Variant C 18650 cells.

The increase in interfacial impedance of the positive electrode from some combination of the three mechanisms listed above likely continues through the life of the cell. While the model is able to estimate an upper bound for the impact of the capacity loss resulting from the isolation of the oxide active material, the model by itself cannot establish the relative importance of the changes in the interfacial ionic pathway vs. changes in the interfacial electronic pathway to the oxide active material. The interfacial ionic pathway tends to be more sensitive to changes in the interface than the electronic pathway for a wide variety of electrochemical systems, including many lithium-ion technologies, which suggests that it is likely the primary source of the impedance increase. This conclusion is further substantiated by experimental studies described above. It is possible that all three mechanisms are related. As an example, chemical or physical changes in the SEI could cause degradation of the ionic pathway, as well as the electronic pathway, at the oxide interface, which could eventually lead to oxide particle isolation and capacity loss. This type of degradation phenomenon would be consistent with the square-root of time impedance growth observed in test cells.

The positive electrode's diffusional Warburg impedance changes shape and size late in the cell's life, as shown in Figure H-11. The slope of the Warburg impedance tail, which is 1.6, is somewhat larger than the theoretical and experimental value of one observed for planar diffusion geometries. As one may expect, the positive electrode diffusional impedance increases also

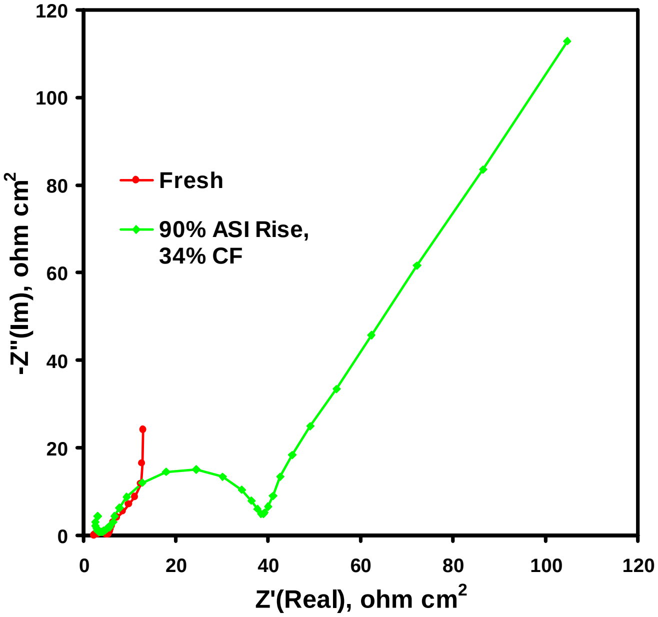

Fig. H-11. Experimental Gen 2 Positive Electrode AC Impedance (100 kHz–1 mHz) at 60% State of Charge Fresh Electrode and an Aged to 90% Impedance Rise Electrode.

make it more difficult to get the lithium in and out of the oxide active material (i.e., the cell has to be cycled at lower rates to obtain its capacity). As is the case for the interfacial impedance increases, and will also be shown below for the diffusional impedance increases, it is not possible to match all observed impedance changes by varying just one model parameter. However, it is instructive to see which parameter changes tend to be the most consistent with the experimental evidence.

In the model, the characteristic diffusion length of lithium through the oxide is assumed to be inversely proportional to the electrochemically active area, and the electrochemically active area is also proportional to the amount of active oxide material. Therefore, any change in capacity or electrochemically active area impacts the diffusion of lithium through the oxide, and thus affects the low-frequency impedance. The particularly high capacity fade (34%) for the aged cell data shown in Figure H-11 is great enough to have a significant impact on the low-frequency impedance, as shown by the simulation results in Figure H-12. Figure H-12 also shows that losing fine particle capacity (i.e., oxide with the shorter characteristic diffusion length) has a greater impact on the impedance, but either way the change cannot account for the impedance increases exhibited in actual cells. Because there is no experimental measurement on the loss of electrochemically active area, its potential impact on the low-frequency impedance is much greater, as shown in Figure H-13. However, simulations indicate that almost all of the area must be lost to generate similar low-frequency impedances compared to those observed in actual cells, even then the slope of the Warburg impedance is approximately 0.9. Simulations also indicate (see Figure H-14) that the preferential loss of coarse active area has a greater impact on the diffusional impedance than the general loss of active area, and the slope of the Warburg impedance is approximately 1.9.

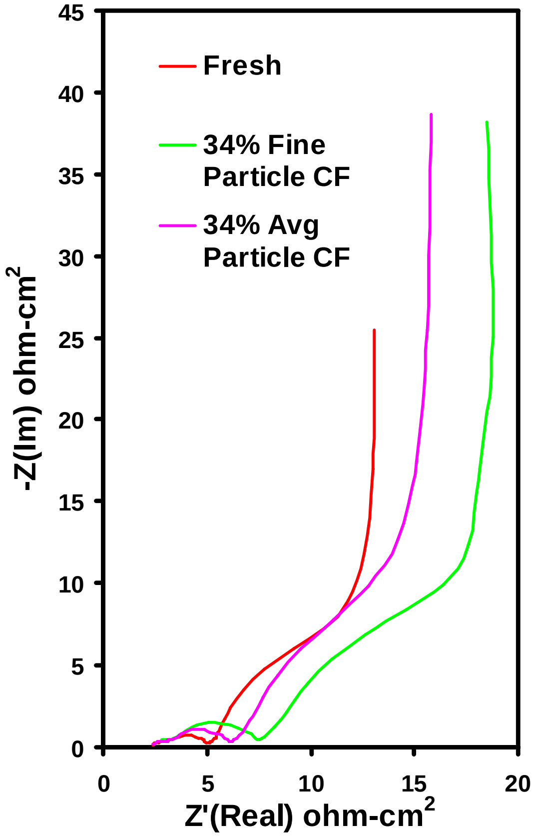

Fig. H-12. Simulation of the Positive Electrode AC Impedance (100 kHz–1 mHz) at 60% State of Charge, Showing the Effect of a 34% Capacity Fade Resulting from the Electronic Isolation of Fine and Average (i.e., both fine and coarse)

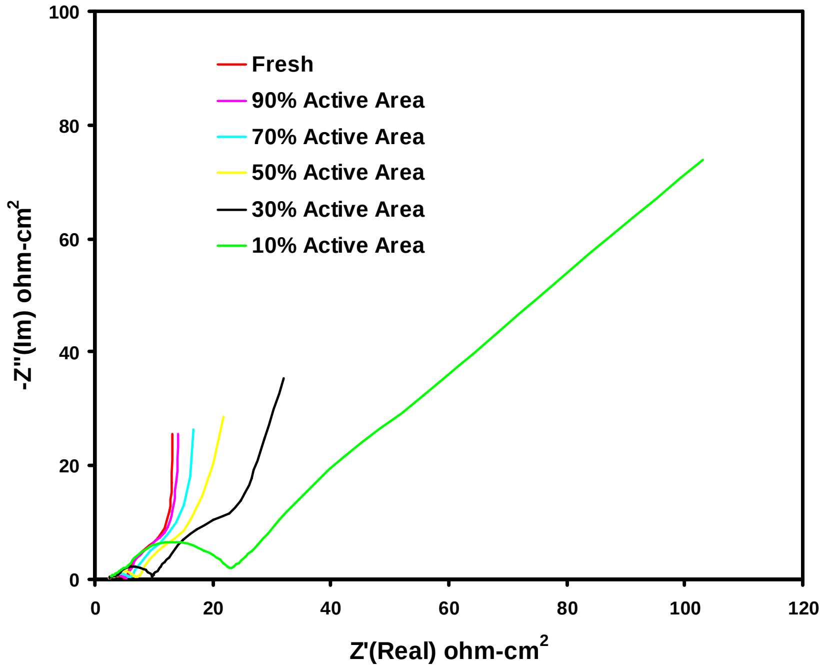

Fig. H-13. Simulation of the Positive Electrode AC Impedance (100 kHz–1 mHz) at 60% State of Charge, Showing the Effect of Losing Electrochemically Active Area.

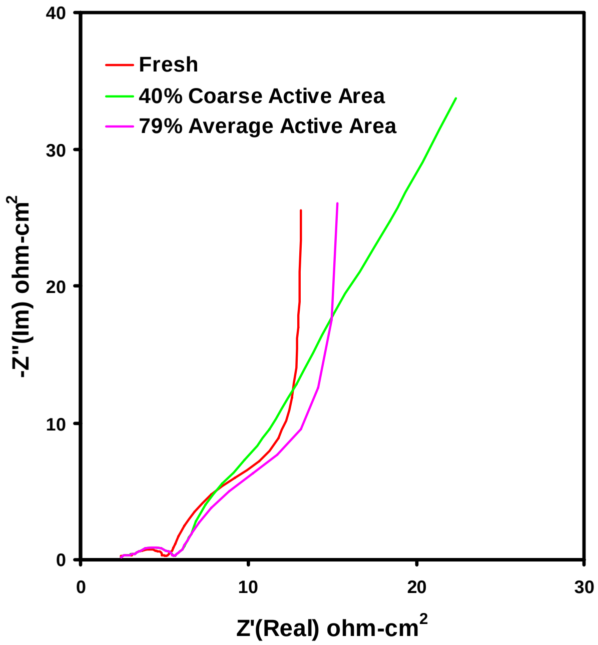

Fig. H-14. Simulation of the Positive Electrode AC Impedance (100 kHz–1 mHz) at 60% State of Charge, Showing the Effect of Losing Coarse and Average (i.e., both fine and coarse) Electrochemically Active Areas.

Reducing the lithium diffusion coefficient through the bulk oxide active material has a direct impact on the low-frequency diffusional impedance, as shown in Figure H-15. The simulations also indicate that the lithium diffusion coefficient through the bulk oxide would need to be reduced by approximately two orders of magnitude to result in low-frequency impedances similar to those observed in actual cells, and the predicted slope of the Warburg impedance would be approximately 0.9. A more detailed examination of the simulated impedance changes (see Figure H-16) shows that most of the impedance increases occur at frequencies less than 0.1 Hz, which is in agreement with experimental observations. Diagnostic studies indicate that there is no major change in the oxide's bulk structure, which would be expected to accompany any significant change in the lithium diffusion coefficient. However, it is important to note here that because solid-state lithium diffusion occurs across primary particle interfaces, a degradation of those interfaces can manifest itself as a lower effective lithium diffusion coefficient.

Finally, the degradation of electrolyte transport properties and/or a change in electrode microstructure that affects the electrode's porosity or tortuosity can affect the positive electrode's low-frequency impedance. Figure H-17 shows the simulated impact on the positive electrode impedance from an increase in the electrolyte's tortuosity. Simulations indicate that the tortuosity must be increased by two orders of magnitude to result in low-frequency impedances similar to those observed in actual cells, and interestingly the predicted slope of the Warburg impedance would be approximately 1.6. However, a more detailed examination of the simulated impedance changes (see Figure H-18) shows that the impedance increases occur over a wide frequency range, which is in direct contradiction to experimental observations. Also, degradation of electrolyte transport properties and/or a change in electrode microstructure that affects the electrode's porosity or tortuosity are not commonly supported by post-test diagnostic studies.

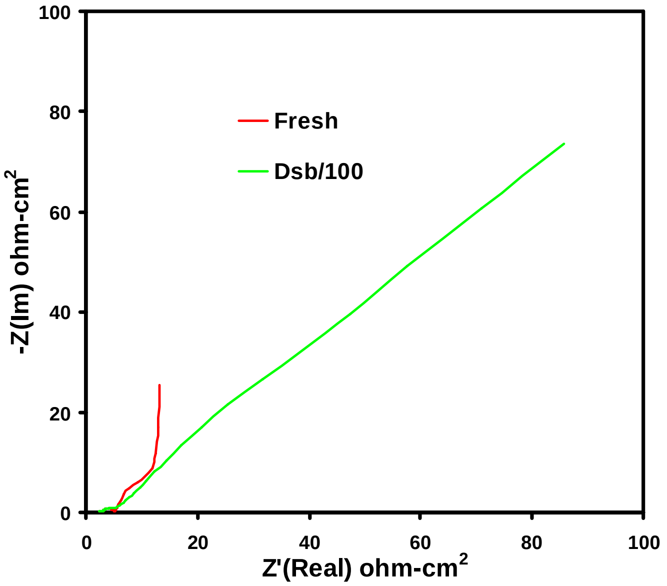

Fig. H-15. Simulation of the Positive Electrode AC Impedance (100 kHz–1 mHz) at 60% State of Charge, Showing the Impact of Slowed Lithium Diffusion through Bulk Oxide Active Material.

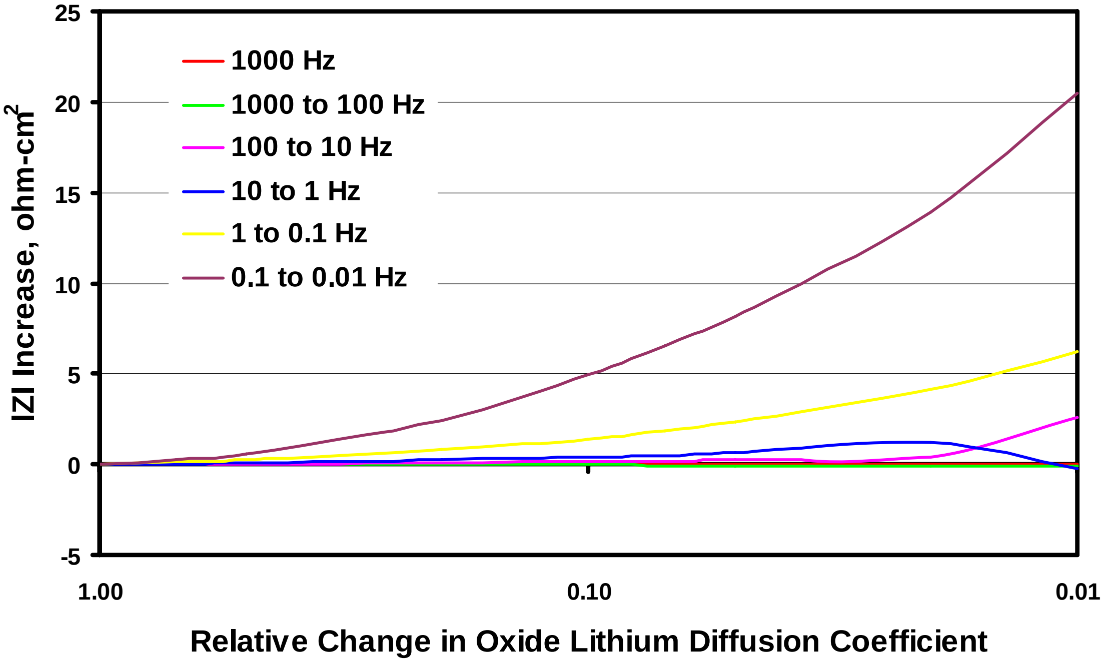

Fig. H-16. Simulation of the Change in Magnitude of EIS Impedance of the Positive Electrode, Showing the Impact of Slowed Lithium Diffusion through Bulk Oxide Active Material.

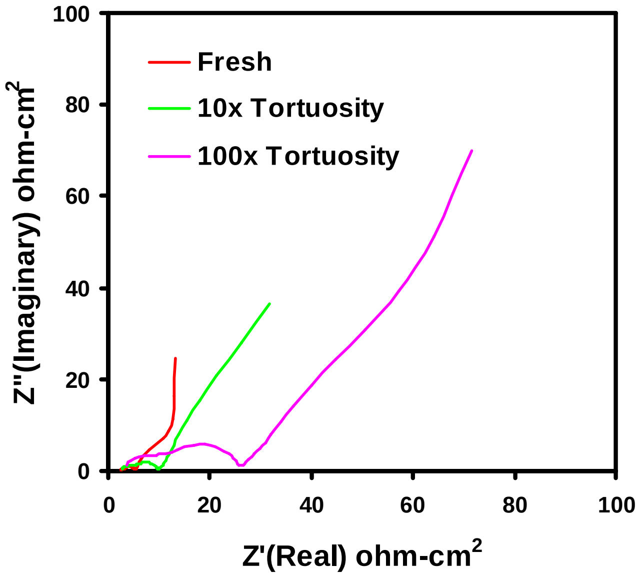

Fig. H-17. Simulation of the Positive Electrode AC Impedance (100 kHz–1 mHz) at 60% State of Charge, Showing the Impact of Increasing Electrolyte Tortuosity in the Positive Electrode.

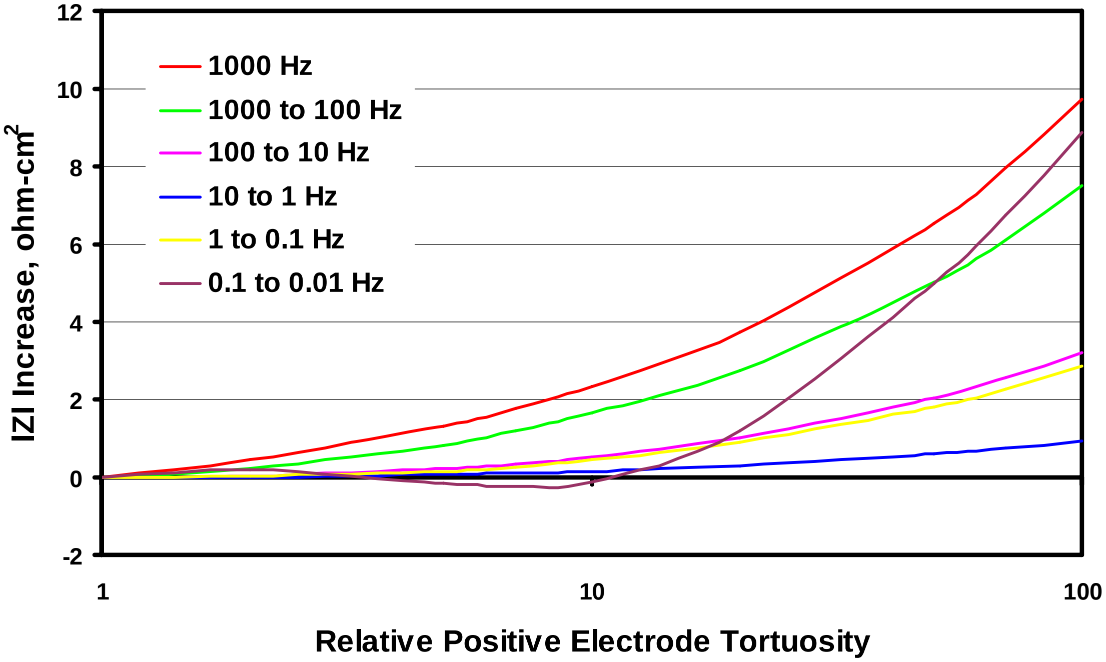

Fig. H-18. Simulation of the Change in Magnitude of EIS Impedance of the Positive Electrode, Showing the Impact of Increasing Electrolyte Tortuosity.

Model simulations of the positive electrode's impedance indicate that more than one aging phenomena likely contribute to the cell's diffusional Warburg impedance rise late in the cell's life. These include a slowing of lithium diffusion through the oxide, a loss of electrochemically active area, and capacity fade. As with the interfacial impedance increases, the measured capacity fade can only account for a small fraction of the impedance increase. Degradation of lithium diffusion through the oxide could be caused by changes in the oxide structure (e.g., micro-cracks), but also could result from changes in the intra-granular region between primary particles. A degradation of the intra-granular region and the loss of electrochemically active area are consistent with an extensive general degradation of the oxide primary particles' interfaces.

A reoccurring theme that has come out of this modeling effort is the importance of the morphology of the oxide primary/secondary particles, more specifically the primary particle interfacial characteristics, to the overall performance and stability of the cell. Because this modeling effort uses volume-averaged transport equations, much of the detail of the individual particles has been averaged out. Clearly, having the ability to include multiple active material fractions in the model is a necessary improvement that adds much to the understanding of the oxide particles. In an effort to more closely examine secondary oxide particle microstructure, a model was developed for an idealized two-dimensional secondary oxide active material particle composed of an agglomeration of hexagonally shaped primary particles. The model includes electron migration and lithium diffusion in the oxide particles. Diffusion and migration resistive effects can be added to the primary particle boundaries as needed. Thermodynamics and kinetics are included on electrochemically active primary particle surfaces, and resistive effects are included at electronic contact surfaces.

Initial studies were conducted using 19 hexagonally close-packed primary particles (1 micron sides) with the electrochemically active surface on the outside perimeter. Varied also was the amount of electronically conducting contact area, also on the outside perimeter. The impact of the contact area on the overall particle impedance is given in Figures H-19 (initial impedance) and H-20 (18 s impedance). It can be easily seen that changes in the electronic contact area of the oxide secondary particles will have little impact on particle impedance, except for very low oxide electronic conductivities or small contact areas. With the electronic conductivity of the oxide active material expected to be in the range of 10^{-2} to 10^{-3} Ω^{-1} cm^{-1}, based on limited literature values, and with five times the amount of carbon black in the positive electrode needed to completely cover all oxide secondary particles, it is not likely that any rearrangement of the carbon in the positive electrode will have a significant impact on cell impedance.

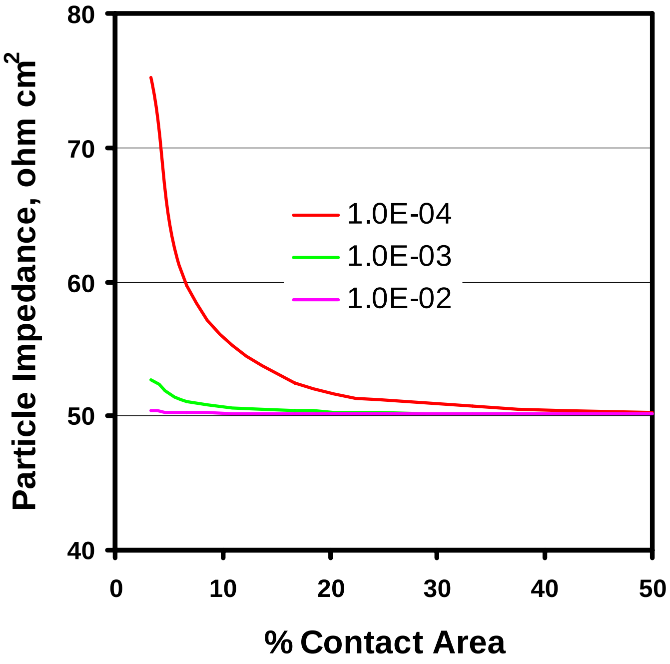

Fig. H-19. Simulated Oxide Particle Initial Impedance after a Current Pulse for Idealized Secondary Particle, Showing the Effect of Electronic Contact Area on Outer Perimeter of Particle for Three Oxide Bulk Electronic Conductivities (10^{-2}, 10^{-3}, and 10^{-4} Ω^{-1} cm^{-1}).

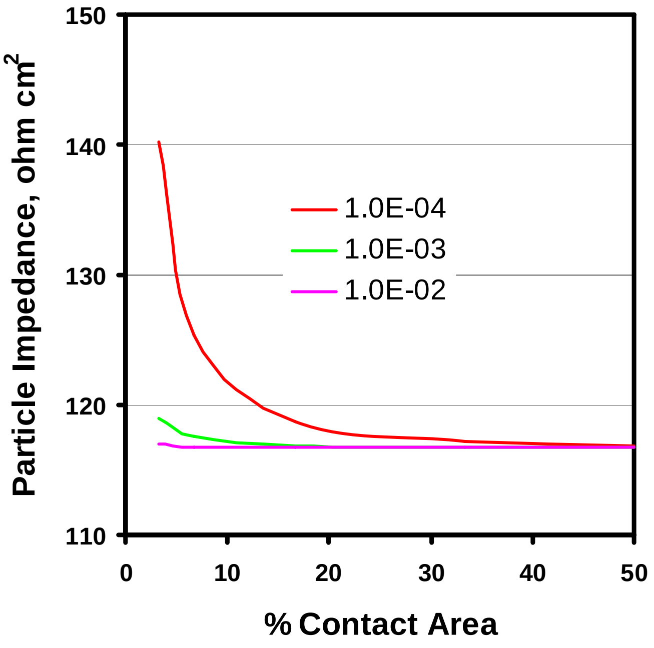

Fig. H-20. Simulated Oxide Particle 18 s Impedance after a Current Pulse for Idealized Secondary Particle, Showing the Effect of Electronic Contact Area on Outer Perimeter of Particle for Three Oxide Bulk Electronic Conductivities (10^{-2}, 10^{-3}, and 10^{-4} Ω^{-1} cm^{-1}).

As discussed above, for an increase in the electronic resistance between the conductive carbon matrix and the oxide active material in the positive electrode to impact the interfacial resistance, the carbon matrix must exhibit significant capacitive effects. The capacitive behavior of the carbon matrix was examined using a special symmetric button cell. The electrodes in the button cell were fabricated according to Gen 2 positive electrode specifications, except that the oxide active material was replaced with alumina. The impedance of the cell is given in Figure H-21 and is compared to the impedances of two other symmetric cells. One cell had only aluminum current collectors as the electrodes, and with the other had Gen 2 positive electrodes at 60% SOC. Comparison of the results from the cell with only aluminum current collectors to the alumina-substituted electrode cell indicates that the carbon is electrochemically active. However, the sharp rise in impedance below 100 Hz for the alumina-substituted Gen 2 positive electrode cell indicates that the carbon's capacitive behavior occurs above 100 Hz. As can be seen from the above discussion, the majority of the Gen 2 technology cell's interfacial impedance increase occurs between 100 and 1 Hz, suggesting that the positive electrode's electronic resistance does not have a significant impact on the cell's overall impedance increase. The same conclusion is implied from differences in the aging of standard Gen 2 and Variant C 18650 cells, as described above.

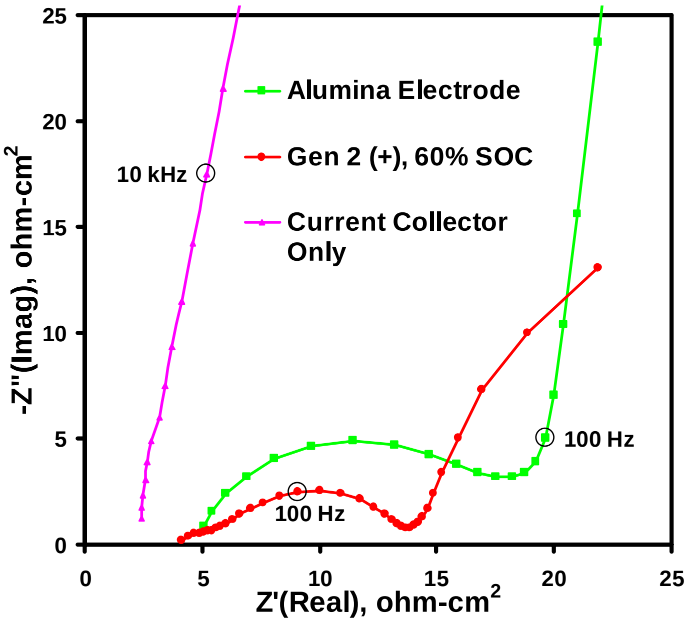

Fig. H-21. AC Impedance Results for Symmetric Button Cells: Gen 2 Positive Electrodes with Alumina Substituted for Oxide Active Material, Gen 2 Positive Electrodes at 60% SOC, and Aluminum Current Collector Electrodes.

Thus far, this appendix has concentrated on positive electrode AC impedance modeling studies as a tool to examine cell aging phenomena associated with the positive electrode. Although most experimental measurements of cell impedance increases are based on HPPC test results, the AC impedance studies more closely examines impedance phenomena with a characteristic time constant less than one second, which is where most of the interfacial impedance increases occur. The model used to simulate HPPC tests has the advantage of showing quantities such as current and concentration distributions in a much more straightforward manner (i.e., not as complex variables). Here, the HPPC test simulations will be used to gain insights into positive electrode operation, examine limitations, and explore performance improvements.

Figure H-22 gives the simulated Gen 2 positive electrode half-cell voltage during a 5C HPPC test at 60% SOC. The electrode resistive and interfacial effects cause the initial change in voltage at the beginning of the pulses. The electrode diffusional effects in the electrolyte and oxide then gradually cause slower changes in voltage during the current pulses. The circled region indicates the relaxation time between discharge and charge current pulses. Even though the relaxation time (32 s) is almost twice the discharge time (18 s), the electrode does not fully relax before the charge pulse. The reason for the slow relaxation of the electrode can be seen from the current distribution during the current pulses shown in FigureH-23 for the times indicated by the arrows in Figure H-22. The variation in the current distribution from the separator side of the positive electrode (50 µm) to the current collector side (85 µm) generates a similar distribution of lithium in the oxide during the discharge pulse. It is this nonuniform distribution of lithium in the positive electrode active material that relaxes through low-level internal currents in the electrode during the open circuit period, causing a slow relaxation of the electrode voltage.

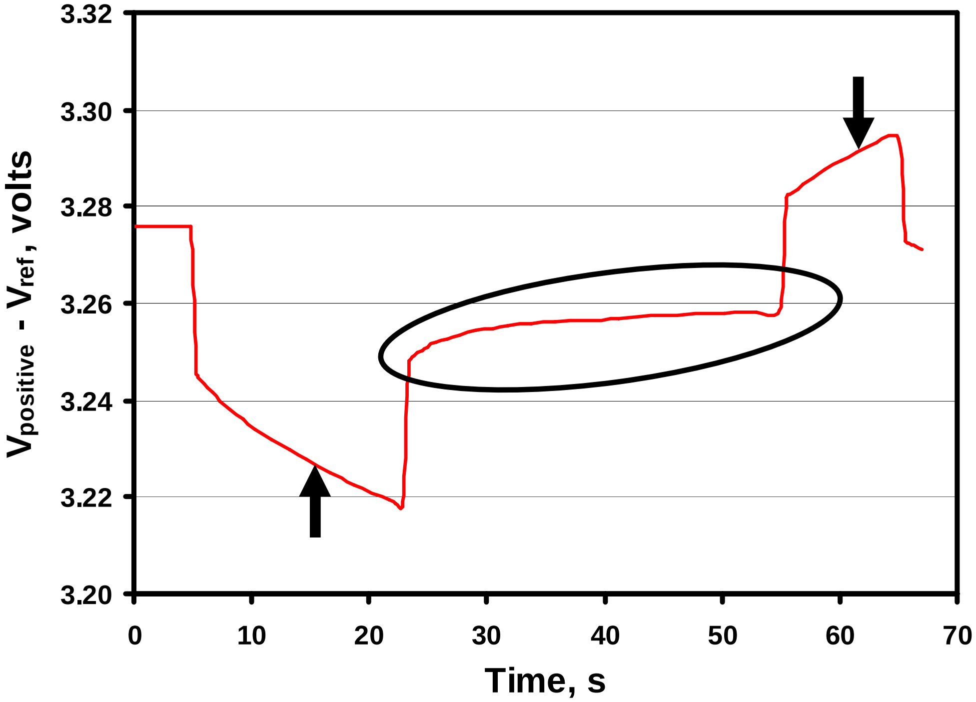

Fig. H-22. Simulation of Positive Electrode Half-Cell Voltage during a 5C HPPC Test at 60% SOC. The arrows indicate current distribution times shown in Figure 23, and circled region indicates slow relaxation between discharge and charge pulses.

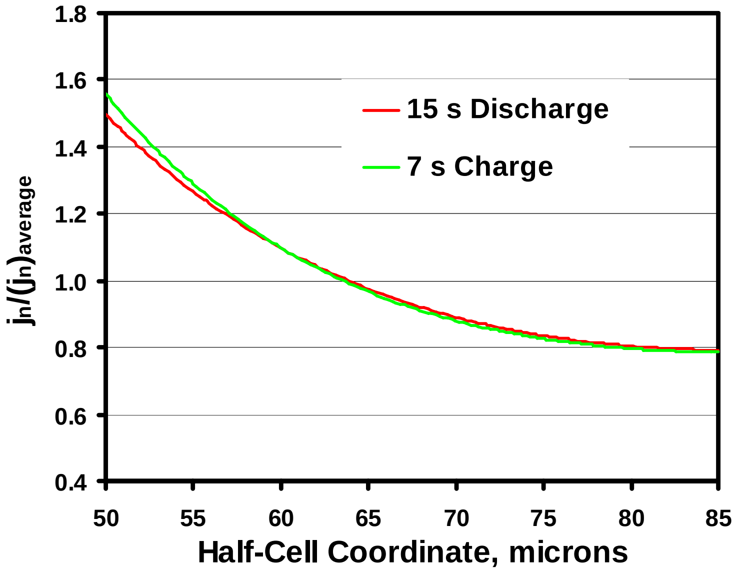

Fig. H-23. Simulation of Positive Electrode Half-Cell Voltage during a 5C HPPC Test at 60% SOC, Showing the Current Distribution from the Separator Side of the Positive Electrode (50 µm) to the Current Collector Side (85 µm) during the Discharge and Charge Pulses.

Even though the current distribution through the positive electrode is nonuniform and does generate lithium concentration gradients (front to back) in the oxide active material during the current pulses, it is relatively uniform (only varying by a factor of two front to back) compared to many other battery technologies. The sloping open circuit voltage curve of the intercalation oxide active material tends to spread out the current through the electrode relatively evenly. Because of a higher electrochemically active area, the fine oxide secondary particles carry a majority of the electrode's total current, but the current densities on the surface of the particles are similar, especially at the beginning of the discharge pulse, as shown in Figure H-24.

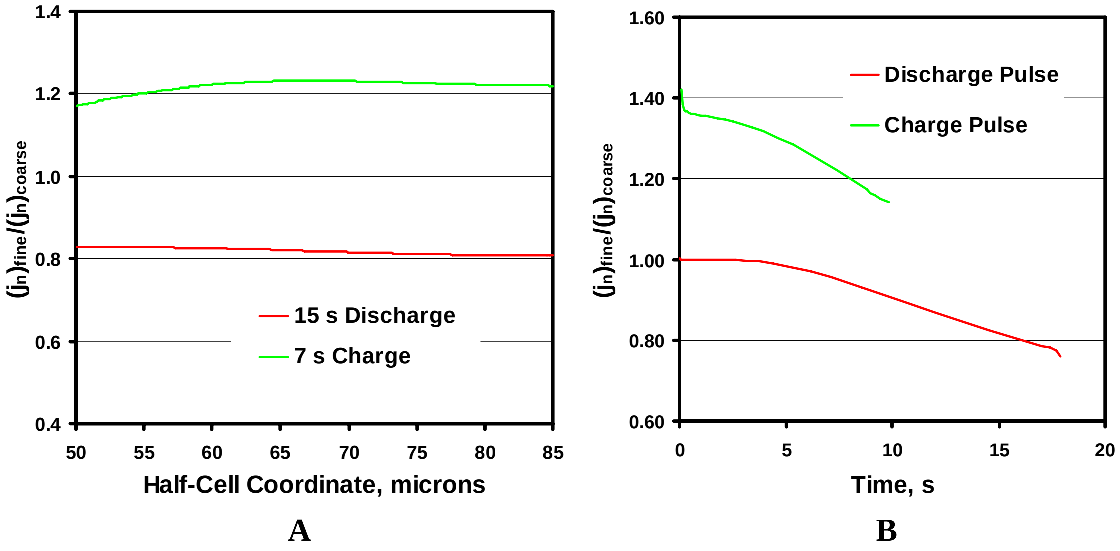

Fig. H-24. Simulation of Positive Electrode Half-Cell Voltage during a 5C HPPC Test at 60% SOC: (A) shows the fine:coarse current distribution ratio from the separator side of the positive electrode (50 µm) to the current collector side (85 µm) during the discharge and charge pulses, and (B) shows the fine:coarse current distribution ratio in middle of the positive electrode (half-cell coordinate = 67.5 µm) during both current pulses.

The high currents that the cell carries during the HPPC tests generate salt concentration gradients in the cell's electrolyte, as shown in Figure H-25 for a positive electrode with a double separator. As can be seen in the figure for a 5C pulse on the Gen 2 positive electrode, the concentration gradients are relatively small, which do not have a major impact on the cell's performance. Because the discharge current pulse is greater and longer than the charge pulse and because it drains the electrolyte in the positive electrode of salt, electrolyte limitations in the positive electrode occur during high current discharge pulses, as shown in Figure H-26. Simulations indicate that lithium-ion transport in the positive electrode half-cell with a double separator can support a 15C discharge pulse. Pulses greater than 15C are difficult to simulate because of the combined lithium-ion diffusional effects in the electrolyte, oxide, and interface.

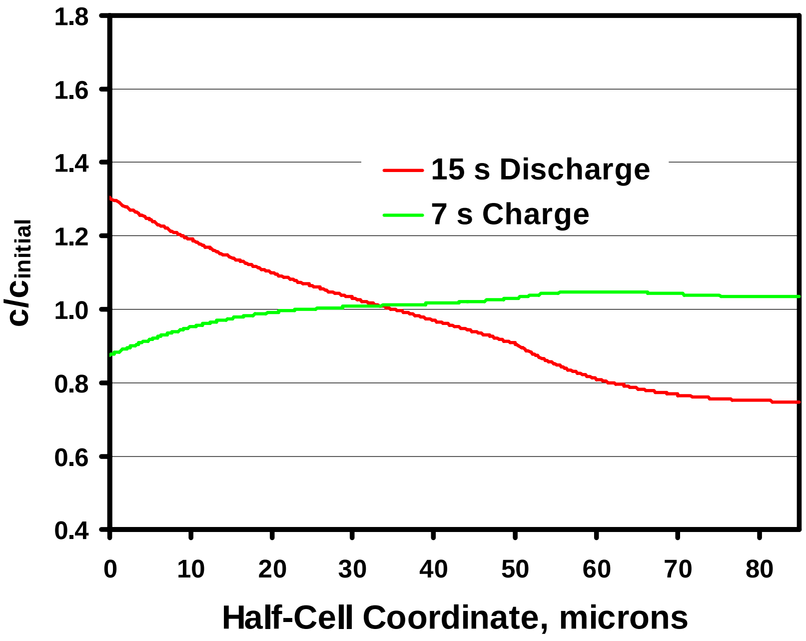

Fig. H-25. Simulation of Positive Electrode during a 5C HPPC Test at 60% SOC, Showing the Salt Concentration Distribution at 15 s into the Discharge Pulse and 7 s into the Charge Pulse. The separator side of the negative electrode is at 0 µm, the separator side of the positive electrode is at 50 µm, and the current collector side of the positive electrode is at 85 µm.

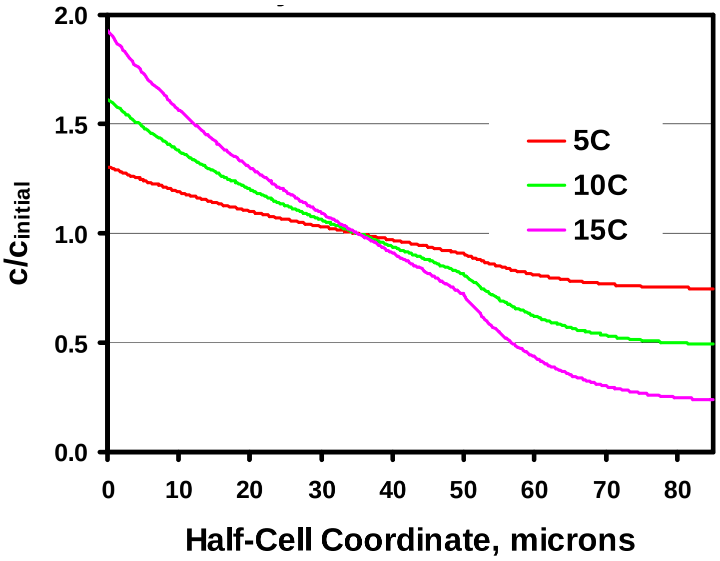

Fig. H-26. Simulation of Positive Electrode during HPPC Tests at 60% SOC, Showing the Salt Concentration Distribution at 15 s into the Discharge Pulse at Increasing Current Pulses. The separator side of the negative electrode is at 0 µm, the separator side of the positive electrode is at 50 µm, and the current collector side of the positive electrode is at 85 µm.

Changing the positive electrode's thickness will certainly impact its performance, as shown in Figure H-27. Electrochemically active area increases with electrode thickness, which improves electrode performance. If the C-rate of the current pulse is kept constant with increasing electrode thickness, the current density and path length also increase with electrode thickness, which would lead to transport problems for very thick electrodes. As can be seen from Figure H-28, the salt concentration for the electrolyte is well above zero for the 70 µm thick electrode, indicating that the transport limitations in the electrolyte would be important only for much thicker electrodes. There are also no oxide diffusional limitations indicated by the current distribution for the 70 µm thick electrode given in Figure H-29.

Changing the positive electrode thickness not only affects the impedance, but also the rate of increase in impedance, as shown in Figure H-30. In Figure H-30, the slope of the 70 µm thick positive electrode line is less than that for the 35 µm electrode, which is true for both the impedance and its percent change. Effectively as the positive electrode ages and the interfacial impedance increases, the thicker electrode will be impacted less. The thicker electrode has more electrochemically active area for the current to spread into, thus reducing the impact of increasing the interfacial impedance on the overall electrode impedance. This effect suggests that increasing the electrode thickness can lower the cell's impedance increase, all other factors remaining constant. Of course, as indicated above, care must be taken to avoid any transport limitations.

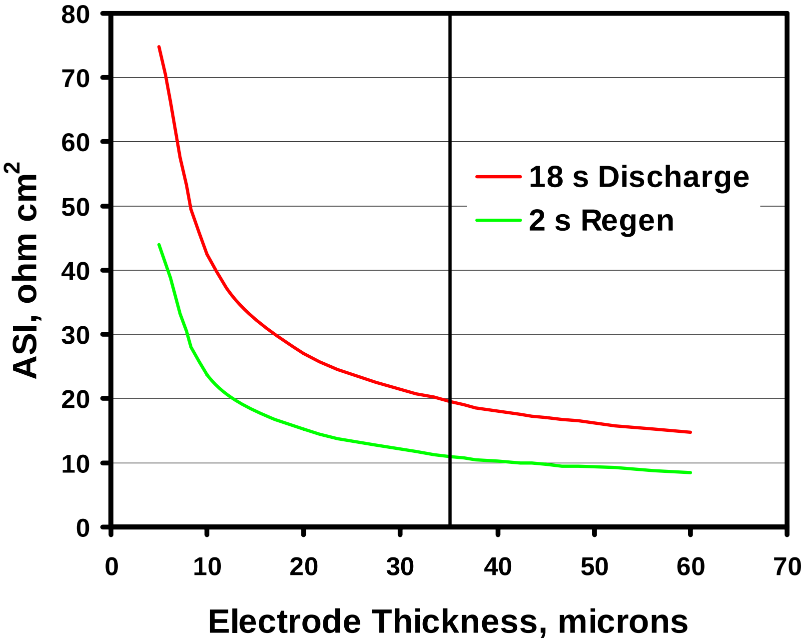

Fig. H-27. Simulation of Positive Electrode Impedance as a Function of Electrode Thickness during a 5C HPPC Test at 60% SOC. The vertical line indicates Gen 2 positive electrode thickness (35 µm).

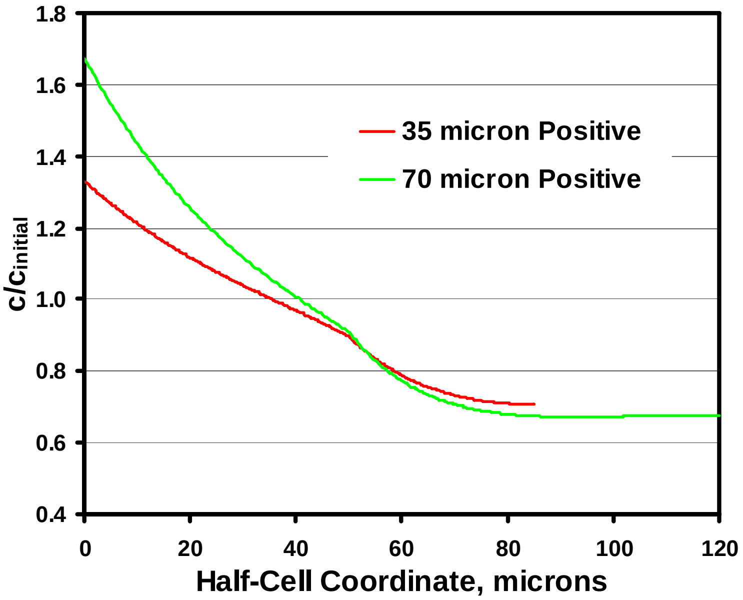

Fig. H-28. Simulation of Positive Electrode during a 5C HPPC Test at 60% SOC, Showing the Salt Concentration Distribution at 18 s into the Discharge Pulse for 35 and 70 µm Thick Electrodes. The separator side of the negative electrode is at 0 µm, the separator side of the positive electrode is at 50 µm, and the current collector side of the positive electrode is at 85 µm for the 35 µm thick electrode and 120 µm for the 70 µm thick electrode.

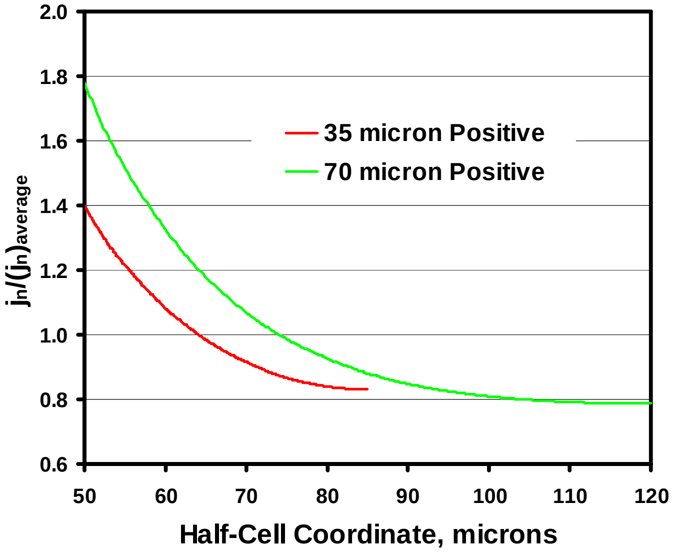

Fig. H-29. Simulation of Positive Electrode during a 5C HPPC Test at 60% SOC, Showing the Current Distribution from the Separator Side of the Positive Electrode (50 µm) to the Current Collector Side (85 µm for the 35 µm Thick Electrode and 120 µm for the 70 µm Thick Electrode) at 18 s into the Discharge Pulse.

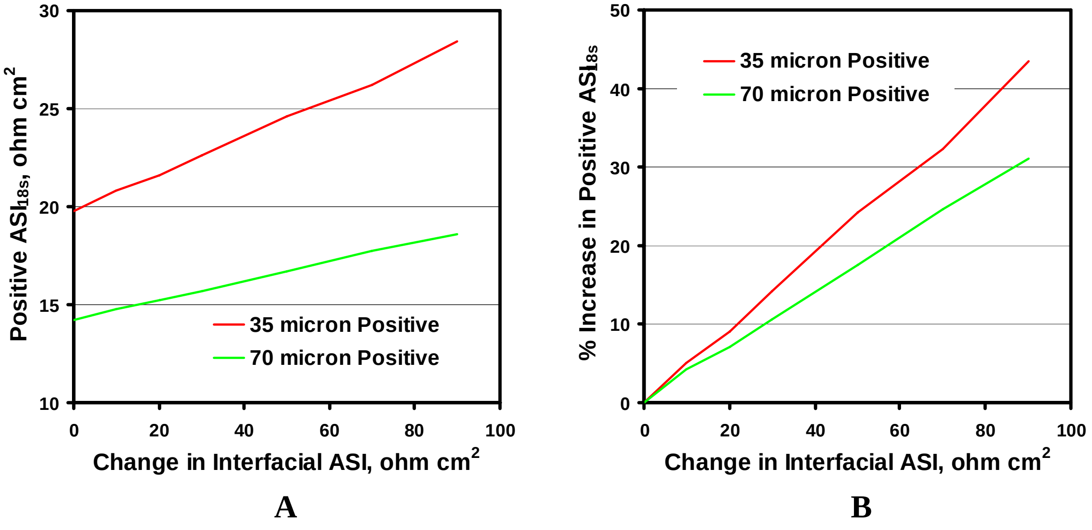

Fig. H-30. Simulation of Positive Electrode 18 s Discharge Impedance during a 5C HPPC Test at 60% SOC as a Function of Increasing Interfacial Impedance for 35 and 70 µm Thick Electrodes. Positive electrode impedance is given in (A), and its percent change is given in (B).

The phenomenological modeling studies presented here, when combined with the experimental effort, has added much to the understanding of Gen 2 lithium-ion cell technology. Future studies will examine variations in cell performance with temperature, as well as the performance of other lithium-ion cell technologies.

References

1. Newman, J., and K. Thomas-Alyea, Electrochemical Systems, John Wiley and Sons, New York (2004).

2. Gúnen, E., Dissertation, Illinois Institute of Technology, Chicago, IL (2003).

3. Dees, D., E. Gúnen, D. Abraham, A. Jansen, and J. Prakash, Alternating Current Impedance Electrochemical Modeling of Lithium-Ion Positive Electrodes, J. Electrochem. Soc. **152**(7), A1409 (2005).

Distribution for ANL-05/21

Internal (Printed and Electronic Copies):

D. P. Abraham (20)
D. W. Dees
G. L. Henriksen (50)

Internal (Printed Copy Only):

J. F. Miller
D. J. Graziano

Internal (Electronic Copy Only):

K. Amine
I. Belharouak
I. D. Bloom
Z. Chen
R. E. Gerald II
A. Jansen
C. S. Johnson
S.–H. Kang
J. Liu
W. Lu
P. A. Nelson
M. M. Thackeray
J. T. Vaughey
D. R. Vissers
Q. Wang
M. R. Hale, TIS
A. Foley
D. Lewis

External (Printed and Electronic Copies):

D. Doughty, Sandia National Laboratories, Albuquerque, NM (2)
K. Gering, INEEL, Idaho Falls, ID (2)
F. R. McLarnon, Lawrence Berkeley National Laboratory, Berkeley, CA (15)
X. Q. Yang, Brookhaven National Laboratory, Upton, NY (2)
E. Sammann, CMM, University of Illinois at Urbana-Champaign (2)

External (Printed Copies Only):

M. Alamgir, Compact Power, Monument, CO
M. Andrew, Johnson Controls Inc., Milwaukee, WI
C. Ashtiani, DaimlerChysler, Rochester Hills, MI
J. Barnes, USDOE, Washington, DC
B. Blakemore, Ford Motor Co., Dearborn, MI
R. Brodd, Broddarp of Nevada, Inc., Henderson, NV
J. Deppe, Davidsonville, MD
J. DiCarlo, Lithion, Inc., Pawcatuck, CT
T. Duong, USDOE, Washington, DC
M. A. Habib, General Motors Corp., Warren, MI
H. Haskins, Corvallis, OR
D. Howell, USDOE, Washington, DC
T. R. Jow, Army Research Laboratory, Adelphi, MD
K. Kepler, Farasis Energy, Inc., Alameda, CA
T. Miller, Ford Motor Co., Dearborn, MI
R. Minck, Laguna Niguel, CA
P. Onnerud, TIAX LLC, Cambridge, MA
N. Raman, SAFT America, Inc., Cockeysville, MD
V. Saharan, Delphi Corp., Flint, MI
J. Stockel, NRO/CIA, Chantilly, VA
J. Symanski, Johnson Controls Inc., Milwaukee, WI
H. Tataria, General Motors Corp., Troy, MI
T. Tran, Sentech, Inc., Bethesda, MD
M. Verbrugge, General Motors Corp., Troy, MI
A. Webber, Energizer, Westlake, OH

External (Electronic Copies Only):

M. A. Buckley, ANL Library-E